IRAS 01072+4954

A laboratory for studying
the star formation − AGN relation
in the local universe

vorgelegt von

Mónica Eilene Valencia-Schneider, geb. Valencia Duarte
aus Bogota, Kolumbien

Köln 2012

To my parents

.

Abstract

Most of the galaxies – if not all – harbor a supermassive black hole (SMBH) at the center. Observationally, several pieces of evidence suggest that the stellar mass growth of the galaxies and the accretion of matter onto their SMBHs are related to each other in a sort of co-evolution. However, the nature of this relation is still not well understood. Detailed studies of nearby sources are fundamental and indispensable to discover tracers and derive observables that can be used to constrain the properties of the higher-redshift galaxy population.

The aim of this Thesis is to study the star formation and the accretion process in the galaxy IRAS 01072+4954 ($z \approx 0.023$). The main analysis is based on near-infrared (NIR) integral-field spectroscopic observations of the central region $\sim (1.4 \times 1.4)\,\mathrm{kpc}^2$, that were performed with Gemini-NIFS on October 2008. The instrument, assisted by the Adaptive Optics system ALTAIR, provides simultaneously high angular and spectral resolution allowing to dissect spatially the nucleus down to few tens of parsecs and probe the stellar and gas kinematics with a resolution of $\sim 24\,\mathrm{km\,s^{-1}}$. The investigation is complemented with measurements at other wavelengths available in the literature.

The stellar mass of the galaxy is estimated to $\sim 10^{10}\,\mathrm{M_\odot}$ based on the constructed surface brightness profile. Its global star formation rate, calculated from the far-infrared photometry, is $\sim 5\,\mathrm{M_\odot\,yr^{-1}}$. This means that IRAS 01072+4954 is a starburst galaxy, with a stellar-mass doubling time-scale of ~ 2.5 Gyr. In the bulge the efficiency of the star formation process is found to be $> 50\%$, implying a depletion timescale (time in which the gas mass is converted into stars) of ~ 1 Gyr. The properties of the stellar populations in selected regions on the bulge are studied using the absorption features in the *HK*-band spectra. Metallicities lower than solar ($-1 < \mathrm{[Fe/H]} \lesssim 0.1$) are found across the bulge, whose continuum emission is dominated by young-to-intermediate age stars ($5 \times 10^6 - 8 \times 10^8$ yr). This combination of properties suggests that the galaxy is moderately young. Most of the stellar population discriminators in the NIR are biased against young supergiant stars. Here, a new spectral index that quantifies the strength of an unexplored feature at $1.55\,\mu\mathrm{m}$ is proposed. This index is sensitive to stars of K-M spectral types and luminosity classes I-III.

The nature of the active galactic nuclei (AGN) of this source has been a mistery, because, while its X-ray emission is typical of a Type 1 AGN, its optical spectrum does not exhibit the characteristic broad emission lines. A recently proposed 'True'-Seyfert 2 type, which is at the odds with the unified model of AGN, could explain these contradictory observations. Here, it is proven that the properties of the AGN are not a matter of obscuration, nor of contrast against the circumnuclear star formation, but probably due to the faintness of the broad line region. If that is the case, IRAS 01072+4954 would power broad lines with widths of only $\sim 450\,\mathrm{km\,s^{-1}}$, one of the narrowest ever detected. If not, it would be one of the most intriguing 'True'-Seyfert 2 candidates in the current research on AGN-classification.

To characterize the AGN, each of its components is analysed in detail: the torus, the accretion disk, the black hole, and the theoretically expected broad

line region. Using several scaling relations, the black hole mass is estimated in $M_{\mathrm{BH}} \sim 10^5\,\mathrm{M}_\odot$. The different estimates are compared and the validity of these relations for low-M_{BH} is discussed. In general, pseudobulges and barred galaxies – like IRAS 01072+4954 – lie under these correlations. Here, it is shown that if the $M_{\mathrm{BH}} - L_{\mathrm{bulge}}$ and $M_{\mathrm{BH}} - M_*$ correlations are broken at $\sim 7 \times 10^7\,\mathrm{M}_\odot$ as some groups have suggested, all M_{BH} estimations for IRAS 01072+4954 agree within the scatter of the correlations. Here, an explicit expression for the $M_{\mathrm{BH}} - L_{\mathrm{bulge},\,K}$ that includes the aforementioned break is proposed. The estimated accretion-disk bolometric luminosity $L_{\mathrm{bol}} \sim 10^{42.5}\,\mathrm{erg\,s^{-1}}$, implies that the black hole is actively accreting mass at a rate $\lambda_{\mathrm{Edd}} \approx 0.2$, i.e., $\dot{M} \sim 5.5 \times 10^{-4}\,\mathrm{M}_\odot\,\mathrm{yr^{-1}}$. A tentative classification as Narrow Line Seyfert 1 is proposed for the AGN.

The excitation mechanisms of the NIR [Fe II] and H_2 are studied in order to disentangle the different ionization sources on the bulge. The [Fe II] kinematics shows signs of a biconical outflow, while the dominant motion of the ionized and molecular Hydrogen is rotation consistent with that of the stars in the disk. It is shown that the starburst cannot produce the observed outflow leaving the AGN feedback as possible explanation. Finally, the feeding and feedback processes are discussed in the context of the Kennicutt-Schmidt law.

IRAS 01072+4954 is probably a unique source, or at least, it is one of the very few galaxies with such extreme star-forming and AGN-accretion properties. According to Heckmann et al. (2004), in the local universe, only $\sim 0.2\%$ of the black holes with $M_{\mathrm{BH}} < 3 \times 10^7\,\mathrm{M}_\odot$ might be active, and they would be responsible for $\sim 50\%$ of the current total mass-accretion. Observations of more sources like IRAS 01072+4954 will help on building the local inventory of highly accreting systems and might help on understanding their effects on the stellar mass growth across the cosmic time.

Zusammenfassung

Die meisten aller Galaxien, wenn nicht alle, beherbergen ein supermassives schwarzes Loch (SMBH, supermassive black hole) in ihrem Zentrum. Beobachtungen liefern Indizien dafür, dass das Wachstum der stellaren Masse der Galaxien mit der Akkretion von Materie auf ihre SMBHs in einem evolutionären Sinne verbunden sind. Die genauen Ursachen dieser Beziehung sind allerdings noch nicht verstanden. Detaillierte Untersuchungen von 'nahen' Objekten sind daher unentbehrlich, um Spuren zu entdecken und Observablen abzuleiten, mit deren Hilfe man die Eigenschaften der weiter entfernten Galaxienpopulation einschränken kann.

Ziel dieser Arbeit ist die Untersuchung der Sternentstehung und des Akkretionsprozesses in der Galaxie IRAS 1072+4954 ($z \approx 0.023$). Der Hauptteil der Analyse basiert auf Nahinfrarot (NIR) Integral-Field Spectroscopy Beobachtungen des zentralen Gebietes der Galaxie $\sim (1.4 \times 1.4) \, \mathrm{kpc}^2$. Diese wurden mit Gemini-NIFS im Oktober 2008 durchgeführt. Unterstützt von Adaptiver Optik (ALTAIR System), liefert das System hohe räumliche und spektrale Auflösung und erlaubt es das Zentralgebiet auf Skalen von 10 pc aufzulösen als auch die Stern- und Gaskinematik mit einer Geschwindigkeitsauflösung von $\sim 24 \, \mathrm{km \, s^{-1}}$ zu untersuchen. Diese Studie wird ergänzt durch Beobachtungsergebnisse bei anderen Wellenlängen, die der Literatur entnommen sind.

Die stellare Masse der Galaxie beträgt schätzungsweise $\sim 10^{10} \, \mathrm{M_\odot}$ und basiert auf dem gemessenen Oberflächenhelligkeitsprofil. Die globale Sternentstehungsrate ergibt sich aus der Ferninfrarot-Photometrie zu $\sim 5 \, \mathrm{M_\odot \, yr^{-1}}$. Damit kann IRAS 01072+4954 als Starburstgalaxie eingestuft werden, mit einer Verdopplungszeitskala der Sternmasse von ~ 2.5 Gyr. Die Sternentstehungseffizienz im Bulge (der zentralen Verdickung) der Galaxie ist $> 50\%$, d.h. dass innerhalb von $\sim 1 \, \mathrm{Gyr}$ das verfügbare Gas in Sterne umgewandelt wird. Die Eigenschaften der Sternpopulationen werden in ausgewählten Gebieten des Bulges mittels Absorptionslinien im HK-Spektrum untersucht. Dabei ergeben sich Metallizitäten im Bulge, die kleiner als die der Sonne sind ($-1 < \mathrm{[Fe/H]} \lesssim 0.1$). Das Kontinuum wird von jungen bis mittelalten Sternen dominiert ($5 \times 10^6 - 8 \times 10^8 \, \mathrm{yr}$). Dies alles deutet darauf hin, dass die Galaxie relativ jung ist. Zu beachten ist, dass die meisten der Indikatoren für Sternpopulationen im NIR eine Bias gegenüber jungen Überriesen aufweisen. Daher wird ein neuer spektraler Index vorgeschlagen, der die stärke eines bisher unerforschten Feature bei $1.55 \, \mu\mathrm{m}$ beutzt. Dieser Index ist sensitiv gegenüber den Sternklassen K-M und Leuchtkraftklassen I-III.

Die Natur des aktiven Kerns (AGN) dieser Galaxie ist ein Mysterium, da, obwohl seine Röntgenleuchtkraft typisch für die von type-1 AGN ist, das optische Spektrum keine breiten erlaubten Emissionslinien zeigt. Eine vor kurzem vorgeschlagene Klasse von 'True'-Seyfert 2 Galaxien, die im Widerspruch zum weitläufig benutzten *vereinheitlichten Modell* von AGN steht, könnte diese Beobachtungen erklären. Hier wird gezeigt das dies nicht durch Absorption oder den Kontrast bezüglich der zirkumnuklearen Sternentstehung hervorgerufen wird, sondern womöglich durch die 'Schwäche' der Broad Line Region. Ist dies der Fall, dann besäße IRAS 01072+4954 mit eine Linienbreite von nur $\sim 450 \, \mathrm{km \, s^{-1}}$ eine der schmal-

sten je detektierten breiten erlaubten Komponenten. Andernfalls wäre sie eine der interessantesten 'True'-Seyfert 2 Kandidaten der gegenwärtigen AGN Forschung.

Um den AGN zu charakterisieren, werden im Folgenden seine einzelnen Bestandteile näher untersucht: der Torus, die Akkretionsscheibe, das Schwarze Loch und die theoretisch erwartete Broad Line Region. Unter Benutzung einer Reihe von Skalierungsrelationen wird die Masse des Schwarzen Lochs auf $M_{\mathrm{BH}} \sim 10^5\,\mathrm{M}_\odot$ geschätzt. Die einzelnen Abschätzungen werden mit anderen Untersuchungen verglichen und im Zusammenhang mit Schwarzen Löchern geringer Masse auf ihre Gültigkeit hin untersucht, Im allgemeinen liegen Galaxien mit Pseudobulges und Balken, wie IRAS 01072+4954, unterhalb der Korrelationen. Hier wird gezeigt, sind die $M_{\mathrm{BH}} - L_{\mathrm{bulge}}$ und $M_{\mathrm{BH}} - M_*$ Korrelationen bei $\sim 7 \times 10^7\,\mathrm{M}_\odot$ gebrochen, wie es einige Forschergruppen vorschlagen, dann stimmen alle Masseabschätzungen von IRAS 01072+4954 innerhalb der Streuung der Korrelationen überein. Ein explizierter Ausdruck für $M_{\mathrm{BH}} - L_{\mathrm{bulge},\,K}$ wird präsentiert. Die abgeschätzte bolometrische Leuchtkraft der Akkretionsscheibe, $L_{\mathrm{bol}} \sim 10^{42.5}\,\mathrm{erg\,s}^{-1}$, deutet darauf hin, dass das Schwarze Loch aktiv Masse mit einer Rate von $\lambda_{\mathrm{Edd}} \approx 0.2$ akkretiert, d.h. $\dot{M} \sim 5.5 \times 10^{-4}\,\mathrm{M}_\odot\,\mathrm{yr}^{-1}$. Damit fällt IRAS 01072+4954 potentiell in die Klasse der Narrow Line Seyfert 1 Galaxien.

Die Anregungsmechismen der NIR Emissionslinen [Fe II] und H_2 werden untersucht, um die verschiedenen Ionisationsquellen innerhalb des Bulges auszumachen. Die [Fe II] Kinematik zeigt Spuren eines bikonischen Ausflusses, wohingegen die vorherrschende Bewegung des ionisierten und molekularen Wasserstoffes konsistent mit der Rotation der Sterne in der Scheibe ist. Es wird gezeigt, dass der Starburst alleine den Ausfluss nicht erklären kann. Somit bleibt eine Wechselwirkung mit dem AGN als Erklärung übrig. Zum Abschluss werden die Speisungs- und Wechselwirkungsprozesse im Zusammenhang mit dem Kennicutt-Schmidt Gesetz besprochen.

IRAS 01072+4954 ist wahrscheinlich eine einzigartige Quelle, oder gehört zu einer kleinen Gruppe von Galaxien mit extremen Sternentstehungs- und AGN-Akkretionseigenschaften. Den Ergebnissen von Heckman et al. (2004) folgend, sind nur $\sim 0.2\%$ der Schwarzen Löcher mit $M_{\mathrm{BH}} < 3 \times 10^7\,\mathrm{M}_\odot$ aktiv und würden für $\sim 50\%$ der gesamten heutigen Masse-Akkretion verantwortlich sein. Mehr Beobachtungen von Galaxien wie der hier vorgestellten werden dabei helfen ein Inventar von stark akkretierenden Systemen zu erstellen, welches widerum von Bedeutung ist, um die Effekte des Wachstums der stellaren Masse über kosmologische Zeitskalen zu erfassen.

Contents

Introduction and Overview

Increasing observational evidence suggests that a supermassive black hole (SMBH) sits at the center of every galaxy, or at least of the most massive ones. Some of them have been detected by their gravitational influence on the stars orbiting close to them – like in the case of SgrA*, the SMBH at the center of our galaxy; others are detected by the enormous amount of energy released when they are actively accreting matter – which in some cases is as much as that emitted by the whole host galaxy. Some of these active galactic nuclei (AGN) also launch powerful jets that can push away the interstellar material of the galaxy creating shells and cavities.

During the past decade it was recognized that there exist tight relations between the black holes and their host galaxy spheroids, i.e. the bulges in spirals, and the whole galaxies in ellipticals. More massive black holes reside in more massive and more luminous systems! Interestingly, these correlations hold for most of the observed black holes, with masses $M_{\mathrm{BH}} \sim 10^7 - 10^9\,\mathrm{M}_\odot$, determining the ratio of spheroid mass-to-black hole mass to be $\sim 10^{2.5-3.0}$ in every galaxy. This has been interpreted in two ways: As a consequence of self-regulated growth of spheroids and black holes, which operates independently of particular characteristics of individual galaxies; or as the result of the mass assembly process in the universe which, through consecutive series of merging events, drives the scaling relations without the need of any internal self-regulation. However, at the low-mass end, these correlations are not longer valid. Most sources with $M_{\mathrm{BH}} < 10^{6.5}\,\mathrm{M}_\odot$ systematically lie below the correlation. Is this an evidence for evolution driven by secular (internal) processes instead of major mergers? Is the self-regulation less efficient in these galaxies? The number of sources with secure photometric and kinematic measurements is still very limited, and most of them are located far away from us ($z \sim 0.1$). *More observations of nearby galaxies with low-mass black holes are needed.*

On the other hand, statistical studies of several thousands of galaxies in the local universe ($z \sim 0.2$) have revealed strong correlations between the AGN activity and the star-formation process in these galaxies. Black holes accrete mass at higher rates in galaxies that are more actively forming stars! The luminosity of the AGN and that of the star formation decrease in similar ways while the stellar population of the galaxy gets older. Is this a sign of a regulated process? The time-scales of the AGN activity and the starburst argue against this possibility. A black hole is not accreting matter all the time. Its duty cycle is on average $\sim 10^7$ yr. Meanwhile,

the process of building the stellar mass in a galaxy, which is directly related with the availability of cold gas, happens in bursts that last $\sim 10^9$ yr and that are not necessarily continuous, nor do they occur across the entire galaxy simultaneously. High-mass black holes have been more active in the past, around $z \sim 2$, where also the starburst activity peaks. According to the downsizing scenario, low-mass black holes should be more active in the local universe. *That makes them wonderful laboratories to test if the relation between AGN and star formation also holds in these systems, and to study its nature.*

How to find nearby galaxies with active nuclei and enhanced star formation? Our approach was to look into the so-called 'Starburst/Seyfert composite' galaxies, which are strong far-infrared emitters indicating ongoing star formation, and which have X-ray luminosities typical of galaxies containing an AGN. This Thesis is a detailed study of one of these systems: IRAS 01072+4954, located at $z \approx 0.02$. The nucleus of the galaxy was observed in the near-infrared with the highest angular and spectral resolutions available in ground-based telescopes. The central ~ 1 kpc was dissected down to a resolution of ~ 70 pc, and the spectra in this region can reveal gas and stellar motions along the line of sight down to ~ 25 km s^{-1}. The data reduction and analysis of these observations were complemented by infrared, optical and X-ray information of this source available in the literature.

In the first chapter, the reader can find an introduction to the AGN paradigm, where I have outlined some of current ideas on the physics of the accretion phenomena, as well as some caveats and challenges for the unified models of AGN. The basic concepts and methods employed in the study of star formation and stellar populations are also presented. In chapter 2, the galaxy IRAS 01072+4954 is introduced. I summarize what was known about the source, and the specific questions addressed in this research. The near-infrared (NIR) regime is a fantastic window to observe tracers of the stellar bursts and of the black hole activity. However, as it is described in chapter 3, the atmosphere is not very cooperative: it is a turbulent medium that emits and absorbs radiation. Only after getting proper control of these aspects, it is possible to access the valuable astronomical information. Thus I mention what are the challenges of the NIR astronomy and how they have been solved in the case of our observations. Chapter 4 deals with the star formation in the galaxy, and particularly in its bulge. I also present the new data, mapping the continuum, line emission, line absorption and extinction in the central ≈ 1 arcsecond. The type of the black-hole activity in this source was a mystery, because the existing optical and X-ray observations offered apparently contradictory results. One of the main aims of the present work was to determine the nature of the AGN. The results are presented in chapter 5. Finally, regarding the AGN – star formation relation, I describe in chapter 6 some efforts on disentangling both contributions in the NIR emission, and I also explore the evidences for AGN feeding and feedback. Every chapter contains a summary of the main results obtained in each topic.

It is fascinating how much we can learn from a single source,
but it is more fascinating all that we still ignore.
Enjoy!

Chapter 1

Astrophysical Background

The stellar mass growth and its relation with the accretion of gas onto the central supermassive black hole play a fundamental role in the evolution process of a galaxy. However, the physics of these two processes is not well understood. This first chapter offers a very brief introduction to current unified model of active galactic nuclei (AGN), which has been very successful in describing a huge range of multi-wavelength phenomenology. However, there are increasing (observational and theoretical) indications that this could be an incomplete picture and some of these cases are discussed here. Further, some of the theoretical efforts to model the star formation and the evolution of the stellar populations are presented. Examples of extreme star forming sources are also shown. The concepts and methods to analyze the AGN and star formation observables introduced here would be used in the following chapters to study these processes in the galaxy IRAS 01072+4954.

1.1 Active galactic nuclei

It is believed that a supermassive black hole (SMBH) resides at the center of every galaxy, or at least, of most of them (Kormendy & Ho 2001). While they are accreting mass at a high rate, an enormous amount of energy across the whole range of the electromagnetic spectrum is released, in some cases, outshining the host galaxy. During this phase, the SMBH and the set of phenomena that are related to the accretion process are called active galactic nucleus (AGN)[1]. Numerous reviews and books have been dedicated to the extended AGN phenomenology. Here, I summarize what I consider the most relevant elements for this Thesis, that include the unified model and its caveats, luminosity and spectroscopic classification schemes, and some discussion about subtypes and 'new' kinds of AGN. The interested reader can find more information in some classic texts like Krolik (1999), Osterbrock &

---

[1]Some authors nowadays also refer to 'non-very active' black holes as AGN that are going through a low activity phase – probably due to variations in the accretion flow. Even Sgr A*, the black hole at the center of the Milky Way, which would not be identified as such if it were located in another galaxy, has been considered as a low luminosity AGN (Contini 2011).

Fernand (2006), and Peterson (2006); in reviews like Antonucci (1993), Urry & Padovani (1995), Risaliti & Elvis (2004), Tadhunter (2008), Ho (2008), Schneider (Chap. 5, 2006), and Antonucci (2012). Recently an interesting summary of fifty years of research on AGN activity has been compiled by D'Onofrio et al. (2012).

1.2   The unified model of active galactic nuclei

Active galactic nuclei are not spherical, but rather axially-symmetric. This implies that observers located at different inclinations with respect to the axis of symmetry, perceive different phenomena. These kinds of orientation effects can be seen in sources that power radio jets, which, when observed along a line of sight close to the axis of the jet, have flat spectra, and at somewhat higher inclinations have steep spectra. Other orientation effects are related with the obscuration of the central engine. Those are seen in the optical and the X-rays, where sources powering broad line emission in the optical show systematically lower X-ray column densities than sources that exhibit only narrow line emission. The unified model combines these two forms of anisotropies to explain the different 'types' of AGN.
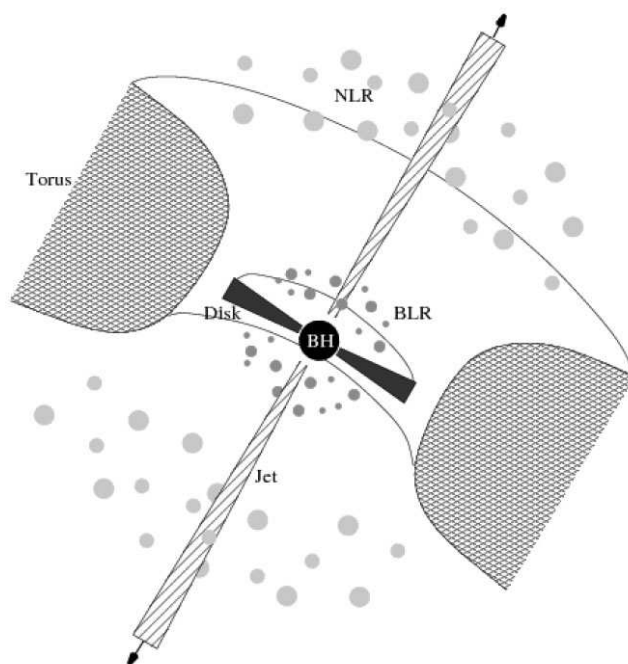

Figure 1.1: Schematic representation of the unified model of Active Galactic Nuclei (not to scale). Taken from: Middelberg & Bach (2008).

The physical model is the following. While the matter falls onto a black hole, it loses energy and angular momentum by the action of viscosity, and forms a

disk. Close to the black hole, if the radiation efficiency of the infalling material is high, the disk is geometrically thin and optically thick. The inner radius of the disk, which is associated with the innermost marginally stable orbit, depends on the spin of the black hole. For a Schwarzschild black hole of mass $M_{\rm BH} \sim 10^8 \, {\rm M_\odot}$, accreting $1 \, {\rm M_\odot}$ per year, the inner radius is $\sim 10^{14} \, {\rm cm}$. The material located at few times that distance has temperatures of few $\times \, 10^5 \, {\rm K}$ and releases energy mainly in the UV and soft X-rays (Frank et al. 2002; King 2008). The size of the outer radius of the disk is not known because the temperature of the disk is proportional to $r^{-3/4}$ and, given that the luminosity depends on the temperature, at larger radii the disk becomes undetectable. For example, at $\sim 10^{17} \, {\rm cm}$, where the emission falls into the infrared domain, the luminosity is 6 orders of magnitude less than that at the peak of the emission.

At about that distance (i.e., 10-100 light-days), the accretion fluid fragments in clouds of ionized species[2] that produce observable broad line emission. The distance from the black hole to the region occupied by these clouds, called broad line region (BLR), is $R_{\rm BLR} \simeq 0.35 \, (L_{\rm bol}/10^{46})^{0.6 \pm 0.1}$ pc, where $L_{\rm bol}$ is the bolometric luminosity of the accretion disk (Netzer 2008). The precise geometry of the BLR is unknown, but reverberation mapping techniques indicate that the radiating clouds must be in approximately keplerian orbits (Kaspi et al. 2000; Peterson et al. 2004). Given the width of the emitted lines, the clouds must also have a substantial motion in the direction perpendicular to the plane of the disk, that can be understood as turbulence. With respect to the radial motion, there is not agreement in the community. Some groups favor the idea of an outflowing 'wind'. One of the supporting arguments is the observation of clear signatures of broad line absorption in the optical/UV spectra of some quasars (Elitzur & Ho 2009; DiPompeo et al. 2012). Others, using velocity-resolved reverberation mapping techniques, argue that in the case of outflowing clouds, the blue side of the emitted line (the spectral side of the line profile located at shorter wavelengths) would respond faster than the red side to the variations of the continuum, which seems not to be in agreement with the observations. In contrast, the results seem to indicate inflowing material (Gaskell 1988; Smith et al. 2005; Denney et al. 2009). However, the time-resolution is still not good enough to provide a clear answer. In any case, it is clear that the gas velocity components $v_{\rm rot} > v_{\rm turb} \gtrsim v_{\rm radial}$ (Gaskell 2009).

Continuing further out, the clouds turn from hot and ionized to cold and dusty. They form a thick ring around the BLR, that gets thicker with radius, and might look like a bird's nest, or like a torus (Elitzur & Shlosman 2006; Nenkova et al. 2008a,b). There are indications, however, that the covering factor remains approximately constant (Gaskell et al. 2007). The innermost radius where dust can be found in the clouds depends on the temperature at which the grains are heated by

---

[2]As a curiosity, the size of one of these clouds can be $\sim 10^{10}$ meter (assuming a broad line region (BLR) of $\sim (10 - 100)$ light-days radius, which is about the size measured by reverberation mapping, and about $10^6 - 10^8$ clouds, as calculated by modelling the emission in the BLR), which is more than 100 times bigger the size of Jupiter!

the radiation field. The limit is set by the sublimation temperature $T \sim 1500\,\mathrm{K}$, which corresponds to $R_{\mathrm{sub}} \simeq 0.5\,(L_{\mathrm{bol}}/10^{46})^{1/2}\,\mathrm{pc}$. The extent of the dusty structure, classically called torus, might be $R_{\mathrm{torus}} \sim (20-30)R_{\mathrm{sub}}$ (Elitzur 2008). However, there is not compelling evidence of that. Moreover, NIR observations have shown ionized molecular hydrogen emission from the central few tens of parsecs in some sources. This suggests the existence of a molecular 'torus-like' structure with high enough column densities that obscures the central engine (Fernandez et al. 1999; Hicks et al. 2009). Optically, extended disk structures have been seen in some nearby nuclei. Figure 1.2 shows a composition of ground-based optical and radio, and HST optical image of the NGC 4261 core. The right panel shows a dusty disk of radius $\sim 150\,\mathrm{pc}$ around the nucleus. As a comparison, the inferred size of the torus derived form the expression above is $R_{\mathrm{torus}} \sim 0.5\,\mathrm{lightyears}$.
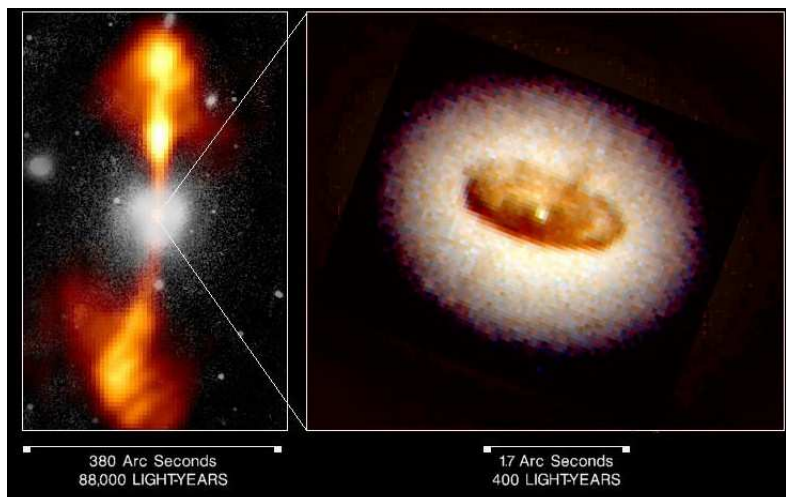
Figure 1.2: Images of the elliptical galaxy NGC 4261. *Left:* Composite image of the optical galaxy and radio jets as observed from the ground. *Right:* High-resolution HST Image of the Core. Credit: Walter Jaffe/Leiden Observatory, Holland Ford/JHU/STScI, L. Ferrarese/Johns Hopkins University, and NASA.

Two other structures that participate in the AGN phenomena are the jet and low-density clouds that extend up to hundreds of parsecs from the black hole and produce narrow emission lines. They are ionized by the radiation from the accretion disk, which reaches the interstellar medium located at both opening angles of the torus. This biconical region is called narrow line region (NLR). Much more collimated is the radiation that escapes through the jet. The physics of the production of these highly energetic flows is not known. Recently, from magneto-hydrodynamic simulations it has been suggested that the Blandford-Znajek mechanism, an electromagnetic version of the Penrose process, could extract from a spinning black hole the necessary energy to accelerate a jet (Tchekhovskoy & McKinney 2012; Narayan & McClintock 2012).

1.2.1 AGN Classification

In general, AGN can be divided into two groups: radio-loud or radio-quiet. The definition of radio loudness is sometimes given by a radio luminosity threshold, and sometimes by the ratio of the radio and optical luminosities. Within both populations, it is possible to identify two types. Type 1 sources display narrow (FWHM $\sim$ few $\times$ 100 km s^{-1}) and broad emission lines (FWHM $\gtrsim$ 1000 km s^{-1}), and have low X-ray absorption column densities $N_{\rm H} < 10^{22}$ cm^{-2}. Type 2s only exhibit narrow lines, and in general are obscured in X-rays. Both types show narrow forbidden emission lines, e.g., [O III], [N II], [S II], [Ne III], and [O II]. In the radio-quiet group, the two types are known as Seyfert 1 and Seyfert 2 (Sy1, Sy2). In QSOs and Low Ionization Narrow Line Regions (LINERs), Type 1s and Type 2s have also been observed. Similarly, among radio-loud AGN, Broad Line Radio Galaxies (BLRG), Narrow Line Radio Galaxies (NLRG), and Weak Low Ionization Galaxies (WLIG) have been found.

According to their optical luminosity, AGN can be divided in two (or three) classes: quasars, (and?) Seyferts, and LINERs + LLAGN. Historically, quasi-stellar radio sources (quasars) were discovered in radio surveys, and were identified with stellar-like optical sources. It was also noticed that they appeared to have blue colors in the optical. Searching for this property, their radio-quiet counterparts, the Quasi-Stellar Objects (QSOs), were discovered. The main characteristic of quasars and QSOs is their brightness, which in most of the cases outshines the host galaxy. On the other hand, Seyfert galaxies were recognized by their strong emission lines in the optical spectra. Some of them are also very bright, but in contrast to quasars, the host galaxies are clearly visible in the optical images. Because of the different methods and wavelength regimes for identification and classification, during the first decade of parallel research, it was not noticed that they were the same kind of objects. The division between quasars and Seyferts has been arbitrarily set to $M_B = -21.5 + 5 \log h$, and is still in use for historical reasons.

While QSOs and Seyferts seem to be the same kind of AGN population, low-luminosity AGN (LLAGN), which are defined by the faintness of the Hα line, $L_{\rm H\alpha} \lesssim 10^{40}$ erg s^{-1}, and some LINERs might indeed be a separate class (Ho et al. 1997b; Ho 2008). Some authors have suggested that the accretion process in LLAGN and some LINERs might happen through geometrically-thick radiatively-inefficient accretion disks (Ho 2003; Macchetto & Chiaberge 2007). It is unknown how that affects the production of broad emission lines (or jets). It seems that at somewhat higher masses these galaxies become radio-loud, a property that has been associated with jet launching (Maoz 2007; Chiaberge & Marconi 2011). There are sources that show signs of both components: a thick disk, and optical broad line emission (Schimoia et al. 2012; Younes et al. 2012). Theoretically, in these radiatively-inefficient cases no BLR is expected to form (Laor 2003; Nicastro 2000; Nicastro et al. 2003; Trump et al. 2011). Finally, also some LINERs and LLAGN look like scaled-down versions of brighter AGN (Netzer 2009, this work).

1.2.2   Caveats and challenges

The unified model of AGN has achieved great success in organizing and integrating a huge range of multi-wavelength AGN phenomenology in one simple scheme (e.g., Barthel 1989; Antonucci 1993; Urry & Padovani 1995). The detection of polarized broad lines and high X-ray column densities ($N_{\rm H} > 10^{22}\,{\rm cm}^{-2}$) in most ($\lesssim$50% and ∼96%, respectively) Seyfert 2 galaxies (Sy2) supports the idea of the presence of toroidal obscuring material ('torus') covering the central engine and the broad-line region (e.g., Miller & Goodrich 1990; Goodrich & Miller 1994). In my view, there are two main caveats to the model. First, the implicit assumption that all AGN are identical: accreting through geometrically thin disks, carrying the same atomic compositions/metallicities in the broad line region clouds, and having in general the same torus and jet properties. Without this assumption, a model based solely on orientation effects cannot work. One might think that the fact that the unified scheme has worked so well in most of the cases is indeed an indication that AGN are in essence very similar to each other. On the other hand, the variety of classes and subclasses of AGN suggests that, although the model is very flexible – i.e., there is not a consensus on the properties of the torus: covering factor, thickness, opening angle, etc. –, the underlying physics is still unknown. The second limitation is related to the character of the astronomical observations. With the development of new techniques and the improvement in sensitivity and resolution of the instruments, sources that were previously classified as non-active, or Type 2, observed under better conditions reveal their active, or Type 1 nature.

One of the major challenges for the development of a more 'physical' unification scheme is the inclusion of different modes of accretion and their relation to the jet production. Early ideas on this aspect can be found in Lawrence (1987) and Dopita (1997). This is well exemplified by the amount of mechanisms proposed to describe the emission of LLAGNs and LINERs, as discussed before. Another problematic case is that of sources lacking a BLR, the so-called True-Sy2s. Theoretically, their existence has been hypothesized (Nicastro 2000; Laor 2003; Elitzur & Ho 2009) and several candidates have been observed (Boisson & Durret 1986; Tran 2001; Panessa & Bassani 2002; Hawkins 2004; Bianchi et al. 2008; Shi et al. 2010; Tran et al. 2011). The absence of broad lines in their spectra cannot be explained by obscuration given the very low $N_{\rm H}$ derived from their X-ray emission. Due to the compelling evidences, extensions of the unified model have emerged (Maiolino et al. 1995; Dopita 1997; Elitzur & Shlosman 2006; Zhang & Wang 2006; Trump et al. 2011), but there are still many open questions. Are all AGN the same? Do all have a torus? In what ranges of black hole mass and bolometric luminosity is an AGN able to sustain a BLR, or to launch a jet?

Unification proposals have to overcome also our attempt to force continuous sequences of properties into discrete bins. A particular example is the case of the Narrow Line Seyfert 1s (NLSy1s), whose differences with general Type 1 sources are undefined (Valencia-S. et al., in prep). Other examples are LINER 2 in relation with Sy 2s, and BL Lacs with quasars (Tadhunter 2008; Antonucci 2012).

1.3   Star formation

Star formation is one of the main processes in the evolution of a galaxy. Through it, the cold gas reservoir is consumed, the chemical composition of the interstellar medium is transformed, and energy is pumped back ('feedback') preventing or enhancing more star formation (Telesco 1988). The spectral energy distribution (SED) of a normal[3] galaxy is shaped by the history of its stellar populations. The galactic spectrum is, therefore, a complex combination of emission from gas and dust at different temperatures, and groups of stars with various ages, metallicities and initial mass functions. Continuous, current and old star formation can be traced by their imprints at particular wavelengths, however observations in different bands are often required to quantify their relative contribution to the overall emission. Synthesis models calibrated on local galaxies are used to reproduce the galaxy spectra (e.g., Bruzual A. & Charlot 1993; Sternberg 1998; Maraston 2005; Leitherer et al. 2010). To do that, stellar spectra (from stellar atmosphere models or from spectral libraries) that correspond to nodes in a grid of stellar evolution tracks – i.e., luminosity and effective temperature of stars as a function of age and initial stellar mass –, weighted by an initial mass function, are added up. It is desirable that the stellar spectra cover a wide range of effective temperatures, surface gravities and metallicities. In this way, the spectrum of a single-age population as a function of age is obtained. A linear combination of stellar populations of different ages reddened to account for the effects of the extinction should reproduce the stellar spectrum of a galaxy (without considering dust and other non-thermal components). However, this procedure is affected by degeneracies, the most known is the age/metallicity degeneracy, which comes from the fact that broad-band colors are not uniquely determined by particular combinations of age and metallicity. Current research on characteristic features in the spectrum produced by a specific stellar population, so called 'spectral indices' (e.g. the Lick Optical indices, Worthey et al. 1994), might help on mitigate these problems in the future.

Star formation in galaxies happens in two different modes: 'normal' star formation that occurs over long periods of time with moderate star formation rates (SFR, measured in $M_\odot \, yr^{-1}$), and 'starburst', when the conversion from gas into stars is very efficient so that the specific star formation rate (sSFR $= SFR/M_*$, with M_* the stellar mass of the galaxy) is enhanced over a small fraction of the cosmic time (Larson & Tinsley 1978; Kennicutt 1998a; Daddi et al. 2010). Blue galaxies – i.e., those in the lower region of the g-i color versus i-band absolute magnitude diagram – in the local universe are actively forming stars with sSFR $\sim 0.2 \, Gyr^{-1}$ (Bauer et al. 2005), but this value depends on M_*. Elbaz et al. (2011) define an infrared main sequence mode of star formation as the median sSFR of star forming galaxies as a function of redshift. A galaxy is considered as starburst if its sSFR is at least twice of that of one on the main sequence. This means that the SFR of a starburst would allow it to double its stellar mass on a time scale smaller than its

---

[3]The adjective 'normal' is used to refer to galaxies without an active nucleus.

age, assuming constant SFR over that time. The redshift dependence implies that a galaxy with a stellar mass of $10^{10}\,\mathrm{M_\odot}$ and SFR $\sim 5\,\mathrm{M_\odot\,yr^{-1}}$ if located nearby is clearly considered a starburst, but at $z \sim 1$ that would not be the case.

1.3.1   Starbursts

Enhanced star formation can occur across the whole galaxy or in compact regions. Starburst galaxies is a category that comprises very heterogeneous kinds of objects.

When young OB type stars are visible, the system can be recognized by the intense UV emission and blue color as in the case of the Blue Compact Dwarf galaxies (BCDs); otherwise, when the systems are enshrouded by dust, the high-energy photons are absorbed and reemitted in the far-infrared, like in Luminous InfraRed Galaxies (LIRGs).

Figure 1.3: XBCD I Zw18 ($z = 0.0025$) optical red-blue composite. Image taken with the HST ACS. Credit: NASA, ESA, and A. Aloisi (Space Telescope Science Institute and European Space Agency, Baltimore, Md.)

The Blue Compact Dwarfs (BCDs) were identified by Sargent & Searle (1970) as "isolated dwarf emission-line galaxies ... observationally indistinguishable from giant H II regions". They have an irregular morphology with compact high-SFR regions which provide $\sim$ 50% of the galaxy optical luminosity. The other 50% comes from the low-surface brightness, typically elliptical, evolved host galaxy, $(V - I) \sim 0.5\,\mathrm{mag}$. Their metallicities are found to be lower than the solar one. In comparison, the eXtreme metal-deficient BCDs (or XBCDs) have $\mathrm{Z_\odot}/43 \leq \mathrm{Z} \leq \mathrm{Z_\odot}/3$ and bluer host galaxies $(V - I) \sim -0.4\,\mathrm{mag}$ (Papaderos et al. 2008). This might indicate that XBCDs are indeed young systems with an age no larger than $10\,\mathrm{Gyr}$ (Guseva et al. 2003). Figure 1.3 shows a composite image of I Zw 18, the prototypical XBCD. Other closely related objects are the ultracompact blue dwarf galaxies that have less than $1\,\mathrm{kpc}$ of diameter and low masses $\sim 10^{7-9}\,\mathrm{M_\odot}$ (Corbin et al. 2006), and the luminous blue compact galaxies, which are brighter, $M_B \leq -17.5$, more massive and have SFR $\sim (1-5)\,\mathrm{M_\odot\,yr^{-1}}$ (Guzman et al. 1997).

Very high-SFR galaxies are the so-called 'Green Peas' (GPs). They were identified with the participation of more than $2\,000\,000$ volunteers in the Galaxy Zoo project (Cardamone et al. 2009). The green appearance of these objects comes from the *gri*-color composites of the SDSS catalog because they are comparatively bright in the *r*-band (Fig. 1.5). The GPs are strong emission-line galaxies with a faint continuum. The broad *r*-band brightness is enhanced because at the redshifts of the sources $0.11 \leq z \leq 0.36$, the [O III] $\lambda\lambda\,4959, 5007$ Å lie in that band. This gives rise to unusually high [O III] equivalent widths $W_{[\mathrm{O\,III}]} \sim (200 - 1500)\,\mathrm{\AA}$.

Their spectra present evidence for an old stellar population that provides at least 80% of their stellar masses (Amorín et al. 2012). Like in the BCDs, their metallicities are low, but the GPs also have enhanced nitrogen abundance. The SFR estimates using the Hα line indicate star forming rates of $\sim (3-30)\,\mathrm{M_\odot\,yr^{-1}}$, which for $M_* \sim 10^{9-10}\,\mathrm{M_\odot}$ galaxies implies among the highest sSFR in the nearby universe, sSFR $\sim (1-10)\,\mathrm{Gyr^{-1}}$. The high SFR seems to be confirmed by high UV luminosities, $L_{\mathrm{FUV}} \sim 10^{10}\,L_\odot$, although in some of these objects the presence of an AGN has been inferred from the BPT diagram. In these cases, the SFR derived from the hydrogen recombination lines is an overestimation. The recent discovery of very similar sources, the 'Green Beans' (Schirmer et al. 2012), which are extreme [O III] emitters with a pure AGN-like spectra, opens the debate on the nature of the GPs and the origin of their line-emission.
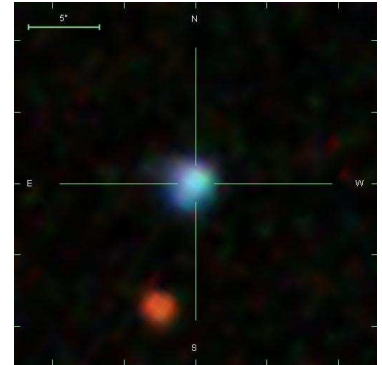

Figure 1.4: GP ($z = 0.1807$) SDSSJ092600+442736. With $W_{\mathrm{[O\,III]}} = 651.5\,\mathrm{\AA}$ its SFR $= 14.35\,\mathrm{M_\odot\,yr^{-1}}$ implying a sSFR $\sim 12\,\mathrm{Gyr^{-1}}$. Credit: SDSS.

Galaxies with infrared excess, characteristic from reprocessed dust emission, were first identified in ground-based studies (Rieke & Low 1972). It was also noticed that star formation is enhanced in systems where merging events are taking place (Toomre & Toomre 1972). With the advent of space missions, like the InfraRed Astronomical Satellite (IRAS), sources with more extreme infrared properties were discovered. The Spitzer and Herschel Observatories have allowed us to perform photometry and spectroscopy of these sources at intermediate and high redshifts (e.g., Floc'h et al. 2005; Yan et al. 2007; Kartaltepe et al. 2012). IRAS also detected thousands of sources, among them spiral galaxies – mostly late-type, irregular galaxies, and interacting systems. In the local universe, Luminous InfraRed Galaxies (LIRGs), i.e. sources with total infrared luminosities $L(8-1000\mu)$ in the range $10^{11}-10^{12}\,L_\odot$, are rare but at a comparable bolometric luminosity, they are more numerous than optically-selected starbursts and AGNs (Veilleux et al. 2009). Their number density per unit comoving volume increases dramatically with redshift and luminosity (e.g., Lonsdale et al. 2006). The total infrared luminosities $L_{\mathrm{IR}} \equiv L(8-1000\,\mu\mathrm{m})$ can be estimated from the specific fluxes f_λ measured by IRAS (Sanders & Mirabel 1996) as

$$\frac{L_{\mathrm{IR}}}{L_\odot} = 4\pi \left(\frac{D}{\mathrm{Mpc}}\right)^2 \left(\frac{F_{\mathrm{IR}}}{\mathrm{W\,m^{-2}}}\right) \left(\frac{9.521 \times 10^{51}}{3.839 \times 10^{33}\,\mathrm{erg\,s^{-1}}}\right), \qquad (1.1)$$

with the infrared flux given by

$$\frac{F_{\mathrm{IR}}}{\mathrm{W\,m^{-2}}} = 1.8 \times 10^{-14}\left[13.48\,f_{12} + 5.16\,f_{25} + 2.58\,f_{60} + f_{100}\right],$$

where the specific fluxes at 12, 25, 60 and 100 μm are in Janskys.

It has been a matter of debate whether the main source of energy in LIRGs is star formation or an AGN. Currently it is commonly accepted that they are

mainly powered by starbursts, in some cases with significant contribution from an AGN. For example, Iwasawa et al. (2011) found in about 50% of the LIRGs at $z < 0.09$ clear signs of an AGN: strong hard X-ray emission and/or coronal lines in the mid-infrared spectra. However, these AGN contribute only $\sim 10\%$ to the total energy budget of their host galaxies. The AGN seems to be more prominent at higher luminosities. Nardini et al. (2010) found that $\sim 70\%$ of the UltraLuminous InfraRed Galaxies (ULIRGs), i.e. those with $10^{12} < L_{IR}/L_\odot < 10^{13}$, host an AGN.

In the local universe, more than 90% of the ULIRGs are strongly interacting systems. They show knots of circumnuclear star formation, characteristic tidal tails in the optical/NIR images, and de-Vaucouleurs or disturbed brightness profiles common in merger remnants (see e.g., Veilleux et al. 2002, and references therein). At higher redshifts, only $\sim 50\%$ (up to 70%) of ULIRGs and $\sim 35\%$ of HLIRGs (i.e., HyperLuminous InfraRed Galaxies, with $L_{IR} > 10^{13} L_\odot$) are involved in merger events. An appreciable fraction of their population consists of bright disk galaxies with extended star formation. Those could be young systems that are building their stellar mass through starburst. If the infrared luminosity is powered only by star formation, ULIRGs and HLIRGs would have SFR ~ 100 to $\sim 1000 \, M_\odot \, yr^{-1}$, respectively.

Figure 1.5: ULIRG NGC 6240 ($z = 0.0245$). Composite image Chandra X-rays (red-yellow) combined with HST optical. Credit: X-ray (NASA/CXC/MIT/C.Canizares, M.Nowak); Optical (NASA/STScI).

Figure 1.6 (left), taken from Sanders & Mirabel (1996), shows the spectral energy distributions (SEDs) of ULIRGs with different infrared luminosities. In general, the far-infrared emission ($25 - 350 \, \mu m$) is identified with re-radiation by cold and warm dust. Big dust grains (radius $\geq 25 \, nm$) heated to $T \leq 20 \, K$ by an old stellar population emit at $100 - 200 \, \mu m$ forming the so-called 'infrared cirrus'. The emission at $60 \, \mu m$, produced by dust at $T \sim 30 - 60 \, K$, has been found to correlate with other star-formation indicators. Some authors ascribe the $L(60 \, \mu m)$ to the bolometric luminosity of the starburst. Emission features at 3.3, 6.2, 7.7, 8.6, and 11.2 μm are produced by polycyclic aromatic hydrocarbons (PAHs). These molecules, found in H II and photo-dissociation regions, and planetary nebulae, are excited by far-UV photons of early-type stars. Peeters et al. (2004) showed that they can be used as quantitative tracers of star formation (although see Calzetti 2011). The dust heated by the AGN is believed to shine in the near($0.75 - 5 \, \mu m$)- and mid($5 - 25 \, \mu m$)-infrared. In particular, the $25 \, \mu m$ emission compared to that at $60 \, \mu m$ has been used to identify (U/H)LIRGs with higher AGN contribution. For comparison, in Fig 1.6 (left), Sanders & Mirabel (1996) plot the SEDs of 'warm' ULIRGs (with $f_{25}/f_{60} > 0.3$). Two of these objects are known QSOs, the other is a Wolf-Rayet galaxy. The similarity of the spectra of warm ULIRGs and QSOs have served as evidence for the evolutionary connection between these two populations
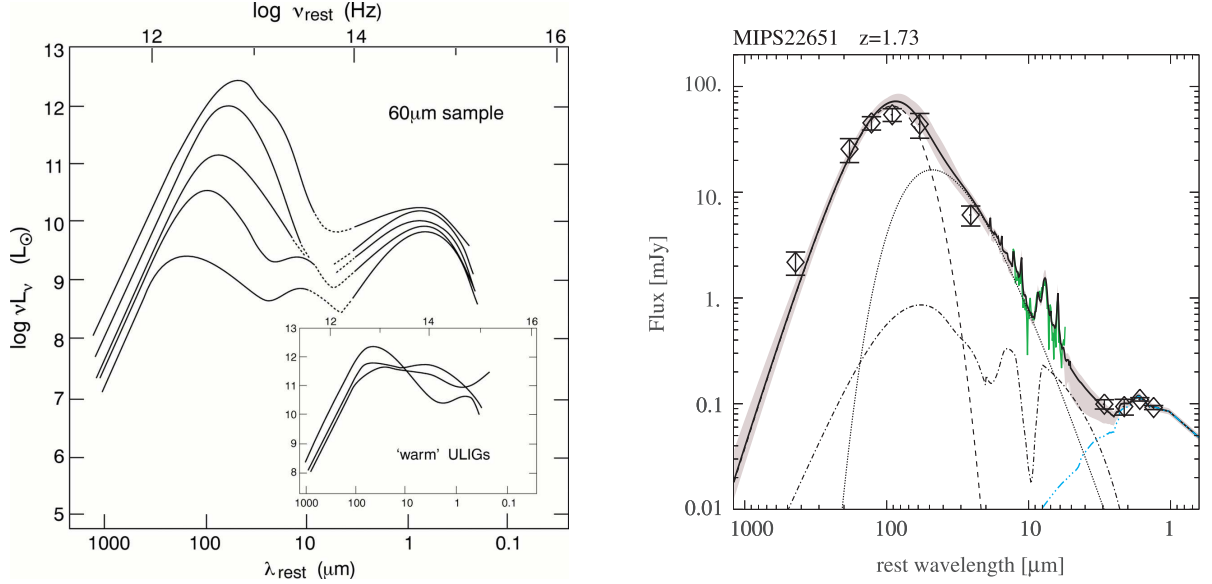
Figure 1.6: Spectral Energy Distribution of ULIRGs. *Left:* Mean SEDs of ULIRGs with different L_{IR}. The curves correspond to smoothed lines that join sub-millimeter-to-UV data points. The inserted diagram shows SEDs of ULIRGs with $f_{25}/f_{60} > 0.3$. Taken from: Sanders et al. (1988). *Right:* Example of a ULIRG SED fit. Diamonds and green spectrum correspond to observed data points. The thick solid line shows the best fit of the components: stellar continuum (dashed-triple dot cyan curve), PAH emission + hot dust model (dot-dashed curve), warm dust (thin solid curve) and cold dust (dashed curve). Modified from: Sajina et al. (2012). Note that the vertical axes of both panels correspond to related (but not the same) quantities, luminosity $\log(\nu L_\nu)$ at the left, and specific flux $\log(f_\nu)$ at the right. When it is put in the same units, the SED of MIPS22651 (right) looks like the third curve in the diagram at left, shifted up by two orders of magnitude (at $100\,\mu m$, $\nu L_\nu \sim 10^{13}\,L_\odot$).

proposed by Sanders et al. (1988). According to them, the ULIGRs would be dust-enshrouded QSOs triggered by major merging events between two gas-rich disk galaxies. Figure 1.6 (right) shows the SED of MIPS22651, a ULIRG at $z = 1.73$, which is part of the sample studied by Sajina et al. (2012). They fit the observed data as a linear combination of the components mentioned.

1.3.2 Star formation diagnostics

With the discovery of LIRGs and the possibility to trace the star formation to intermediate and high redshifts, the necessity of methods to quantify this process is evident. Studies of high-SFR galaxies challenge our understanding of galaxy evolution. When have these objects built the major fraction of their stellar mass? Are they young systems? Which populations are the progenitors of these systems and of the present-day galaxies? To answer these questions, estimations of stellar pop-

ulations, gas content, and star formation are required[4]. Many specialized papers and comprehensive reviews have been dedicated to these subjects, e.g., Maraston (2003), Dopita (2005), Leitherer (2005), Renzini (2006); Solomon & Vanden Bout (2005), Sanders et al. (1991); and Condon (1992), Kennicutt (1998a), Ranalli et al. (2003); and more recently, Bruzual (2010); García-Burillo, S. et al. (2012), Kennicutt & Evans (2012); and Calzetti et al. (2010), Murphy et al. (2011), Calzetti (2012); and references therein. In the following, I briefly summarize how to estimate SFR, gas content and stellar populations in extragalactic sources, indicating the main assumptions of the different methods. The interested reader is referred to the aforementioned literature for a deeper discussion of each topic.

1.3.2.1   Star formation rate

The star formation rate (SFR) is, by definition, a quantity that refers to the recently formed stars ($\sim 10 - 100\,\mathrm{Myr}$). Therefore, the use of UV and optical/near-infrared indicators is desirable. The conversion between the flux over certain wavelength intervals and the SFR can be derived from synthesis models (briefly described on page 11). It is assumed that i) the studied region is isolated, ii) the contribution from external agents has been removed, e.g. an AGN, iii) the emission is corrected for extinction along the line of sight, iv) the SRF has been approximately constant over the time probe by the employed indicator, and v) the stellar Initial Mass Function (IMF) is known and fully sampled. For example, Calzetti (2012) shows that for a constant star formation over $\geq 100\,\mathrm{Myr}$, assuming the Kroupa IMF in the mass range $(0.1 - 100)\,\mathrm{Myr}$, with the stellar SEDs and tracks from the code Starburst99 (Leitherer et al. 1999), the SFR can be estimated from the UV continuum as

$$\frac{\mathrm{SFR\ (UV)}}{\mathrm{M_\odot\,yr^{-1}}} = 3.0 \times 10^{-47} \left(\frac{\lambda}{\mathrm{\AA}} \right) \left(\frac{L_\lambda}{\mathrm{erg\,s^{-1}}} \right). \qquad (1.2)$$

The calibration constant depends on the previous considerations; e.g., it changes by a factor of 1.4 if the upper limit of the stellar mass range is $30\,M_\odot$, and 0.7 if the star formation time scale is $10\,\mathrm{Myr}$. When using the Salpeter IMF, the calibration constant increases by 1.6. Nonetheless, the UV is still the best band to directly probe the photospheric emission from young stars, when those are not enshrouded by dust.

Given that the intensity of the hydrogen recombination lines is proportional to the Lyman continuum flux, they are reliable tracers of the star formation. Only stars with masses $\gtrsim 15\,M_\odot$ and ages $\lesssim 40\,\mathrm{Myr}$ produce measurable ionizing photon flux (Kennicutt 1998a). If the SFR is constant over more than $6\,\mathrm{Myr}$ and the same

---

[4]Here I only refer to the observables related to the stellar content of a galaxy, without intending to oversimplify the problem. Many other aspects determine the evolution of a galaxy including the influence of the environment, the importance of secular processes and the relation of the central SMBH with its host galaxy.

considerations as in the previous case apply,

$$\frac{\text{SFR (H}\alpha)}{\text{M}_\odot \,\text{yr}^{-1}} = \frac{L_{\text{H}\alpha}}{1.82 \times 10^{41} \,\text{erg s}^{-1}}.$$ (1.3)

Here, the constant also varies by $\sim 15\%$ in H II regions with electron temperatures $T_\text{e} = 5000 - 20\,000 \,\text{K}$ and is independent of the electron density. This estimate has the advantage of being easily extrapolated to H I lines in other bands using the case-B recombination and an appropriate extinction correction. In this thesis, I use this relation with the calibration of Panuzzo et al. (2003) for the Brγ $\lambda 2.164 \,\mu\text{m}$ to estimate SFR in some regions ($r \approx 100 \,\text{pc}$) in the bulge of the galaxy IRAS 01072+4954.

Although both young and old stars heat up the dust, the former produce higher temperatures dominating the emission around $60 \,\mu\text{m}$, while the latter are associated with the flux at $> 100 \,\mu\text{m}$. However, this is not the case in circumnuclear starburst galaxies where all the dust is heated mainly by young stars, nor in very low-sSFR sources where young populations contribute only $\sim 10\%$ (Kennicutt & Evans 2012). Because the infrared emission depends also on the geometry, distribution, composition, and emissivity of the dust grains, there is no unique relation between the UV and the infrared photons. Another caveat is that not all the emission from young stars is absorbed by dust. In spite of that, observations of star-forming galaxies have shown that their infrared luminosities correlate with other star-formation tracers making it suitable to evaluate SFRs. The relation between the SFR and the total infrared luminosity (Eq. 1.1 on page 13) for a system with continuous star formation and Salpeter IMF in the mass range[5] $(0.1 - 100) \,\text{Myr}$ is given by (Kennicutt 1998a)

$$\frac{\text{SFR (IR)}}{\text{M}_\odot \,\text{yr}^{-1}} = \frac{L_{\text{IR}}}{2.23 \times 10^{43} \,\text{erg s}^{-1}}.$$ (1.4)

This applies to starbursts younger than $100 \,\text{Myr}$. When using this expression as a global SFR indicator in a galaxy, the constant in the denominator changes by a factor of ~ 1.75 to account for star-formation time scales of $\sim 10 \,\text{Gyr}$ (Calzetti 2012).

As it was mentioned in the previous section, the presence of an AGN also contributes to the dust heating and thereby to the total infrared luminosity, predominantly in the mid-infrared. In the case the AGN contribution cannot be disentangled from that of the star formation, e.g. due to the lack of a good SED-data coverage, the SFR can be estimated from the far-infrared (FIR) luminosity where young stars dominate the energy input. The FIR luminosity $L_{\text{FIR}} \equiv L(4-120 \,\mu\text{m})$ can be computed following Helou et al. (1988) as

$$\frac{L_{\text{FIR}}}{\text{L}_\odot} = \frac{L_{\text{FIR}}}{3.839 \times 10^{38} \,\text{erg s}^{-1}} = 4\pi \left(\frac{D}{\text{Mpc}}\right)^2 0.313 \left[2.58 \, f_{60} + f_{100}\right],$$ (1.5)

---

[5]The original expression from Kennicutt (1998a) was calculated in the mass range $(10 - 100) \,\text{M}_\odot$, but comparing the expression with the recalibration of Persic et al. (2004), who extended the lower mass limit to $0.1 \,\text{M}_\odot$, the calibration constant stays approximately the same.

where the specific fluxes measured by IRAS at 60 and $100\,\mu$m are in Janskys. This luminosity can be translated into the total luminosity using the infrared bolometric correction derived by Dale et al. (2001) from a sample of local star-forming galaxies

$$\log\left(\frac{L_{\rm IR}}{L_{\rm FIR}}\right) = 0.2738 - 0.0282\,x + 0.7281\,x^2 + 0.6208\,x^3 + 0.9118\,x^4, \qquad (1.6)$$

with $x = \log(f_{60}/f_{100})$. Then, the SFR can be found using Eq.(1.4) or through the calibration of Panuzzo et al. (2003)

$$\frac{\rm SFR\ (FIR)}{\rm M_\odot\,yr^{-1}} = \frac{L_{\rm FIR}}{1.134 \times 10^{43}\,\rm erg\,s^{-1}}, \qquad (1.7)$$

which refers to a Salpeter IMF in the mass range $(0.15 - 120)$ Myr, with a time scale of $12\,$Gyr. Both methods provide comparable results. Furthermore, infrared SFR-calibrations reported by different authors agree within a range of $\sim 15\%$. Other calibrators that are best suited for sources observed with Spitzer at 24 and $70\,\mu$m, and Herschel at 70 and $160\,\mu$m have also been reported by several groups (for a review see Kennicutt & Evans 2012).

The tight correlation between the radio-continuum and the FIR emission of star-forming and starburst galaxies is usually expressed by the 'q' parameter

$$q \equiv \log\left(\frac{2.58\,f_{60} + f_{100}}{2.976\,f_{1.4\,\rm GHz}}\right) \approx 2.34 \pm 0.26, \qquad (1.8)$$

with f_{60}, f_{100} and $f_{1.4\,\rm GHz}$ in Jy (Condon 1992). This allows us to use the specific flux at $1.4\,$GHz as global SFR indicator, combining the previous expression with Eq.(1.5) (see e.g., Murphy et al. 2011). The physical connection is the synchrotron radiation from charged particles produced by supernovae in star-forming regions, which dominates the radio emission at frequencies $\leq 5\,$GHz. SFR-indicators based on mixed processes that combine direct probes of star formation and reprocessed light are also available in the literature. In general, it is important to be aware of the assumptions underlying the SFR-calibration constants, in particular related to the time scale of the star formation. Short time scales ($\sim 100\,$Myr) are associated with local (radius $< 1\,$kpc) star formation, while time intervals comparable to the Hubble-time are related to global (galaxy wide) processes. With the exception of the estimations based on hydrogen recombination lines, the SFR calibrations are very sensitive to this parameter.

1.3.2.2   Gas content

The star formation process is driven by the availability of cold gas. Stars are born in highly dense environments, therefore a tight relation between the star formation rate and the gas density is expected (Schmidt 1959, 1963). However, we only have access to luminosity-weighted projected averaged observables. The relationship between the star formation rate density $\Sigma_{\rm SFR} \equiv {\rm SFR}/\pi r^2$ and the total gas surface

density $\Sigma_{\mathrm{gas}} \equiv (M_{\mathrm{H\,I}} + M_{\mathrm{H_2}})/\pi r^2$, known as the Kennicutt-Schmidt (K-S) law, has the form

$$\Sigma_{\mathrm{SFR}} = \epsilon_{\mathrm{SF}}\, \Sigma_{\mathrm{gas}}^{N}, \tag{1.9}$$

with ϵ_{SF} the star formation efficiency and $N \sim 1.4 - 1.5$ (Kennicutt 1998b). By definition, its inverse is the depletion timescale, which is equivalent to the time it takes to convert all the gas mass into stars at a constant SFR.

The K-S law seems to apply for global star formation in galaxies, as well as for resolved clouds. The star formation rate density can be traced in many ways, as described above, and in most of the cases the star formation estimates derived using different indicators are consistent with each other. This is not the case for the gas mass. In low-density environments the K-S law is driven by the Σ_{SFR} vs $\Sigma_{\mathrm{H\,I}}$ relation. However, around $\Sigma_{\mathrm{H\,I}} \sim 9\,\mathrm{M_\odot\,pc^{-2}}$ the atomic hydrogen emission saturates and actually shows an anticorrelation with the star formation rate density (see e.g., Bigiel et al. 2008). For higher gas densities the molecular hydrogen dominates the gas content. However, the first excited rotational level of H_2 is at $500\,\mathrm{K}$, therefore line emission from H_2 – like that observed in the near-infrared – do not trace the dense clouds whose temperature is $\sim 20\,\mathrm{K}$. Moreover, the molecule

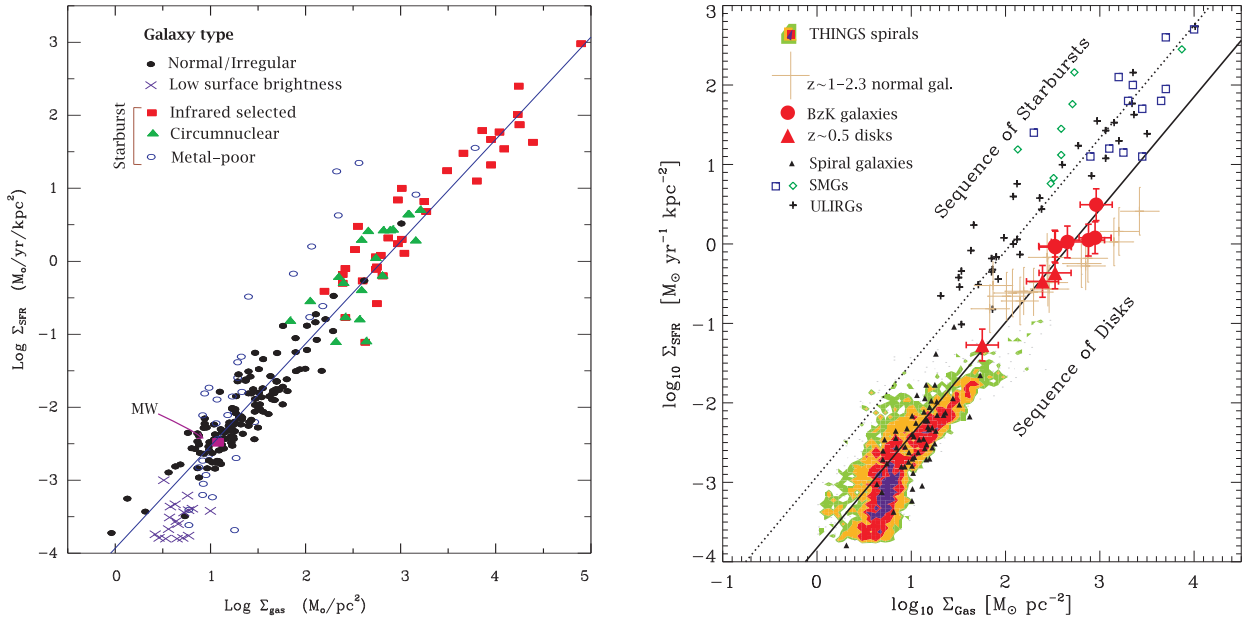**Figure 1.7:** Σ_{SFR} vs. Σ_{gas} relation. *Left:* The data points correspond to disk-averaged star formation surface densities. Sources are marked as shown in the label. The infrared selected galaxies are mainly LIRGs and ULIRGs. The magenta filled square represents the Milky Way (MW). A constant X(CO) factor was applied to all galaxies. Taken from: Kennicutt & Evans (2012) *Right:* Bimodal Kennicutt-Schmidt law. The different samples: submillimeter galaxies (SMGs), ULIRGs, BzK galaxies, local and medium-redshift galaxies are marked as shown in the label. Contours correspond to THINGS galaxies from Bigiel et al. (2008). Taken from: Daddi et al. (2010)

has no dipole moment, therefore it can only be detected by assuming a certain association with the CO molecule, which is the second most abundant in the cold interstellar medium. The so-called $X_{\mathrm{CO}} = M_{\mathrm{H_2}}/L_{\mathrm{CO,1-0}}$ factor relates the gas mass with the luminosity of the CO $J = 1 - 0$ transition. Usually, values of this factor close to the galactic one $X_{\mathrm{CO}} \sim (3-6)\,\mathrm{M_\odot}\,(\mathrm{K\,km\,s^{-1}\,pc^2})^{-1}$ are used, although in general, X_{CO} depends on the average properties of the interstellar medium.

Using a single X_{CO} to derive the gas masses in a sample of star-forming galaxies, all the measurements seem to converge to the classical K-S law with the fiducial $N = 1.4$ slope (see Fig. 1.7, left-hand panel). However, recently it has been argued that ULIRGs and high-z LIRGs might have highly turbulent non-self-gravitating gas distributions, so that the X_{CO} factor would be only a fraction of the galactic one $\langle X_{\mathrm{CO}} \rangle \sim (1/4 - 1/5)\,X_{\mathrm{CO,\,Gal}}$ (Daddi et al. 2010; Genzel et al. 2010). This is reflected in the appearance of a bimodality in the K-S law (Fig. 1.7, right-hand panel). The lower relation would hold for local sources, while the upper one would be valid for high-redshift ULIRGs and SubMillimeter Galaxies (SMGs). This might imply the existence of two well-defined modes of star formation with different global efficiencies. On the other hand, Papadopoulos et al. (2012) have shown that in some cases the low-J transitions of the CO molecule may not be sensitive to the properties of the gas with densities $n_{\mathrm{H_2}} > 10^3\,\mathrm{cm^{-3}}$, and therefore the gas masses of many local and high-z ULIRGs might be underestimated. This subject is currently a matter of intense research and debate.

1.3.2.3 Stellar populations

The term stellar population here is used to designate a collection of stars that are born in the same burst event – which can be instantaneous or continuous for some period of time. The integrated emission of a galaxy is a luminosity- and time-weighted average of the emission produced by many stellar clusters, born under different physical conditions across the galaxy during its lifetime. Stars develop in different ways depending on the mass they have when they start on the zero-age mean sequence (ZAMS; Fig. 1.8). OB stars with masses $> 25\,\mathrm{M_\odot}$ evolve fast, turning into blue supergiants and Wolf-Rayets in few Myr. While OB stars with $\lesssim 25\,\mathrm{M_\odot}$ can stay 10^6 to $10^9\,\mathrm{yr}$ on the main sequence, evolve by increasing their luminosities to a super-giant or a giant phase, and end their lifes as neutron stars or white dwarfs. It is possible to identify two (or three) stages in the evolution of a stellar population during which particular emission features associated to young, (intermediate) and old stars are present in the spectrum (Fig. 1.9).

Young stellar populations have an age $\lesssim 3 \times 10^7\,\mathrm{yr}$. During the first million years after the birth, the stars are enshrouded by dust clouds and not observable. Approximately $3 - 4\,\mathrm{Myr}$ later, the UV ionizing continuum and the stellar winds from OB stars and Wolf-Rayets push the dust away and create H II regions. As a result, strong hydrogen recombination lines and, in some cases, P Cygni profiles can be seen in the spectrum. The Lyman photons also excite PAH molecules that emit

at specific transitions in the mid-infrared. The presence of highly ionized atoms in the atmosphere of Wolf-Rayet stars produce visible bumps in the integrated spectrum at $\sim \lambda 4650\,$Å, or at $\sim \lambda 5750\,$Å, due to the blending of N III with C III and He II in the first case, and of C III with C IV in the latter. After $\sim 10\,$Myr, the near-infrared emission is dominated by massive (with $\sim 10-40\,M_\odot$ on the ZAMS) red supergiants. In the radio band, the thermal (free-free) emission at frequencies $\geq 5\,$GHz is directly related to the ionizing continuum from young massive stars, while the synchrotron radiation from supernovae explosions dominate at lower frequencies. Then at $\sim 25\,$Myr, shock-sensitive lines appear strongly in the spectra like [O II], [Fe II] and H_2.

Intermediate stellar populations are $\sim (7 \times 10^7 - 10^9)\,$yr old. Reaching $100\,$Myr, in an scenario where the star-formation time scale is $< 10\,$Myr, most of the OB stars have exploded as supernovae or cooled down, and therefore the ionization of the H II regions can not be sustained. In the X-rays, the emission from high-mass X-ray binaries which have as donors massive $(10 - 40\,M_\odot)$ OB stars, also fades. Supergiants and intermediate mass stars in the Asymptotic Giant Branch (AGB) dominate the infrared emission. From $\sim 5 \times 10^8$ to 1.5×10^9 years,
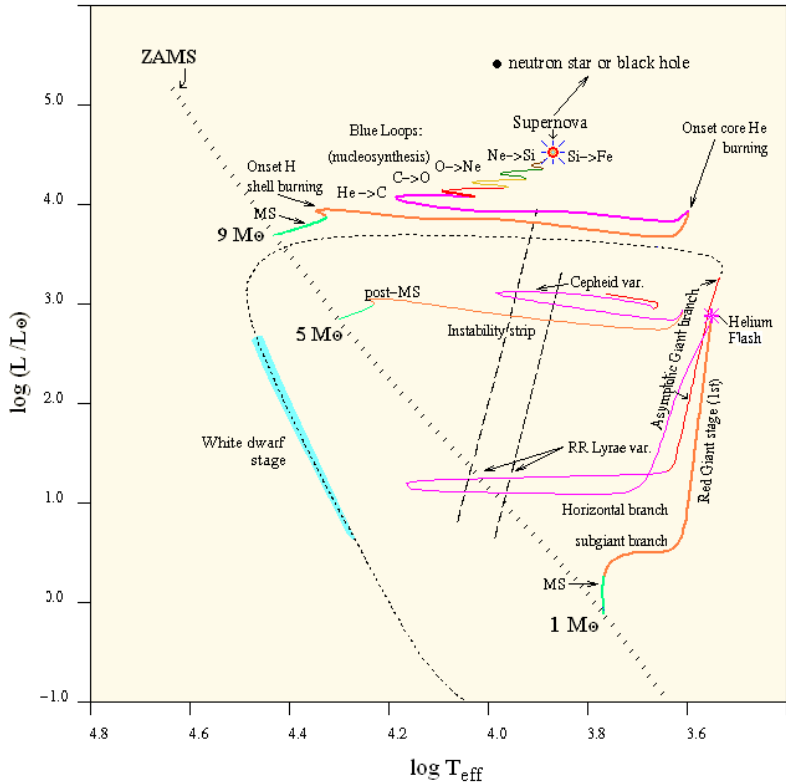

Figure 1.8: Stellar evolution during (green) and post (thick red) main sequence (MS). Evolutionary tracks of solar-metallicity stars of 1, 5, and $9\,M_\odot$. Intermediate evolutionary stages are labeled. Modified from: http://faculty.northgeorgia.edu/jjones/astr1020home/evoltracks.htm.

prominent CH, CN, and C_2 molecular absorption features from carbon stars in the thermally pulsing AGB (TP-AGB) phase are expected from synthesis models (Maraston 2005). These kinds of signatures have been observed in a sample of 14 Seyfert galaxies (Riffel et al. 2007). However, recently Zibetti et al. (2012) presented spectra from 16 optically-selected galaxies with intermediate age stellar populations that show featureless near-infrared continuum as predicted by the 'TP-AGB light' models of Bruzual & Charlot (2003). In the literature, those galaxies are usually called post-starburst galaxies and are characterized by strong and broad Hydrogen absorption lines in the optical spectra associated to late-B, A, and early-F type stars.

Old stellar populations have an age $\gtrsim 3 \times 10^9$ yr. At this time, only populations with continuous star formation rates over more than 10^9 yr can ionize H II regions producing detectable recombination lines in emission. For shorter star-formation time scales, the hydrogen features in the spectrum are present as absorption lines whose depth decreases with age. The near-infrared light is dominated by low mass giants evolving through the Red Giant Branch (RGB). Low-mass X-ray binaries, that have a red giant or a white dwarf as a donor star, become fully developed systems emitting most of their luminosity in the X-rays. The continuum emission around 4000 Å shows a break that increases with the age of the population and is due to a number of metal cooling lines in the stellar atmospheres.
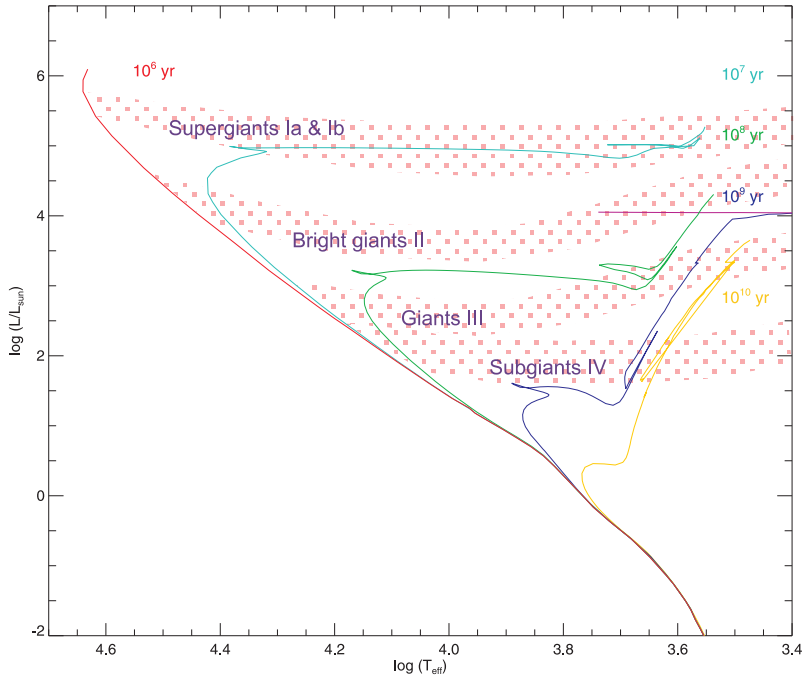

Figure 1.9: Evolution of a stellar population. Isochrones of 10^6, 10^7, 10^8, 10^9, and 10^{10} yr, of a solar-metallicity population assuming a Chabrier IMF in the $(0.5 - 100 \, M_\odot)$ mass range. The shaded areas indicate stellar luminosity types. Created using the libraries for stellar evolution of Girardi & Bertelli (1998) and Bertelli et al. (2009).

Observations in specific spectral bands allow us to probe the stellar populations that dominate the flux in certain wavelength regimes, or those that produce particular features with enough power to be detected in the spectrum. To determine the average dominant stellar populations of a spatially unresolved source (where individual stars can not be distinguished from each other), it is possible to follow two approaches. One uses the evolutionary synthesis models to reproduce the emission of a stellar population as a function of time, which then can be compared to the observed galaxy spectrum. In particular, the time-evolution of characteristic stellar features is followed allowing the determination of the average age of a population. In the other approach, one fits the observed data with a linear combination of different components, including spectra of stars with a range of types, luminosities and metallicities. In both cases, stellar models or observed spectra with similar (or higher) resolution than that of the data are required. By the time of this thesis none of the two in the combination of resolution and wavelength coverage of our observations of IRAS 01072+4954 ($R \sim 5\,300$ in HK-bands)[6] are available. For the stellar population analysis, the first technique is preferred because the comparison with high and medium resolution data from the literature is possible.

Spectral indices

Since the early 80's, the strength of the absorption features compared to the spectral continuum has been used as an indicator of the stellar population in unresolved spectra. In the optical ($4000 - 6000\,\text{Å}$), the Lick Observatory equipped with a Cassegrain spectrograph and an image dissector scanner (IDS) observed hundreds of stars during more than a decade. The team led by D. Burstein and S. M. Faber defined, in a series of papers, a set of 26 spectral bands around stellar characteristic features to be used in the identification of stellar types and for establishing correlations with metallicity or superficial gravity (the first contributions contained 11 indices, but they have undergone modifications and additions). Among them, the spectral break at $4000\,\text{Å}$, denoted as $\text{D}_n(4000)$, and the equivalent width of the Hδ line, Hδ_A, are widely used as age estimators (e.g., Kauffmann et al. 2003); while the iron absorption at $5570\,\text{Å}$, Fe 5270, and the iron/magnesium one around $5175\,\text{Å}$, Mg$_2$, have proven to be good metallicity tracers. This set of spectral-index definitions is nowadays known as Lick/IDS system (see e.g., Burstein et al. 1984; Faber et al. 1985; Worthey et al. 1994). In the infrared, similar efforts have been made (e.g., Baldwin et al. 1973; Kleinmann & Hall 1986; Origlia et al. 1993; Ivanov

---

[6]In the literature, it is possible to find stellar spectra with high resolution in K-band (e.g., Kleinmann & Hall 1986; Wallace & Hinkle 1996; Winge et al. 2009), or of some small spectral regions in the H-band (e.g., Rich & Origlia 2005). An important contribution is the IRTF stellar library, which compiles observed spectra of F – M stars in the range of $0.81 - 5.02\,\mu\text{m}$ at medium resolution $R \sim 2000$ (Cushing et al. 2005; Rayner et al. 2009). However the community is still missing high-resolution libraries that cover both bands in the near-infrared. To date I am aware of two efforts in this direction. Lebzelter et al. (2012) and Chen et al. (2011) are in the process of constructing stellar spectral libraries with resolutions of $R \sim 10\,000$ that cover from UV/optical to near-infrared wavelengths.

et al. 2004; Mármol-Queraltó et al. 2008). Lancon & Rocca-Volmerange (1992) defined a sort of broad spectroscopic indices, where they included the CO and H_2O photometric indices of Baldwin et al. (1973). Origlia et al. (1993) presented the ratios of CO(6-3)/Si I and CO(6-3)/CO(2-0) as sensitive temperature indicators. A combination of CO(6-3), Na I and Ca I in the K-band (Ramirez et al. 1997), and of CO(2-0) with Mg I at $1.50\,\mu$m and at $1.71\,\mu$m in the H-band (Ivanov et al. 2004) have been shown to probe the stellar luminosity allowing one to disentangle giants and supergiants from dwarf stars. However, the different quality of the data, the corruption of the astronomical window by telluric features and the difficulties of the continuum estimation – mainly in H-band due to the blending of a number of absorption lines – have hindered a consensus on the definitions of the infrared spectral indices.

In general, a spectral index is the quantification of the strength of a feature X, which could be for example its equivalent width defined as

$$W_X = \int_{\lambda_1}^{\lambda_2} \left(1 - \frac{f_{\lambda,X}}{f_{\lambda,C}} \right) \mathrm{d}\lambda, \tag{1.10}$$

where λ_1 and λ_2 are the band edges of the feature, $f_{\lambda,X}$ is the portion of the spectrum inside this interval, and $f_{\lambda,C}$ is the continuum flux in that wavelength range, calculated as the flux over a straight line fitted to the mean values of the spectral intervals defined to be the continuum bands for that particular feature. The spectral index can be also measured in magnitudes as

$$X = -2.5 \times \log \left[\left(\frac{1}{\lambda_2 - \lambda_1} \right) \int_{\lambda_1}^{\lambda_2} \frac{f_{\lambda,X}}{f_{\lambda,C}} \, \mathrm{d}\lambda \right]. \tag{1.11}$$

The definitions of the features used in this study are listed in Table 1.1, and are plotted in Figs. 1.10 and 1.11 over a median spectrum taken from our data. K-band spectral indices are the most studied in the near-infrared. Different groups have adjusted the definitions of the indices according to the resolution and wavelength coverage of their studies. Table 1.1 contains two of those definitions, chosen for their impact on the subject and the high number of studied objects. The comparison between these definitions is shown in Fig 1.11. From figures 1.10 and 1.11 it is possible to notice that an absorption feature, even at high resolution – the plotted spectra have $R \sim 5300$ – is the integrated contribution of several species. The exception is the CO(2-0) bandhead, which is formed by the superposition of many roto-vibrational transitions from a $0.32\,$eV energy state and whose depth depends on temperature, luminosity and metallicity. The contribution from other metal lines to the CO(2-0) band is negligible. Here, the identification of the lines has been done using Kleinmann & Hall (1986) and Rayner et al. (2009) as references.

By construction, the spectral index depends on the definition of the continuum bands and on the resolution of the data. Figures 1.10 and 1.11 show that the continuum defined for the absorption features does not correspond necessarily to the overall continuum of the spectrum, and therefore it is usually called 'pseu-

Table 1.1: Equivalent width definitions for *HK*-band selected features.

Species	Band Edges		Resolution	Ref.
	Absorption	Continuum	$(\lambda/\Delta\lambda)$	
Mg I $\lambda1.50$	$1.5020 - 1.5060$	$1.4990 - 1.5020$	1500, 3000	1
		$1.5060 - 1.5090$		
Si I $\lambda1.59$	$1.5870 - 1.5910$	$1.5835 - 1.5857^a$	1500	2
		$1.5915 - 1.5945^{a\,,b}$		
CO(6-3) $\lambda1.62$	$1.6175 - 1.6220$	$1.6145 - 1.6175^a$	1500	2
		$1.6255 - 1.6285^a$		
Mg I $\lambda1.71$	$1.7100 - 1.7130$	$1.7085 - 1.7100$	1500, 3000	1
		$1.7130 - 1.7160$		
Na I $\lambda\lambda2.21$	$2.2040 - 2.2110$	$2.2140 - 2.2200$	1380	3
		$2.2330 - 2.2370$		
	$2.2040 - 2.2110$	$2.1910 - 2.1970$	1380, 4830	4
		$2.2130 - 2.2170$		
Ca I $\lambda\lambda\lambda2.26$	$2.2580 - 2.2690$	$2.2490 - 2.2530$	1380	3
		$2.2550 - 2.2580$		
		$2.2700 - 2.2740$		
	$2.2580 - 2.2690$	$2.2450 - 2.2560$	1380, 4830	4
		$2.2700 - 2.2720$		
CO(2-0) $\lambda2.29$	$2.2924 - 2.2977$	$2.2880 - 2.2920^c$	1500	2
	$2.2880 - 2.3010$	$2.2460 - 2.2550$	2500	5
		$2.2710 - 2.2770$		

Note. Wavelengths in microns.

[a] A window of 30Å around the continuum positions suggested by the authors was used.

[b] The upper limit was changed from 1.5865 to 1.5857 due to the presence of a telluric residual in the spectrum

[c] A window of 40Å around the continuum positions suggested by the authors was used.

References. (1) Ivanov et al. (2004); (2) Origlia et al. (1993); (3) Ali et al. (1995) only the closest continuum regions to the feature are listed; (4) Ramirez et al. (1997); (5) Mármol-Queraltó et al. (2008).

docontinuum'. The resolution of the data can also affect the estimation of the pseudocontinuum, and through it the value of the spectral index. In Figs. 1.10 and 1.11, the smooth red/purple spectra correspond to the resolution of the data from which the indices were defined, and the dotted lines of the same color mark the continuum derived for our data at that resolution. Ramirez et al. (1997) compared the infrared indices of medium, high and very high spectral resolution data ($R \sim 1380 - 3000$, 4800, and $48\,000$, respectively) finding higher discrepancies in stars with effective temperatures $T_{\mathrm{eff}} < 3800\,\mathrm{K}$, i.e., in stellar types later than
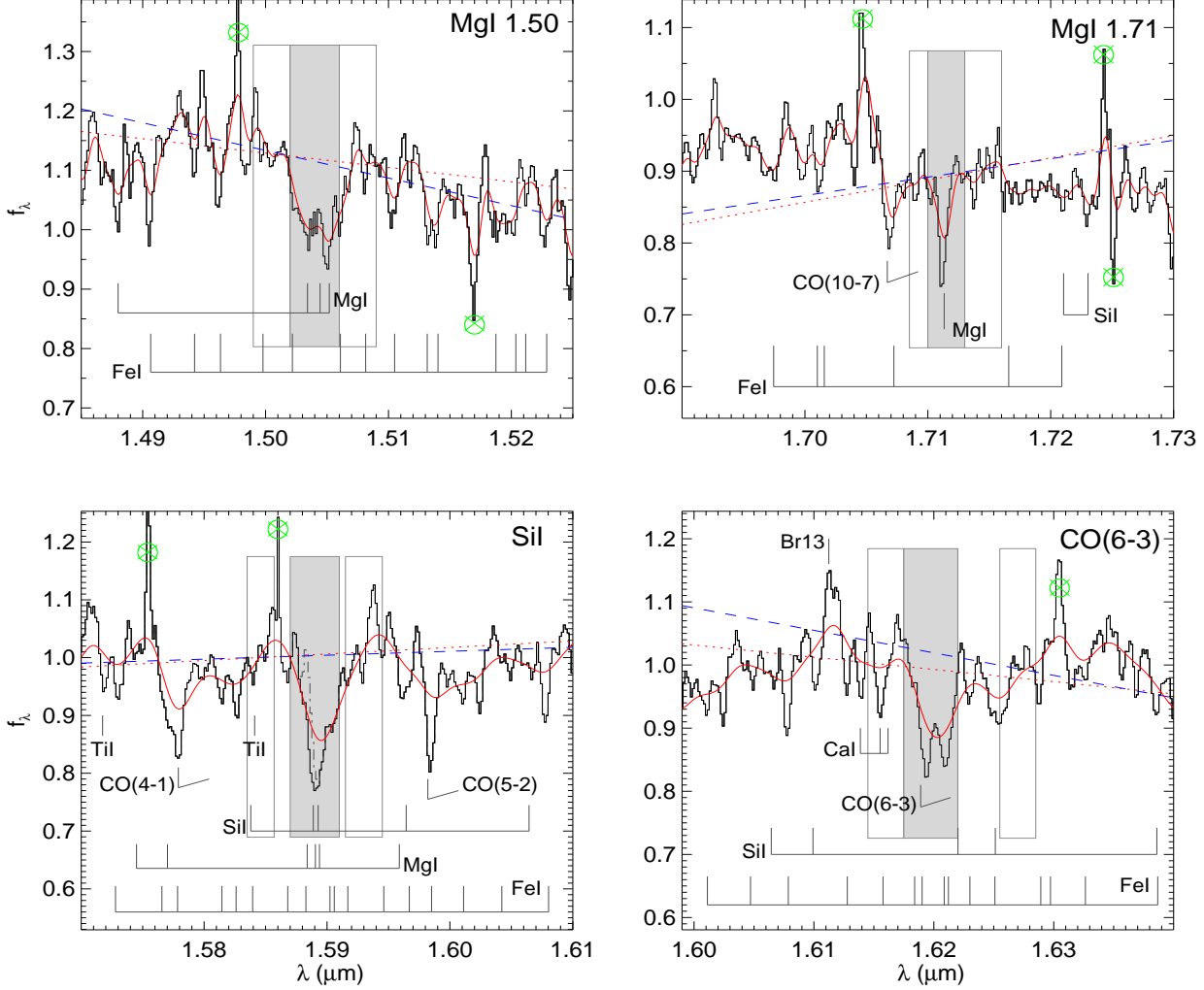
Figure 1.10: *H*-band spectral indices. The panels show detailed regions in the *H*-band spectrum of the mean stellar emission of the bulge of IRAS 01072+4954. The specific density is in units of $10^{-12}\,\mathrm{erg\,s^{-1}\,cm^{-2}\,\mu m^{-1}}$. The empty and shaded rectangular areas represent the continuum and feature bandpasses defined for the spectral index indicated in the upper right corner of each panel. The spectra have been smoothed to match the resolutions at which the indices were defined and overplotted in red: for the Mg I features (*at the top*) $R = 3000$ as in Ivanov et al. (2004), and for the Si I and CO(6-3) (*at the bottom*) $R = 1500$ as in Origlia et al. (1993). The dashed blue and red dotted lines correspond to the pseudocontinuum of each index for the unsmoothed and smoothed spectra, respectively. Other contributing species are identified. The green symbol $\otimes$ indicates strong emission/absorption atmospheric lines that remained after the reduction process.

$\sim$ M0. This must be taken into account when analyzing stellar populations from near-infrared data, because the emission in the *HK*-bands is dominated by K $-$ M type stars.
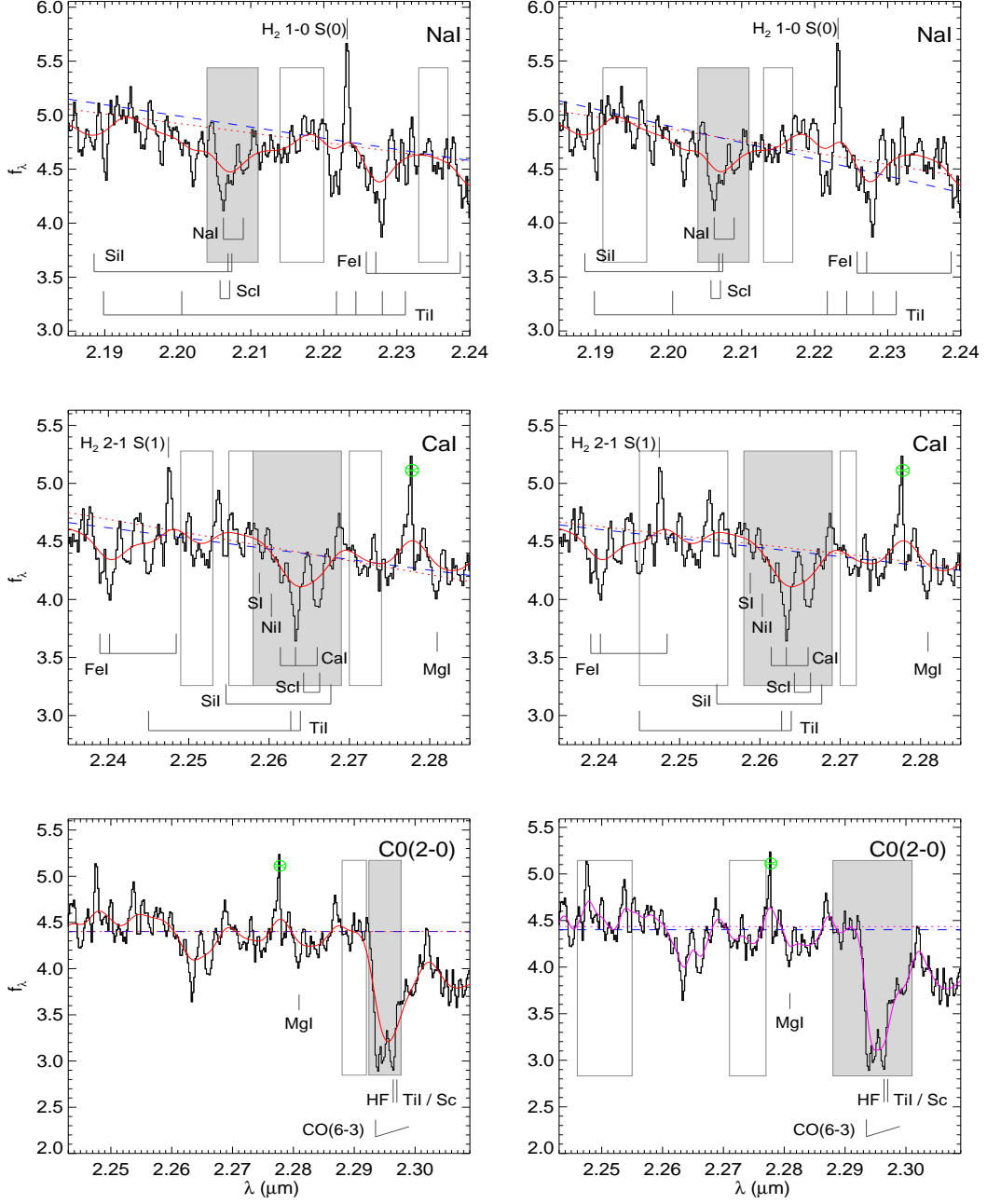
Figure 1.11: *K*-band spectral indices. Detailed regions in the *K*-band spectrum of the mean stellar emission of the bulge of IRAS 01072+4954 are shown. The specific density is in units of $10^{-13}\,\mathrm{erg\,s^{-1}\,cm^{-2}\,\mu m^{-1}}$. *Left* and *right* panels show two different definitions of the same spectral index. Symbols are the same as in Fig. 1.10. For Na I and Ca I the spectra have been smoothed to $R = 1380$ to match that of Ali et al. (1995) and Ramirez et al. (1997). For the CO(2-0), the red spectrum (*left*) has $R = 1500$ as Origlia et al. (1993) and the magenta one (*right*) $R = 2500$ as in Mármol-Queraltó et al. (2008). The continuum in this last panel is plotted only for comparison, because this index is defined in a different manner (see text).

In unresolved spectra, the spectral index is also affected by the broadening of the absorption features due to the velocity dispersion of the stars in the region covered by the observed aperture. Oliva et al. (1995) derived an empirical correction for sources with a velocity dispersion $60\,\mathrm{km\,s^{-1}} \geq \sigma_* \geq 200\,\mathrm{km\,s^{-1}}$,

$$W_{X,\mathrm{true}} \simeq W_{X,\mathrm{observed}} \left[1 + a_X(\sigma_* - 60)\right], \tag{1.12}$$

with σ_* measured in $\mathrm{km\,s^{-1}}$ and $a_X = 8.70 \times 10^{-4}$, 7.10×10^{-4}, and 8.75×10^{-4} for Si I, CO(6-3) and CO(2-0), respectively. Förster Schreiber (2000) extended the analysis to other absorption features and smaller dispersion $20\,\mathrm{km\,s^{-1}} \geq \sigma_* \geq 200\,\mathrm{km\,s^{-1}}$; for example, for Na I and Ca I,

$$W_{X,\mathrm{true}} \simeq W_{X,\mathrm{observed}} \left[1 + a_X(\sigma_* - 20) + b_X(\sigma_* - 20)^2\right], \tag{1.13}$$

where $a_{\mathrm{Na\,I}} = 1.67 \times 10^{-3}$, $b_{\mathrm{Na\,I}} = 4.43 \times 10^{-6}$, $a_{\mathrm{Ca\,I}} = 2.33 \times 10^{-4}$, and $b_{\mathrm{Ca\,I}} = 6.24 \times 10^{-6}$. At low resolution, $R \sim 1000$, these corrections amount to 22% and 10% of $W_{\mathrm{Na\,I}}$ and $W_{\mathrm{Ca\,I}}$, respectively.

Recently, Mármol-Queraltó et al. (2008) proposed a new type of spectral index, similar in definition to the optical $D_n(4000)$, that they denominated 'generic discontinuity' and used it to study the CO(2-0) bandhead. It is calculated as the ratio of the average specific fluxes in the continuum and in the absorption bands,

$$\mathrm{D_{CO}} = \left[\frac{\sum\limits_{i=1}^{n_C} \int_{\lambda_{C,i_1}}^{\lambda_{C,i_2}} f_{\lambda,Ci}\,\mathrm{d}\lambda}{\sum\limits_{i=1}^{n_C} (\lambda_{C,i_2} - \lambda_{C,i_1})}\right] \cdot \left[\frac{\int_{\lambda_1}^{\lambda_2} f_{\lambda,X}\,\mathrm{d}\lambda}{(\lambda_2 - \lambda_1)}\right]^{-1}, \tag{1.14}$$

where $f_{\lambda,Ci}$ is the i-th continuum in the interval $(\lambda_{C,i_1}, \lambda_{C,i_2})$. The authors showed that this definition is more robust with respect to the spectral resolution (and stellar velocity dispersion) and signal-to-noise ratio compared to previous definitions of the same index.

Chapter 2

Problem Statement

In this chapter, I introduce the galaxy IRAS 01072+4954. I summarize the available information about this object and expose why it is thought to be a good candidate to study the AGN - starburst connection. The specific questions that lead the research, together with some possible answers are presented in the second part.

2.1 IRAS 01072+4954

The galaxy IRAS 01072+4954 is a late type spiral (Fig. 2.1), located $\sim 12.6\,°$ south of the Galactic Plane. That makes it subject of extinction from the dust and the H I of our own Galaxy. Its effects are more prominent in optical ($A_B \sim 0.673\,\mathrm{mag}$)
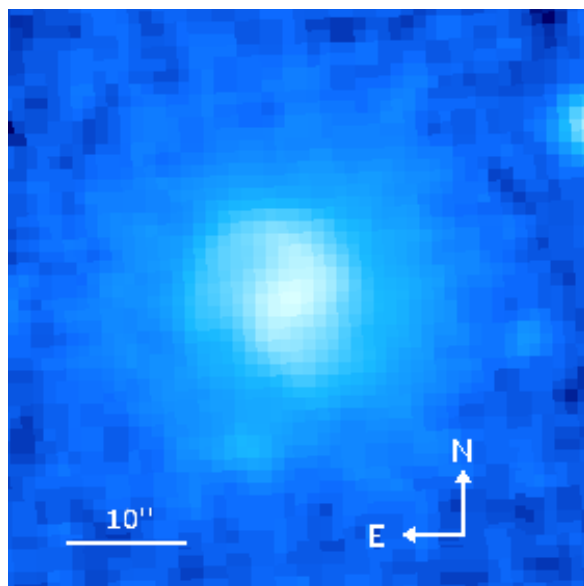

Figure 2.1: Optical POS-II image of the galaxy IRAS 01072+4954. The size of the figure corresponds to $50'' \times 50''$. The color coding corresponds to a logarithmic scale of the intensity. Taken from the Second Palomar Observatory Sky Survey.

and in the X-Ray regimes ($N_{\mathrm{H,\,Gal}} = 15.5 \times 10^{20}\,\mathrm{cm}^{-2}$)[1]. Table 2.1 summarizes the basic data of the galaxy, i.e. position, redshift, as well as spectro-photometric measurements reported in the literature, which are used in the analysis of the overall emission (chapters 4 and 5).

Table 2.1: IRAS 01072+4954 Basic Information and Photometry

Other Names	CGCG 551-008
	2MASX J01101406+5010313
	1RXS J011014.0+501021
R.A.(J2000.0)	$01^h10^m14^s.096$
Dec.(J2000.0)	$+50°10'30''.89$
Redshift	0.023616
Lum. distance	96.7 Mpc
$f_{170\,\mu\mathrm{m}}$	1.01 Jy
$f_{100\,\mu\mathrm{m}}$	1.802 Jy
$f_{60\,\mu\mathrm{m}}$	0.828 Jy
$f_{25\,\mu\mathrm{m}}$	< 0.25 Jy
$f_{12\,\mu\mathrm{m}}$	< 0.25 Jy
m_B	15.7 mag
$F_{0.3-2\,\mathrm{keV}}$	$4.6 \times 10^{-14}\,\mathrm{erg\,s^{-1}\,cm^{-2}}$
$F_{2-10\,\mathrm{keV}}$	$0.31 \times 10^{-12}\,\mathrm{erg\,s^{-1}\,cm^{-2}}$

Note. X-ray data from Panessa et al. (2005), far-infrared flux densities from the IRAS database, all other information taken from the Nasa/IPAC Extragalactic Database NED.

IRAS 01072+4954 is part of a small group of starburst/Seyfert composite galaxies identified by Moran et al. (1996) when studying the optical properties of sources that are bright in the far-infrared (IRAS) and that also are detected by ROSAT in X-rays. The starburst/Seyfert composites were described as objects with optical spectra dominated by starburst features and X-ray emission typical of broadline AGN. The Baldwin-Phillips-Terlevich (BPT) diagram, which compares the emission-line ratios [O III]/Hβ and [N II]/Hα Baldwin et al. 1981; Veilleux & Osterbrock 1987, together with other optical diagnostic diagrams, can help identifying the main ionizing source at the nucleus (Fig. 2.2). In the BPT diagram, the starburst/Seyfert galaxies are located in between the H II galaxies and the AGN. IRAS 01072+4954 exhibits the lowest [O III]/Hβ ratio of the sample. Other sources, marked in the figure with empty symbols, show indications of broad Hα emission with widths in the range $(2500 - 3600)\,\mathrm{km\,s^{-1}}$. The presence of the ac-

---

[1] Calculated as $N_{\mathrm{H}} = 3.84\,\csc|b| - 2.11$ (Dickey and Lockman, 1990).

tive nucleus in all sources of the sample, is indicated in the optical spectra by the broader width of the [O III] $\lambda\lambda 4959, 5007$ lines compared to any other permitted or forbidden lines. IRAS 01072+4954 does not show the broad Hα component and given the faintness of the narrow Hα emission it can be classified as a Low Luminosity AGN (LLAGN; Ho et al. 1997a). Using BeppoSAX and Chandra, Panessa et al. (2005) confirmed the Type 1 character of the spectrum of this source: steep power-law photon-spectral index $\Gamma = 2.1$, and very low Hydrogen column density $N_H < 0.04 \times 10^{22} \, cm^{-2}$). Long- and short-term X-ray flux variations were also detected.
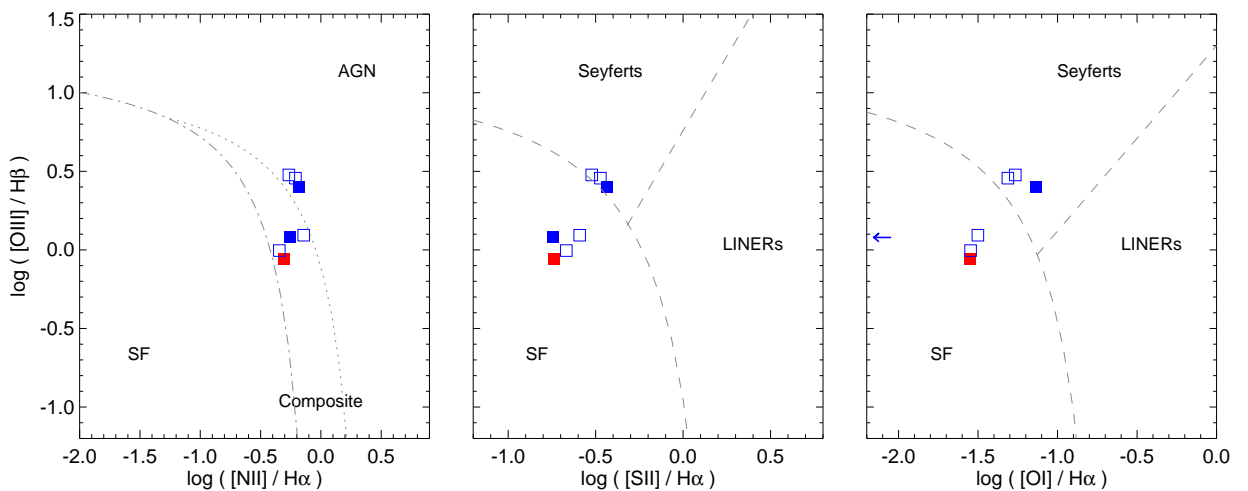

Figure 2.2: Starburst/Seyfert composite galaxies in the optical diagnostic diagrams. Empty symbols correspond to the sources that show faint Hα broad component in the optical spectrum. The red square represents IRAS 010724954. No broad lines are visible in this source. Image courtesy: M. Vitale.

The lack of broad lines in starburst/Seyfert composite sources has received different explanations: (i) The nuclear star formation outshines the optical signatures of accretion (aperture effect; e.g. Moran et al. 1996; Gliozzi et al. 2010). (ii) Very strong obscuration towards the nucleus hides the broad line region (BLR) and creates an X-ray reflected spectrum that mimics the spectral profile of sources with little absorption (as in the case of the starburst/Seyfert composite NGC 6221; Levenson et al. 2001). (iii) A clumpy ionized absorber obscures selectively the optical emission while leaving the X-rays unobscured (Georgantopoulos 2000; Maiolino et al. 2001b). (iv) The accretion process is radiatively inefficient or the AGN feeding material is blown-away by winds or outflows (this is a common property of LLAGN; Macchetto & Chiaberge 2007; Ho 2003. (v) The AGN is intrinsically weak or there is no BLR at all, so that the source can be considered as a True-Sy2 (like in other unabsorbed Sy2s; Panessa & Bassani 2002; Panessa et al. 2009). High angular resolution data are necessary to provide better constraints on the physical processes at $\sim 100 \, pc$ scales.

2.2 Research Questions

What is the nature of the AGN?

Is IRAS 01072+4954 a typical LLAGN, i.e. does it host a black hole that accretes mass inefficiently? or does it belong to the newly hypothesized class of True-Seyfert 2s? Why have broad lines do not been detected? Given that infrared radiation can arise from deeply embedded – optically absorbed – sources, it is possible that observing in the near-infrared (NIR), broad components around Hydrogen lines emerge. This has been the case of other optically classified Seyfert 2 galaxies, like NGC 5506 (Nagar et al. 2002), NGC 2992 (Reunanen et al. 2003), and NGC 7172 (Smajić et al. 2012). On the other hand, if no-broad lines are observed, it is possible to use the H II lines to determine if selective extinction is responsible for the apparently contradictory optical/X-ray classifications. NIR colors can also give hints on the inclination of the torus. This means, we can test hypotheses (ii) and (iii) mentioned in the previous paragraph. Moreover, studying the star formation at the nucleus in comparison with other Seyfert galaxies can help on deciding whether there is enhanced star formation activity that might outshine a faint AGN – hypothesis (i). Finally, it is possible that IRAS 01072+4954 behaves as a LLAGN or as True-Seyfert 2. Deciding among this two possibilities requires the estimation of the black hole mass and of the bolometric luminosity. Several correlations and scaling relations can be used for these purposes. Cross matching the obtained results can indicate if they still valid in the case of this source.

What is the star formation mode?

The IRAS photometry of this source, and the extended soft X-ray emission detected by Panessa et al. (2005) indicate that star formation might be the main activity in the galaxy not only globally, but also particularly in the bulge. It is known that spirals are forming stars, but most of them do it in a 'normal mode', in contrast to other galaxies where this process is more powerful and overwhelming. Is IRAS 01072+4954 a starburst galaxy? Where is the star formation taking place, in the disk, in the bulge, both? In order to find this out, the global star formation rate and the stellar mass of the galaxy must be determine. Combining 2MASS images of the entire galaxy with high resolution data of the bulge, it is possible to construct the brightness profile of the source and calculate its mass. Beside, the star formation rate can be estimate from the IRAS global photometry shown in Table 2.1. How old are the stellar populations in the bulge? Are there signs of newly formed stars? What is the metallicity at the center? How do the estimates of the star formation in the NIR compare to those derived from the X-rays and the radio? Do they trace the same populations?

What is the relation between the star formation and the AGN?

The study of the AGN – star formation relation has two aspects. One is how to disentangle both contributions, and the other is searching for indications of fulling and feedback. In the first case, it is possible to use NIR-diagnostic diagrams to

identify the main source of gas excitation. In these diagrams, the fluxes of bright emission lines are compared, in analogy to the optical ones shown in Fig. 2.2. High spatial resolution observations are fundamental for this purpose. How are the star formation and the AGN fueled? Using low-pass filtering of the NIR images it is possible to discover the presence of bars or asymmetric structures that are thought to be responsible for the transport of gas from the outer regions to the center. The 2MASS and the high resolution NIFS data can indicate what is the extension of such structures, if present. How is the gas reservoir in the bulge? Is there enough gas to power both kind of activities? The best tracers of cold gas are the CO and high density molecules emitting in the radio and submillimeter wavelengths, however the atomic and molecular Hydrogen emission, which is ionized in the NIR, can also be used to estimate the mass of the cold gas through an analog to the X_{CO} that relates the cold and hot H_2. Are there any signs of stellar or AGN feedback? The kinematics of the gas compared to that of the stars can give powerful hints in this direction. For this reason, high spectral resolution is essential in this case. Are the star forming activity and the black hole accretion happening simultaneously in this source? How do their time-scales compare in this case? Are those processes in agreement with the cosmological downsizing scenario?

Chapter 3

Observations and Data Reduction

IRAS 01072+4954 was observed in the near-infrared (NIR) using a technique called Integral Field Spectroscopy (IFS), that allows one to obtain photometric and spectroscopic information of the source simultaneously. Compared to the optical regime, in the NIR the atmosphere is much more sensitive to the weather conditions (turbulence, wind, water vapor content). Any source of heat, like the detectors and the telescope themselve, can completely dilute the faint signal from an extragalactic object. Then, why to observe in the NIR, how to overcome the observational difficulties, and which techniques can be used to obtain highly resolved images and spectra? This chapter is dedicated to answer these questions. First, the observations are presented. Then, the most relevant phenomena that affect NIR observations are described and their effects on the data of IRAS 01072+4954, as well as the employed techniques to eliminate them, are shown. In the third part, the basic principles of the IFS are presented with special emphasis on the characteristics of the instrument used for the observations. The calibration and further reduction procedures related with the IFS are also described and summarized in a flow chart. In Summary and Conclusions, I recapitulate the main ideas and present a short overview of the employed techniques.

3.1 Observations of IRAS 01072+4954

The galaxy IRAS 01072+4954 was observed on October 6, 2008 with the Near-Infrared Integral Field Spectrometer NIFS (McGregor et al. 2003) mounted on the 8.1 m "Frederick C. Gillett" Gemini North telescope on Mauna Kea, Hawaii (4213 m altitude). The dome of the Gemini North observatory has vent gates on the cylindrical walls that can be opened to allow the flow of air over the primary mirror to regulate its temperature (Fig. 3.1). All mirrors are coated with silver to reduce their thermal emission. To minimize the effects of the atmospheric turbulence, the adaptive optics module ALTAIR was used in Laser Guide Star mode (see more information about the instrument in Sect. 3.3, and about the adaptive optics correction in Sect. 3.2.3.1).

Figure 3.1: Gemini North telescope. *Left:* 50-second exposure of Gemini North interiors under full moonlight with opened vend gates. *Right:* Nighttime image of the Gemini North Observatory during a Laser Guide Star run. Credit: Gemini Observatory.

The observations cover H-band ($1.64\,\mu$m) and K-band ($2.20\,\mu$m). In each band, continuous integration intervals of $300\,$s were observed. A sequence of TSTTST was followed, where T is an observation of the target and S one of a nearby empty region on the sky (Fig. 3.2). In total, IRAS 01072+4954 was observed $8 \times 300\,$s per band. All the exposures were dithered by small amounts in order to correct for possible spatial defects on the detector. For the reduction and calibration of the data, observations of standard stars located close to the target were also performed.

3.1.1   Observing in the Near-Infrared

The active galactic nuclei shine mainly in the X-rays and in the UV/optical bands, while most of the emission radiated by young stars is detected in the UV band directly, and in the far-infrared (FIR) if obscured. Then, why to observe in the NIR? A huge advantage is that in contrast to the X-rays, UV and FIR, NIR observations can be perfomed from the ground. But there is more, in comparison to the optical, the NIR regime offers the following advantages for studying AGN with possibly faint broad line emission: (i) Higher angular resolution achieved with the AO-system that allows to dissect the central few tens of parsecs in nearby objects; (ii) the possibility of detecting emission from deeper embedded sources – and fainter broad lines – ; (iii) lower star light contamination leading to a better estimation of the continuum close to broad lines, but clear absorption features that allow the determination of the stellar velocity dispersion, and with it the black hole mass; (iv) the presence of star formation and feedback tracers in this portion of the spectrum, (v) possibility of detecting directly the emission from the hot dust of the putative torus.

3.1.2 Near-Infrared spectral bands

The Earth's atmosphere is opaque to most of the electromagnetic spectrum. Ground-based observations are possible in spectral ranges where the atmospheric transmissivity is high. Molecules of H_2O, CO_2, O_2, O_3, N_2O and CH_4 are the main sources for the absorption of light. In the near-infrared (NIR) from 0.9 to $2.7\,\mu$m, water and carbon dioxide produce the broadest absorption features in the transmission curve, defining the spectral bands suitable for astronomical observations. Figure 3.3 shows the broad-band atmospheric transmission with a zoom-in to the NIR regime. The NIR filters are optimized for those astronomical windows. The response of the MKO filters, used in the Gemini North Telescope, is overplotted in the same figure. Their center, cut-on, and cutoff wavelengths are given in Table 3.1.
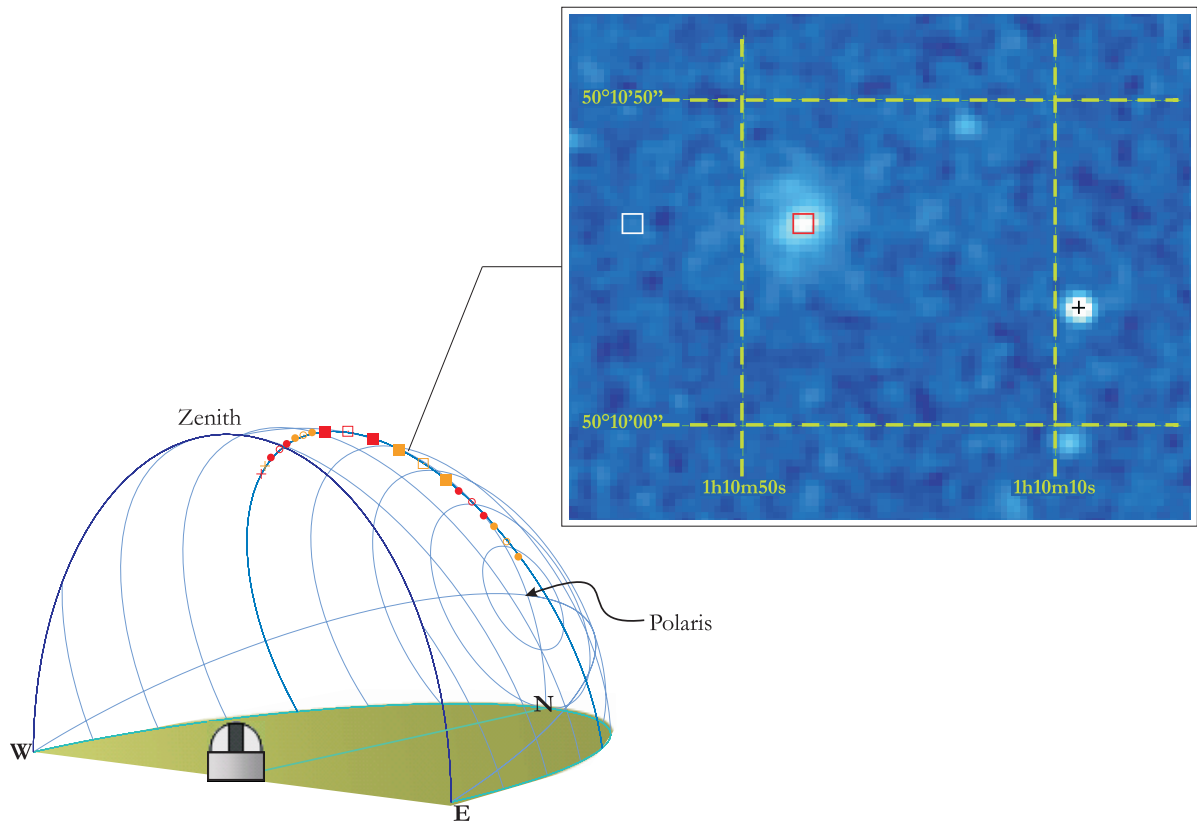

Figure 3.2: Quarter of the celestial sphere showing the motion of the galaxy IRAS 01072+4954 on the sky in the night when the observations were performed. The symbols along the diurnal circle of the source indicate the approximate position at which the calibration star (circles), the target (squares) and the PSF star (crosses) were observed. The colors stand for the two bands, *H* in orange, *K* in red. For simplicity, only one cycle of the TST sequence (fill-empty-fill symbols) is drawn. The panel at the *top-right* shows the NIFS field of view (red square) pointing toward the target, the chosen sky region (white square) and the PSF star (cross). The calibration star is only $\sim 2°$ away from the target, though out of the zoomed area. Equatorial coordinates are marked as reference.

Table 3.1: Properties of the near-infrared MKO filters. Taken from: Tokunaga et al. (2002).

Filter	Central Wavelength (μm)	Cut-on (μm)	Cut-off (μm)
J	1.250	1.170	1.330
H	1.635	1.490	1.780
K_s	2.150	1.990	2.310
K	2.200	2.030	2.370

Note. Cut-on and cutoff defined as the wavelength at which the transmission is 50% of the peak.
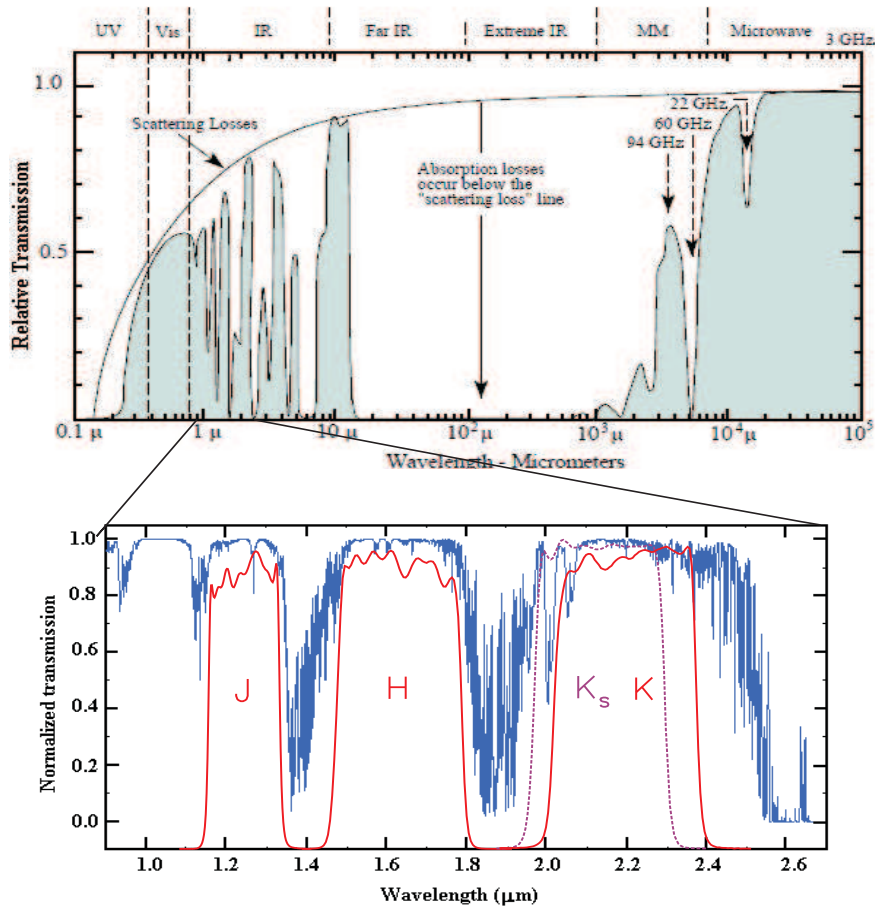
Figure 3.3: Atmosphere transmission and NIR bands. *Top:* Relative atmospheric transmission with AM = 1. At short wavelengths, Rayleigh scattering becomes an important source of extinction. *Bottom:* NIR atmospheric transmission for Mauna Kea with AM = 1, and water vapor of 1.6 mm. The profiles of the MKO filters, *J, H, K* (red), and K_s (magenta) taken from Tokunaga et al. (2002) are superposed. Modified from: Gemini Observatory.

The precipitable water vapor and optical path length through the atmosphere decrease with the elevation. At $\sim 4000\,\text{m}$ of altitude, where the Gemini North Telescope is located, the transmissivity is nearly insensitive to the water vapor content and depend mostly on the airmass (AM). The airmass is the path length that an incoming light ray travels compared to that of a ray emitted from a source the zenith when the detector is at sea level. Quantitatively, it can be approximated as $\text{AM} \approx \sec\zeta$ for $\zeta \gtrsim 60°$, where ζ is the the angle between the lines of sight to the zenith and toward the target source. At sea level, by definition $\text{AM} = 1$ for sources at the zenith ($\zeta = 0°$), while close to the horizon $\text{AM} \sim 38$. In the case of our observations of IRAS 01072+4954, with stable weather conditions, $\text{AM} \sim (1.16 - 1.26)$.

Precipitable water vapour: A measure of the atmospheric water vapor content. It is equivalent to the depth (in mm) of the liquid water in a vertical column of one unit cross-sectional area (e.g. $1\,\text{cm}^2$) that would result from the vapor condensation.

3.2 Observational challenges and techniques for data processing

3.2.1 Telluric absorption

The atmospheric absorption in the NIR is strong even within the photometric bands (Fig. 3.3). The common technique to eliminate it is to divide the target spectrum by the spectrum of a bright neighboring standard star observed shortly before or after the target. Hipparcos 4844, located $\sim 1.5\,\text{deg}$ North-west of IRAS 01072+4954 was observed as standard star. Its data was reduced in the same way as those of the target and its spectrum was extracted from an aperture that enclosed the whole star. Given that we were interested in the sky absorption lines, the intrinsic spectral features of A3V type stars had to be identified and manually removed. To do that, I compared the extracted spectrum with the A3V stellar template of Pickles (1998). Those features and some OH line residuals were fitted and removed using the IRAF task SPLOT.

The telluric correction was performed with the NFTELLURIC task, that is part of the GEMINI IRAF package used for the reduction of the NIFS data. In the NFTELLURIC task, the telluric spectrum was compared with every spectrum taken from the target (29 in total, corresponding to the 29 slitlets of the NIFS instrument), and according to each case, it was shifted and scaled until the best match of the telluric absorption lines was obtained. This procedure guarantees that any sub-pixel spatial deviation in the detector and the variations of the atmospheric absorption lines are removed. After the division of target spectra by the telluric spectrum, in order to account for the stellar spectral shape of the star, a normalized blackbody with the approximate temperature of the Hipparcos star, $T = 8750\,\text{K}$, was multiplied to the target.

3.2.2 Sky emission

The atmosphere also emits radiation. The major contribution to the HK background is the narrow line emission of the hydroxyl (OH). OH^- radicals are pro-

duced in the upper atmosphere, at ~ 87 km height, in the reaction between atomic hydrogen and ozone. Hydroxyl vibrational and rotational emission lines are strong and vary on time scales of $5 - 10$ min. The amplitude of the variations is different for each roto-vibrational group of lines, which makes them difficult to remove from the observational data of low brightness sources. Figure 3.4 shows the *HK*-band OH spectrum from Davies (2007).
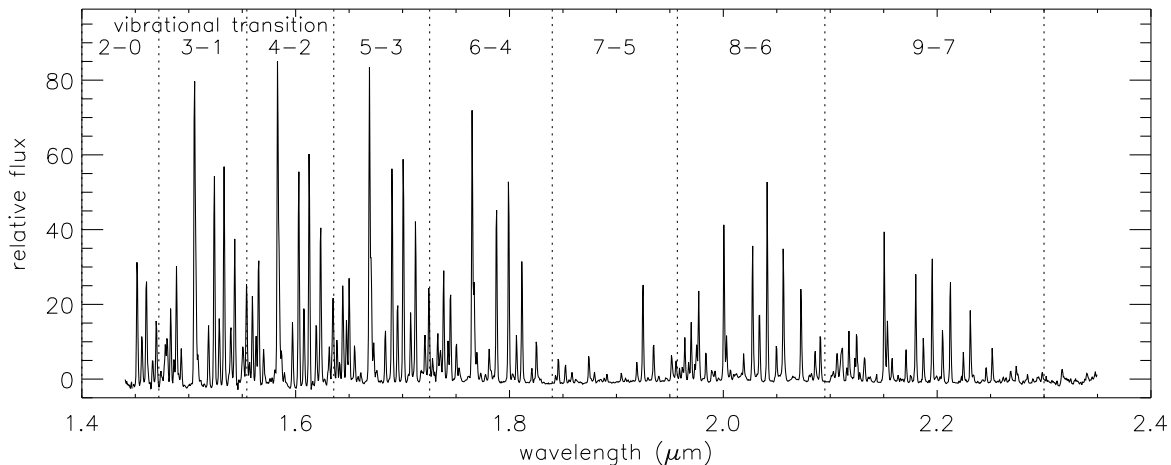

Figure 3.4: Spectrum of the hydroxyl in *HK*-bands with rotovibrational levels signaled. Taken from Davies (2007).

Other sources of NIR radiation are some H_2O lines at the long wavelength end of the *K*-band; the zodiacal continuum which is scattered sun-light by dust particles preferentially located in the Solar System plane and that can be modelled as a blackbody of 5800 K; and the thermal emission from the atmosphere, which for Mauna Kea is treated as a 273 K blackbody radiation.

The method to correct the atmospheric emission is to subtract from the target data an image of an empty region of the sky (i.e., free from obvious emitting sources) with equal exposure time. In our case, the telescope was pointed ~ 40 arcsec in R.A. away from the target (Fig. 3.2).

A caveat of this process is the rapid variation of the sky emission lines, because of the short coherence time (~ 5 min). Given that our integration time on source was 300 s, the intensity of the OH lines changed appreciably in comparison to that of the immediately preceding/following sky observations. Therefore, after the subtraction, strong OH lines remained, in some cases as emission and in others as absorption features (Fig. 3.4). Davies (2007) proposed an algorithm to avoid this problem. His method consists in creating a OH spectrum template from one sky exposure where different groups of lines are free to scale to the level of the OH emission in the target observations. In our case, however, the OH line ratios change

all across the field of view, and applying this algorithm would imply setting scale factors for every pixel of the image, every vibrational and rotational group of OH lines (and in some cases also for shifting the spectra to correct for small misalignments). To avoid excessive manipulation of the data, I preferred to conserve the OH residuals in emission and absorption, which in most of the cases compensate each other after the combination of all target exposures, and kept track of the OH spectral positions to avoid a misinterpretation of the data.

3.2.3   Atmospheric turbulence

The atmosphere is not homogeneous. Fluctuations in temperature and pressure generate cells of air mass that are arranged in hierarchical structures and move with the wind (see a schematic view in Fig. 3.5). According to the Kolmogorov-Tatarski turbulence model (Kolmogorov 1941; Tatarski 1961), shear wind and convection act as energy sources on the bigger cells, which have a typical length of L_0. This energy is transferred to the smaller inner cells down to length scale l_0, and during the process the energy is dissipated via viscosity. L_0 and l_0 are the 'outer' and 'inner scales' of the turbulence. Their actual sizes are of the order of tens to hundreds of meters for the former, and few millimeters for the latter.

   The turbulence mixes cells that are located at different layers of the atmosphere, and therefore have different temperatures. Since the atmosphere is approximately
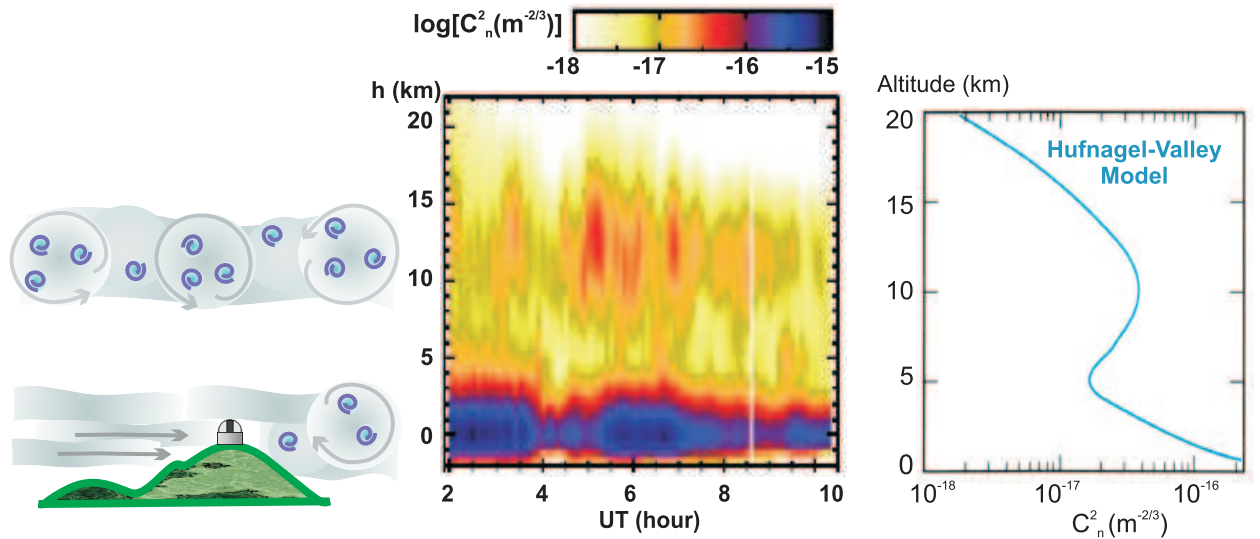

Figure 3.5: Turbulence strength. *Left:* Squematical representation of the main two layers of turbulence in the atmosphere. Measurements and model in the center and right-hand panels. *Center:* Temporal evolution of the turbulence $C_n^2(h)$ measured with Generalized Scidar mounted on the 2 m Vatican Advanced Technology Telescope on Mt. Graham (USA).*Right:* Median $C_n^2(h)$ profile from a sample of 43 nights. First and third quartiles in dotted lines. Modified from: Masciadri et al. (2010).

in pressure equilibrium, cells with lower temperature will have higher densities, and thereby higher refractive indices. This implies that the refractive index of the air depends on position and time, $n(\vec{r}, t)$, with $\vec{r} = (x, y, z)$. If the turbulence is homogeneous and isotropic, the structure function of the refraction index D_n only depends on the separation between two points; in other words, the expectation value of the difference of refraction indices measured at two positions $\vec{r_1}$ and $\vec{r_2}$ is only a function of the separation between them,

$$D_n(\vec{r_1}, \vec{r_2}) = C_n^2(h) \cdot |\vec{r_2} - \vec{r_1}|^{2/3},$$

or simply,

$$D_n(r) = C_n^2(h) \cdot r^{2/3}, \tag{3.1}$$

with $r \equiv |\vec{r_2} - \vec{r_1}|$. This holds as long as the spatial scales are in the range (l_0, L_0). The structure constant of the refraction index fluctuations $C_n^2(h)$, introduced in Eq. (3.1), describes the vertical distribution of the turbulence or the strength of the turbulence with the altitude h. In the Hufnagel-Valley model (Roddier 1981), the turbulence is located mainly in two layers of the atmosphere: an upper one, in the transition region between the troposphere and the stratosphere at $\sim (10 - 15)\,\mathrm{km}$ high; and a lower one, within about one kilometer over the surface (Fig. 3.5).

In the absence of an atmosphere, the maximum resolution – i.e. the minimum angular separation of two distinguishable sources in an image – that can be reached is given by the telescope-diffraction limit at the wavelength λ of the observation,

$$\theta_{\mathrm{diffrac}} = 1.22\,\frac{\lambda}{D} = 0\!''\!252 \left(\frac{\lambda}{\mu\mathrm{m}}\right) \left(\frac{D}{\mathrm{m}}\right)^{-1}, \tag{3.2}$$

where D is the diameter of the telescope. When observing through the atmosphere, the image gets degraded because the refractive index inhomogeneities act as lenses distorting the incoming radiation which enters the atmosphere as plane wave fronts. The distortion is a combination of mainly three effects: (i) an overall tilt of the wave front – i.e., the wave front planes are not any more parallel to the surface of the Earth, but inclined with respect to it – so that the light rays do not converge at the desired position on the focal plane. Because the tilt changes on time, the centroid of the image 'dance' across the detector. (ii) on smaller spatial scales, the wave front becomes curved, producing a blurred image. (iii) small-scale 'wrinkles' on the wave front make the light rays coming from neighboring spatial regions to diverge. In other words, a particular pixel in the detector receives light from spatially separated regions on the wave front – in the NIR, that separation can amount to several tenths of arcsecond. In this way, spots of different intensities and diffraction-limited sizes, called 'speckles', are formed on the detector. They disappear and move on time scales of few milliseconds. In longer exposures, required in astronomical observations, these distortions average out, forming an extended pattern called 'seeing disk' (Fig. 3.6). If the object is a point source, e.g. a star, the seeing disk is called point spread function and can be modelled with a two-dimensional Gaussian profile. The full width at half maximum FWHM of the observed profile, used as

an estimation of the combined effects of the atmospheric turbulence, is known as 'seeing' or PSF.

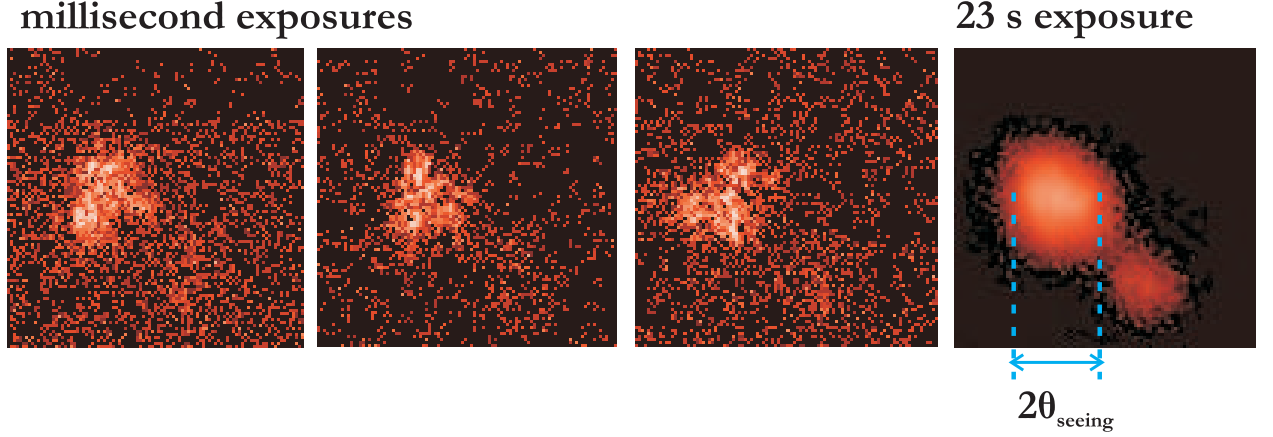**millisecond exposures** **23 s exposure**

Figure 3.6: Speckles and seeing disk. First three panels show short exposures (of order of milliseconds) of the Orion Trapezium Theta 1 Ori B. Observations in *H*-band obtained with the 6.5 m Multiple Mirror Telescope on Mt. Hopkins (USA). *Right:* 23 s exposure image of the same area. The FWHM of seeing disk is 0.45″. Adapted from: Close et al. (2003) and G. Brusa, CAAO, Steward Observatory.

The deformations of the wavefront correspond to variations of the phase $\delta\phi(\vec{x})$ of the electromagnetic wave,

$$\delta\phi(\vec{x}) = \frac{2\pi}{\lambda} \int_{h}^{h+\delta h} [n(\vec{r}) - 1]\, \mathrm{d}z, \tag{3.3}$$

where $\vec{x} = (x, y)$. Here, it is assumed that the light crosses a turbulence layer of thickness δh, located at an altitude h. The layer is considered a thin screen, so that the diffraction effects are negligible; but at the same time, it is thick compared to the correlation scale of the refractive index fluctuations. Equation (3.3) relates the three-dimensional distribution of the refractive index inhomogeneities to the two-dimensional distribution of the phase variations. The length of the spatial scale over which the time-averaged phase variations is about $1\,\mathrm{rad}^2$ is called 'Fried parameter' r_0 Fried (1965, 1966). Hence, r_0 represents the scale above which the turbulence effects are significant. In the Kolmogorov model, r_0 is defined as

$$r_0 \equiv \left[0.423 \left(\frac{2\pi}{\lambda}\right)^2 \sec\zeta \int_0^\infty C_n^2(h)\, \mathrm{d}h\right]^{-3/5}, \tag{3.4}$$

with ζ the zenith angle (defined in Sect. 3.1.2, page 39). This means that r_0, as a characteristic scale of the atmospheric turbulence, depends on the wavelength as $r_0 \propto \lambda^{6/5}$, varies across the celestial sphere through $r_0 \propto (\cos\zeta)^{3/5}$, and might

change during an observing night with C_n^2, as shown in Fig. 3.5. The seeing can be expressed in terms of r_0 as

$$\mathrm{PSF} \equiv \theta_{\mathrm{seeing}} = 0.98 \, \frac{\lambda}{r_0} = 20''\!.214 \, \left(\frac{\lambda}{\mu\mathrm{m}}\right) \left(\frac{r_0}{\mathrm{cm}}\right)^{-1}, \tag{3.5}$$

where λ is the wavelength of the observation.

The ratio D/r_0 sets the limit between the diffraction- and the seeing-limited observations. Although Eq. (3.2) might give the impression that increasing the telescope collecting area – i.e., the size of the primary mirror – results in increasing resolution, in fact, due to the turbulence in the atmosphere, when $D > r_0$ the maximum achievable resolution is given by the seeing, Eq. (3.5), which means that the resolution would not be larger than the one of a telescope of size $D = r_0$. Table 3.2 shows typical values of seeing and r_0 compared to the diffraction-limited resolution of a typical portable telescope (size $D = 20\,\mathrm{cm}$) and of a large telescope at Mauna Kea Observatory or at the Very Large Telescope in Chile.

Table 3.2: Typical seeing conditions in optical and infrared and telescope diffraction limits

Band (ref. wavelength)	r_0	Seeing	$\theta_{\mathrm{diffrac}}$	
			$D = 20\,\mathrm{cm}$	$D = 8\,\mathrm{m}$
Optical (500 nm)	$5\,\mathrm{cm} - 20\,\mathrm{cm}$	$\sim 1''$	$0.69''$	$0.016''$
Near-infrared (1.6 μm)	$50\,\mathrm{cm} - 2\,\mathrm{m}$	$\sim 0.5''$	$2.77''$	$0.069''$
Mid-infrared (10 μm)	$5\,\mathrm{m} - 20\,\mathrm{m}$	$\sim 0.2''$	$12.6''$	$0.3''$

Table 3.2 shows that the resolution of optical observations are, in most of the cases, seeing limited ($\theta_{\mathrm{seeing}} \gtrsim \theta_{\mathrm{diffrac}}$). Note that for a 1 m telescope, the atmosphere degrades the angular resolution by about two orders of magnitude. Also evident is the strong dependence of r_0 on wavelength – expressed in Eq. (3.4) – which makes it easier to reach the diffraction-limited resolution in the NIR.

In the case of the IRAS 01072+4954 observations, if performed in seeing-limited mode, the spatial resolution element would have covered the whole galaxy bulge. In order to achieve better resolution on the nucleus of this faint source, active and adaptive optics have been used to reduce the effects of the atmospheric turbulence.

3.2.3.1 Active and adaptive optics

Adaptive optics (AO) systems are designed to correct, in real time, phase variations of electromagnetic waves from astronomical sources, that are introduced by the turbulence in the atmosphere while the signals travel to the detector. Active optics operates under the same principles, but is dedicated to correct lower frequency and

larger spatial fluctuations, some of them related to the telescope deformation and errors while tracking a source on the sky. The systems consist of three main types of elements: (i) the deformable and the tip-tilt mirrors that make the physical corrections; (ii) the wavefront sensor, which is an instrument that detects and quantifies the phase variations; and (iii) the control system, which calculates the deviations of the wave front shape and translates them into a set of voltages that codifies the corrections the mirrors apply (Fig. 3.7). The success of these systems lies on their capability of tracking and correcting in real time the fast variations of the wavefront. The time scale of these phase variations is related to the temporal coherence of the turbulence that passes in front of the telescope aperture. The
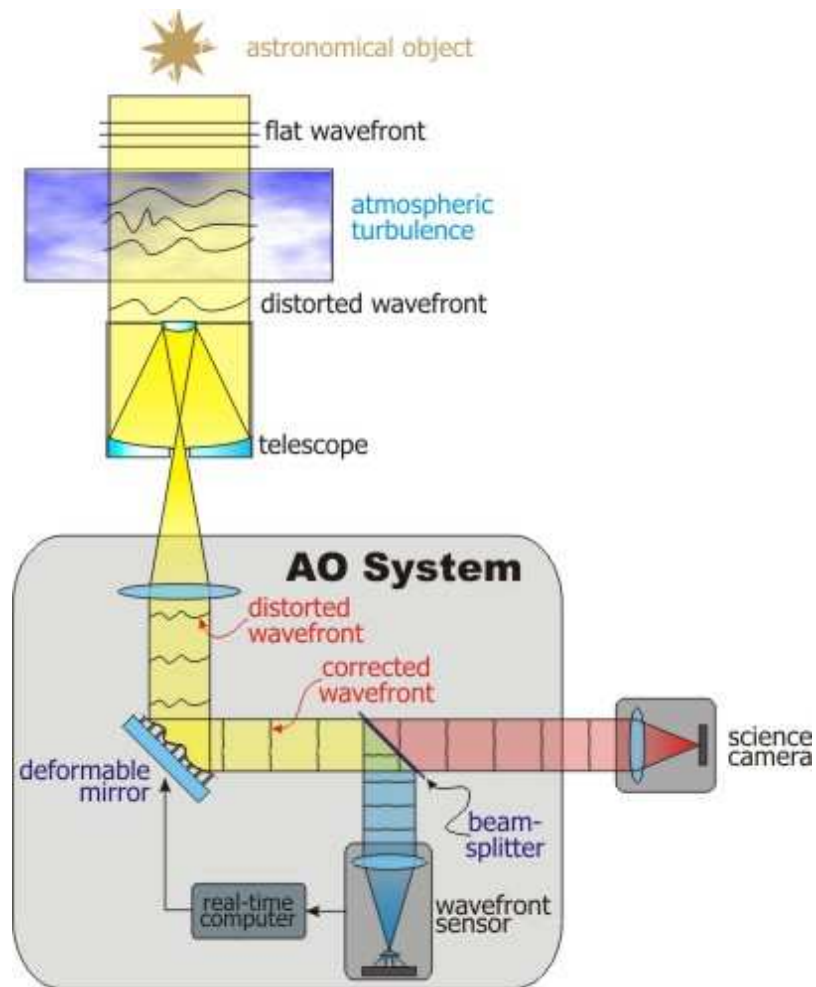
Figure 3.7: Active and adaptive optics system. The signal from the target and from the reference star, distorted by the atmospheric turbulence, enters the telescope where the beams are splitted. That of the star is redirected to the wavefront sensor, which measures the degree of the distorsions in every spatial element. This information is processed by the control system, which sets in real-time the deformation of the internal mirror in such a way that the initial distorsions of the wavefront are corrected.

time scale τ_0 above which the effects of the turbulence become significant, depends mainly on the wind speed v,

$$\tau_0 = r_0/v, \tag{3.6}$$

which can be interpreted as the time it takes a refractive index fluctuation with characteristic size r_0 to move its own diameter by the action of the wind. The typical wind speed at the observing locations is $\sim (10-20)\,\mathrm{m\,s^{-1}}$, so for r_0 of few tenths of centimeters, $\tau_0 \sim 1\,\mathrm{ms}$, which implies reaction frequencies up to $1\,\mathrm{kHz}$.

In order to correct the incoming light from a target, AO systems require a guiding source i.e., a point-like source in the field of view. This source is used to determine the deformations of the wavefront and the corrections that should be applied to the target. To assure that the turbulence affecting the guiding source and the target is the same, their light rays must go through regions of the atmosphere where the refractive index fluctuations are approximately the same. If only one turbulence layer located at a height h is considered, when the light paths cross the layer, the maximum distance between them must be r_0. In that extreme case, the angular separation between the two sources on the sky $\theta_0 \sim r_0/h$ is called 'isoplanatic angle', and the area subtended by a circular cone of θ_0 opening angle is the 'isoplanatic patch'. In other words, all sources located on the same isoplanatic patch suffer approximately the same distortions, which consequently can be corrected in the same way. In the general case of several layers of turbulence, the isoplanatic angle is defined as

$$\theta_0 \equiv \left[2.914 \left(\frac{2\pi}{\lambda} \right)^2 (\sec\zeta)^{8/3} \int_0^\infty C_n^2(h)\, h^{5/3}\, \mathrm{d}h \right]^{3/5} = 0.314\,(\cos\zeta)\,\frac{r_0}{H}, \tag{3.7}$$

where

$$H \equiv \left[\frac{C_n^2(h)\, h^{5/3}\, \mathrm{d}h}{C_n^2(h)\, \mathrm{d}h} \right]^{3/5} \tag{3.8}$$

is the mean effective turbulence height. In the NIR, with $r_0 \sim 1.2\,\mathrm{cm}$ (see Table 3.2) and assuming that the effective height of the turbulence is $H \sim 10\,\mathrm{km}$, $\theta_0 \lesssim 10''$. In the optical, turbulence in the lower layers of the atmosphere, $\sim (1-2)$ km height, dominates the seeing resulting in similar isoplanatic angles.

Two kinds of guiding sources are available: natural guide stars (NGSs) and laser guide stars (LGSs). In the case of NGS, a bright and compact astronomical object is used, typically a star of magnitude $R \sim 11-14$; but an extended source can also be suitable if it offers enough contrast to the background. However, as explained before, the guiding star must be closer than $10-15''$ to reach a good AO performance. Only under excellent seeing conditions, NGSs at $\sim 25''$ from the main target might be used. The probabilities of finding a NGS that fulfills the requirements for a desired target are not high. The sky coverage achievable with this technique is $\lesssim 10\%$ (Hubin & Noethe 1993; Davies & Kasper 2012). In order to overcome that problem, artificial point-like LGS sources can be created as close to the target as necessary. The technique employs a laser beam to excite sodium
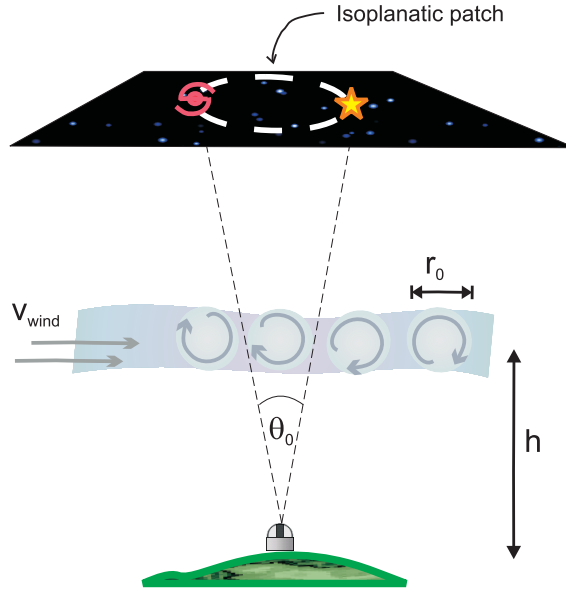
Figure 3.8: Schematic representation of the isoplanatic patch. The characteristic scale of the turbulence r_0 is located in a turbulence layer at a height h.

atoms at an altitude of $90 \, \text{km}$, or molecules in the low stratosphere, at 20 to $40 \, \text{km}$ height, creating an artificial star. The wavefront sensor is designed to detect the back-scattered light originating from a few kilometers around those altitudes. The main drawback of this technique is that the light from the LGS does not cross the same amount of turbulence layers as the that coming from the target. This leads to an error in the phase corrections that could be reduced using several LGSs to model high altitude turbulence. Observations in LGS mode also require a tip-tilt star of $R \sim (12 - 18) \, \text{mag}$, within $< 1 \, \text{arcmin}$ from the science target, to correct the overall tilt of the wavefront that produces the image centroid shifts on the detector. With this technique a sky coverage of $\sim 90\%$ is reached. In both cases, the guiding star is observed in the visual band $(450 - 900) \, \text{nm}$ with highest sensitivity around $650 \, \text{nm}$. Detectors of this wavelength are more efficient and produce less read-noise. This is possible because to a first order, phase variations are achromatic, i.e., the distorted shape of the wavefront is the same at all wavelengths. Any atmospheric refraction difference between the optical guiding wavelength and the observation filter is also corrected by the control system.

In the case of the IRAS 01072+4954 observations, the AO system ALTAIR (ALTitude conjugate Adaptive optics for the InfraRed) in LGS mode was used. The AO module uses a $10 - 20 \, \text{cm}$ deformable mirror (equipped with 177 actuators that control the deformations) and an internal tip-tilt mirror to correct higher-order phase variations. The Shack-Hartmann wavefront sensor (WFS), located at the pupil of the telescope, uses an array of lenslets to split the wavefront into many subapertures, which creates an arrangement of spots on the WSF detector (Fig. 3.9). Each spot corresponds to a distinct region on the deformable mirror. In

the absence of turbulence, the spots form a rectangular aligned grid, any deviation from this pattern indicates a wavefront distortion. The positions of the spots are measured with high accuracy to determine the high-order distortions to be corrected by the AO system. Lower-order distortions, e.g., like the overall shift of the pattern, are corrected by the active optics system, which controls the shape of the primary mirror and the tilt of the secondary mirror.
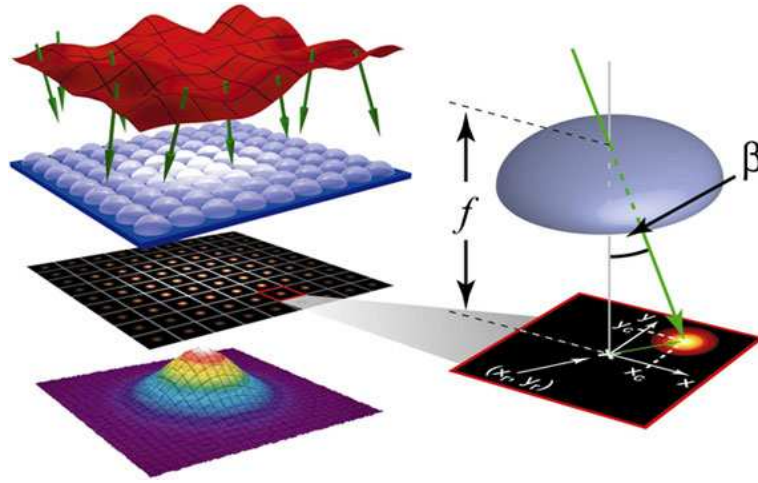

Figure 3.9: Shack-Hartmann wavefront sensor. The red corrugated sheed represents the distorted wavefront with the directions of the light-rays drawn as green arrows. The array of lenslets forms a image of the source focusing the light of each sub-aperture on the grid of the wavefront sensor. When the incomming wavefront is planar, the light of is focused at the center (x_r, y_r) of each cell. Otherwise, the sub-image will be formed at (x_c, y_c) in the direction β (*Left*). This image was kindly provided by M. Konnik.

The 'Strehl ratio', i.e. the ratio between the peak intensity of the image of a source compared to the maximum intensity of the Airy pattern it would produce in the theoretical diffraction-limit case, is often used as quality criteria of the AO performance. Without AO corrections and in the case of r.m.s. phase errors less than 2 rad, the Strehl ratio S can be approximated as

$$S = \exp\left[-1.03(D/r_0)^{5/3}\right]. \tag{3.9}$$

This indicates that, for $D \gtrsim r_0$, the larger the telescope diameter or the shorter the wavelength, the lower the Strehl ratio. With the current AO systems it is possible to increase the angular resolution and the Strehl ratio up to $S \sim 0.8$ (Esposito et al. 2010). Fig. 3.10 shows the same field of view as Fig. 3.6, observed with and without AO. Active and adaptive optics systems in NGS mode achieve somewhat better Strehl ratio than in LGS mode, but in general, the AO NGS performance depends strongly on the seeing and the brightness of the guiding star.

The AO systems have pushed forward many astrophysical areas of research. For example, mapping the surface of asteroids, planets and satellites; discovering disks and planets around young stars; and resolving stellar crowded fields like the
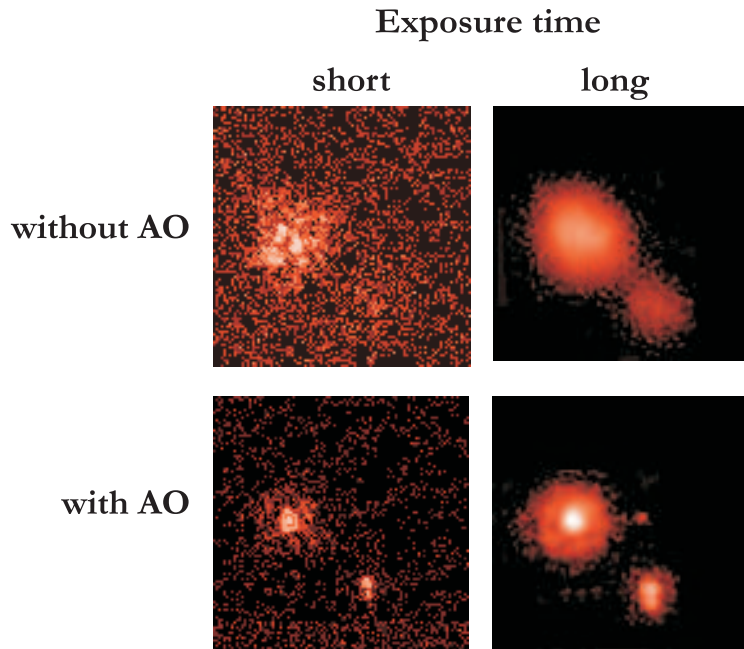
Exposure time

Figure 3.10: Adaptive optics image correction. Comparison between short/long exposures, with/without AO of the Orion Trapezium Theta 1 Ori B stellar group with MTT. Without AO, after 23 s the system appears to be two stars. When using AO, a long exposure reveals 4 of the members, including a visual binary B2/B3 separated $0.1''$, a very faint star B5 – to the right of the bright one –, and the brightest source B1/B5 which is an eclipsing spectroscopic binary with 0.16 AU separation between them. Using AO, the PSF reduces to $0.077''$ and the Strehl ratio improves from 0.005 to 0.1. Credit: L. Close and G. Brusa, CAAO, Steward Observatory

Galactic Center, which allowed the most accurate measurement of the mass of a supermassive black hole. In the case of extragalactic sources, the high angular resolution reached in AO observations allow us to estimate black hole masses of AGN, resolve stellar populations, map the kinematics of gas and stars, find indications for inflow or outflow of material toward the nucleus, and discover traces of accretion onto a supermassive black hole.

3.3 Integral Field Spectroscopy

Integral field spectroscopy (IFS) allows one to obtain spatial and spectral information of a source simultaneously. Some of the advantages of the IFS over the long-slit spectroscopy are: (i) the elimination of slit losses when observing seeing-broadened objects (although see Robertson 2001); (ii) the unbiased mapping of velocity fields, in contrast to velocity profiles (rotation or dispersion curves) that depend on the position and orientation of the slit; like photometric observations: (iii) the acquisition of a source is faster – with a long-slit, the target has to be located accurately to match the aperture of the slit; (iv) it is easier to feed the AO system for atmospheric turbulence correction. On the other hand, some disadvan-

tages are: (i) the smaller field of view, although this problem has been overcome by flexible systems that can map separated regions of the sky like VIMOS MOS at VLT; (ii) the long integration times, comparable to long-slit spectroscopy; (iii) depending on the IFS technique, the larger deadspace on the detector.
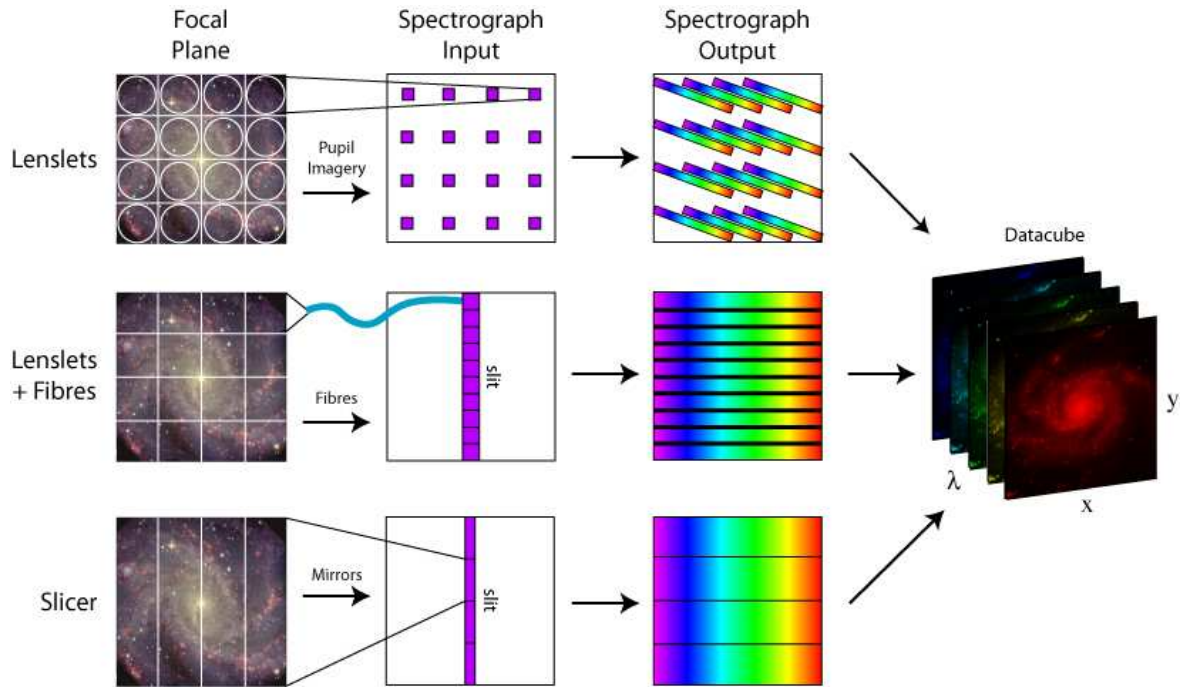

Figure 3.11: Techniques of Integral field spectroscopy. Credit: M. Westmoquette, adapted from Allington-Smith & Content (1998).

The three major techniques are shown in Fig. 3.11. The 'Lenslet arrays' use a rectangular arrangement of microlenses (lenslets) to segment the field of view in small elements. Each of these elements is observed by one lenslet generating, as a whole, an imagery of the telescope pupil. Since the set of pupil images forms a two-dimensional configuration, the dispersion axis has to be tilted in order to avoid spectra overlapping and enough detector deadspace must be provided in between the spectra to prevent mixing light of different wavelengths.

Focal ratio: the ratio of the focal length f to the diameter D of the aperture. It can be interpreted as the cone angle of the beam. Large focal ratios $(f/D \gtrsim 8 \equiv f/8)$ indicate small cone angles and slow beams.

The 'Fiber arrays' are a more flexible system, where a bundle of optical fibers are disposed in a two-dimensional array at the telescope focus, and then they are reformatted into one (or more) linear pseudo-slit(s) to be dispersed. This system clearly reduces the deadspace on the detector and it is commonly used in optical devices. The major disadvantage of this technique is the 'focal ratio degradation'. The telescope focal ratio defines the angular distribution of the beam, which is 'slow' compared to the focal ratios used by most of the optical fibers $\sim f/5$. All

fibers tend to reduce the incident focal ratio producing a loss of information

The 'Fiber-lenslets' are designed to solve this problem. They have a set of lenslets at the entrance of the fiber bundle to speed up the beam before it enters the optical fibers, and in some cases, another set is also attached to the exit to match the focal ratio at which the spectrograph operates. Some instruments that use these techniques are INTEGRAl at William Herschel Telescope (without lenslets) and GMOS at Gemini South/North (with lenslets).

The 'Image slicers' use a curved panel of narrow mirrors to slice the field of view in several thin rectangles which are reflected in different directions. Then a series of mirrors deflect the reflected beams and arrange them one over the other to form a pseudo-slit. In this form they enter the spectrograph producing a good detector coverage. Each of the dispersed slices is called slitlet. One of the main advantages of this technique is the possibility of usage at cryogenic temperatures which are required when observing in the NIR.

The Near-infrared Integral Field Spectrometer (NIFS), used in this study, is an Image-slicer IFS. The instrument divides the $3'' \times 3''$ field of view in 29 slices and disperses them along the horizontal axis of the 2048×2048 pixels detector area. The resulting resolution is $0.103''$ across and $0.047''$ along the slices. The spectral resolution in HK-bands is $R = 5290$. The system is fed with AO module ALTAIR arriving to a spatial resolution PSF $\approx 0.1''$ in the HK-bands. More information about the instrument is available in the Gemini Observatory web pages and in McGregor et al. (2003).

3.3.1 Reconstruction of the source information

he reduction of NIR IFS data obtained with the Image-slicer technique includes the application of the usual procedures to correct for dark current, flat field, dead pixels, and sky absorption/emission in every slitlet. Besides, a spatial rectification for the proper alignment of the slitlets must be applied. This is realized comparing the orientation of the slitlets in the raw images with a spatially calibrated pattern e.g., a Ronchi mask. This information, together with the wavelength calibration, provides the necessary input for the construction of the 3-D data cubes (2 spatial + 1 spectral dimensions).

I performed the reduction using the GEMINI IRAF[1] package, released Version 2.14, of September 15, 2008. Mainly the NIFS and GNIRS packages were used in combination with generic IRAF tasks. The Cosmic-Ray Removal Algorithm of W. Pych (2004) was also applied as described below. The final reconstruction of the data cubes (8 per band, corresponding to 8 exposures, and then, 2 final cubes in H and K, from the combination of the cubes in each band), flux calibration and further data manipulation were accomplished using own IDL routines.

---

[1]IRAF is distributed by the National Optical Astronomy Observatory, which is operated by the Association of Universities for Research in Astronomy (AURA) under cooperative agreement with the National Science Foundation.

3.3.1.1   Cosmic rays

Cosmic rays are usually recognized for their extended imprints on the images. They can be eliminated from the final realization taking a median over several exposures. In the case of IFS units as NIFS, their imprints affect the spatial and the spectral dimension simultaneously. In our observations, given the long exposures, significant amounts of cosmic rays were collected by the detector. The usual procedure could not be applied to the raw data, because it is possible that different exposures had slightly different alignments and therefore taking a median would not only deselect cosmic rays. This also could not be done with the final
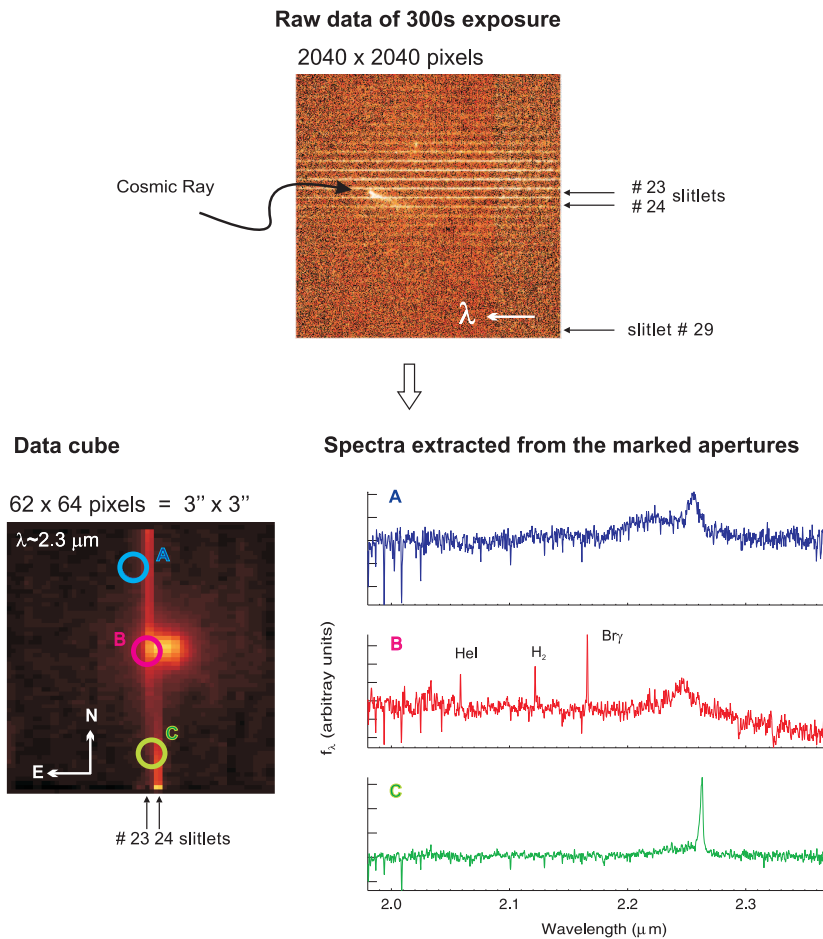
Figure 3.12: Cosmic rays in the NIFS data. *Top:* 300 s K-band exposure of IRAS 01072+4954. Sky correction and W. Pych algorithm for cosmic-rays removal have been applied to the data. The zoom-in area shows the extent of the cosmic ray. *Bottom:* Narrow-band (2.293 μm to 2.322 μm) image extracted from the data cube reconstructed with the raw data shown on top. At the left, spectra from three different regions affected by the event are shown. Each spectrum is obtained integrating the emission within the drawn apertures. Notice that the presence of the cosmic ray affect the continuum slope of the overall K-band spectrum. This exposure was therefore discarded.

data cubes, because depending on the energies of the particles and hit positions on the detector the cosmic rays can affect the fitting algorithm of the 2D-to-3D transformations. For this reason, I decided to use an algorithm developed by Pych (2004) which can be applied to single raw images before the IRAF reduction process. The algorithm is based on the fact that cosmic-rays imprints do not have a Gaussian distribution and can be selected from the distribution of counts in the image. With this procedure many compact X-rays were eliminated. However, particularly in the last K-band exposure, a low-energetic and wide-extended cosmic ray close to the center of the image could not be removed. Its effects can be seen in the reconstructed cube (Fig. 3.12), which for this reason had to be discarded.

3.3.1.2 Data reduction and calibration

Here, I summarize the procedure for reducing and calibrating the IRAS 01072+4954 NIR data. First, sky emission lines were corrected by subtracting from the target exposures the associated sky observations. Then, as explained before, the Pych algorithm for the cosmic ray correction was applied. The files were put in the multi-extension format required as an input of the GEMINI IRAF routines (15.09.2008 Version 2.14). Within the IRAF environment, the task NFPREPARE attached to each image a MDF file with the information about the slicer pattern and the mapping between the detector and the sky fields. With NSREDUCE the slitlets were cut and appended in different extensions to their original file; also in this task, the image was corrected for the detector inhomogeneous sensitivity (flat field). The bad or dead pixels were fixed with NFFIXBAD. In order to perform the spatial and spectral rectifications, the Ronchi mask and the calibration lamp were prepared using the IRAF-NIFS routines. Then, they were used as input of the NSFITCOORDS and NSTRANSFORM tasks, which derived and applied the transformations. For the telluric correction, the images of Hipparcos 4844 were reduced in the same way as the galaxy images, the stellar spectrum was extracted with the task NFEXTRACT, and the correction was applied with NFTELLURIC. Finally, the multi-extension files corresponding to the target exposures were converted into data cubes with the task NIFCUBE. Fig. **??**. In this way, eight data cubes in each band were produced. The eight H-band and seven K-band cubes were shifted and combined to create the final cubes.

For the estimation of the point spread function, the star J01100963+5010180 was observed as a reference (see Fig. 4.1 on page 58) and its images were reduced in the same way as those of the galaxy. The FWHM of a two-dimensional Gaussian fitted to the image of the reference star indicated a spatial resolution of $0.16''$ in H-band and $0.13''$ in K-band.

The wavelength calibration was performed with the GEMINI IRAF routines. In order to check its accuracy, the same reduction procedure used in the target frames was applied to one of the sky exposures in each band and an average spectrum of the sky was obtained. The deviation of the OH spectrum was estimated fitting Gaussians to the most prominent OH emission lines (P1, R1, Q1 and Q2 transi-

tions) and taking the median of the differences between the centroids of the fits and the theoretical values (Rousselot et al. 2000). A deviation of $(0.43 \pm 0.08)\,\text{Å}$ was found in the H-band and $(-0.29 \pm 0.12)\,\text{Å}$ in K-band. These values are low compared to the spectral resolution, however, given their systematic presence along the data, I decided to correct for them. Finally the wavelength axes of the data cubes were transform to the rest frame of the galaxy using the published redshift value $z = 0.023616$.

Absolute Flux calibration

The procedure I followed for the flux calibration of IFS data is based on that of long-slit spectra. A star with known apparent magnitude in the desired band must have been included in the observations, because the aim is to establish the conversion between counts per second at each wavelength and specific flux – in e.g., $\text{erg}\,\text{s}^{-1}\,\text{cm}^{-2}\,\mu\text{m}^{-1}$. In our case, the observations of two stars could be used for that purpose, the PSF reference star or the telluric standard star. Using both separately served to cross-check the accuracy of the calibration.

The first step is to find the 'zero point' ZP, which is defined as the apparent magnitude m of an object that would produce $1\,\text{count/s}$ at an airmass of 1.0, i.e.,

$$\text{ZP}_{\text{X}} = m_X + 2.5\log\left(\frac{R_X}{\text{count/s}}\right),\qquad(3.10)$$

where the subscript X stands for the spectral band, and R_X is the instrumental response in the same band. In our case, the known 2MASS magnitudes of the stars were converted to the MKO magnitudes using the relations by Leggett et al. (2006, their Table 4.). Given that the magnitude of a star corresponds to the mean value of its specific flux (corrected by extinction) over the wavelength interval of the band, the instrumental response also has to be calculated as the mean number of counts/s that the star produces on the detector over the band. In order to do that, a stellar spectrum was extracted from the data cube of each star. The aperture for the extraction had a radius $3 \times \text{FWHM}$, with the FWHM derived from a two-dimensional Gaussian fitted to the mean image of the star. The stellar spectrum obtained in this way, divided by the exposure time, represents the instrumental response along the wavelength $R_X(\lambda)$ and its mean is R_X.

The instrumental response $R_X(\lambda)$ must be compared to the intrinsic specific flux $f_\lambda(\lambda)$ – i.e., the spectra – of the stars to find the 'sensitivity curve' of the detector along the wavelength axis. The stellar spectra was modelled as blackbodies at the temperatures corresponding to their spectral types. To determine the amplitudes, so that the functions resemble the intrinsic stellar emission, it is necessary to estimate the specific fluxes of the stars at the reference wavelength of the band $f_\lambda(\lambda_0)$. By definition, $f_\lambda(\lambda_0)$ is equal to the mean specific flux of the source over the considered band $f_\lambda(\lambda_0) = \langle f_\lambda \rangle$. Therefore, it can be found as

$$f_{\lambda,X}(\lambda_0) = f_{0,X} \cdot 10^{-0.4\,m_X},\qquad(3.11)$$

where $f_{0,X}$ is the flux of a magnitude zero star. In our case, I used the $f_{0,H}$ and $f_{0,K}$ of Vega (αLyr) computed by Tokunaga & Vacca (2005) for the MKO NIR filter set, assuming a water vapor of 2 mm at an airmass of 1.0. Then, the blackbodies are scaled such that at λ_0 their specific fluxes are $f_\lambda(\lambda_0)$.

The sensitivity curve $s(\lambda)$ is simply the ratio between the intrinsic emission of a star, represented by the scaled blackbody $f_{\mathrm{star},\lambda}$, and the observed instrumental response,

$$s_\lambda = \frac{f_{\mathrm{star},\lambda}}{R_X(\lambda)}. \tag{3.12}$$

The units of $s(\lambda)$ are e.g., $\mathrm{erg\,s^{-1}\,cm^{-2}\,\mu m^{-1}}\,/\,\mathrm{(counts/s)}$. Given that $R_X(\lambda)$ corresponds to the observed stellar spectra, a collection of absorption and emission lines would be present. Assuming that the intrinsic instrumental response is smooth along the wavelength axis, those features can be masked or $s(\lambda)$ can be fitted with a continuous function and used as a proxy for $s(\lambda)$. Finally, to calibrate the data cubes, the spectrum of every spatial pixel was multiplied by the sensitivity curve. To get an impression of the accuracy of the flux calibration, this procedure was applied to the star Hipparcos 4844 and its HK magnitudes were calculated and compared with published 2MASS values. The measured H-band magnitude of Hip 4844 was 6.05 mag, in comparison to 6.007 ± 0.016 mag, and its K-band magnitude was 6.00 mag, in contrast to 6.038 ± 0.016 mag that is reported. In a conservative approach, the uncertainty of the calibration calibration can be estimated in $\sim$10%.

3.4   Summary and Conclusions

The reduction procedure was performed using the GEMINI IRAF[2] package, released Version 2.14, of September 15 2008. Mainly the NIFS and GNIRS packages were used in combination with generic IRAF tasks. The Cosmic-Ray Removal Algorithm of W. Pych (2004) was also applied as described bellow. The final reconstruction of the data cubes, flux calibration and further data manipulation were accomplished using our own IDL routines.

Inside the IRAF package, the standard reduction procedure was followed. Sky emission lines were corrected by subtracting from the target exposures the associated sky observation. Then the task NFPREPARE attached to each image a MDF file with information about the slicer pattern and the mapping between the detector and the sky fields. With NSREDUCE each slit was cut and placed in different extensions, also in this task the image was flat-fielded using a previously created flat image. The bad pixels are corrected then with NFFIXBAD. In order to perform the spatial and spectral rectifications, a preprocessed Ronchi frame and a wavelength calibrated arc are required. These were used as inputs to the NSFIT-COORDS and NSTRANSFORM tasks, which derived and applied the spatial and

---

[2]IRAF is distributed by the National Optical Astronomy Osbervatory, which is operated by the Association of Universities for Research in Astronomy (AURA) under cooperative agreement with the National Science Foundation.

spectral transformations to every extension of the target.

Finally, the multiextension target image is transformed into a 2-D photometrical $\times$ 1-D spectroscopical data cube with the task NIFCUBE. The individual cubes were combined to obtaine a final data cube in each band. The flux calibration was perform in as similar manner as it is done in the case of spectroscopic data. The estimated flus error is $\sim 10\%$. Finally, the Galactic extinction correction of $E(B-V) = 0.156$ mag (Schlegel et al. 1998) weas applied to the data.

Chapter 4

Star Formation in the central kiloparsec

The high far-infrared luminosity of IRAS 01072+4954 and its strong Hydrogen emission in the optical suggest that this source is currently building a significant portion of its stellar mass. When did the process start? How significant is it for the galaxy? Is it taking place also in the bulge? How can it be seen in the near-infrared? This chapter is dedicated to answer these questions. First, the near-infrared (NIR) photometrical properties of the galaxy as a whole are presented, including some evidences for a nuclear bar or inner-nuclear disk – which is not directly visible in the images. Then, the data obtained with the Near-infrared Integral Field Spectrograph (NIFS) in *HK*-bands are presented. These constitute the first high angular resolution observations and the first near-infrared (NIR) spectrum of this source. Two methods to estimate the obscuration along the line of sight are also discussed. In the second part, I use global star formation tracers to determine the importance of this process for the whole galaxy. Then, the Integral Field (IF) capabilities of the NIFS observations of the bulge are exploit to determine the properties of the stellar population(s) at $\sim 1\,\mathrm{kpc}$ around the nucleus. A summary of the main findings and results is presented in the Conclusions.

4.1 IRAS 01072+4954 in the near-infrared

To the date, the only available images of the whole galaxy in the NIR are those provided by the 2MASS Survey[1] (Skrutskie et al. 2006). In the 2MASS images, IRAS 01072+4954 appears as a source with very low surface brightness, with less than $16\,\mathrm{mag\,arcsec}^2$ at the center. This is due to the faintness of the target, but also because of the low angular resolution of the images, $\sim 1.7''$ (as explained below, Sect. 4.1.2). With the NIFS observations we were able to probe up to

---

[1] Two Micron All Sky Survey is a joint project of the University of Massachusetts and the Infrared Processing and Analysis Center/California Institute of Technology, funded by the National Aeronautics and Space Administration and the National Science Foundation.

$\sim 17\,\mathrm{mag\,arcsec}^2$ – where the noise level is reached – at a resolution of $\sim 0.16''$. The $3'' \times 3''$ NIFS field of view (FOV) encloses the optical[2]/NIR bulge of the galaxy (Fig. 4.1).
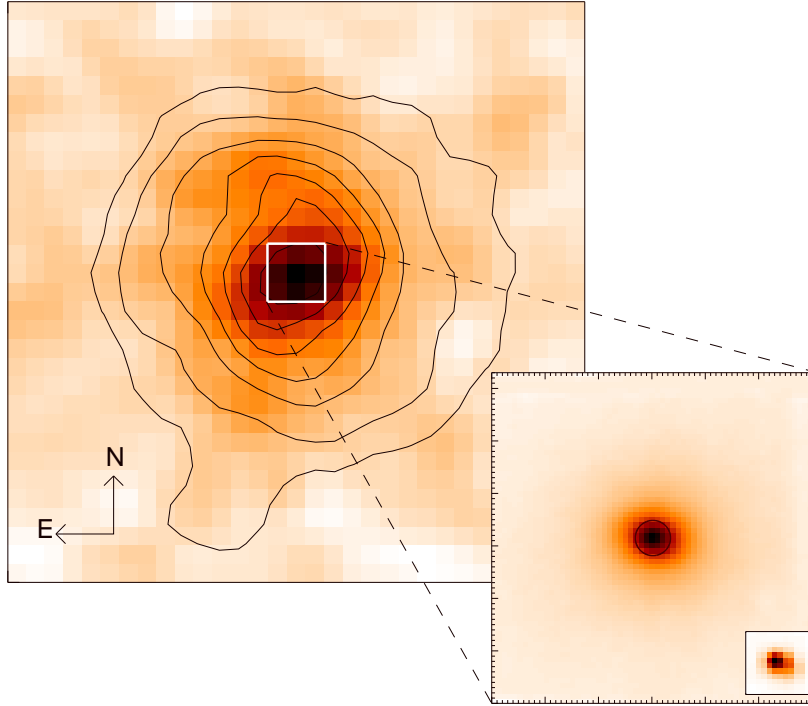

Figure 4.1: $30'' \times 30''$ 2MASS K-band image of the galaxy IRAS 01072+4954. The overlaid contours correspond to the optical POSS-II image of the galaxy. The levels are 0.3,0.4,0.5,0.6,0.7,0.8 and 0.9 of the optical peak flux. The central white square represents the $3'' \times 3''$ NIFS FOV. The NIFS K-band continuum is shown in the amplified region. The tick marks on the borders indicate the pixel scale $\sim 0.04''$. The image of the angular-resolution (or PSF) reference star is shown at the bottom-right corner.

4.1.1 Photometrical evidence of a nuclear bar

At first glance, the NIR surface brightness of IRAS 01072+4954 in the 2MASS and in the NIFS data look smooth and uniform. In order to recognize the presence of sub-structures in the disk or in the bulge, I use the unsharp masking method. It essentially consists on subtracting a smoothed image of the galaxy from the original one, adjusting the smoothing function to strengthen the compact structures.

Figure 4.2 shows in the second panel at the top the result of this process applied to the $15'' \times 15''$ 2MASS K-band image (left top panel). The subtracted image was

_____

[2]Optical image was taken from the Second Palomar Observatory Sky Survey (POSS-II)

convolved with a 2D Gaussian with a width of $\sigma = 1.5''$. An elongated structure, that resembles a bar, emerges at the center. Comparing the shape of this feature with that of the 2MASS PSF ($\text{PSF}_{\text{2MASS}}$, image at the bottom right corner on the second panel) it is possible to evaluate how significant this elongation is. Fitting elliptical 2D Gaussians to both shapes, axis ratios (a/b) of 1.00 for the $\text{PSF}_{\text{2MASS}}$, and 1.68 with orientation P.A. = 105° for the central structure are obtained. This seems to indicate that the shape is intrinsic to the sub-structure. However, the sizes are comparable, implying that the bar-like feature is not resolved in the 2MASS image.

When the same procedure is applied to the $3'' \times 3''$ NIFS image, the AGN and hot dust emission at the center dominate the residuals. Their contribution corresponds to the NIFS PSF (PSF_{NIFS}), which is assumed to be well described by the image of a star close to the field of view. To remove this emission, the PSF_{NIFS} is subtracted from the K-band continuum image, in the maximum amount possible such that the residual image is still smooth at the center. Then, the unsharp masking procedure is applied convolving the image with a Gaussian of $\sigma \approx 0.07''$. The second panel at the bottom of Fig. 4.2 shows the results. In the bottom-left panel, the K-band continuum image, created by taking a median of the NIFS data cube over the wavelength range $2.00 - 2.35\,\mu$m, is shown. The unsharp masking method reveals an elongated structure. The faint and more extended emission at the center probably corresponds to residuals of the PSF subtraction. When fitting the elongated feature with a 2D Gaussian, I find that the axis ratio $a/b = 1.74$ and the orientation P.A. = 97° are comparable to the values found previously with the 2MASS data. This allows to suspect that both residuals are related to the same sub-structure. In this case, the sensitivity of the observations is not high enough to obtain a better map of it, and for the same reason, cannot be resolved. As shown in Fig. 4.2 (bottom-right), its surface brightness is on average $\sim 3.0 \times 10^3\,\text{L}_{\odot,\text{K}}\,\text{pc}^{-2}$. This is the same brightness as that observed in the continuum image at about 1 arcsecond from the center. An exact estimation of the significance of the bar contribution to the NIR emission is not possible, because all emission fainter than $\sim 17\,\text{mag}\,\text{arcsec}^{-2}$ – which includes the disk – in the NIFS observations is missing.

4.1.2 Near-infrared Brightness profile

The brightness profile of a galaxy allows to know how the different emitting components are distributed, can help on identifying substructures and gives hints on the galaxy evolution process. To make a proper decomposition of the photometric components (AGN, bulge, disk, bar), it is necessary to have an image of the whole galaxy, because they are co-spatial. The faintness of the source in the 2MASS observations does not allow a 2D decomposition. As a first approximation, I obtained the brightness profile $I_{\text{observ}}(r)$ integrating the 2MASS K-band image over circular rings of $1''$ width, centered at the continuum peak. This procedure does not allow to get any information about a non-axisymmetric structures like a bar. As in the previous section, the $\text{PSF}_{\text{2MASS}}$ was derived from a star in the field and modeled
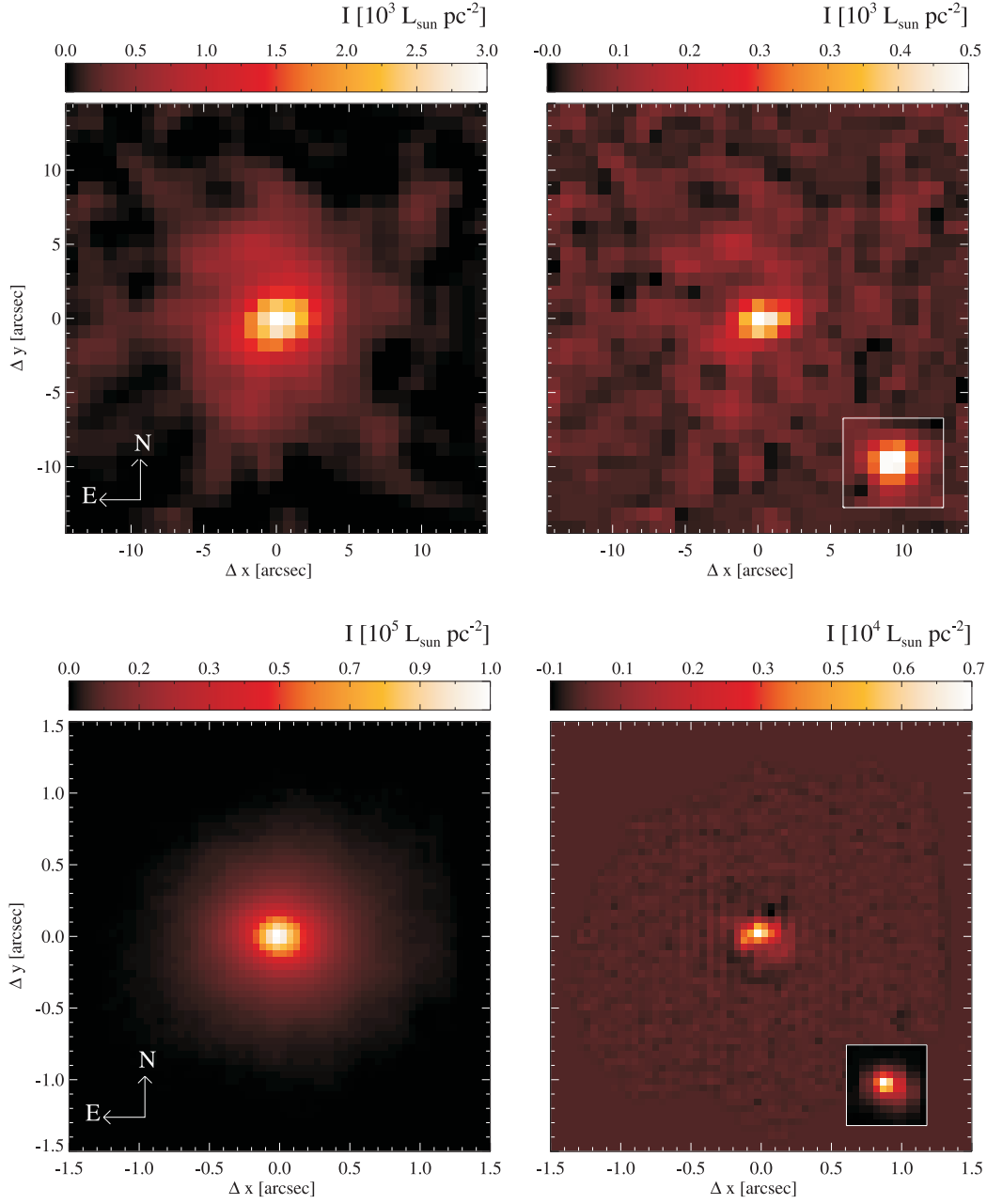
Figure 4.2: Photometrical evidence of a nuclear bar in IRAS 01072+4954 from the 2MASS and NIFS *K*-band images. The images at the *left* show the calibrated K-band surface brightness distribution of IRAS 01072+4954. *Top:* $15'' \times 15''$ 2MASS image. *Bottom:* $3'' \times 3''$ NIFS image. On the *right* panel, the result of the unsharp masking procedure applied to the left images is shown. Images of a star in the field, that represent the PSF in each case, are shown at the bottom-right corner. In the case of the NIFS data, the unsharp masking was performed after the removal of the strong PSF contribution (see text for details).

as a Gaussian with FWHM $= 3.34''$. The bulge was assumed to follow a general Sersic profile with effective radius r_e and index n as parameters. The disk was described by an exponential profile with scale radius h. The fit was done using the IDL based routine MPFITEXPR (Markwardt 2009) to minimize the expression $|I_{\mathrm{observ}}(r) - I_{\mathrm{model}}(r)|^2$, where

$$I_{\mathrm{model}}(r) = \left[c_0 \, \exp\left\{ -\nu_n [(r/r_e)^{1/n} - 1] \right\} + c_1 \, \mathrm{e}^{(-x/h)} \right] * \mathrm{PSF}_{\mathrm{2MASS}}, \qquad (4.1)$$

here, c_0 and c_1 are constants, '$*$' means convolution and ν_n is a function of the Sersic index that can be determined from n using the approximation

$$\nu_n = 2\,n - \frac{1}{3} + \frac{4}{405\,n} + \frac{46}{25515\,n^2} + \mathcal{O}\left(n^{-3}\right). \qquad (4.2)$$

The minimum value for the Sersic index was set to $n = 1$. Otherwise the procedure was giving $n \approx 0.5$, which corresponds to a Gaussian profile, and might imply a degeneracy between the AGN and bulge components.

Figure 4.3 presents the best fit to the 2MASS K-band data with the photometric parameters: $r_e = (0.8\pm0.3)\,\mathrm{kpc}$, $n \approx 1$ and $h = (1.75\pm0.8)\,\mathrm{kpc}$. As Fig. 4.3 shows, the fitted effective radius, which corresponds to $\sim 1.7''$, is about the same as the $\mathrm{PSF}_{\mathrm{2MASS}}$, meaning that probably the bulge component is not resolved in the 2MASS image.

A second attempt to obtain the bulge parameters was done including the NIFS data. Fig. 4.4 shows the best fit to the H- and K-band NIFS+2MASS data. In the case, the Sersic profile was convolved to the resolution of the NIFS observations, while the exponential function to the one of the 2MASS image. One extra component was used for the K-band profile, where the AGN + hot dust contribution was modeled as a Gaussian with the width of the NIFS PSF ($\mathrm{PSF}_{\mathrm{NIFS}}$). Hence, the surface-profile model in this case was

$$
\begin{aligned}
I_{\mathrm{model}}(r) \;=\;& k_0\,\mathrm{PSF}_{\mathrm{NIFS}} \\
+\;& \left[k_1 \, \exp\left\{ -\nu_n [(x/r_e)^{1/n} - 1] \right\} \right] * \mathrm{PSF}_{\mathrm{NIFS}} \\
+\;& \left[k_2 \, \mathrm{e}^{(-x/h)} \right] * \mathrm{PSF}_{\mathrm{2MASS}}, \qquad (4.3)
\end{aligned}
$$

where k_0, k_1 and k_2 are coefficients and the other symbols have the same meaning as before. In the H-band, the contribution from the AGN and the hot dust are negligible – or not significant compared to the stellar one – , therefore when fitting the H-band profile, I used $k_0 = 0$. On the other hand, for the K-band modeling, k_0 was fixed to account for the detected 25% of non-stellar emission in the central $r = 0.16''$ (see Sect. 5.2). The photometric parameters r_e, n and h of the best fit of the H- and K-band profiles are listed in Table 4.1.

The fits shown in Fig. 4.4 must be taken as a first approximation to the actual brightness profile, because the data sets do not properly overlap with each other.

<div style="border-top:1px solid; border-bottom:1px solid;">

Surface brightness: It can be measured in $\mu\,/(\mathrm{mag/arcsec}^2)$ or $I\,/\,(\,\mathrm{L}_{\odot,\mathrm{x}}\,/\,\mathrm{pc}^2\,)$. To convert between them in the NIR, $I = 10^{-0.4(\mu-\mu_{\odot,\mathrm{x}})}$, $\mu_{\odot,H} = 24.89\,\mathrm{mag/arcsec}^2$ $\mu_{\odot,K} = 24.85\,\mathrm{mag/arcsec}^2$.
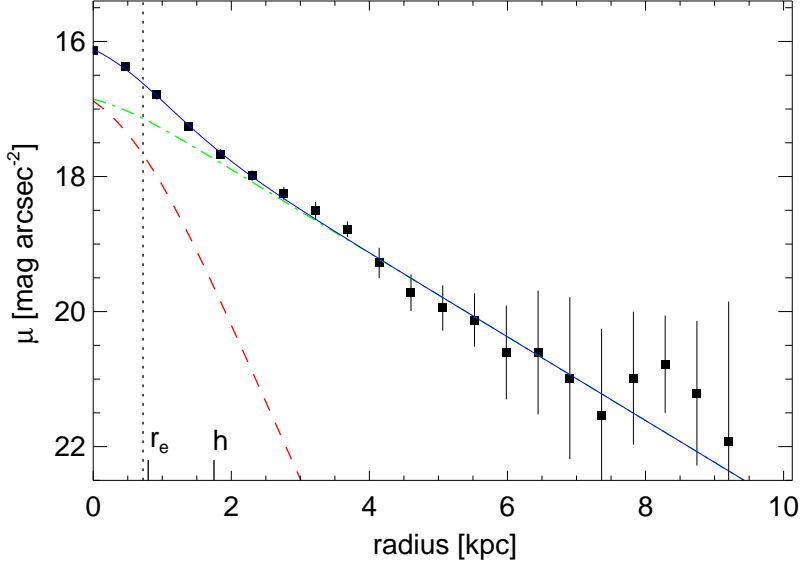
</div>

Figure 4.3: *K*-band brightness profile derived from the 2MASS image of IRAS 01072+4954. The solid blue line is the best fit of the data (filled squares). The two components of the model, bulge (dashed red line) and disk (dot-dashed green line), are shown. In the horizontal axis the positions of the effective radius r_e and the scale radius h are marked. The width of the 2MASS *K*-band PSF is signaled with the vertical dotted line. The 'hump' at $\sim 3.2\,\mathrm{kpc} \approx 6.8''$ correspond to the position of bright clumps in the spiral arms (compare e.g. with the top-right panel of Fig. 4.2). The sky level is reached at $\sim 21\,\mathrm{mag\,arcsec}^{-2}$.

Table 4.1: Photometric parameters derived from the fitting of the NIFS+2MASS surface brightness profile

		H-band	*K*-band
Sersic index	n	1.02 ± 0.07	1.17 ± 0.08
Effective radius	r_e (pc)	152.5 ± 12.9	159.2 ± 17.8
Scale radius	h (kpc)	1.42 ± 0.26	1.47 ± 0.53

The bulge of the galaxy fitted from the NIFS data extend until $\sim 0.9''$ (i.e., $\sim 0.4\,\mathrm{kpc}$), and the noise level is reached at $\sim 1.3''$ (i.e., $\sim 0.6\,\mathrm{kpc}$) which corresponds to $\lesssim \mathrm{PSF_{2MASS}}$. While it is clear that the NIFS observations captured the bulge of the galaxy and that the 2MASS image describes better the extended component, physically both components overlap along the projected radius implying that in Eq. (4.3) the second and third terms are not independent of each other, as it was
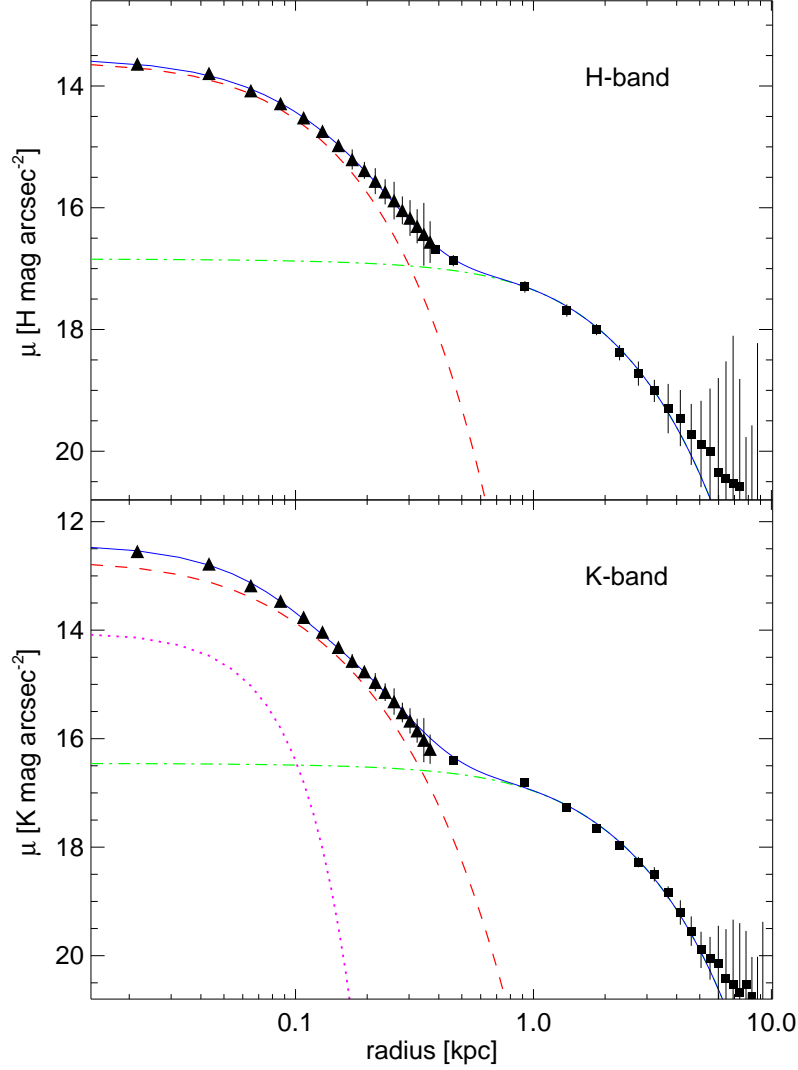
Figure 4.4: *HK*-band brightness profiles of IRAS 01072+4954 obtained by combining the NIFS (triangles) and 2MASS (squares) data. *H*-band profile is shown in the *top* panel and the *K*-band at the *bottom*. In both cases, the dashed red line corresponds to a Sersic profile fitted to the bulge, and the dash dotted green line to an exponential function that fits the disk component. The blue solid lines show the overall fits. The dotted purple line in the lower panel represents the AGN + hot dust contribution fixed to the 25% of the inner $r \approx 75\,\mathrm{pc}$ emission, based on the results presented in Sect. 5.2. The photometric parameters of the profiles in both bands are listed in Table 4.1.

assumed. Given the very different resolutions and sensitivities, it is possible that the flux at the center of the 2MASS image is spread-out and therefore, part of the disk flux at small radii is missing. A proper decomposition of the surface brightness requires high angular resolution observations of the whole galaxy or a major portion of it.

Brightness profiles similar to those of Fig. 4.4 have been observed in pseudo-bulge galaxies, like in NGC 1353 shown in Fig 4.5. Kormendy & Kennicutt (2004) presented some examples where a combination of HST WFPC2 and 2MASS *JHK* photometry allowed to study in great detail the photometric components of nearby galaxies that have pseudobulges. In these kind of bulges, the shape is mainly sustained by rotation of the stars in a plane than by dispersion. This might indicate a galaxy evolution triggered by internal/secular processes, instead of a mayor merger (see e.g., Orban de Xivry et al. 2011; Mathur et al. 2011). One of the main indications of the presence of a pseudobulge is the low Sersic index $n \lesssim 2$, however this is not conclusive. For example, most of the – claimed – pseudobulge galaxies studied by Hu (2008) are also barred galaxies. In that case, the low Sersic index could be related to the presence of the bar. In our case, the bar component does not seem to dominate the emission in the central $\sim 1\,\mathrm{kpc}$, but its contribution was not taken into account when constructing the 1D profile. However, if we accept that the NIFS data represent reasonably well the bulge of the galaxy, then IRAS 01072+4954 has a pseudobulge. In fact, this seems to be a common property of late-type galaxies (Andredakis & Sanders 1994; Andredakis et al. 1995; Ganda et al. 2009). In many Sc galaxies the bulge profile is close to an exponential, as observed in this case (see Kormendy & Kennicutt 2004, and references therein).
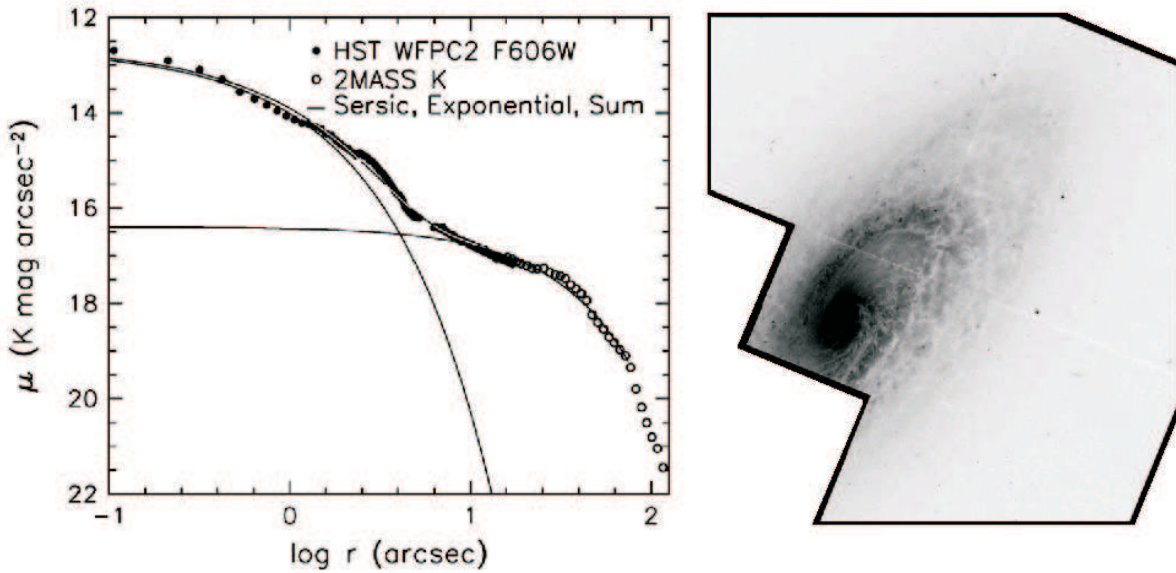
Figure 4.5: *Left: K*-band brightness profile along the mayor axis of the pseudobulge galaxy NGC 1353 ($z = 0.0051$). The fit combines HST (filled circles) and 2MASS (empty circles) data. *Right:*. Full WFPC2 F606W image taken with HST by Carollo et al. (1998). Taken from: Kormendy & Kennicutt (2004).

4.2 IRAS 01072+4954 as seeing by NIFS

As shown in the previous section, the NIFS observations cover the bulge of the galaxy, which extends until $r \approx 0.8''$ (i.e., $\approx 460\,$pc). Given that the HK continuum was also studied above, I concentrate here on the line emission. The absorption features are only briefly mention because they are analyzed in detail in Sect. 4.5.

4.2.1 Line maps

The observations cover the wavelength ranges $1.4510-1.730\,\mu$m in the H-band, and $1.9656-2.3701\,\mu$m in the K-band, at the rest frame of the galaxy. The most prominent emission lines in the spectrum of IRAS 01072+4954 are [Fe II] $\lambda 1.644\,\mu$m, Br10 $\lambda 1.737\,\mu$m, He I $\lambda 2.059\,\mu$m, H$_2$(1-0)S(1) $\lambda 2.122\,\mu$m and Brγ $\lambda 2.166\,\mu$m. Other lines like Br11 $\lambda 1.6811\,\mu$m and H$_2$(1-0)S(0) $\lambda 2.223\,\mu$m are not resolved, but detected over 3σ of the noise level. The coronal line [Ca VIII] $\lambda 2.322$ is also found at the nucleus. Deep absorption lines are present in the HK data. Several CO absorption bands – like CO(4-1) $\lambda 1.578\,\mu$m, (6-3) $\lambda 1.618\,\mu$m, (7-4) $\lambda 1.640\,\mu$m, (2-0) $\lambda 2.294\,\mu$m, (3-1) $\lambda 2.323\,\mu$m , and (4-2) $\lambda 2.352\,\mu$m – as well as Si I $\lambda 1.598\,\mu$m, Na I $\lambda\lambda 2.206\,, 2.209\,\mu$m and Ca I $\lambda\lambda\lambda 2.261\,, 2.263\,, 2.266\,\mu$m can be identified.

Emission line maps were extracted from the final cubes. The maps presented in Fig. 4.6 were created by integrating the spectrum in spatial each pixel over a $\sim 12\,$Å window around the central value of the emission line (in the case of Brγ, a wider window of 34 Å was used) after the subtraction of the underlying continuum, which was estimated as the average of two featureless adjacent sections of the spectrum placed at each side of the considered line. In all maps, north is up and east is left.

In general, the line emission is concentrated in the central $r \sim 0.5''$, which could be due the steep decrease in signal-to-noise toward larger radii. The distribution of the emission of the different species, as seen in Fig. 4.6, is very heterogeneous. While Brγ is very symmetric – though with a faint extension to the south-west –, He I and H$_2$ are elongated and inclined around 45 degrees. Br10 shows two flux peaks one at the center and the other $0.02''$ to the north. Although not fully resolved, [Fe II] emission seems to have an inclined "8" shape.

4.2.2 The HK-Spectrum

The Integral Field Spectroscopic technique allows to obtain a spectrum in each pixel of the field of view. Figure 4.7 shows the total emission integrated over an aperture with radius $r \approx 0.8''$ (*bottom*) and that of an aperture with the size of the H-band PSF centered at the continuum peak (*top*). The K-band data cube has been previously convolved to match the H-band spatial resolution. This is in order to ensure that the integrated emission in both bands arises from the same region. In the figure, the spectral position of emission and absorption lines from species present in these bands are signaled as reference. Therefore, the marks do not necessary imply detections.
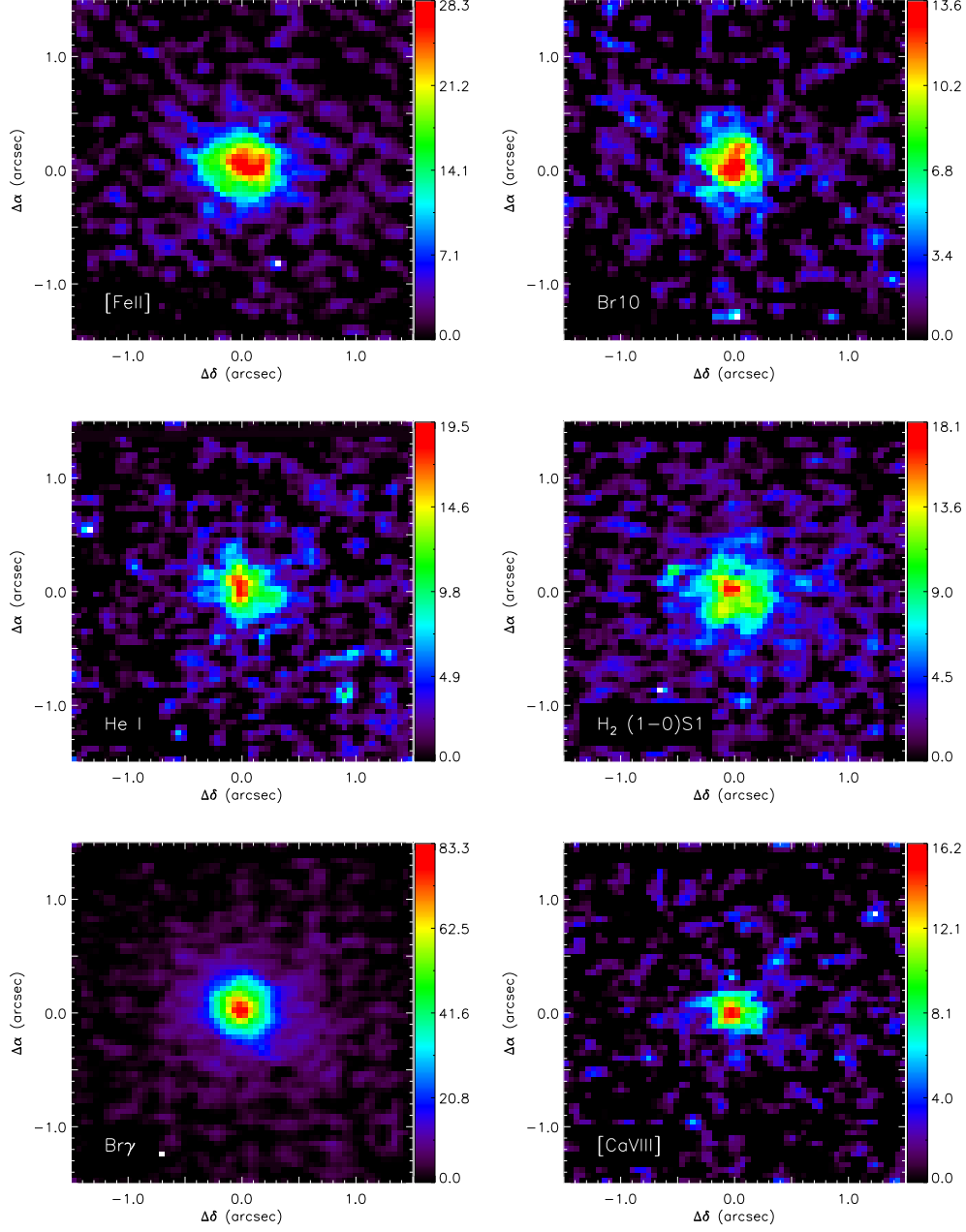
Figure 4.6: Emission line maps of the strongest features in the *HK* spectrum of IRAS 01072+4954. The maps are created by integration of the emission around each feature after subtracting the underlying continuum (see text for details). No minimum threshold was applied to the flux, therefore all emission out of $r \sim 1''$ is at the noise level. The color code is set to the minimum and maximum flux in each plot and is in units of $10^{-15}\,\mathrm{erg\,s^{-1}\,cm^{-2}}$. From *left* to *right* and *top* to *bottom* the emitting species are, as indicated in the panels, [Fe II], Br10, He I, H_2 1-0 S(1), Brγ and [Ca VIII]. North is up, east is left.

As I mention in Sect. 3.2.2 (see also Fig. 3.4, page 40), the long exposure periods per individual target observation, combined with a rapid variation of the sky, did not allow a proper removal of the OH sky emission lines. Their identification as such in the spectra is not straight forward, especially when some of the emission lines from the target are also very narrow. In this case, I have recorded their positions from the data cubes of the individual exposures, where they appear sometimes in absorption and others in emission. Another possibility, is to create line maps of those features in the same way as it is done for the recognized species. OH lines show emission across the whole field of view and no structure. In the spectra of Fig. 4.7 they are marked with the green symbols.

Table 4.2: Emission line fluxes and widths of the central region $r \approx 75\,\mathrm{pc}$ and of the bulge $r \approx 460\,\mathrm{pc}$ of IRAS 01072+4954

Species	λ (μm)	Center Flux^a ($10^{-16}\,\mathrm{erg\,s^{-1}\,cm^{-2}}$)	FWHM^b ($\mathrm{km\,s^{-1}}$)	Bulge Flux^c ($10^{-16}\,\mathrm{erg\,s^{-1}\,cm^{-2}}$)	FWHM^b ($\mathrm{km\,s^{-1}}$)
H I (Br13)	1.611 37	0.92 ± 0.40	217 ± 60	2.79 ± 0.96	206 ± 47
[Fe II]	1.644 00	2.96 ± 0.20	106 ± 6	7.25 ± 0.53	104 ± 6
[Fe II]	1.676 90	0.47 ± 0.17	103 ± 32	1.76 ± 0.92	178 ± 54
H I (Br11)	1.681 11	0.55 ± 0.10	38 ± 7	1.50 ± 0.31	60 ± 13
H I (Br10)	1.736 69	1.17 ± 0.48	165 ± 40	1.96 ± 0.59	107 ± 23
He I	2.058 69	1.04 ± 0.09	70 ± 6	2.95 ± 0.28	80 ± 7
H$_2$ 2-1 S(3)	2.073 50	0.27 ± 0.06	40 ± 9	0.73 ± 0.17	40 ± 10
H$_2$ 1-0 S(1)	2.121 83	1.70 ± 0.08	62 ± 3	6.12 ± 0.25	77 ± 3
H I (Brγ)	2.166 12	3.38 ± 0.11	80 ± 3	9.88 ± 0.28	82 ± 3
H$_2$ 1-0 S(0)	2.223 29	0.54 ± 0.11	115 ± 25	1.67 ± 0.26	87 ± 17
H$_2$ 2-1 S(1)	2.247 70	0.35 ± 0.10	96 ± 20	0.93 ± 0.15	50 ± 11
[Ca VIII]^d	2.321 41	0.79 ± 0.10	290 ± 42	–	–

^{a} Fluxes corrected by $A_V = 2.5\,\mathrm{mag}$. This value was obtained from the recombination line ratio, as explained in Sect. 4.3, see also discussion in Sect. 5.6.1.

^{b} The instrumental broadening has been removed.

^{c} Fluxes are not reddening corrected.

^{d} Flux and width measured as described in Sect. 5.1.1. The flux is not reddening corrected.

The flux of the emission lines was measured by fitting a Gaussian to them using the IDL based routine MPFITEXPR[3] (Markwardt 2009). The resulting fluxes and widths (full-width at half maximum, FWHM) of the lines in the spectra of the two regions shown in Fig. 4.7 are reported in Table 4.2. The stated errors were calculated using the noise on the two adjacent continuum regions in the spectra as

---

[3] See http://purl.com/net/mpfit

an estimation of the noise along the emission-line and then propagating this error to the parameters of the fit. Given that a reliable estimation of the reddening in the full data set is not possible with the available data, the reported fluxes of the bulge aperture in the Table 4.2 are not corrected by extinction effects (see Sec. 4.3).
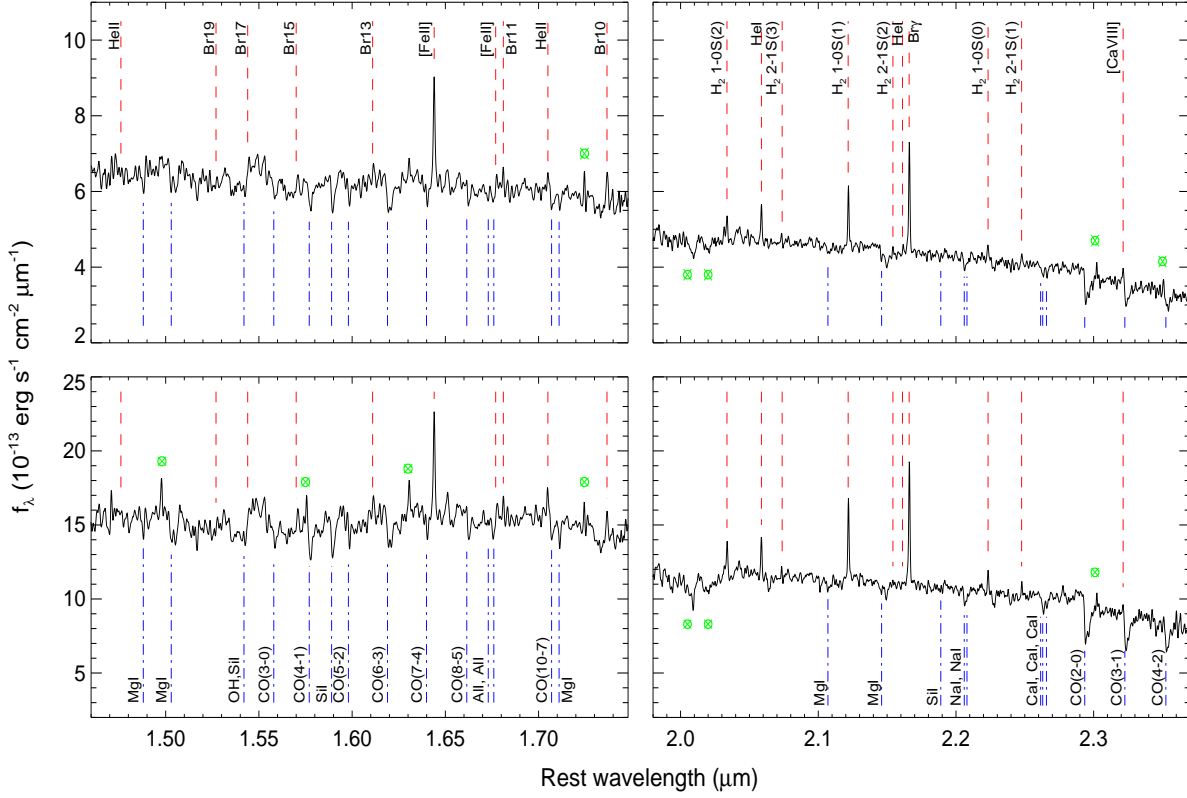

Figure 4.7: *HK*-band spectra of IRAS 01072+4954 in its rest frame. *H*-band is at the *left* and *K*-band at the *right*. In the upper panels correspond to the central region extracted at the resolution limit (radius of aperture equivalent to the PSF.) The bottom panels show the emission integrated over a circular aperture of $r \approx 0.8''$, which is about the size of the bulge of the galaxy. The positions of some emission (red dashed lines) and absorption (blue dot-dashed) features of the NIR spectra are shown. The marked lines do not imply detections. The symbol $\otimes$ indicates strong emission/absorption atmospheric features that remained after the reduction process.

Despite the fact that NIR observations are less affected by dust obscuration and even thought the NIFS instrument mapped the nucleus of the galaxy at high angular resolution, a classical broad component with a $\mathrm{FWHM_{broad}} \gtrsim 2\,000\,\mathrm{km\,s^{-1}}$ was not detected in the spectrum. The median width of the strong emission lines is $\mathrm{FWHM} \sim 80\,\mathrm{km\,s^{-1}}$. A discussion on the possibility of detecting broad lines in the NIR and the characteristics of the broad line region of this source is presented in Sect. 5.5 (page 115).

4.3 Extinction

Here, I refer to extinction A_λ as the net effect of the absorption and the scattering of the light along the line of sight produced by dust grains of different sizes and chemical compositions (see e.g., Natta & Panagia 1984; Calzetti et al. 1994). Given its physical origin, estimating the extinction requires to make several assumptions on the distribution of the dust, the origin of the emission and the extinction curve. In the simplest case, a homogeneous scatter-free dust screen placed in front of the galaxy is assumed to represent the distribution of the absorbers. However, in principle, the dust is mixed with the stars and most probably distributed in clumps with higher densities in and close to star forming regions.

The nebular hydrogen emission lines can be used as a proxy for the overall extinction. They are produced by photons coming from an ionizing stellar population and/or an AGN. For a particular temperature and density of the emitting region, a dust screen of optical depth τ, placed along the line of sight, produces a variation in the relative flux of two recombination lines $F_{\lambda_1}/F_{\lambda_2}$, such that the observed ratio

$$
\begin{aligned}
\left(\frac{F_{\lambda_1}}{F_{\lambda_2}}\right)_{\text{observ}} &= \left(\frac{F_{\lambda_1}}{F_{\lambda_2}}\right)_{\text{emit}} e^{-\tau} \\
&= \left(\frac{F_{\lambda_1}}{F_{\lambda_2}}\right)_{\text{emit}} 10^{-0.4\left(A_{\lambda_1} - A_{\lambda_2}\right)},
\end{aligned}
\tag{4.4}
$$

where $A_\lambda = 1.0857\,\tau$ is the absolute extinction at certain λ wavelength. This function, usually parametrized with respect to the extinction in the visual A_V, is called extinction curve and here is symbolized as $A_{\lambda,V}(\lambda) \equiv A_\lambda(\lambda)/A_V$ (e.g., Rieke & Lebofsky 1985; Cardelli et al. 1989; Calzetti et al. 2000).

It is common to use the Balmer decrement (Hα/Hβ) in the optical, or any other recombination-line ratio to correct the effects of the extinction over whole observed spectrum, i.e., to apply the same correction to the stellar continuum, and to the gas emission from different regions. However, to do a better interpretation of the line ratios, one has to consider some caveats: (i) The extinction of the stellar continuum emission is not necessarily the same as that that affects the gas, e.g. Calzetti et al. (1994) estimate it to be roughly one-half of the ionized-gas extinction, i.e., an extinction of $(A_B - A_V)_{\text{gas}} = 1\,\text{mag}$ corresponds to $(A_B - A_V)_{\text{star}} = 0.44\,\text{mag}$. (ii) Highly ionized lines are probably produced in a region different from the partially ionized zone where the hydrogen lines are originated, and therefore they might be subject of a different extinction. From line ratios of [Fe II] lines, Mazzalay & Rodríguez-Ardila (2007) found ≈ 1 magnitude more extinction in the nucleus of Mrk 1210 than that obtained with the H I line ratios. (iii) Other mechanisms like collisional excitation in high-density regions can increase selectively the population in the hydrogen energy levels from ground up producing higher intensity in the redder lines (Netzer 1975). (iv) Another aspects related to the detection of the desired nebular lines like: their intensity and extension, the proximity to spectral regions of high telluric contamination, etc.

The most prominent lines in the near infrared regime are Paα, Paβ, Brγ and Brδ. In our observations, Brγ, Br10, Br11 and Br13 are detected, but the last two are spatially unresolved. Therefore, the former ones were used to probe the extinction. From Eq. (6.12) and using Cardelli's extinction curve, it is possible to evaluate A_V as

$$A_V = 50.2745 \times \log \left[\frac{(F_{\mathrm{Br}\gamma}/F_{\mathrm{Br}10})_{\mathrm{observ}}}{3.0253} \right], \tag{4.5}$$

where A_V is the extinction in the visual band in magnitudes. The theoretically expected line ratio, i.e. $(F_{\mathrm{Br}\gamma}/F_{\mathrm{Br}10})_{\mathrm{emit}}$, was calculated assuming the case-B recombination for a region with electron density of $10^4\,\mathrm{cm}^{-3}$ and temperature $T = 10^4\,\mathrm{K}$ (Osterbrock & Fernand 2006).
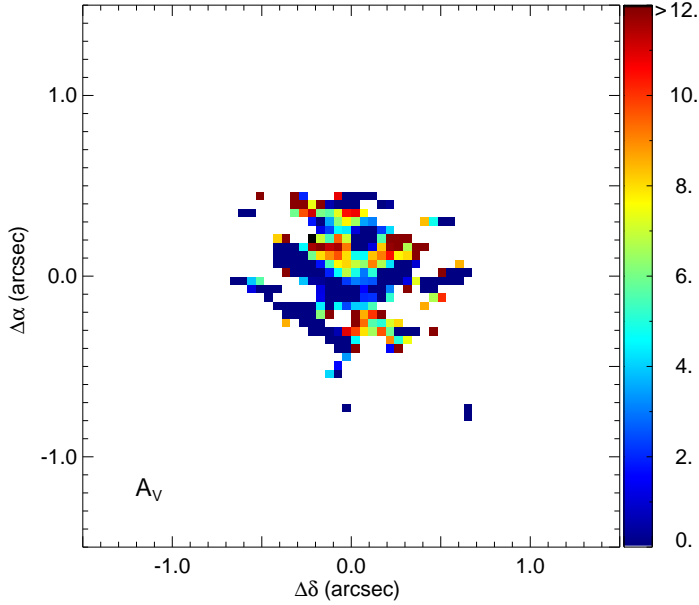
Figure 4.8: Extinction map of the central $r \sim 1''$ of IRAS 01072+4954. The extinction is estimated from the ratio of the recombination lines Brγ and Br10, following Eq. (4.5), as explained in the text. The color code represents A_V in magnitudes. The white pixels replace unreliable data points. North is up, east is left.

Figure 4.8 shows the extinction map, which is the result of evaluating the A_V as described above, in every spatial pixel of the *HK* data cubes. The *K*-band data cube was previously convolved to match spatially the *H*-band resolution. Brγ is the most intense and extended line in our NIR data. In contrast, Br10 is not very bright and is located in a spectral zone highly contaminated by the sky. The telluric absorption not only diminished directly the flux of the line, but mainly affected the continuum determination and from it, the flux estimation. In each spatial pixel, the lines were fitted with Gaussians. To minimize the effects of the telluric window, the continuum under the Br10 line was estimated from two thin

regions of ~ 0.6 Å at each side of the line. The Br10 emission higher than 2 times the noise level was considered. In that area, the Brγ line is clearly detected (its flux is higher than 3 times the noise level). The minimum value of scale of the figure was set to zero, although negative A_V were found in the central region.

The extinction map of the Fig. 4.8 is very irregular. In the region of $\sim 0.15''$, around the center of galaxy, where both H I lines are detected with high signal-to-noise, the extinction is low. A similar situation occurs $\sim 0.25''$ to the north-west, where the Br10 flux exhibits a second peak (see Fig. 4.6, page 66). This position also coincides with the highest value of the Brγ equivalent-width, and it will be discuss in Sect. 4.5. East and west of this A_V-deep region, the extinction is very high. In the easter area, Br10 is detected over 3 times the noise level, and the A_V is considered reliable. In the wester one, pixels where $A_V \gtrsim 15$ mag correspond to spectra with non-fully detected Br10. The more extended Brγ flux at the south compared to Br10 also produces high and probably unreliable values of A_V. The diagonal white line that crosses the map at the south-east (from which two empty/white regions are distinguishable in the figure) is produced by the clear absence of Br10 emission. Interestingly, when looking at the line emission maps (Fig. 4.6), it seems that all lines with extended flux are diminished there. This might indicate a dust line crossing the galaxy or highly dust enshrouded regions. Due to the inhomogeneous extinction across the field of view, and given the caveats mention previously, a general extinction correction is not applied the data cubes. I use this method when required, after integrating the flux in the individual apertures.

Comparison with extinction measured in other wavelengths

The Brackett fluxes from the integrated emission over the full NIFS field-of-view can be used to derive a general extinction in the NIR that can be compared with previously published A_V values estimated from similar apertures. From the H I line ratio, for the full NIFS data set, $A_V \approx (12.9 \pm 1.5 \pm 6.0)$ mag, where the uncertainties reflect the high dependency on the definition of the continuum of the Brγ and the Br10 lines, respectively. The high estimated extinction reflects the fact that Br10 is not detected in most of the field-of-view (as shown in Fig. 4.8) and that our observations are sensitive only to the central $r \sim 1.3''$ emission. Another possibility is to use fluxes of bright H I lines measured in the optical. Under the premise that the area covered by the former aperture is comparable with the $3'' \times 3''$ of our NIR observations, it is possible to combine the optical and NIR hydrogen recombination emissions via

$$A_{V,\mathrm{NIR/opt}} = 2.3858 \times \log \left[\frac{(F_{\mathrm{Br}\gamma}/F_{\mathrm{H}\beta})_{\mathrm{observ}}}{0.02753} \right]. \tag{4.6}$$

The extinction obtained in this way is $A_V \approx (2.20 \pm 0.3)$ mag The uncertainty was calculated assuming $\sim 20\%$ error in the flux of each line. The Balmer decrement[4] estimated from the Hα and Hβ fluxes published by Moran et al. (1996)

---

[4]Using Eq (6.12) and case-B recombination, $A_V = 6.67 \times \log[(F_{\mathrm{H}\alpha}/F_{\mathrm{H}\beta})/2.87]$.

gives a comparable result, $A_V = 2.14$ mag. This corresponds to the extinction of the integrated emission over $2'' \times 4''$ aperture centered at the nucleus.

These results can have multiple interpretations. If one assumes that the more intense and extended lines lead to more accurate obscuration estimations, then it can be conclude that this galaxy has a very low extinction towards few arseconds around the center with some dust-embedded regions in $r \sim 1''$ around the nucleus. On the other hand, the A_V values might indicative of a multi-layer distribution of the emission, where the optical lines come from the outer layers and then are susceptible to less extinction than the deeper NIR emission. The low $A_{V,\mathrm{NIR/opt}}$ could be explained by the decrease of the Brγ by the same mechanism. A better estimation requires the detection of other strong NIR nebular lines like Paα or Brδ.

4.3.1 H-K color

The dust along the line of sight not only extinguishes the light at wavelengths $\lesssim 3\,\mu$m, it also produces continuum emission at $\lambda > 1\,\mu$m. When heated close to the dust sublimation, i.e. $T \sim (1000 - 1500)$ K, its emission peaks around K-band, $\lambda_{\mathrm{peak}} \sim (2.0 - 3.0)\,\mu$m. Lower dust temperatures peak at longer wavelengths. Dust heated by young stars ($T \sim 100$ K) emits preferentially at $\sim (30 - 70)\,\mu$m, while old stellar population mainly contribute at $\lambda > 70\,\mu$m. This means that the $H - K$ color can be used also as a light-extinction diagnostic or to reveal the presence of hot dust ($T > 600$ K).

From the HK NIFS data cubes, the H-K color map Fig. 4.9 was created. The continuum emission in the bands, $f_{\mathrm{cont},H}$ and $f_{\mathrm{cont},K}$, was obtained as a median over $\sim 300\,$Å around $1.6\,\mu$m and $2.2\,\mu$m, respectively. Only the spatial pixels where the specific flux was higher than the rms of the noise were considered. Previously the K-band data cube was convolved to the H-band spatial resolution. The H-K color was calculated as

$$H - K = -2.5 \times \log\left(\frac{f_{\mathrm{cont},H}/f_{0,H}}{f_{\mathrm{cont},K}/f_{0,K}}\right), \tag{4.7}$$

where $f_{0,H} = 1.18 \times 10^{-6}\,\mathrm{erg\,s^{-1}\,cm^{-2}\,\mu m^{-1}}$ and $f_{0,K} = 4.00 \times 10^{-7}\,\mathrm{erg\,s^{-1}\,cm^{-2}\,\mu m^{-1}}$ are the fluxes of Vega (αLyr) computed by Tokunaga & Vacca (2005) for the Mauna-Kea Observatory NIR filter set. The minimum value in the map is set to match the H-K color of a late-type stellar population, 0.26 ± 0.08 mag (Willner et al. 1984).

The H-K map shows higher colors than those typical of a normal stellar population. If they were only due to extinction, in the central region, lower values would be expected given the low A_V measured from the H I lines. Figure 4.10, modified from Alonso-Herrero et al. (1998), shows the NIR color-color diagram with the effects of the extinction and the hot dust emission signaled. The circular region at the left represents the colors of normal galaxies, while the one at the right corresponds to the typical colors of quasars corrected to zero redshift (see e.g., Hyland & Allen 1982; Alonso-Herrero et al. 1998). The arrow at the top-left corner shows
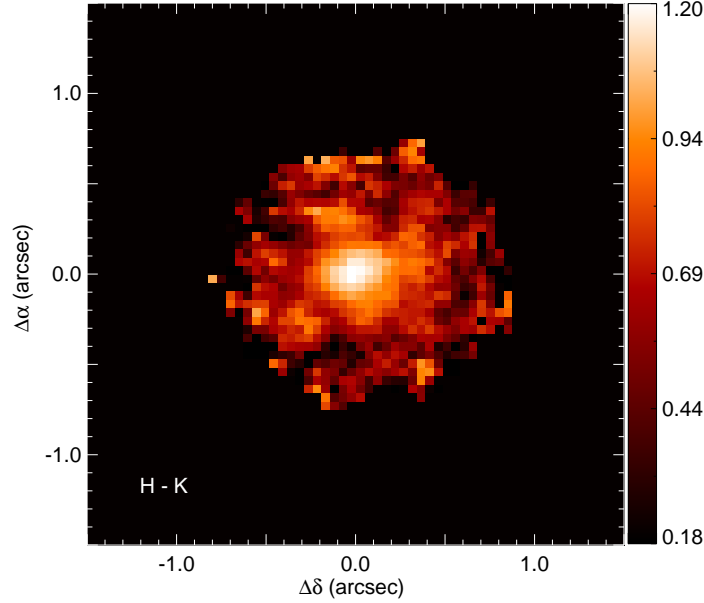
Figure 4.9: *H-K* color map of IRAS 01072+4954. The map was created by subtracting the continuum magnitudes, calculated as the median over narrow windows centered at $1.6\,\mu$m and $2.2\,\mu$m, as explained in the text. The black pixels replace unreliable data points. The minimum value has been set to the lowest *H-K* color of normal galaxies. North is up, east is left.

the direction towards which the *J-H* and *H-K* colors increase when the extinction increases (derived from the extinction curve of Rieke & Lebofsky 1985). Its length indicates the effect of $A_V = 2\,$mag. The curves represent the observed colors when hot dust at different temperatures is present. The relative contributions from the hot dust and the stars are shown with black dashed lines and quantified in the numbers near to the curves. Those values correspond to the ratio between the dust and the stellar emission in K-band.

In our case, *J*-band observations of the source are missing and therefore it is possible to locate only the observed colors in one dimension of the diagram. However, as we will see, the previously measured A_V can help in constraining the other direction. Fig. 4.10 shows the *H-K* colors of apertures with $r \approx 0.16''$ and $r \approx 0.05''$ centered on the nucleus. To get to the plotted vertical lines, starting from the colors of a normal galaxies, it is possible to have a mixture of stars and hot dust, or an extinction of $A_V \approx 5.5\,$mag for the $r \approx 0.16''$ aperture, and $\approx 10\,$mag for the smaller one. Now, given that the extinction of the stellar continuum is nearly the half of that of the gas (Calzetti et al. 1994), an A_V of the double of these values must have been found at the center. Because this is not the case – inclusive when considering the A_V error bars –, it means that there is dust at the center heated at temperatures $T > 500\,$K, i.e. by a non-stellar source. Reducing the aperture size

produces an increment in the measured H-K color. Assuming the same extinction and hot dust temperature, this implies a decrement in the stellar contribution, or in other words, an increment in the dust-to-stellar luminosity as signaled by the small numbers in the figure. Further analysis of this finding (relative contribution of the dust at the center, its temperature, and mass) is presented in Chapter 5.
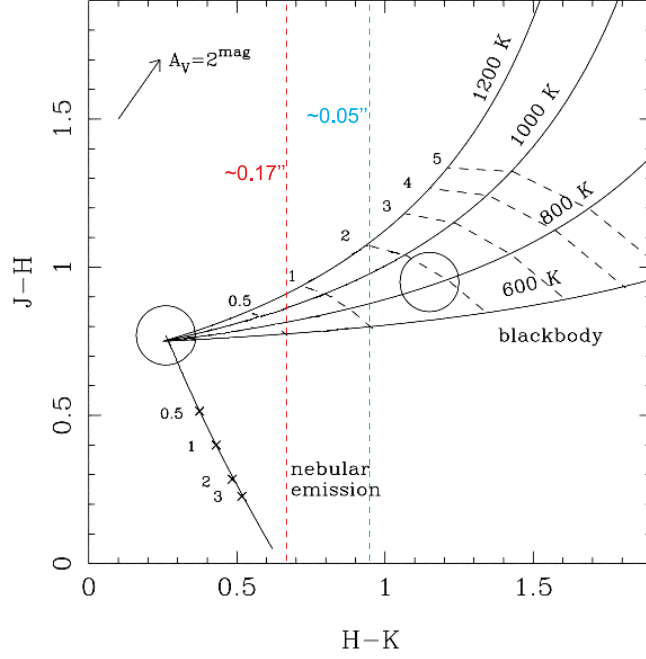
Figure 4.10: *J-H* vs. *H-K* color diagram. The left circle represents the mean and spread of normal galaxy colors. The right one, the typical colors of quasars corrected to zero redshift. The arrow at the top-left indicates the effect of the extinction, and the curves that of hot dust emission at different temperatures. The small numbers and black dashed lines signify the relative contributions of the dust and the stars. The colored-dashed vertical lines are the *H-K* colors of two apertures centered at the nucleus. That of size $\sim 0.17''$ corresponds to our spatial resolution element in *H*-band, while the smaller one covers only the central 2×2 pixels. Given the low extinction – it is not possible to reach the the colored vertical lines starting from the normal galaxy colors moving in the direction and approximately the same length as the arrow on the top-left – , a reasonable explanation of the observed *H-K* colors is hot dust emission. If the extinction and the temperature of the dust are the same in both apertures, the relative contribution of the stars in the smaller aperture is about half of that in the bigger one. Modified from: Alonso-Herrero et al. (1998).

4.4   Star formation

IRAS 01072+4954 is a bright source in the infrared (IR). Its IR luminosity, $L_{\mathrm{IR}} \equiv L(8 - 1000\mu)$, calculated from the specific fluxes measured by the IRAS satellite using Eq.(1.1), is $L_{\mathrm{IR}} < 1.73 \times 10^{44}\,\mathrm{erg\,s^{-1}} = 10^{10.7}\,\mathrm{L_\odot}$. This means that, although IRAS 01072+4954 is not an Luminous InfraRed Galaxy (LIRG, with $10^{11} \le L\mathrm{IR} < 10^{12}\,\mathrm{L_\odot}$), it is still a strong IR emitter. The emission in the far-IR

(FIR; $25 - 350\,\mu$m) is produced mainly by cold and warm dust. Big grains in nearly steady balance with the overall starlight emit at $\lambda > 70\,\mu$m, while dust warmed up by young/intermediate stellar population shines at $\lambda \sim 60\,\mu$m. It is believed that the main contribution of the AGN to the dust-heat is at shorter wavelengths in the near- and mid-infrared. In particular, Ultra LIRGs ($10^{12} < L_{IR}/L_\odot < 10^{13}$), whose main power source is the starburst, have spectral energy distributions with a clear marked peak at $\sim 60 - 100\,\mu$m, while specific-flux ratios $f_{25}/f_{60} > 0.3$ have been measured in QSOs (Sanders & Mirabel 1996). See more extended discussion in Sect. 1.3.1 (page 12). In the case of IRAS 01072+4954, this ratio is not accessible because its specific fluxes at 12 and $25\,\mu$m are only upper limits – hence the L_{IR} is also un upper limit. Nevertheless, it is possible to estimate the relative contribution of the star formation to the FIR emission from the color-color diagrams. Figure 4.11, modified from Kewley et al. (2000), shows three basic trends of the FIR colors. The straight line depicts the change in color of a typical Sy1 spectrum under a dust screen with increasing optical depth at $12\,\mu$m. The "starburst line" crosses the region ocupied by the starbursts observed by Rush et al. (1993), and the "extreme mixing line" shows the colors of a mixure between typical Sy1 and starburst spectra (see also Dopita et al. 1998). IRAS 01072+4954 colors, $\log(f_{60\,\mu m}/f_{12\,\mu m}) > 0.52$, $\log(f_{60\,\mu m}/f_{25\,\mu m}) > 0.52$, $\log(f_{100\,\mu m}/f_{25\,\mu m}) > 0.86$, $\log(f_{100\,\mu m}/f_{60\,\mu m}) = 0.34 \pm 0.06$, indicate that more than 75% of the FIR contribution arises from star formation.

4.4.1 Star formation Rate

The global star formation rate (SFR) in the galaxy can be estimated from the FIR luminosity (following Helou et al. 1988), using the calibration of Panuzzo et al. (2003; Eqs. (1.5) and (1.7), in Sect. 1.3.2.1.) This relation, which was obtained assuming the Salpeter (1955) IMF in the mass range $(0.15 - 120)\,$Myr, yields for IRAS 01072+4954 a SFR$_{global} = 4.9$ M$_\odot$ yr^{-1}. Careful must be exercised when selecting a calibration to estimate the SFR, because it can vary by a factor of ~ 2 depending on the assumed time scale. Small time scales (few hundreds of Myr), associated to relatively small star forming regions (size $\lesssim 1\,$kpc), yield higher SFR than time scales of the order of Gyr, which are used to calculate the global star formation in systems with ages comparable to the Hubble time (Calzetti 2012). In our case, the chosen Panuzzo et al. calibration assumes a star-formation time scale of 12 Gyr. It is also important to notice that the SFR found here might be a lower limit because implicitly assumes a dusty star formation, i.e., the power of young stars is absorbed and reprocessed by dust. But in a general case, part of the emission of young stellar regions can be seen directly in UV or optical light. We lack of tracers at those wavelengths that cover the whole galaxy, and therefore, it is only possible to establish a lower limit of the SFR.

The radio emission can serve as an extinction-free star formation tracer, because it has been found to correlate with the FIR flux (Condon 1992). In a cross-matched sample between the IRAS catalog and the NRAO VLA Sky Survey (NVSS; more
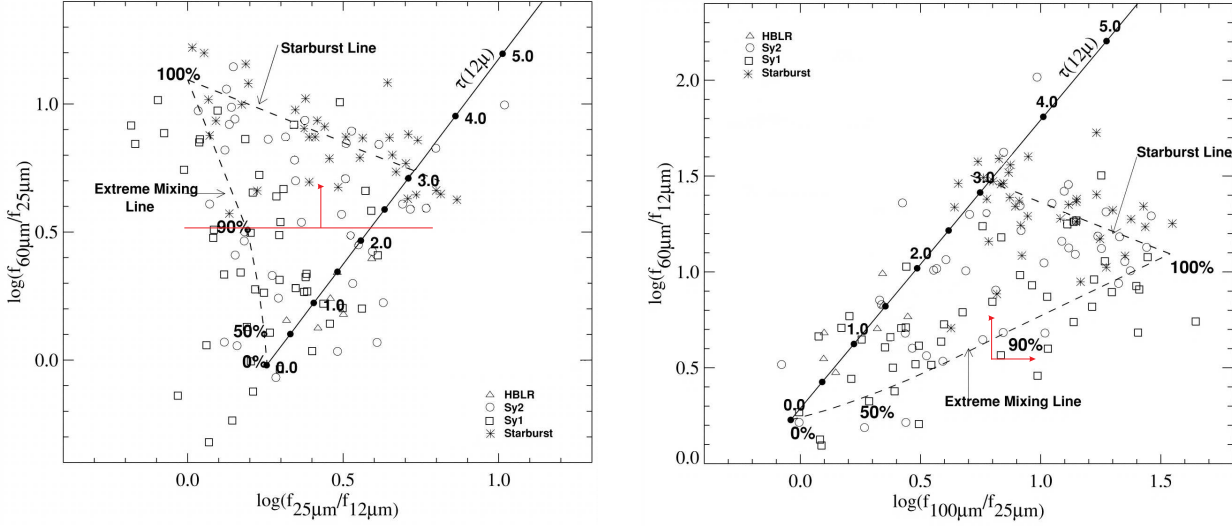
Figure 4.11: Far-infrared color-color diagrams. *Left:* $\log(f_{60}/f_{25})$ vs. $\log(f_{25}/f_{12})$ diagram. *Right:* $\log(f_{100}/f_{12})$ vs. $\log(f_{60}/f_{25})$ diagram. In both panels, the black straight line is the reddening line calculated by Dopita et al. (1998). Straight dashed line shows the region populated by starbursts. The extreme mixing curve corresponds to a mixure of a typical 'warm' Sy1 spectrum and the denoted percentage of a 'typical' cold starburst spectrum. The symbols correspond to starbursts (stars), Sy1s (empty squares), Sy2s with observed polarized broad lines (empty triangles) and without (empty circles), from the sample of Rush et al. (1993). The red line and arrows indicate the lower limits of IRAS 01072+4954 colors. Modified from: Kewley et al. (2000).

than 1800 sources), Yun et al. (2001) found that the median 'q' parameter, that relates the FIR with the 1.4 GHz emission (see Eq. (1.8), page 18), is 2.34 with only 0.26 dex scatter. Given that most of the sources have $L_{60\,\mu m} \gtrsim 10^9\,L_\odot$, this '$q$' value has been taken as typical for local starburst and star forming galaxies. In the case of IRAS 01072+4954, with $f_{1.4\,GHz} = 5.5 \pm 0.5\,$mJy from the NVSS (Condon et al. 1998), $q = 2.38 \pm 0.05$ which is in the range of local starbursts and gives indications for the origin of its FIR and radio emission.

Star formation also powers X-ray emission. The hard X-rays $(2 - 10\,\mathrm{keV})$ originate mainly from high and/or low mass X-ray binaries (HMXRBs or LMXRBs), while diffuse soft X-rays $(0.5 - 2\,\mathrm{keV})$ are dominated by shock-driven winds from supernovae and massive stars, which heat the interstellar gas to temperatures of $\sim 10^3 - 10^4\,\mathrm{K}$ (i.e., $\sim 0.2 - 1\,\mathrm{keV}$; e.g. Strickland & Stevens 2000). Assuming that in the central $r \approx 3''$ of IRAS 01072+4954, the SFR is about the same as calculated above from the FIR luminosity, it is possible to estimate an upper limit of the star-formation emission in the X-rays. According to Persic & Rephaeli (2007; see also Franceschini et al. 2003), at SFR $\approx 5\,M_\odot\,\mathrm{yr}^{-1}$ a population of long-lived LMXRBs dominate the star-formation component at hard X-rays. However, in regions with recent star formation (like that $\sim 0.3''$ north of the nucleus) contribution from HMXRBs is expected. Figure 4.12, modified from Lehmer et al. (2010), shows that

at this SFR, typical star-formation emission (dashed line fit) might account for $L_{2-10\,\text{keV}} \leq 10^{40}\,\text{erg}\,\text{s}^{-1}$.

In nearby spiral and elliptical galaxies (Colbert et al. 2004), LIRGs and ULIRGs from the Great Observatories All-sky LIRG Survey (GOALS; Iwasawa et al. 2009) and from the sample of Lehmer et al., the hard X-ray emission seems to correlate with the SFR. The linear relation shown in Fig. 4.12 has a zero point of 39.24 in agreement with previous studies (Franceschini et al. 2003; Ranalli et al. 2003; Gilfanov et al. 2004). IRAS 01072+4954 hard X-ray emission is well over the relation, indicating a dominant AGN contribution. Assuming that $L_{0.5-2\,\text{keV}} \sim L_{2-10\,\text{keV}}$ – which seem to be the case for local galaxies, see e.g. Ranalli et al. (2003) – , the soft X-ray luminosity would correspond to the $\sim 20\%$ of that measured by Panessa et al. (2005). This would explain why the soft X-ray energies

Figure 4.12: Hard X-rays vs. SFR. Symbols are, as indicated, local galaxies from Colbert et al. (2004), LIRGs and ULIRGs from GOALS (Iwasawa et al. 2009), and LIRGS from Lehmer et al. (2010). The zero point of the fit is $A = 39.24$. Modified from: Lehmer et al. (2010)

can be fitted with a blackbody with a temperature typical for star formation ($kT = 0.82\,\text{keV}$), but also the fact that most of the short term X-ray variability comes from this band implying a non-negligible AGN component.

4.4.2 Is IRAS 010724954 a starburst galaxy?

In order to know whether IRAS 01072+4954 is a starburst galaxy or not, it is necessary to calculate its specific star formation rate (sSRF), i.e., the rate of forming stars per unit of stellar mass, and compare it with that of a galaxy of the same mass in the main sequence (see Sect. 1.3). In the local universe, regularly star forming galaxies – also called blue galaxies – follow a narrow path in the sSFR versus stellar-mass M_* diagram (Fig 4.13; Kauffmann et al. 2003; Brinchmann et al. 2004; Salim et al. 2007; Schiminovich et al. 2007). This trend viewed at different redshifts constitutes the main sequence of star forming galaxies (e.g., Martin et al. 2007; Peng et al. 2010; Daddi et al. 2010; Elbaz et al. 2011). Galaxies that form stars at a sSFR larger than about two times that of the main sequence galaxies can be considered starbursts.

Stellar Mass of the Galaxy

The stellar mass can be estimated from the mass-to-light ratio M_*/L, when photometric measurements are available. Given that we have already found the photometric parameters of the H- and K-band brightness distributions (Sect. 4.1.2), it is possible to use them to get a more accurate estimation of the stellar mass in

comparison to the broad band magnitudes. The integrated luminosity of the bulge fitted with a general Sersic profile can be computed as

$$L_{\text{bulge}} = 2\,\pi\,\frac{I_0\,r_e^2\,n}{(\nu_n)^{2n}}\,(2n-1)!, \tag{4.8}$$

where all symbols have the same meaning as in Eq.(4.1), I_0 is the surface brightness at the center in units of $\text{L}_{\odot,X}\,\text{pc}^{-2}$, and the effective radius is measured in parsecs. The disk luminosity from an exponential profile is

$$L_{\text{disk}} = 2\,\pi\,I_0\,h^2, \tag{4.9}$$

with the same considerations as before and the disk scale length also measured in parsecs. This yields for IRAS 01072+4954, $L_{*,H} = L_{\text{bulge}} + L_{\text{disk}} = 2.35 \times 10^{10}\,\text{L}_{\odot,H}$ and $L_{*,K} = 3.29 \times 10^{10}\,\text{L}_{\odot,K}$.

Using the relation between the NIR M_*/L and the optical B-V color found by Bell et al. (2003) from evolution-model fits to SDSS and the 2MASS fluxes, it is possible to find the stellar mass. The authors assumed a 'diet' Salpeter IMF, i.e., a Salpeter IMF with a cut at low masses, yielding at a given color M_*/L ratios 30% lower than the original Salpeter IMF. This model corresponds to the maximum stellar mass for a disk galaxy with luminosity L (see discussion in Bell et al. 2003). The relations have the general form

$$\log\left(\frac{M_*}{\text{M}_\odot}\right) = \log\left(\frac{L_{*,X}}{\text{L}_{\odot,X}}\right) + a_X + b_X(B-V), \tag{4.10}$$

with $a_X = -0.942, -0.209, -0.206$; and $b_X = 1.737, 0.210, 0.135$ for $X = B$-, H-, and K-band, respectively. The zero points (a_X) have to be modified when other 'submaximal' IMFs are used, e.g., in case of Kroupa IMF, 0.15 dex must be subtracted to a_X.

In the case of IRAS 01072+4954, taking the average color of Sc galaxies $B - V = 0.52$, Eq.(4.10) results in $\log(M_*/\text{M}_\odot) = 10.27$ and $\log(M_*/\text{M}_\odot) = 10.38$ for the H- and K-band luminosities, respectively; while using the optical magnitude $m_{4400\,\text{Å}} = 15.7\,\text{mag}$ (Zwicky & Kowal 1968), $\log(M_*/\text{M}_\odot) = 9.84$. The error of these calculations can be estimated in $\sim 0.4\,\text{dex}$ for the NIR tracers, and $\sim 0.2\,\text{dex}$ for the optical one. They are derived from the errors in the luminosities and the scatter of the M_*/L vs. $(B-V)$ color relation – which is $0.1 - 0.2\,\text{dex}$ for NIR M_*/L ratios with larger scatter for bluer galaxies, and $\sim 0.1\,\text{dex}$ for optical M_*/L ratio (Bell et al. 2003, their Table. 7).

Specific Star Formation Rate

A galaxy experiences a starburst if the time needed to double its stellar mass at its current SFR is small compared to its age. This is called 'stellar-mass doubling timescale' $\tau \equiv 1/\text{sSFR}$, and it is usually measured in Gyr. Assuming for IRAS 01072+4954, $\text{SFR} \sim 5\,\text{M}_\odot\,\text{yr}^{-1}$ and $\log(M_*/\text{M}_\odot) = 10.0 - 10.2$, the sSFR is correspondingly $\sim (0.50 - 0.32)\,\text{Gyr}^{-1}$, which implies $\tau \sim (2.0 - 3.2)\,\text{Gyr}$.
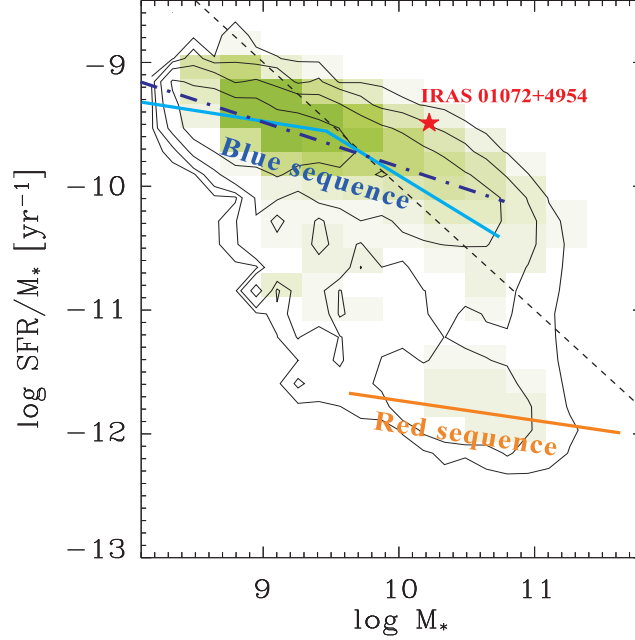
Figure 4.13: Specific star formation rate vs. stellar mass. The green shadow show the distribution of $\approx 5 \times 10^4$ galaxies with photometric measurements from SDSS and GALEX. The contours enclose 38%, 68%, 87%, and 95% of the distribution. The fits to the blue-sequence galaxies, from Salim et al. (2007), show the BPT H II galaxies (blue thick dot-dashed line) and the BPT H II galaxies + composites (cyan solid line) relations. The orange fit is an approximation to the relation in non-star forming galaxies. The thin dotted line shows $\mathrm{SFR} = 1\,\mathrm{M}_\odot\,\mathrm{yr}^{-1}$ as a reference. Modified from: Schiminovich et al. (2007)

Figure 4.13, modified from Schiminovich et al. (2007), shows the sSFR vs. M_* for a sample of $\approx 50\,000$ galaxies ($z < 0.25$) with photometry from the SDSS and SFR calculated from the GALEX far- and near-UV magnitudes. The bimodality in the sSFR values between star-forming ('blue sequence') and non-star forming ('red sequence') galaxies is evident. It is also clear that in the local universe, there is a tight relation between sSFR and the stellar mass in blue systems. The linear fit in Fig. 4.13 (blue thick dot-dashed line), derived by Salim et al. (2007) using only the star forming galaxies of the sample defined as such by their positions in the BPT diagram, is

$$\log\left(\frac{\mathrm{SFR}/\mathrm{M}_*}{\mathrm{yr}^{-1}}\right) = -0.35 \log\left(\frac{M_*}{\mathrm{M}_\odot}\right) - 6.33. \tag{4.11}$$

The broken linear relation (cyan solid line) corresponds to the fit when considering also composite galaxies as star-forming systems (see Salim et al. 2007, their Eq.(12)).

The position of IRAS 01072+4954 in the diagram shown in Fig. 4.13 indicates a sSFR above the average of the blue galaxies of its mass. In fact, according to Eq. (4.11), a main sequence star-forming galaxy of $M_* = 10^{10.0} - 10^{10.2}\,\mathrm{M}_\odot$ has a $\mathrm{sSFR_{MS}} = 0.148 - 0.126\,\mathrm{Gyr}^{-1}$, or equivalently, the stellar-mass doubling time-

scale $\tau_{\rm MS} = 6.76 - 7.94\,{\rm Gyr}$. Therefore, IRAS 01072+4954 can be considered a starburst galaxy because its sSFR is around three times larger than that of normal star-forming galaxies of the same mass and age – assuming that galaxies at the same epoch, in this case $z \lesssim 0.2$, have the same age. In other words, if one assumes that IRAS 01072+4954 has normally formed stars during its life in a similar way as other galaxies of the same mass and age, its averaged past specific star formation rate would be $\langle {\rm sSFR} \rangle \sim {\rm sSFR}_{\rm MS}$, implying that currently its rate of stellar birth has increased by more than the double. In terms of the 'starburstiness' $R_{\rm SB}(M_*)$, defined by Elbaz et al. (2011)[5], it is possible to show that for IRAS 01072+4954

$$R_{\rm SB}(M_* = 10^{10.0-10.2}\,{\rm M}_\odot) = \frac{\rm sSFR}{\rm sSFR_{MS}} = \frac{\tau_{\rm MS}}{\tau} > 2. \qquad (4.12)$$

On the other hand, compared to the mass-averaged sSFR at low redshift, IRAS 01072+4954 would be just of the border between normal star-forming galaxies and starbursts (see footnote). It is interesting to note that in the local universe, the peak of the star formation activity occurs in galaxies with about the same stellar mass as IRAS 01072+4954. It is also at this mass $\sim 4 \times 10^{10}\,{\rm M}_\odot$ where the rapid transition between the blue and red sequence occurs (Kauffmann et al. 2003).

4.5   Stellar population

Near-infrared *HK*-bands are ideal to probe stellar populations. IRAS 01072+4954 shows an enhanced star formation rate compared to that of star-forming galaxies of the same mass. NIFS IFS observations reveal that part of this bursting process is happening in the bulge and help on characterizing it.

Spectral indices are a powerful tool to expose the properties – e.g., distribution, age, compactness – of the stellar populations, in most of the cases (depending on the particular definition of the index) independent of extinction. In the NIR, the spectral indices can be defined as the equivalent width W_λ – measured in Angstroms or in magnitudes – of absorption features or emission lines, or as generic discontinuities (see Sect. 1.3.2.3, page 23). The NIR spectral indices appear to depend on the spectral resolution – when comparing very high to median/low resolution – mainly because of the blending of absorption features of different species (see e.g., Ramirez et al. 1997), and on the selection and estimation of the continuum. Therefore, in order to properly compare with published samples it is necessary to agree on the definitions.

Figure 4.14 shows the equivalent-width maps of the main absorption lines in the *HK* spectra of the central $3'' \times 3''$ of IRAS 01072+4954. Here I use the definitions of Origlia et al. (1993) presented in Table 1.1 (see also Figs. 1.10-1.11 in Sect. 1.3.2.3) for the absorption lines Si I, CO(6-3) and CO(2-0). The equivalent

---

[5]Although they do not consider the variation with M_*, and fitting the local SFR vs. M_* relation as linear, find a mass-averaged ${\rm sSFR}_{\rm MS} \sim 0.25\,{\rm Gyr}^{-1}$, $\tau_{\rm MS} \sim 4\,{\rm Gyr}$.
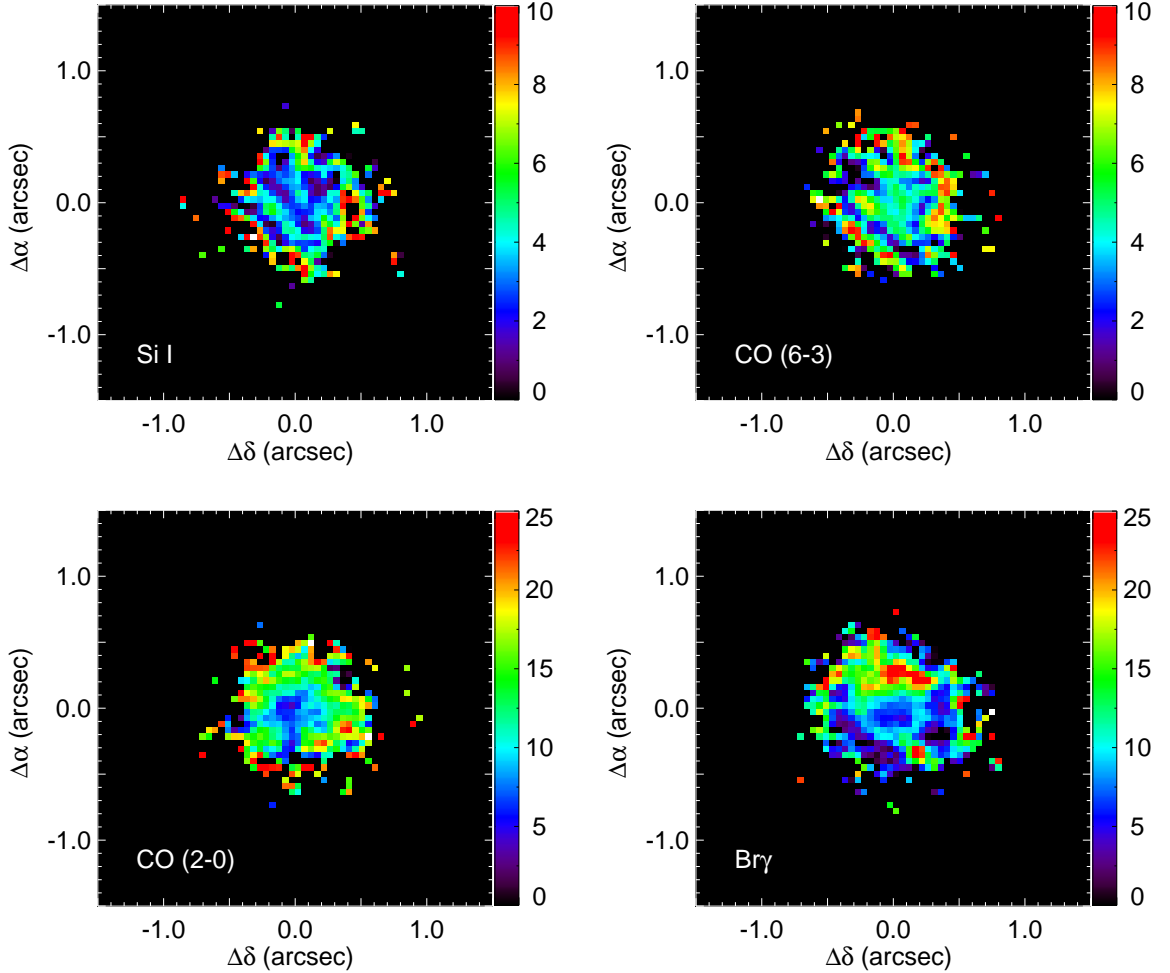
Figure 4.14: Equivalent width maps of the central 3"×3" of IRAS 01072+4954. Species are, as indicated, from *top-left* to *bottom-right*: Si I, CO(6-3), CO(2-0), and Brγ. The color code represents the width in Angstroms. See text for the definitions of each index.

widths were measured in the spectrum of each spatial pixel of the field of view, following the Eq.(1.10, page 24). Pixels where the median specific flux over the feature-spectral window was lower than 2.5 times the noise of the defined continuum windows, or where the continuum was too faint (less than three times the noise level) were marked as unreliable and W_λ set to zero. This procedure was done on the spectra at the NIFS spectral resolution, after testing that smoothing to the Origlia et al. resolution results in W_λ values that agree within the errors. The Brγ equivalent-width map was obtained by integrating the emission in the range $(2.16395 - 2.16855\,\mu m)$ after normalizing the spectrum by the continuum, which was fitted with a straight line that crossed the median of two narrow windows, one

at each side of the emission line: $(2.1562 - 2.1602)\,\mu$m and $(2.1713 - 2.1753)\,\mu$m.

The equivalent-width maps show some interesting features not revealed by the emission-line maps. First, the presence of the hot dust is visible in the K-band features (CO(2-0) and Brγ) as an apparent decrement in W_λ at the center. CO(2-0) shows also a clumpy structure around the nucleus, while Brγ has two visible peaks, one ~ 120 pc toward the north, and another at about the same distance in the south-west direction. Second, there is an apparent ring-like structure with enhanced $W_{\mathrm{C0(6-3)}}$ and low $W_{\mathrm{Br}\gamma}$. $W_{\mathrm{Si\,I}}$ seems to follow the same distribution, but values at $r \sim 0.5''$ from the center are not reliable. Third, at the north-east where Br10 line emission is also observed, $W_{\mathrm{Br}\gamma}$ and $W_{\mathrm{C0(2-0)}}$ have high values, but the opposite is observed in $W_{\mathrm{C0(6-3)}}$. The reason in this case, is a strong variation in the spectral continuum windows of CO(6-3) in that particular area.

Spectral indices in selected regions of the bulge

In order to study the variations of spectral indices across the bulge, it is convenient to integrate the spectra over some apertures and in that way get a better S/N. Figure 4.15 shows the apertures selected to enclose regions with clear spectral index peaks.
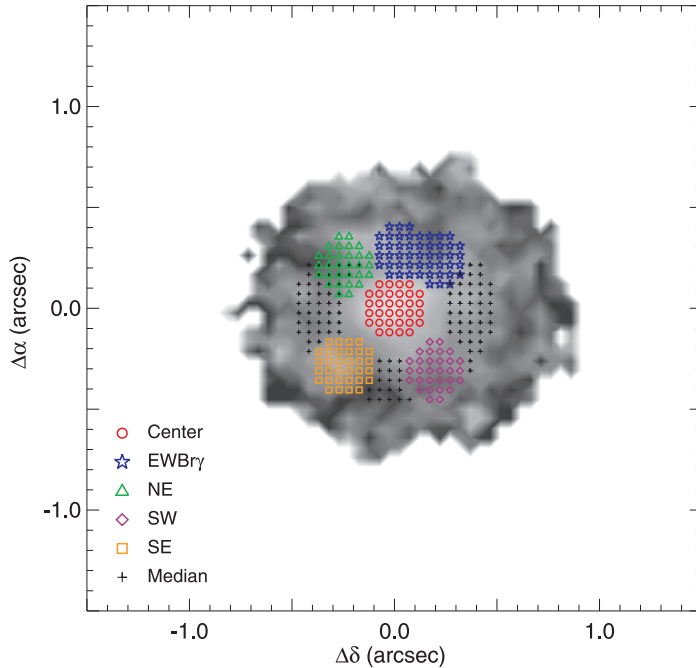
Figure 4.15: Selected apertures to study the bulge stellar populations. The apertures are named, as indicated by the labels, by their position with respect to the center, with the exception of the 'EWBrγ' aperture which was selected to enclose the region with the deepest Brγ equivalent width (see Fig. 4.14), and that signaled by the cross marks, which is assumed to represent the average stellar population in the bulge. The background image is the H-K color map.

From their positions, the regions were called: north-east (NE), south-east (SE), south-west (SW) and Center. These are approximately circular with a size $r \approx$ 0.17$''$, that is the NIFS spatial resolution element and corresponds to $r \approx 75$ pc on source. At the position of the northern $W_{\mathrm{Br}\gamma}$ peak, an elongated aperture – named EWBrγ – was used. Under the assumption that there is an underlying stellar population in the bulge that can be identified with the median emission produced far from the center and from evident star forming clumps, the areas within a ring with inner and outer radii 0.26$''$ and 0.48$''$, respectively, from which the other apertures were subtracted, were integrated (crosses in Fig. 4.15). In this way, an 'averaged bulge stellar-population spectrum' – called Median – was obtained. The spectra extracted form the depicted apertures is shown in Fig. 4.16.
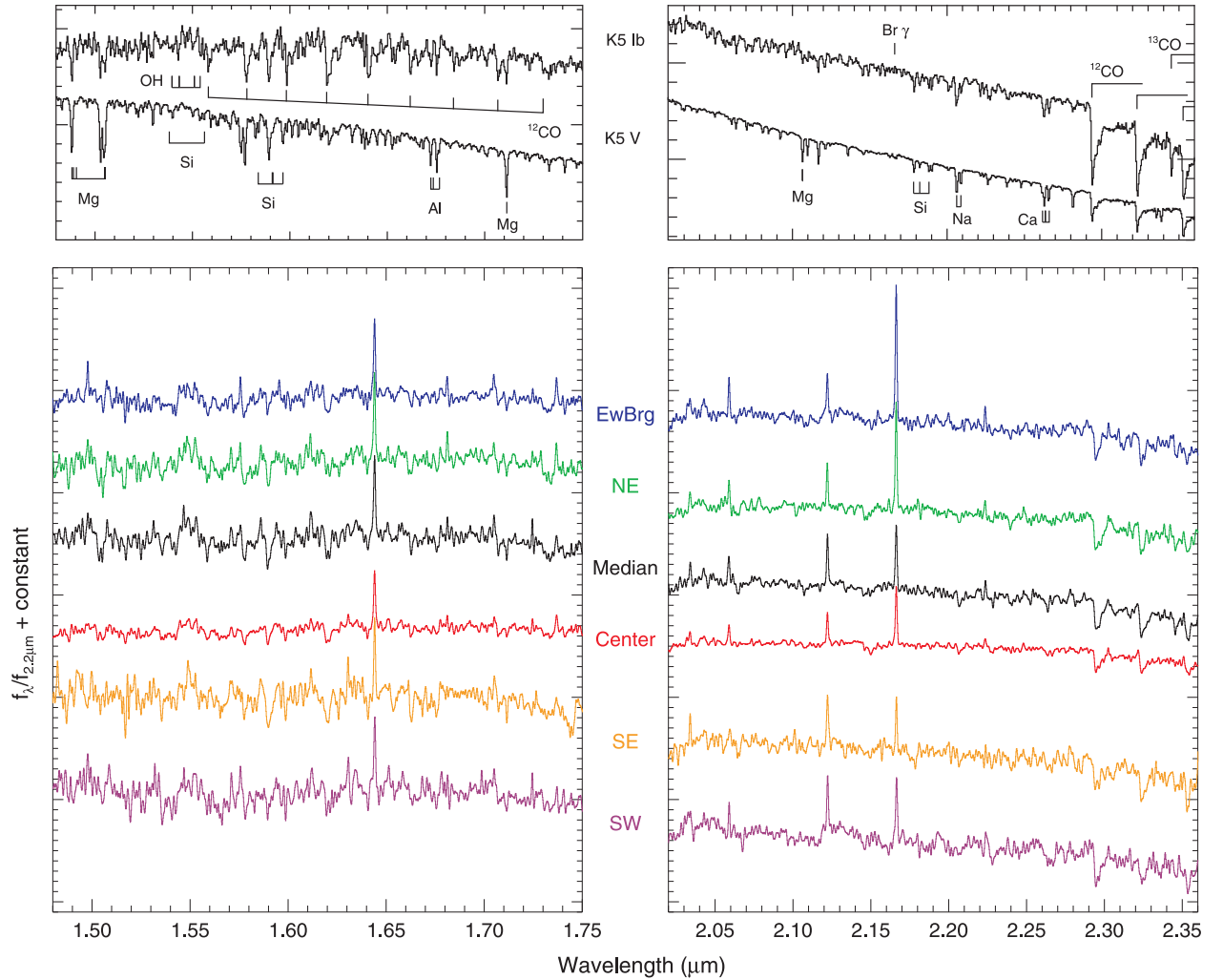
Figure 4.16: Spectra of the bulge selected apertures. The *H*-band (*left*) and *K*-band (*right*) spectra integrated over the selected apertures (see Fig. 4.15) are plotted in colors. *Top:* spectra of a supergiant (K5 Ib) and a dwarf star (K5 V), taken from Rayner et al. (2009), are shown for comparison.

The NIR continuum is dominated by late-type stars (K-M). Giants and super-giants produce most of the luminosity, while dwarfs make the major part of the stellar mass content. In contrast to dwarfs and giants that are associated with intermediate and old stellar populations (see adopted definitions in Sect. 1.3.2.3, page 20), supergiants are expected in currently active star forming regions. In Fig. 4.16 the spectra of a supergiant and a dwarf K-type stars are plotted for comparison on top of the spectra taken from the bulge of IRAS 01072+4954. Please note that the K-band portion of the spectra of these stars have been shifted up vertically with respect to their H-band data, for displaying reasons; while the spectra of the apertures keep their overall spectral shape, i.e. in each case, the additive constant in both bands is the same. From the Fig. 4.16 it is possible to notice that the depth of the stellar absorption features relative to each other changes with the luminosity. In fact, this differences depend on the effective temperature (stellar type), the surface gravity (luminosity), the metallicity and the microturbulent velocities of the stars. Although, in general, the relation between particular combinations of these properties and the spectral-index ratios derived from them is not unique (Origlia et al. 1993; Ivanov et al. 2004; Mármol-Queraltó et al. 2008), some observational trends have been used to probe average stellar populations in extragalactic sources (e.g., Oliva et al. 1995; Mannucci et al. 2001).

Table 4.3 shows the spectral indices of the main NIR features measured in each selected aperture on the bulge of IRAS 01072+4954. Here, I used the same index definitions as those employed for the equivalent-width maps. In the case of the central aperture, the spectral indices do not reflect directly the properties of the stellar population, because the continuum at the center is contaminated by the emission from the hot dust as shown above. Some of the properties derived below are also affected by this situation. A deeper analysis of the HK emission in this central aperture is described in Chapter 5, while the measurements reported for this aperture in Tables 4.3-4.4 are presented for completeness.

Table 4.3: Spectral indices in selected regions of the bulge

Aperture	$W_{\mathrm{Si\,I}}$	$W_{\mathrm{CO(6-3)}}$	$W_{\mathrm{Na\,I}}$	$W_{\mathrm{Ca\,I}}$	$W_{\mathrm{CO(2-0)}}$	$W_{\mathrm{Br\gamma}}$
Center	2.78	4.49	1.67	1.96	7.94	8.59
EWBrγ	2.20	3.88	2.46	< 0.25	13.09	18.66
Median	4.41	4.57	2.83	3.65	11.74	7.39
NE	3.48	2.87	2.14	1.02	14.74	14.36
SW	3.36	3.50	5.66	6.65	12.73	9.55
SE	4.10	4.56	1.74	4.92	13.77	5.72

Note. All equivalenth widths in Angstroms.

Other characteristic stellar parameters derived from the spectra of the selected apertures are presented in Table 4.4. The extinction A_V was estimated from the

hydrogen emission-line ratios, and the (H-K) color from narrow spectral windows in each band, following the methods described in Sect. 4.3. The metallicity was evaluated using the expression found by Frogel et al. (2001, their Table 10.),

$$
\begin{aligned}
[\text{Fe/H}] = -1.811 \quad &+ \quad 0.389\,W_{\text{Na I}} - 0.047\,(W_{\text{Na I}})^2 \\
&- \quad 0.030\,W_{\text{Ca I}} + 0.024\,(W_{\text{Ca I}})^2 \\
&+ \quad 0.043\,W_{\text{CO}(2-0)} - 0.001\,\big(W_{\text{CO}(2-0)}\big)^2, \quad (4.13)
\end{aligned}
$$

which was originally established for globular clusters, but Ramírez et al. (2000) showed that it also reproduces moderately well the metallicity of red giants in the Galactic bulge with $[\text{Fe/H}] \lesssim -0.2$, due to the ovelap of the two populations in the spectral indices vs. NIR color diagrams. The last two columns of the table are the luminosity of the Brγ line and the specific luminosity[6] at $2.2\,\mu$m.

Table 4.4: Properties of the stellar populations in selected regions of the bulge

Aperture	A_V [a] (mag)	H-K [b] (mag)	$[\text{Fe/H}]$ [c] (dex)	$L_{\text{Br}\gamma}$ [d] ($10^{38}\,\text{erg s}^{-1}$)	$l_{2.2\,\mu\text{m}}$ [d] ($10^{37}\,\text{erg s}^{-1}\,\text{\AA}^{-1}$)
Center	2.5	0.87	-0.98	3.72	4.73
EWBrγ	12.8	0.78	-0.75[e]	9.24	2.42
Median	8.2	0.58	-0.51	2.60	3.05
NE	8.4	0.64	-0.78	3.23	2.38
SW	–	0.57	0.13	1.12	1.31
SE	–	0.61	-0.44	0.62	0.89

[a] From the Brγ/Br10, following Eq. (4.5).

[b] From narrow bands around $1.6\,\mu$m and $2.2\,\mu$m according to Eq. (4.7).

[c] Using Eq. (4.13) derived by Frogel et al. (2001), see text.

[d] Corrected for reddening, see text.

[e] The result is the same for $0.0 \leq W_{\text{Ca I}} \leq 0.25$

In general, the extinction out of the center is high. This is partially because of the faint Br10 line used to evaluate it, as discussed previously in Sect. 4.3. In case of the southern apertures, Br10 is not detected at all, and A_V has not been calculated. I considered the hydrogen line ratios in the Center, EWBrγ, and NE apertures as reliable, and used them to de-redden these spectra. In the other cases, the reddening derived from the H-K color was used. The errors in the H-K colors are ~ 0.1. The uncertainty in the metallicity calculation was estimated by Ramírez

---

[6]In this case, the nomenclature can be misleading, because L_λ is used in the literature to designate luminosity in some cases, and specific luminosity in others. To keep an homogeneous nomenclature along the text, in analogy to flux and specific flux, designated here as $F_\lambda\,(\text{erg s}^{-1}\,\text{cm}^{-2})$ and $f_\lambda\,(\text{erg s}^{-1}\,\text{cm}^{-2}\,\mu\text{m}^{-1})$, the luminosity and specific luminosity have been symbolized by capital and lower case letters, respectively.

et al. (2000) to be $\pm(0.12 - 0.23)$ dex. In the SW region, [Fe/H] is relatively high compared to that measured in the other apertures – though it is closer to the solar one. This is the result of very high equivalent widths of Na I and Ca I in this aperture. However, given that the continuum is very noisy, probably these indices do not reflect accurately the stellar population features. The Brγ luminosities and the specific luminosities at $2.2\,\mu$m were calculated after the reddening correction. The former have errors of the order of few percent, and the latter of $\sim 10\%$.

Comparison with observed stellar spectral indices

Some observed stellar spectral-index ratios have been shown to be sensitive to the temperature, and/or luminosity class. Figure 4.17 shows the diagrams proposed by Origlia et al. (1993) as good temperature indicators. The reason is that the strength of the CO(6-3) is related mainly to the stellar temperature, but it also depends on the superficial gravity and metallicity. On the other hand, although the $CO(2-0)$ absorption band positively correlates with the spectral type – i.e. with the temperature – , its increment is directly related to the microturbulent velocities ξ, that are higher in supergiants and in cooler stars. The Si I absorption feature varies only very slowly with the spectral type. Therefore, the ratios $\left(W_{CO(6-3)}/W_{Si\,I}\right)$ and $\left(W_{CO(6-3)}/W_{CO(2-0)}\right)$ are expected to trace the stellar temperature – hotter to the right of the diagrams and cooler to the left – with some caveats related to the metallicity and the superficial gravity that will be commented further down.

In the diagrams of Fig. 4.17, giants and supergiants observed by Origlia et al. (1993) are plotted. Interestingly, in the $W_{CO(6-3)}$ vs. $\left(W_{CO(6-3)}/W_{CO(2-0)}\right)$ plot, the supergiants are somewhat displaced toward the left with respect to the giants-trend, while in the other diagram, both types follow approximately the same path. This might be understood due to the increment of $W_{CO(2-0)}$ with ξ in lower surface-gravity stars. But this is not the only factor that can produce an horizontal displacement in the diagrams. The evolutionary track of a stellar population depends on its metallicity. In more metallic populations, red giant stars reach lower temperatures than those with lower metallicity. This means that systems with higher [Fe/H] will tend to populate the right-hand side of the sequences in Fig. 4.17, and viceversa. This is nicely exemplified by the spectral-index ratios of several globular clusters of the sample of Origlia et al. (1993), which have metallicities close to solar and are located at the bottom-left side – with the exception of Ter1 (see more in Origlia et al. 1993). Our measurements are also consistent with this interpretation. Most of the apertures have [Fe/H] lower than solar, their index ratios lie close to those of globular clusters and are cooler than the starbursts. Although a circular argument between the method for deriving the metallicity and the location in the diagrams might be invoked, the trend is the same in the $W_{CO(6-3)}$ vs. $\left(W_{CO(6-3)}/W_{Si\,I}\right)$ plot that only employs H-band indices, somehow independent to those in K-band used for the metallicity. But metallicity and temperature are in general independent of each other, which impedes the direct interpretation of
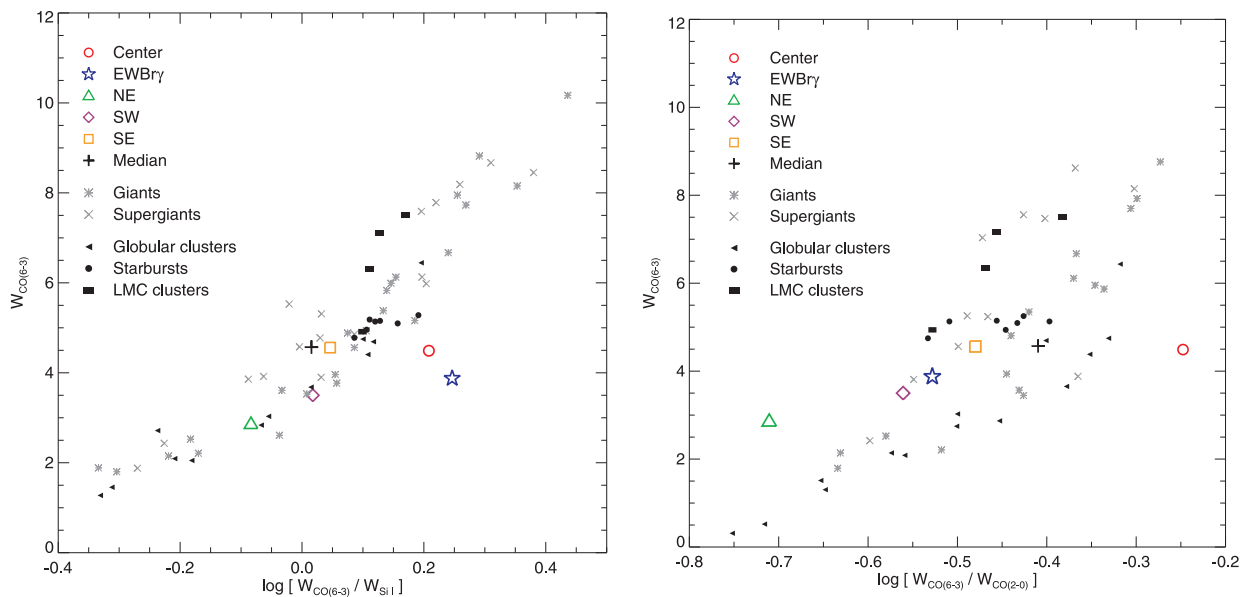
Figure 4.17: Spectral-index ratio diagrams. *Left:* $W_{CO(6-3)}$ vs. $\log\left(W_{CO(6-3)}/W_{Si\,I}\right)$ diagram. *Right:* $W_{CO(6-3)}$ vs. $\log\left(W_{CO(6-3)}/W_{CO(2-0)}\right)$ diagram. The spectral-index ratios in the abscissas are primarily sensitive to temperature, hot stars are located toward the bottom-left and cooler ones toward the top-right. Weak dependency on the metallicity and surface gravity can also be seen (see text for details). Spectral-index ratios of the selected apertures on the bulge of IRAS 01072+4954 are shown. Their symbols are the same as in Fig. 4.15. Stars and systems observed by Origlia et al. (1993) are also presented for comparison. Modified from Origlia et al. (1993).

these diagrams. For example, in four very young and low metallicity stellar clusters located in the Large Magallanic Cloud, Origlia et al. (1993) found that cool supergiants dominate the emission, and then the stellar temperature is the parameter that rules their spectral-index ratios. They are located towards the top-right in both diagrams.

The indices of the central and EWBrγ apertures behave differently to those of other apertures. The position of the Center index-ratios to the bottom of the stellar trend in the H-band indices diagram, and to the bottom-right in the other one, indicates dilution of the absorption lines by hot dust and a possible featureless continuum. In contrast, the K-band indices of the EWBrγ aperture appear to be similar to those of the other selected regions. The reason for the displacement in the H-band index-ratio plot is the partial filling of the Si\,I absorption feature, that produces a very low $W_{Si\,I}$. Inspecting the data, I do not find particular reasons for this behavior. In all apertures, the presence of the Br14 $\lambda1.5884\,\mu$m emission in the Si\,I absorption has been subtracted by fitting the Br13 $\lambda16114\,\mu$m line with a Gaussian, and assuming the same width for both lines and the case-B recombination, i.e. Br14/Br13 = 1.25076 (Hummer & Storey 1987), for an electron density of $10^4\,\mathrm{cm}^{-3}$ and $T = 10^4\,\mathrm{K}$. No anomalies could be noticed during this procedure for the EWBrγ aperture.

Figure 4.18 shows the spectral-index diagram proposed by Mannucci et al. (2001). This diagram is sensitive to the luminosity class. It can be notice in Fig. 4.16 that the ratio between the Na I or Ca I to CO(2-0) varies strongly from dwarfs to supergiants.
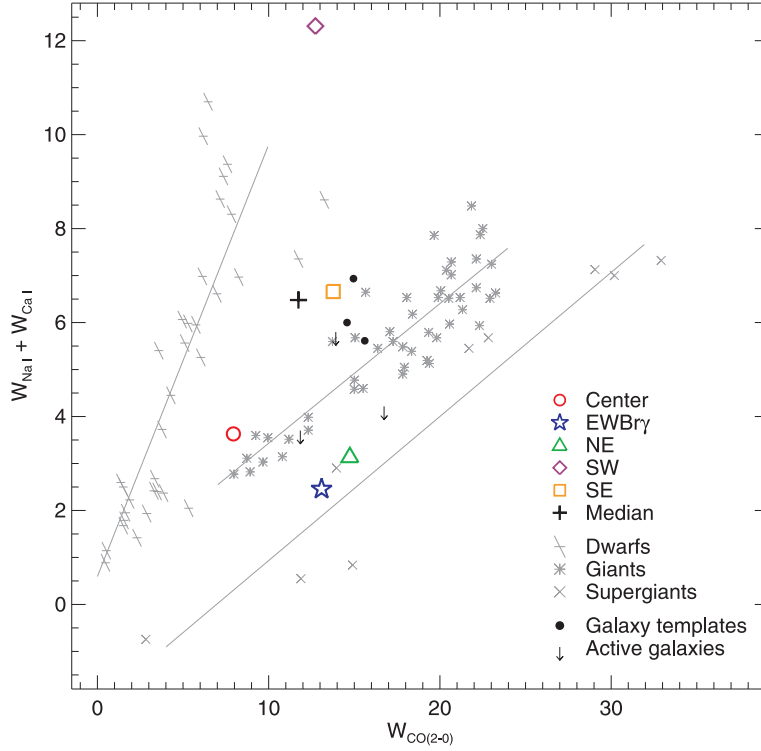
Figure 4.18: K-band spectral indices diagram. The ratio between the Na I or Ca I to CO(2-0) is sensitive to the superficial gravity of the stars and therefore it can trace the luminosity class of the dominant stellar population in a region. Spectral indices of the selected apertures on the bulge of IRAS 01072+4954 are shown. Their symbols are the same as in Fig. 4.15. Stars and galaxies observed by Mannucci et al. (2001) and their linear fits to the stellar data are also shown. The filled circles correspond to templates of galaxies grouped by type: E-Sa, Sb and Sc. Galaxies with detected line emission and only upper limits in $W_{\mathrm{Na\,I}}$ and $W_{\mathrm{Ca\,I}}$ are signaled by the arrows (see reference for details). Modified from Mannucci et al. (2001).

The $\left(W_{\mathrm{Na\,I}}+W_{\mathrm{Ca\,I}}\right)$ vs. $W_{\mathrm{CO(2-0)}}$ diagram offers an estimation of the dominant stellar population in the apertures. Three facts can be stressed from this figure: (i) The EWBrγ and the NE apertures are regions with recent star formation. From Table 4.3 it is possible to notice that these two regions have the highest $W_{\mathrm{Br\gamma}}$ and $W_{\mathrm{CO(2-0)}}$, both are indicative of young stars. However, given that in regions located close to an AGN enhanced Brγ is expected, and that the CO(2-0) feature is not much stronger than that in the Median aperture, the Mannucci et al. diagram plays an important role confirming the presence of young stellar population from the absorption lines. (ii) The Median spectrum is located close to the giants-trend, where systems that combine populations formed at different epochs also are located. Its spectrum shows features associated to dwarfs like

the high $W_{\mathrm{Ca\,I}}/W_{\mathrm{CO(2-0)}}$ ratio, but also with supergiants like the boxy-like hump at $\sim 1.55\,\mu$m. (iii) Because of the spectral proximity of the indices used in this diagram, the position of the central aperture is consistent with an intermediate/old stellar population, without evident signs of the hot dust emission. Finally, the uncertainties on the Na I and Ca I indices of the SW aperture are very high as discussed before, not allowing for any physical interpretation of its position in the plot.

A new NIR spectral index
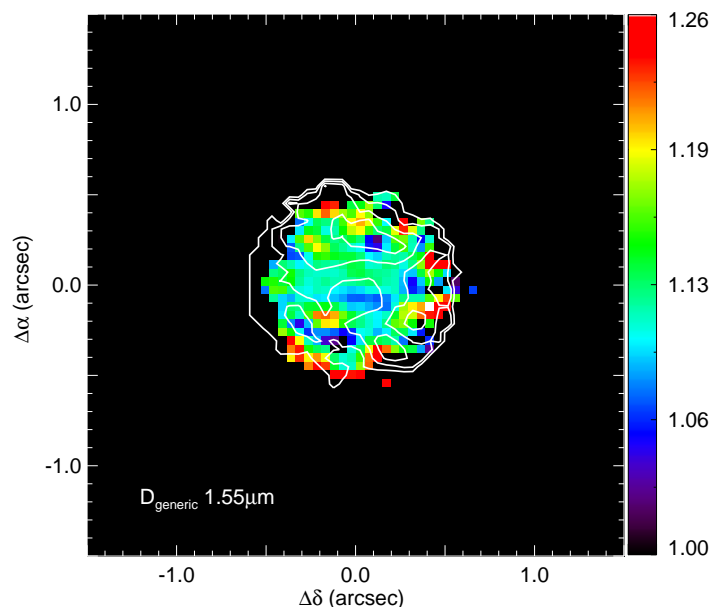
Figure 4.19: $1.55\,\mu$m generic-discontinuity map of IRAS 01072+4954. This new NIR spectral index (see text for definition) seems to be sensitive to the luminosity class. In the spectra of individual stars, it can only be recognized in types later than KIII and luminosity classes I to III. The contours correspond to 4, 8, 13 and 19Å of $W_{\mathrm{Br}\gamma}$.

The spectra of most luminous late-type stars (KIII and later, luminosity class III and higher) show a boxy-like feature formed between $1.540\,\mu$m and $1.555\,\mu$m. This feature is produced mainly by the strong absorption of CO(3-0) $\lambda1.5582\,\mu$m and the multiple absorption of the OH(2-0) at both ends. The OH(4,2)R band-head, that starts at $1.537\,\mu$m had been already identified and modeled by Origlia et al. (1993) as present in the H-band spectra of M-type supergiants, but they did not noticed its potential as a luminosity tracer. The strength of both, the CO and the OH, increases with the microturbulent velocities, which is higher in high-luminosity stars. The Si I is also responsible for the absorption at $1.5381\,\mu$m and at $1.5562\,\mu$m, but moving toward later types, the OH becomes the dominant absorber in this part of the spectrum. I propose the new index as the inverse of a

generic discontinuity (see definition in Eq. (1.14), Sect. 1.3.2.3), with feature limits: $1.545\,\mu$m and $1.555\,\mu$m

and two pseudo-continua $(1.5350 - 1.5400)\,\mu$m and $(1.557 - 1.562)\,\mu$m, which basically account for the absorption at both sides. The inspection of several stellar libraries indicates that this is a good potential luminosity indicator. Figure 4.19 shows the map of the '1.55 μm generic discontinuity' $D_{1.55\,\mu m}$ overlapped with $W_{\mathrm{Br}\gamma}$ contours. Both maps seem to trace similar areas. As expected from the spectra of the individual apertures, cool giants-to-supergiants are present in the northern regions. In the SE region and at west, the high values are very close to the S/N limit, longer-exposure observations are needed to confirm the presence of young stars there. The characterization of the new index behavior with respect to other parameters is beyond the scope of this Thesis.

4.6   Conclusions

The stellar mass content and the star formation process in the galaxy and particulary in the bulge are studied. The main finds are:

- Through a process of low-pass filtering a structure that resembles a bar or a inner disk is found to extent all the way to the nucleus and that has an orientation P.A. $\sim 100°$.

- Combining the low resolution 2MASS images of the whole galaxy with the high resolution NIFS data of the bulge, it was possible to construct the brightness profile of the galaxy. Interestingly, the Sersic index of the bulge is $n \sim 1$, which is indicative for a pseudobulge and for a psecular evolution process of the galaxy.

- Here the NIFS data is presented. In general the spectrum at the nucleus, as well as in the whole galaxy bulge, exhibits strong emission lines. No signs of broad (FWHM $> 2000\,\mathrm{km\,s^{-1}}$) line components is found.

- The Brγ and Br10 emission were used to create a map of the extinction. Unfortunately, the Br10 line is very faint and only allow for measurements very close to the nucleus and in the northen regions. Caveats in the interpretation of the A_V map are also discussed.

- From the (H-K) color map and the previous A_V estimation, it is possible to predict the presence of a hot dust component at the center. This dust

- IRAS 01072+4954 is a sttarburst galaxy. With a global star formation rate SFR $\sim 5\,\mathrm{M_\odot\,yr^{-1}}$, and a stellar mass $M_* \sim 10^{10.0-10.2}\,\mathrm{M_\odot}$, its doubling mass timescale $\tau \sim (2.0 - 3.5)\,\mathrm{Gyr}$ is more than 3 times smaller than that of star forming galaxies of the same age and mass.

- Using different spectral indices, the stellar populations in five regions of the bulge of the galaxy were studied. In general it was found that in the EWBrγ and in the NE regions the stellar populations are young, while across the bulge they are consistent with intermediate/old ages. The metallicity is very low in the entire bulge.

- A new feature in the H-band spectra of late-type K-M stars was found. This boxy-like feature at $1.55\,\mu$m was found to be very prominent in supergiants (stellar types later than KIII and luminosities between I to III. This feature might be a good alternative to trace young stellar populations in the NIR.

Chapter 5

Nature of the AGN

IRAS 01072+4954 is a starburst/AGN composite galaxy. Its low optical and near-infrared extinction toward the nucleus, together with the short Hydrogen column density in the X-rays indicate a clear view of the central source. The presence of the AGN is notorious in the X-ray spectrum. Can it also be recognized in the *HK*-band data? The high resolution of NIFS allows us to discover some properties of the AGN. How big is the torus? What is its orientation, and its mass? What is the black hole mass? Is it actively accreting matter? How bright is the accretion disk around it? If the IRAS 01072+4954 central source behaves as other AGN with similar X-ray properties, it is possible to estimate the brightness and width of the lines emitted in the broad line region. They are not visible in the optical spectrum, but could they be detected in the near infrared? I show some evidences of a possible detection in the *K*-band spectrum of IRAS 01072+4954, extracted at the resolution limit, of one of the narrowest broad lines discovered so far in AGN, and discuss the nature of the central source. The summary of the main findings is presented at the end of the Chapter.

5.1 Signs of the AGN in the Near-Infrared data

Although in X-rays IRAS 01072+4954 looks like a galaxy with a very active nucleus (Panessa et al. 2005), the optical and the near-infrared (NIR) emission seems to be dominated by the stellar component. From the low hydrogen column density estimated from the soft X-rays, broad lines powered by the AGN are expected in the spectrum. However, even in the case of hidden broad lines, other spectral features in high spatial resolution observations can reveal the presence of the AGN. Two of them are the coronal emission and the filling of the stellar absorption lines.

5.1.1 Coronal Emission

Coronal lines are reliable AGN tracers, since pure starbursts produce few ionizing photons with energies higher than $54\,\mathrm{eV}$. With the high spatial resolution data of NIFS, it was possible to detect the [Ca VIII] $\lambda2.322\,\mu\mathrm{m}$ line, which requires an

ionizing potential of 127 eV to be excited. The line is unresolved and has very low signal to noise (for a line map see Fig. 4.6, page 66). Despite its faintness, the [Ca VIII] line can be seen in the spectrum integrated over an aperture with the size of the spatial resolution element, $r \approx 75$ pc. Given the spectral position of this line, just at the border of the CO (3-1) band-head, a clear detection is not possible without removing the stellar contribution. Unfortunately, the procedure used to remove the stellar continuum – described in more detail in the following Sect. 5.1.2 – also introduces additional noise in the residuals. After subtracting a stellar template spectrum from the one at the nucleus, the continuum turns flatter, and the presence of the [Ca VIII] coronal line is more evident (Fig. 5.1). The flux of the line estimated from a Gaussian fit is $7.9 \times 10^{-17} \, \mathrm{erg \, s^{-1} \, cm^{-2}}$, with a width of FWHM $\simeq 290 \, \mathrm{km \, s^{-1}}$ and the signal-to-noise $(S/N) \simeq 2.5$.
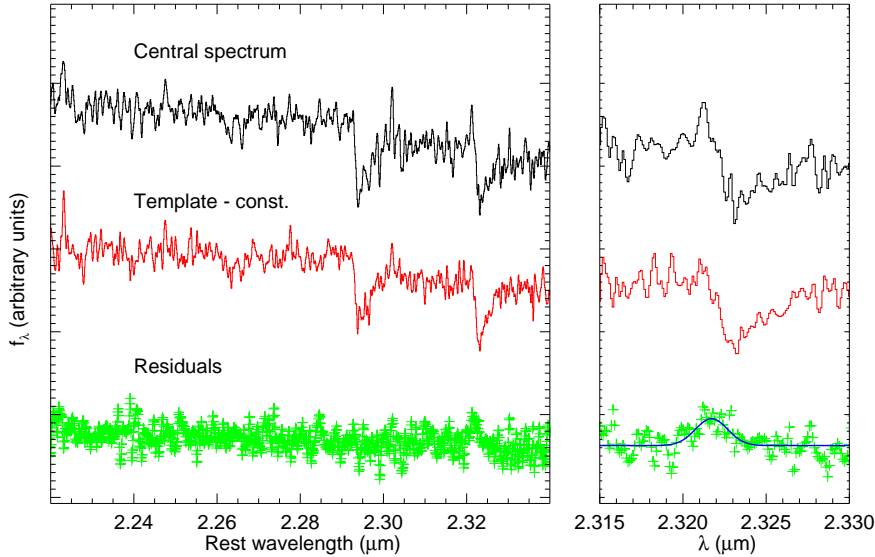
Figure 5.1: Coronal [Ca VIII] emission in the central $r \approx 75$ pc spectrum of IRAS 01072+4954. The black spectrum on top is extracted from the center with an aperture of the size of the K-band PSF. The red spectrum in the middle is the constructed stellar template, which is vertically shifted for clarity. The residuals from the subtraction of the latter from the former are shown with green crosses. At the *right*, a zoom-in around the [Ca VIII] spectral position, and a Gaussian fitted to the line (solid blue line) are shown.

5.1.2 The AGN through the equivalent widths of absorption lines

IRAS 01072+4954 has very low extinction toward the nucleus, as shown in Sect. 4.3 from the hydrogen recombination line ratio, and which is in agreement with the low column density detected in the X-rays (Panessa et al. 2005). This means that it must be possible to detect direct emission from the AGN. In *JH*-bands, the so-called 'featureless continuum' is associated with the accretion disk and is

more evident in the optical and UV. In the K-band, the emission from the dust heated by the accretion disk (and by the corona?) is expected, and as I showed in Sect. 4.3.1 is actually present in the data. Here I show a method to estimate the relative contributions of the stars and the hot dust in the central $r \approx 0.16''$ using the equivalent widths of the absorption lines.

Origlia et al. (1993) and Oliva et al. (1995) showed that the stellar populations of normal galaxies (ellipticals and spirals) span a small range of equivalent widths W. In the presence of an AGN, the continuum flux increases due to the emission from hot dust, which has its maximum in the NIR, and as a consequence a decrease in the values of W is observed. In some Seyfert galaxies, also a power-law contribution, possibly originating from the accretion disk, has been detected (see e.g. Rodríguez-Ardila et al. 2005a; Riffel et al. 2009b, 2010). Following the same idea, Davies et al. (2007) produced synthetic spectra using the code STARS (e.g., Sternberg 1998; Thornley et al. 2000) to reproduce the behavior of the stellar-population properties as a function of time. They showed that after $10\,\mathrm{Myr}$, independent of the star-formation history, the values of the $W_{\mathrm{CO}\,(6-3)}$, $W_{\mathrm{Na\,I}}$ and $W_{\mathrm{CO}\,(2-0)}$ vary only by $\sim 20\%$ around some typical values. Similar results can be obtained with the code SB99 (Leitherer et al. 1999; Vázquez & Leitherer 2005). The equivalent widths predicted by these codes are in agreement with the previous measurements of Origlia et al. (1993) and Oliva et al. (1995).

I measured the equivalent widths of the CO(6-3) and and CO(2-0) bands, the Si I and the Na I lines in the spectrum extracted from the central $r = 0.16''$ and compared them with the theoretically typical ones W_{int}, and with the ones measured from a stellar template W_{temp} (Fig. 5.2). The template was obtained by integrating the emission over an annulus[1] with inner radius $0.24''$ and outer radius $0.43''$. The typical equivalent widths for populations older than $10\,\mathrm{Myr}$ obtained from the STARS and SB99 codes, and the measured equivalent widths in the central and in the template spectra are listed in Table 5.1. I used the integration limits quoted by Origlia et al. (1993) for the W_{SiI}, $W_{\mathrm{CO}(6-3)}$ and $W_{\mathrm{CO}(2-0)}$ and those by Förster Schreiber (2000) for W_{NaI} (for the definitions of the wavelength-integration ranges, see Table 1.1 in page 25), and estimate the continuum from the featureless neighboring regions that best suited our data[2]. The stated errors represent 1σ intervals assuming that the noise over the integrated area is the same as that in the continuum. The error corresponding to 1% of uncertainty on the continuum-level estimation is $\sim 0.4\,\text{Å}$.

---

[1]The northern part of the annulus was cut out, because it crosses a region of very recent star formation (see Sect. 4.5).

[2]For this reason, some values might vary with respect to those presented in Chapter 4. However, this does not affect the results obtained here because in both apertures they equivalent widths are calculated in a consistent way, using the same continuum intervals.

The fraction of stellar emission in the central aperture f^{stellar} was calculated as the ratio between W at the center and a reference value, following the prescription of Davies et al. (2007). Taking as reference values the equivalent widths predicted from the synthetic stellar-population codes W_{int} and the equivalent widths measured in the template spectrum W_{temp}, two estimates of the stellar fraction in the central region can be obtained, $f^{\text{stellar}}_{\text{int}} = W/W_{\text{int}}$ and $f^{\text{stellar}}_{\text{temp}} = W/W_{\text{temp}}$ for each absorption feature in the study. These values are also presented in Table 5.1.

Although the theoretically typical W_{int} of the Si I and Na I are lower than the measured equivalent widths in both absorption features, the values are still consistent within the errors of the measurements and with the scatter of the equivalent widths in stellar populations of different ages. In general, it is possible to notice that the H-band spectrum appears to be dominated by the stellar emission, while at least 20% of the K-band emission has a different origin.

This, together with the H-K color maps, is a clear evidence for the AGN in the NIR emission at the center of this galaxy. On the other hand, it is still possible that some contribution from the hot dust and/or a featureless continuum are/is present in the H-band data, in an amount that this method can not quantify. In order to find and disentangle these contributions, it is necessary to model the non-stellar continuum spectrum, as shown in the next section.

Table 5.1: Equivalent widths measured in the central region, W in the stellar template W_{temp}, and predicted by synthetic stellar-population codes W_{int}.

Feature	W^a (Å)	W_{int} (Å)	$f^{\text{stellar}}_{\text{int}}$ (%)	W_{temp} (Å)	$f^{\text{stellar}}_{\text{temp}}$ (%)
Si I	3.5 ± 0.2^b	2.5^c	100^d	4.2 ± 0.3^b	80
CO(6-3)	4.9 ± 0.3	4.5	100^d	4.6 ± 0.3	100^d
Na I	3.0 ± 0.2	2.5	100^d	4.5 ± 0.3	65
CO(2-0)	8.6 ± 0.3	12	70	13.6 ± 0.4	65

Note. The fraction of the continuum at the center that is emitted by stars f^{stellar} was obtained by comparing W with W_{temp}, and with W_{int}.

^{a} From the spectrum integrated over a region of $r \approx 75\,\text{pc}$.

^{b} Corrected for the contribution of Br14 $\lambda 1.588$.

^{c} Calculated using SB99 code.

^{d} Set to the maximum value, 100%.
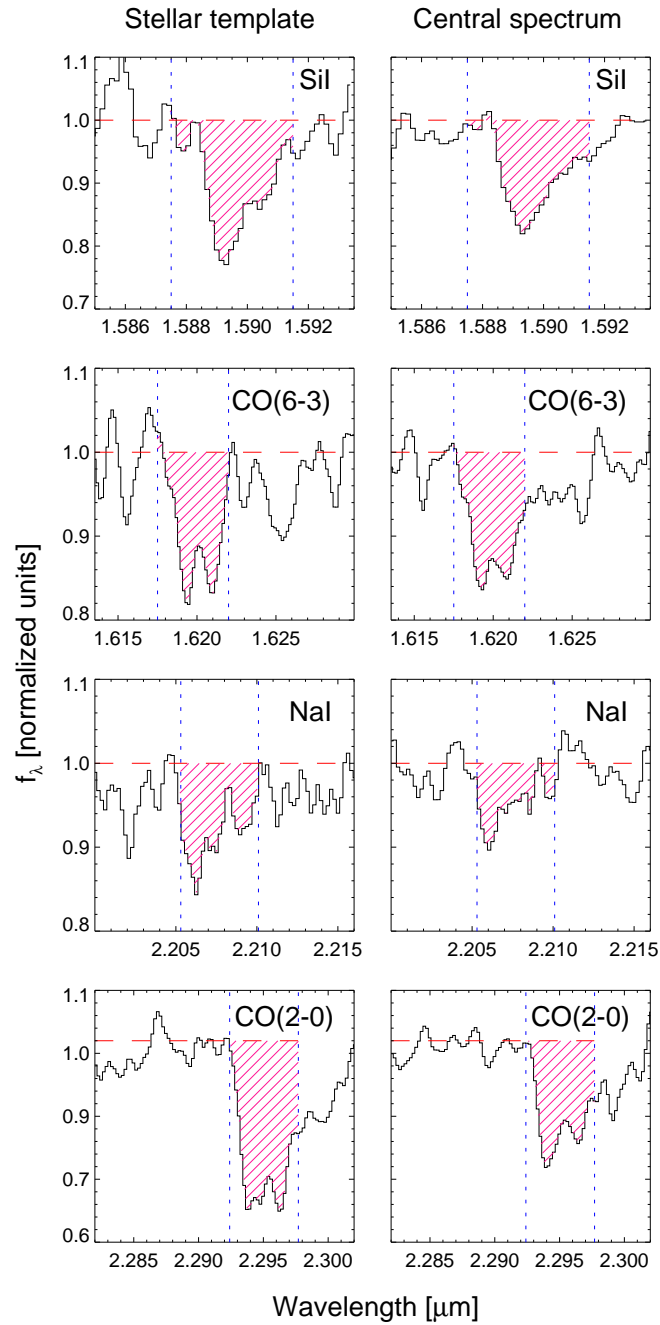
Figure 5.2: Absorption lines in the stellar template spectrum (*left*) and the spectrum extracted at the center (*right*) of IRAS 01072+4954. The spectra are normalized to the continuum level, which is shown as a dashed line in each case. The vertical dotted lines mark the limits of the integration regions, and shaded areas the equivalent widths. The measured values are reported in Table 5.1. From top to bottom the absorption features are, as indicated, Si I, CO (6-3), Na I and CO (2-0).

5.2   The torus

The high *H-K* color in the central $r \approx 75\,\mathrm{pc}$ of IRAS reveals the existence of dust heated by a non-stellar source. This material could be associated with the toroidal obscuration around the central source, required by the unified model. In the following, I use the high spatial resolution NIFS data to quantify the amount of hot dust emission at the center, and to put constraints on its size, orientation, and mass. In particular the orientation of the torus is a fundamental parameter in the classification of an AGN.

Quantifying the non-stellar emission at the center

Following the method described by Rodríguez-Ardila et al. (2005a), it is possible to assume the spectrum at the center to be the linear combination of three components: stellar emission, blackbody radiation from hot dust and a non-thermal source described as a power law $f_\lambda \propto \lambda^\alpha$. The stellar contribution is represented by the stellar template obtained as explained in the previous section (Sect. 5.1.2) and corrected for extinction. This selection implies the assumption that the stellar populations at the center and in the surroundings share the same characteristics. The template was scaled to have about the same $W_{\mathrm{CO(2-0)}}$ (within the errors) as the central spectrum and then was subtracted from it. The scaling factor of the template was also restricted such that the emission lines of H_2 and [Fe II] were not oversubtracted. The next step was fitting the blackbody and power-law contributions to the residual emission. In the wavelength range of our data, it was not possible to constrain the power-law component and therefore the independence of the blackbody and the power-law contributions could not be assured. In a conservative approach, I fitted the residuals only with a blackbody using the IDL based routine MPFITEXPR (Markwardt 2009), which performs Levenberg-Marquardt least-squares minimization (Fig. 5.3). To get a better approximation to the continuum, small spectral regions with residuals of strong absorption or emission lines were masked.

The appropriate estimation of the obscuration in the central spectrum and in the template was critical, because the reddening acts over the spectrum in the opposite way as the hot-dust contribution. Observations over a larger wavelength baseline could help to overcome the degeneracy problem. The central spectrum was corrected for an extinction of $A_V = 2.5\,\mathrm{mag}$, as discussed in Sect. 4.3. Given that the Br10 line was very faint in several regions from where the template was taken, the *H-K* color was used to calculate the extinction acting on the template spectrum $A_{V,\mathrm{temp}}$. A window of $\sim 0.5\,\mathrm{\AA}$ around $1.61\,\mu\mathrm{m}$ and $2.20\,\mu\mathrm{m}$ were employed to determine the *H-* and *K*-band magnitudes, respectively. Using the fact that the *H-K* color of a late-type stellar population is about $0.26 \pm 0.08\,\mathrm{mag}$ (Willner et al. 1984), the extinction was computed as

$$A_{V,\mathrm{temp}} = \frac{(H-K) - 0.26}{0.0765},\tag{5.1}$$

which in our case implies $A_{V,\text{temp}} = 3.8\,\text{mag}$.
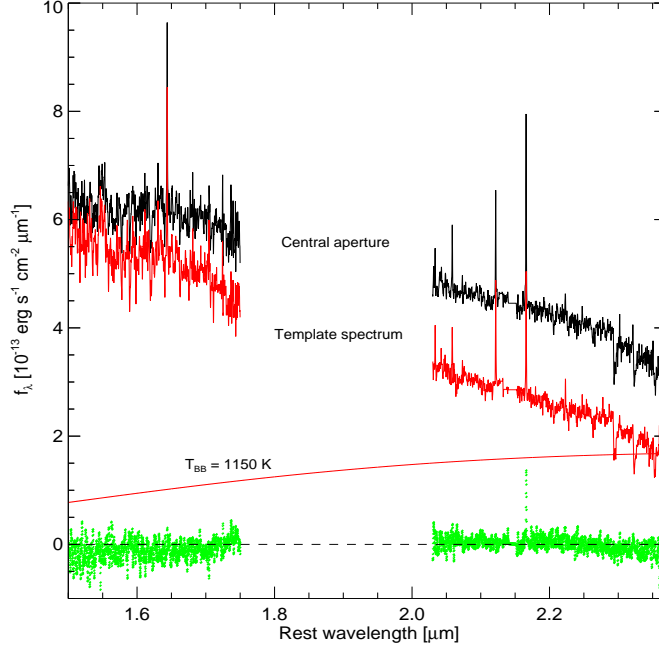
Figure 5.3: Fit of the NIR central spectrum of IRAS 01072+4954. The spectrum of the nucleus integrated over an aperture of $r = 0.16''$ is presented on *top*. The stellar (red spectrum) and hot-dust (red blackbody curve) fitted contributions are shown. They were modeled with the constructed stellar-template and a blackbody of $T = 1150\,\text{K}$, respectively. Small spectral regions with spurious residuals were masked and replaced by the median of the values at their borders. The residuals of the fitting procedure are shown at the *bottom* with green dots. The dashed line marks the zero flux. The curvature of the residual noise might indicate an underestimation of the stellar-template extinction, and thereby an underestimation of the hot-dust temperature.

Figure 5.3 shows the best fit to the central spectrum. The result of the modeling indicates that 75% of the central $r \approx 75\,\text{pc}$ emission is produced by stars and the remaining 25% is associated to the hot dust, in agreement with the estimates based on the equivalent width of the absorption lines.

The hot dust temperature / Torus orientation

The hot dust emission is well described by a blackbody of $T \approx 1150\,\text{K}$. Possible errors in the estimation of the extinction of the stellar component affect mainly the value of the temperature of the fitted blackbody. A variation of $0.5\,\text{mag}$ in the $A_{V,\text{temp}}$ causes an increase/decrease of $\sim 80\,\text{K}$. Lower obscuration of the stellar component results in higher temperatures, while an $A_{V,\text{temp}} \geq 5.0\,\text{mag}$ (which implies $T \leq 980\,\text{K}$) produces negative residuals in the H-band and a low-quality fit. The weak trend present in the residuals of the best model fit (Fig. 5.3), though, is consistent with the error of $\sim 10\%$ in the flux calibration, could indicate that

the stellar extinction is slightly overestimated – and, consequently result in an underestimation of the temperature.

Previous studies that used the same method in NIR spectra (e.g., Rodríguez-Ardila et al. 2005b; Riffel et al. 2009b, 2010) or broad-band SED modeling (e.g., Marco & Alloin 1998; Kishimoto et al. 2007; Exposito et al. 2011) found temperatures of $\gtrsim 1000\,\mathrm{K}$ in Type 1 AGN and $\lesssim 800\,\mathrm{K}$ in Type 2s. From *JHK* spectroscopy, Landt et al. (2011) also found temperatures ranging from 1100 to $\sim 1700\,\mathrm{K}$ for a sample of 23 type 1 sources. Recently, Mor & Trakhtenbrot (2011) showed that the NIR emission of $\sim 80\%$ type 1 AGN can be explained by emission from hot, pure-graphite dust clouds. Given that for $T \gtrsim 1000\,\mathrm{K}$ most astrophysical grain compositions sublimate (Salpeter 1977; Barvainis 1987; Granato & Danese 1994), emission at these temperatures must correspond to dust located very close to the accretion disk (clouds in the inner region of a torus?), while further out the temperature of the dust decreases rapidly as a result of a larger distance from the source and the shadowing effect caused by other dust clouds (Elitzur 2008). A dust temperature of $\approx 1150\,\mathrm{K}$ in IRAS 01072+4954 indicates that we have – at least partially – a clear view towards the center. With the wavelength range of our data, it was not possible to fit the expected featureless continuum power-law emission coming from the central source. The presence of such component with a typical flux density $f_\lambda \propto \lambda^{-0.5}$ would imply higher temperature of the hot dust emission.

The hot dust extension / Torus size

The hot-dust central emission has been interpreted as evidence for the putative torus predicted by the unified model. Earlier models of the toroidal obscuration predicted sizes up to few hundred parsecs based on the assumption of a uniform distribution of dust (Pier & Krolik 1992; Granato & Danese 1994). In those models, the temperature of the dust was directly related to the radial position. However, later calculations showed that it is possible to have smaller structures with mixed temperatures, when the dust is assumed to be clumpy distributed (see e.g., Elitzur 2008, and references therein). High angular resolution observations of nearby AGN suggest torus sizes smaller than few tens of parsecs (e.g., Prieto et al. 2010).

In the case of IRAS 01072+4954, evidence that the hot dust emission is very compact is shown in Fig. 5.4. There, the slopes of the *H*- and *K*- band continuum are calculated in every spatial pixel of the field-of-view. The maps were created by subtracting the median of the continuum over two narrow windows in each band – $\sim 150\,\text{Å}$ at $1.5656\,\mu\mathrm{m}$ and $1.6830\,\mu\mathrm{m}$ in *H*, and $\sim 290\,\text{Å}$ at $2.0973\,\mu\mathrm{m}$ and $2.3020\,\mu\mathrm{m}$ in *K*-band –, and then dividing by the median wavelength separation of the windows. Please note that the color bars in the two maps are inverted for displaying reasons. From the maps it is clear that the increment in the spectral slope in both bands is unresolved, i.e. it is evident in the central $\sim 3 \times 3$ pixels, while our spatial resolution is $r \sim 4$ pixels in *H* and $r \sim 3$ in *K*-band. The 'donut'-shape area around the center in the *K*-band map indicates cooler colors at $\sim 50\,\mathrm{pc}$ away from the center.
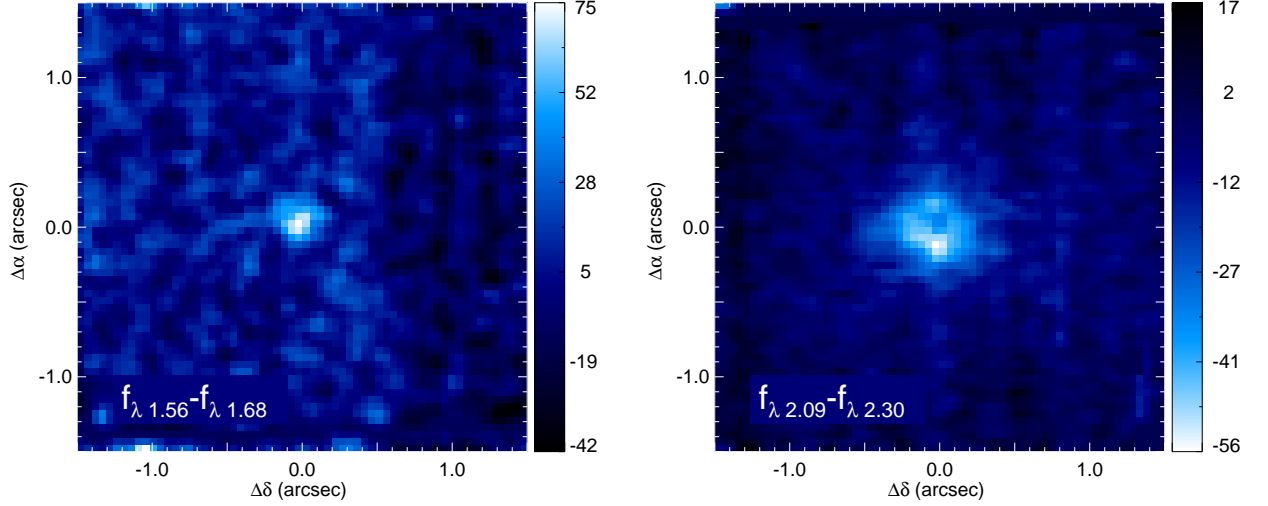
Figure 5.4: *Left: H*-band continuum slope. The color bar is in units of $10^{-16}\,\mathrm{erg\,s^{-1}\,cm^{-2}}$. The slope was measured from two narrow band windows placed at $1.56\,\mu$m and 1.68. *Right: K*-band continuum slope. The color bar is in the same units as in the left-hand panel, but inverted for displaying purposes. The hot dust emission can be seen as the darker pixels at the center, surrounded by cooler *H-K* areas (bright ring). The spectral windows used for measuring the slope were $2.09\,\mu$m and $2.30\,\mu$m.

It can be concluded that dust close to the sublimation temperature is present in a region of radius $r < 65\,$pc, which is the scale of the NIFS *K*-band PSF. Nevertheless, given the high *H-K* colors in the central $r \sim 80\,$pc, warmer dust that extends few tens of parsecs out of the nucleus, and that is linked to the inner hot dust, can not be discarded. On the other hand, the high central dust temperature implies that we are observing along a line of sight that allows a clear view toward the nucleus, in agreement with the X-ray findings (Panessa et al. 2005). In the same scenario, continuum featureless emission from the accretion disk is also predicted. However, Fig. 5.4 (left) shows an increment of the *H*-band slope at the center, while the featureless continuum is expected to produce an effect in the opposite direction. It might be that the effects of both components, hot dust and featureless continuum, are present in the data, but our wavelength coverage is insufficient to disentangle them. High spatial resolution *J*-band observations can help finding the accretion-disk emission tail – whose peak corresponds to the big blue bump –, or putting upper limits on the presence of this component.

Mass of the hot dust

Following Barvainis (1987), it is possible to estimate the mass of the hot dust from its NIR emission. The idea is to infer the number of shining dust grains N_{HD} from the ratio between the observed luminosity L_{HD} in the infrared, and the predicted IR luminosity L_{gr} of a single dust grain. Then, the mass can be

calculated simply as

$$M_{HD} \approx \frac{4\pi}{3} a^3 N_{HD} \rho_{gr}, \tag{5.2}$$

where a is the radius of a grain and ρ_{gr} its density.

The IR spectral luminosity of a single grain is given by (Barvainis 1987)

$$\frac{l_{\nu,gr}}{\mathrm{erg\,s^{-1}\,Hz^{-1}}} = 4\pi^2 a^2 Q_\nu B_\nu(T), \tag{5.3}$$

where $B_\nu(T)$ is the Planck function for a grain temperature T, and Q_ν is the absorption efficiency of the grains, which is higher at shorter wavelengths – a dust grain absorbs more UV/optical than IR radiation –, and can be approximated by a power law $Q_\nu = q_{IR}\,\nu^\gamma$. The composition of the dust grains in AGN is not known. For this analysis, it is assumed that graphite is their main constituent. That allows to use the values derived by Draine & Lee (1984): $a = 0.05\,\mu$m, $q_{IR} = 1.4 \times 10^{-24}$ and $\gamma = 1.6$. Integrating Eq.(5.3) one obtains

$$L_{gr} = \int l_{\nu,gr}\,d\nu = 8\pi^2 a^2 q_{IR} \frac{h}{c^2} \left(\frac{k}{h}\right)^{4+\gamma} T^{4+\gamma} \Gamma(4+\gamma)\,\zeta(4+\gamma), \tag{5.4}$$

where c is the speed of light, h and k are the Planck and Boltzmann constants, Γ is the gamma function and ζ is the Riemann zeta function. The luminosity of the observed hot dust emission, calculated by the integration of the fitted blackbody curve to the non-stellar continuum, is $L_{HD} = 7.24 \times 10^{42}\,\mathrm{erg\,s^{-1}}$.

Adopting $\rho_{gr} = 2.26\,\mathrm{g\,cm^{-3}}$ (Granato & Danese 1994), from Eq.(5.2) we obtain $M_{HD} = 1.1 \times 10^{-3}\,\mathrm{M_\odot}$. This value is in the range of those found in other AGN (see compilation in Riffel et al. 2009b). In particular this mass is very similar to that derived for NGC 1068 – the archetypical Sy2 – by Marco & Alloin (1998), that of Mrk 766 – a Narrow-Line Seyfert 1 – (Rodríguez-Ardila et al. 2005a) and of NGC 7582 – Sy1 – (Riffel et al. 2009a). No general trend has been found between the derived mass and the AGN type or luminosity.

5.3   The black hole mass

The black hole mass has been found to be correlated with several properties of the host galaxy bulge, among others the mass (Magorrian et al. 1998; Häring & Rix 2004; Graham 2012a), the optical or NIR luminosity (Marconi & Hunt 2003; Graham 2007; Gültekin et al. 2009), the stellar velocity dispersion (Gebhardt et al. 2000; Ferrarese & Merritt 2000; Tremaine et al. 2002; Gültekin et al. 2009; Graham et al. 2011), and the Sersic index (Graham & Driver 2007). In this section, I use these scaling relations, valid for galaxies with black hole masses between 10^7 to $10^9\,\mathrm{M_\odot}$, under the assumption that they are valid in the case of IRAS 01072+4954. However, they yield values that are different from each other by more than one order of magnitude. This implies that some of the relations are not suitable in this case. The reasons and possible ways to remove the discrepancies are discussed further below.

5.3.1 Black hole mass vs. Bulge luminosity relation

Using the luminosity of the bulge to determine the mass of the black hole M_{BH} requires a proper photometric decomposition of the galaxy brightness profile. I showed in Sect. 4.1.2 (page 59) that the 2MASS and our NIFS data can be combined to produce radial averaged H- and K-band brightness profiles, that were fitted with a linear combination of a Sersic and an exponential profiles, previous subtraction of the AGN component. The photometric parameters are shown in Table 4.1. The bulge luminosity in each band can then be derived using the Eq. (4.8), which is obtained by integrating the bulge profiles. The central surface brightness, the bulge luminosity and similarly the absolute magnitude in each band are presented here in Table 5.2.

As mention before, the 2MASS and the NIFS data sets do not overlap properly with each other and they have very different resolution and sensitivity, therefore it is possible that part of the disk emission – mainly fitted by the 2MASS data – at the center is spread-out and some disk flux at small radii is missing. On the other hand, although the bar component does not seem to dominate in the central $\sim 1\,\mathrm{kpc}$, its contribution was not taken into account when constructing the 1D profile. As an overall result, the bulge luminosity could be overestimated by up to one order of magnitude.

Figure 5.5 shows the M_{BH} vs. K-band bulge luminosity $L_{\mathrm{bulge},K}$ correlation of Marconi & Hunt (2003) and the M_{BH} vs. K-band bulge absolute magnitude $M_{\mathrm{bulge},K}$ updated correlation of Graham (2007). In the latter, the author homogenized the Hubble parameter and the galaxy colors for the whole sample, and also included corrections for reddening. The position of IRAS 01072+4954 in the plots of the Fig. 5.5 is given by the measured abscissa values and the assumption that it follows the same correlation as the sources of the Marconi & Hunt and Graham samples.

Black hole sphere of influence: radius until which it dominates the gravitational potential $R_{\mathrm{BH}} = GM_{\mathrm{BH}}/\sigma_*^2$. It is spatially resolved when $2R_{\mathrm{BH}}/\mathrm{PSF} > 1$.

Table 5.2: *HK* bulge luminosities of IRAS 01072+4954 and black hole mass estimations

		H-band	K-band
Central surface brightness[a]	I_0 (10^3 $\mathrm{L}_{\odot,\lambda}\,\mathrm{pc}^{-2}$)	34.2 ± 0.5	74.6 ± 2.0
Bulge luminosity[b]	$L_{\mathrm{bulge},\lambda}$ (10^9 $\mathrm{L}_{\odot,\lambda}$)	1.71 ± 0.60	3.24 ± 1.91
Bulge absolute magnitude[c]	$M_{\mathrm{bulge},\lambda}$ (mag)	-19.75 ± 0.39	-20.50 ± 0.64
Black hole mass[d]	M_{BH} (10^6 $\mathrm{M}_\odot$)	$1.2^{+1.8}_{-0.7}$	$2.5^{+4.7}_{-1.7}$

[a] Photometric parameters derived from the fitting procedure of Sect. 4.1.2.

[b] Calculated from Eq. (4.8).

[c] With absolute magnitudes of the Sun: $\mathrm{M}_{\odot,H} = 3.33$ mag and $\mathrm{M}_{\odot,K} = 3.28$ mag.

[d] Upper limit, as explained in the text. Calculated using Marconi & Hunt (2003, their Table 2).
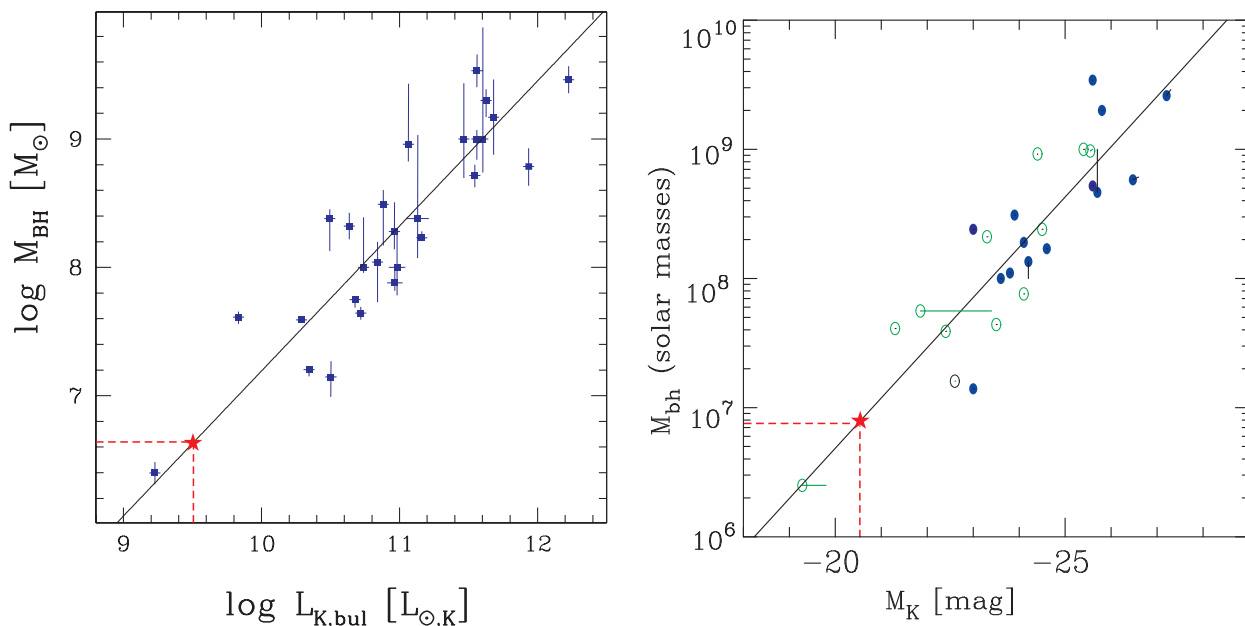
Figure 5.5: Black hole mass vs. K-band bulge luminosity/absolute magnitude relation. *Left:* Marconi & Hunt fit to galaxies for which the black hole sphere of influence has been clearly resolved. The sources have 2MASS photometry and kinematically measured M_{BH}. Modified from: Marconi & Hunt (2003). *Right:* Updated version of the relation of the left-hand panel. Ellipticals are shown as filled circles, and lenticulars and spiral bulges as empty circles. Modified from: Graham (2007). In both panels, the star represents the position of IRAS 01072+4954 if, given its K-band bulge photometry, it lies on the fitted correlations.

The black hole mass calculated using the linear fits to the H- and K-band data of Marconi & Hunt (2003, see their Table 2) is also presented in Table 5.2. The stated errors do not include the intrinsic rms scatter of the correlations of ~ 0.52 dex. The upper limit on M_{BH} obtained in this way is $2.5 \times 10^6 \, M_\odot$. When using the Graham updated version of the same relation, $M_{BH} = 7.5 \times 10^6 \, M_\odot$, while the expression found by McLure & Dunlop (2002, their Eq.(1)) gives $M_{BH} = 1.3 \times 10^6 \, M_\odot$.

5.3.2 Black hole mass vs. Sersic index relation

In contrast to the previous photometric method of black hole mass estimation, using the Sersic index n of the fitted bulge profile does not required the absolute flux calibration of the images. It also seems that n is less affected by any kinematical substructure at the center, nor by aperture corrections.

Graham & Driver (2007) fitted the M_{BH} vs. n relation with a linear and with a quadratic function. They favor the later because it predicts finite masses at the high-mass end, and is consistent with $M_{BH} < 10^5 \, M_\odot$ in dwarf galaxies and in the galaxy M 33. Their expressions for estimating the black hole mass and its error

are

$$\begin{aligned}
\log M_{\mathrm{BH}} &= (7.98 \pm 0.09) + (3.70 \pm 0.46) \log\left(\frac{n}{3}\right) \\
&- (3.10 \pm 0.84)\left[\log\left(\frac{n}{3}\right)\right]^2
\end{aligned}$$

(5.5)

$$\begin{aligned}
(\delta \log M_{\mathrm{BH}})^2 &= \left[\log\left(\frac{n}{3}\right)\right]^4 + \frac{\left[\log\left(\frac{n}{3}\right)\right]^2}{4} + 0.09^2 \\
&+ \frac{\left[3.70 - 6.20\log\left(\frac{n}{3}\right)\right]^2 \left(\frac{\delta n}{n}\right)^2}{(\ln 10)^2} + \epsilon^2,
\end{aligned}$$

(5.6)

where δn is the error of the Sersic index, $\epsilon = 0.18$ is the intrinsic scatter of the correlation, and M_{BH} is measured in solar masses. Applying these relations in the case of IRAS 01072+4954 gives $\log(M_{\mathrm{BH}}/\mathrm{M}_\odot) = 5.77 \pm 0.41$.

5.3.3 Black hole mass vs. Bulge mass relation

The black hole mass also correlates with the mass of the host bulge/spheroid. Magorrian et al. (1998) were the first group to explore this correlation, finding $M_{\mathrm{BH}} \sim 0.005\,M_{\mathrm{bulge}}$ with very high scatter. Latter, Häring & Rix (2004) refined the estimations of M_{bulge} through the modeling of the Jeans equation, obtaining similar results but with only ~ 0.3 dex of intrinsic scatter. This is desired because the tightness of a correlation has been taken as an indication for a fundamental physical link between the two quantitites.

Interestingly, the M_{BH} vs. M_{bulge} correlation persists even when different methods for estimating the bulge mass are used. For example, the Häring & Rix obtained consistent results with those of Marconi & Hunt (2003) who used virial bulge masses. Under the assumption that in the bulge the motions of the stars are predominately random, the bulge dynamical mass can be computed as

$$M_{\mathrm{bulge,\,dyn}} = \kappa \frac{r_e\,\sigma_*^2}{G},$$

(5.7)

where $\kappa = 8/3$ would be used if bulges are considered as isothermal spheres. However dynamical modeling (e.g., Magorrian et al. 1998) indicates that $\kappa = 3$ gives a better agreement between the two methods. Further, Cappellari et al. (2006) showed that κ is a function of the Sersic index and that using an average value of $\bar{\kappa} = 5$, the estimations of $M_{\mathrm{bulge,\,dyn}}$ are within 0.10 dex. Other way to estimate the bulge mass is through the M/L ratio. Using Eqs. (4.8) and (4.10), as shown previously, gives a mass estimate that depends on the stellar initial mass function employed to calibrate the M/L relation, which in this case is assumed to be 'diet' Salpeter IMF (see Sect. 4.4.2, page 78).

Figure 5.6 shows the relations found by Sani et al. (2011) between the black hole mass and the bulge mass calculated with the the two methods: $M_{\mathrm{bulge,\,dyn}}$, and that

from the M/L ratio, which they represent as M_{star}. The photometry of the sample is from the Spitzer/IRAC database at $3.6\,\mu$m. The photometric parameters and the M/L calibration are performed at that wavelength. Here, it is assumed that the HK-band photometry and calibration give M_{bulge} values consistent with those at $3.6\,\mu$m. The positions of IRAS 01072+4954 in the plotted correlations correspond to its dynamical mass $M_{\mathrm{bulge,\,dyn}} = 2.00 \times 10^8\,\mathrm{M_\odot}$, calculated from Eq. (5.7) using the average effective radius in H- and K-bands, and assuming $\kappa = 5$ as in Sani et al. (2011); and to its stellar mass calculated in each band: $M_{\mathrm{star},\,H} = 1.39 \times 10^9\,\mathrm{M_\odot}$ and $M_{\mathrm{star},\,K} = 2.37 \times 10^9\,\mathrm{M_\odot}$.

Sani et al. (2011) distinguish in the plots between bulges and pseudobulges (Fig. 5.6). No significant difference can be recognized between the two samples in the selected mass range. They relations fitted to the whole group of galaxies are

$$\log\left(M_{\mathrm{BH}}\right) = 8.20 + 0.79\left[\log(M_{\mathrm{bulge,\,dyn}}) - 11\right], \tag{5.8}$$

$$\log\left(M_{\mathrm{BH}}\right) = 8.16 + 0.79\left[\log(M_{\mathrm{bulge,\,star}}) - 11\right], \tag{5.9}$$

where all masses are measured in $\mathrm{M_\odot}$ and the intrinsic scatter is $\sim 0.35\,\mathrm{dex}$.

Like IRAS 01072+4954, all pseudobulges seem to have smaller $M_{\mathrm{bulge,\,dyn}}$ than those derived from their luminosities $M_{\mathrm{bulge,\,star}}$ – in the case of IRAS 01072+4954,
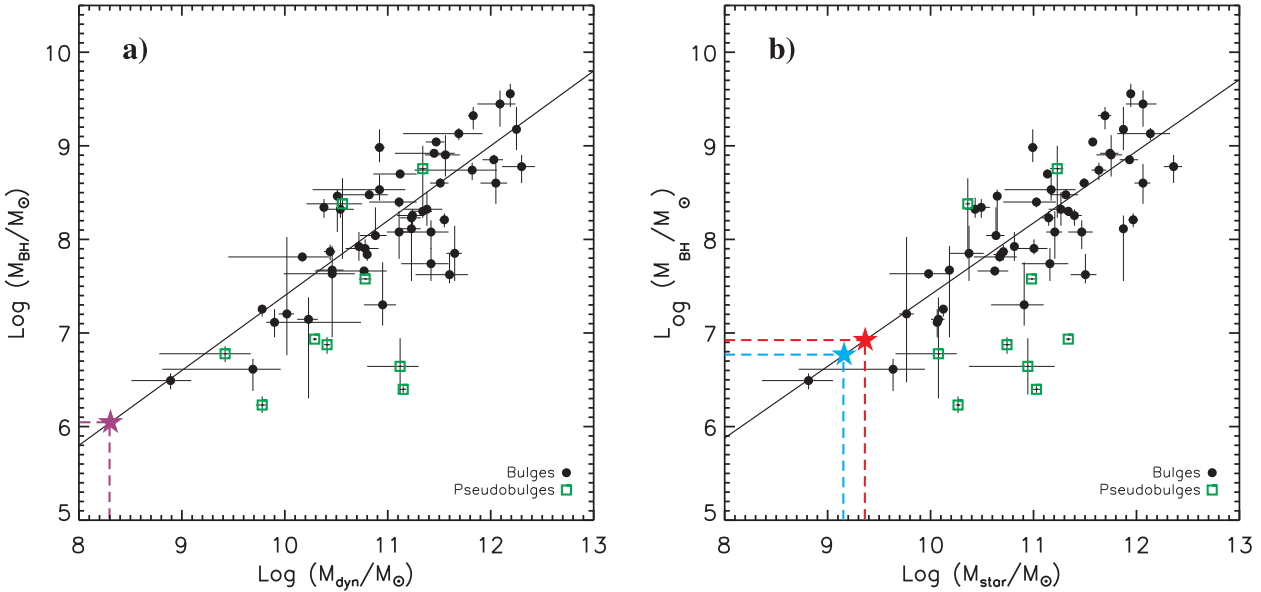
Figure 5.6: Black hole mass vs. bulge mass relation. *Left:* M_{BH} vs. $M_{\mathrm{bulge,\,dyn}}$. The purple star represents the position of IRAS 01072+4954 if given its $M_{\mathrm{bulge,\,dyn}}$, calculated using the average effective radius in the NIR, it lies on the fitted relation. *Right:* M_{BH} vs. $M_{\mathrm{bulge,\,star}}$. The cyan and red stars are the positions of the IRAS 01072+4954 on the fitted correlation, derived from its H- and K-band bulge luminosities, respectively. Bulges are marked with filled circles, and pseudobulges with open squares. Modified from: Sani et al. (2011)

the difference is about one order of magnitude. This might indicate that their bulges are by a non-negligible fraction rotationally supported. Following the relations of Sani et al. (2011), IRAS 01072+4954 black-hole mass estimated with the bulge dynamical mass is $\log(M_{\mathrm{BH}}/\mathrm{M}_\odot) = 6.08$ and with the H- and K-band luminosities, $\log(M_{\mathrm{BH}}/\mathrm{M}_\odot) = 6.69$ and $\log(M_{\mathrm{BH}}/\mathrm{M}_\odot) = 6.88$, respectively.

5.3.4 Black hole mass vs. Stellar velocity dispersion relation

First, I describe the technique employed to fit the line of sight velocity distribution to a K-band aperture with the radius $r \approx 160\,\mathrm{pc}$, that corresponds to the fitted bulge effective radius. Then, I determine the black hole mass from the M_{BH} vs. stellar velocity dispersion σ_* correlation.

Line of sight velocity distribution

I derive the line-of-sight velocity distribution (LOSVD) of the stars in the photometric bulge, by fitting a set of high spectral resolution stellar templates to the spectrum integrated over an aperture of $r \approx 0.34''$, which corresponds to the scale radius of the bulge found above. We assume that the stellar LOSVD can be described by a truncated Gauss-Hermite series parametrized by the radial velocity V, the velocity dispersion σ_*, and coefficients of the third and fourth Hermite polynomials h_3 and h_4. The deep and narrow CO absorption features at $2.294\,\mu$m and $2.323\,\mu$m indicate that the velocity dispersion of the stars in the bulge is low. This implies that, despite the high spectral resolution of the NIFS data, it is not possible to constrain significantly all the LOSVD parameters simultaneously (Cappellari & Emsellem 2004). In this cases, one would like to bias the solution towards the pure Gaussian one and, in that way, avoid the coupling of the parameters, V with h_3 and σ_* with h_4. The penalized pixel fitting routine (pPXF) of Cappellari & Emsellem (2004) applies such procedure, allowing to recover the LOSVD in moderately low signal-to noise (S/N) and/or undersampled data. This routine minimizes the difference between the galaxy spectrum and the combination of the stellar templates convolved with the LOSVD. The algorithm allows different weights of the stellar templates.

The pPXF routine is sensitive to template mismatch and therefore one has to select the templates to closely match the galaxy spectrum. In our case, the stellar templates were taken from the Gemini spectroscopic library of NIR stars observed with the NIFS IFU in K-band, because of the need for high spectral resolution (Winge et al. 2009). The library contains 11 giant and supergiant stars with stellar types from G8 to M5. When using the full library as an input of the pPXF routine the quality of the fit was not good and the velocity dispersion ($\sigma_* = 64.0\,\mathrm{km\,s^{-1}}$) was clearly overestimated (Fig. 5.7). Therefore, I selected a sub-sample of objects whose absorption features better resemble the HK-band continuum of the galaxy. For this selection, I used the medium-resolution ($R \sim 2000 - 3000$) NIR library of Ivanov et al. (2004), given the lack of high-resolution H-band templates. I compared the HK spectra of all the stars that have the same spectral type as those of the
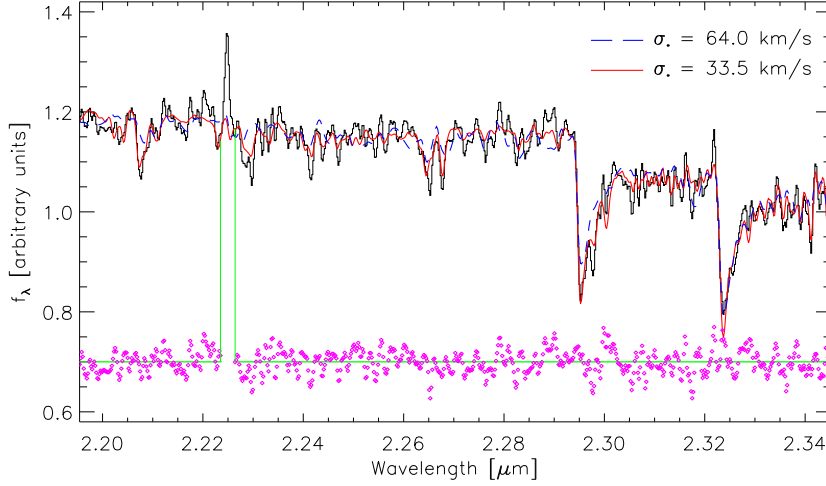
Figure 5.7: Fit of the stellar kinematics of the K-band spectrum integrated over an aperture $r = r_e = 160\,\mathrm{pc}$. The observed spectrum is shown as a thin solid line. Two different fits to the data are shown: one obtained when using the whole stellar NIFS library (blue dashed line) and the other with the selected NIFS stellar templates (red solid line). Small spectral regions with emission or spurious lines were masked and are marked by the vertical lines. The residuals shown at the bottom with points are shifted vertically for clarity.

Gemini library with the galaxy-continuum spectrum and discarded the objects with stellar type earlier than K2. The sub-sample consisted of 7 stellar spectra of the following types: K2III, K5Ib, K5II, K5III, M2III, M3III and M5III.

For the fitting procedure, spectral regions with emission lines and residuals of sky lines were masked. Figure 5.7 shows the best fit of the LOSVD to the galaxy bulge spectrum using the parameters: $V = (-17.1 \pm 1.6)\,\mathrm{km\,s^{-1}}$, $\sigma_* = (33.5 \pm 3.7)\,\mathrm{km\,s^{-1}}$, $h_3 = 0.059 \pm 0.046$ and $h_4 = 0.011 \pm 0.076$. The fit was obtained after adopting a bias $= 0.5$ and the addition of a Legendre polynomial of degree 10. In a conservative approach, the errors were calculated via Monte Carlo simulations, where 1000 realizations of an input spectrum were fitted with the pPXF routine without any penalization (bias $= 0.0$). The input spectrum was created by convolving a stellar template with the LOSVD and adding Poisson noise to the level of the galaxy spectrum, in this case, to reach $S/N \sim 40$. Then, the effects of undersampling were simulated allowing the velocity scale ($\mathrm{km\,s^{-1}}$ per pixel) of the input spectrum to vary in such a way that the second moment of the LOSVD, found by fitting the spectrum with the pPXF routine, varied in the range $\sim 14 - 140\,\mathrm{km\,s^{-1}}$. Given the moderate S/N of the data and that σ_* is low compared to the velocity scale (less than two pixels), the higher moments h_3 and h_4 of the LOSVD suffer from large uncertainties. Fitting only the first two moments one obtains $V = -16.1\,\mathrm{km\,s^{-1}}$ and $\sigma_* = 32.9\,\mathrm{km\,s^{-1}}$, which agree with the values found previously within the estimated errors.

Estimating the black hole mass

The black hole mass vs. stellar velocity dispersion relation has been predicted by simple theoretical models of self-regulated black hole-galaxy host growth. According to Silk & Rees (1998), during the galaxy formation process, a black hole with mass higher than

$$M_{\mathrm{BH}} = \frac{f_{\mathrm{gas}}}{f_w} \frac{\sigma_T}{2\pi \, G^2 \, m_p \, c} \, \sigma_*^5 \qquad (5.10)$$

could expel a fraction of the galaxy's gas mass F_{gas} out of the galaxy via energy-driven wind emitted at some fraction of its Eddington luminosity f_w. In the expression above, σ_T is the Thomson cross section and m_p is the proton mass. On the other hand, for a momentum-driven wind $M_{\mathrm{BH}} \propto \sigma_*^4$ is expected.

The first observational estimations of the $\log(M_{\mathrm{BH}}) = \alpha + \beta \log(\sigma_*)$ relation indicated $\beta = 5.27$ (Ferrarese & Merritt 2000), and $\beta = 3.75$ (Gebhardt et al. 2000) with somewhat large scatter. For inactive galaxies, the slope was settled on $\beta = 4.02$ (Tremaine et al. 2002).

Lately two updates to the Tremaine relation were published. Using the correlation parameters found by Gültekin et al. (2009, their Eq. (3)), for IRAS 01072+4954 one obtains $M_{\mathrm{BH}} = (0.68^{+0.97}_{-3.98}) \times 10^5 \, \mathrm{M_\odot}$. Whereas with the fit parameters of Graham et al. (2011, their Table 2.) the black hole mass reduces to $M_{\mathrm{BH}} = (3.41^{+6.18}_{-2.20}) \times 10^3 \, \mathrm{M_\odot}$. The intrinsic rms scatter in both cases is $\sim 0.4 \, \mathrm{dex}$. In the former case, $\beta = 4.24$, while in the latter $\beta = 5.3$. This means that observations still can not help on discriminating between the theoretical models.

Whether or not AGN follow the same correlation is still not clear. Several authors have pointed out that the M_{BH} - σ_* relation in AGN might have a different slope (Greene & Ho 2005; Woo et al. 2010; Xiao et al. 2011). With the Xiao et al. fit parameters, IRAS 01072+4954 black hole mass is $M_{\mathrm{BH}} = (1.43^{+1.13}_{-0.64}) \times 10^5 \, \mathrm{M_\odot}$.

5.3.5 Validity of the scaling relations for low-mass black holes

Table 5.3 summarizes the black hole mass estimations derived before. These M_{BH} estimations differ by about one or two orders of magnitude. Table 5.3 shows that while some correlations indicate $M_{\mathrm{BH}} \sim 10^{6.5} \, \mathrm{M_\odot}$, others agree with $M_{\mathrm{BH}} \sim 10^5 \, \mathrm{M_\odot}$. After a careful revision of every relation, it is clear that some of them are not suitable at the low-mass end, and another one can only provide an upper limit given the measurements used to construct the relation. In the following, I will discuss the validity of the used correlations and argue that most likely IRAS 01072+4954 hosts an intermediate mass black hole[3] (IMBH) of $M_{\mathrm{BH}} \sim 10^5 \, \mathrm{M_\odot}$.

---

[3]This expression is used in the context of the extragalactic black holes for those with $M_{\mathrm{BH}} < 10^6 \, \mathrm{M_\odot}$. It is probably a term that should be replaced in the literature by low-mass black-holes (low-M_{BH}), given that there is no physical – only terminologically arbitrary – distinction between intermediate and supermassive black holes.

Table 5.3: Black hole mass estimates of the SMBH at the center of IRAS 01072+4954 derived from scaling relations

$\log\left(\frac{M_{\mathrm{BH}}}{\mathrm{M}_\odot}\right)$	Notes on the applied scaling relation	Ref.
	$M_{\mathrm{BH}} - L_{\mathrm{bulge}}$	
6.40^a	27 bright, mainly ellipticals. K-band luminosity.	1
6.01^a	27 bright, mainly ellipticals. H-band luminosity.	1
6.82^a	22 bright objects.	2
5.54	Bending the Eq.(14) of Graham (2007).	3
	$M_{\mathrm{BH}} - n$	
5.77	27 objects. Quadratic relation.	4
	$M_{\mathrm{BH}} - M_{\mathrm{bulge}}$	
6.08^a	47 sources. Dynamical bulge mass.	5
6.88^a	47 sources. K-band stellar bulge mass.	5
6.69^a	47 sources. H-band stellar bulge mass.	5
4.95	40 sources. Broken relation.	6
	$M_{\mathrm{BH}} - \sigma_*$	
4.83	49 sources + 18 upper limits.	7
6.83^a	8 + 11 upper limits barred galaxies.	7
3.53	64 sources.	8
3.75	20 barred galaxies.	8
5.10	155 low-M_{BH} sources.	9
4.61	25 low-M_{BH} barred galaxies.	9

[a] Not suitable in the case (see text).

References. (1) Marconi & Hunt (2003); (2) Graham (2007); (3) Valencia-S et al. (2012); (4) Graham & Driver (2007); (5) Sani et al. (2011); (6) Graham (2012a); (7) Gültekin et al. (2009); (8) Graham et al. (2011); (9) Xiao et al. (2011).

M_{BH} vs. L_{bulge} relation

Although the about 10% maximum bulge luminosity overestimation – because of the imprecise data overlap and the neglected bar-like component – and the scatter of the $M_{\mathrm{BH}} - L_{\mathrm{bulge}}$ correlation bring the estimated M_{BH} value to an agreement with that found though the $M_{\mathrm{BH}} - \sigma_*$ relation, the scaling relation with the bulge luminosity is not suitable in the case of low-M_{BH} (A. Graham, private communication, also Graham 2012a). The reason is that the M_{BH} vs. L_{bulge} relation has been calibrated using mainly bright (elliptical) galaxies, also called 'core galaxies', with $M_{\mathrm{BH}} > 10^7\,\mathrm{M}_\odot$. Elliptical galaxies show a bimodality in their photometric param-

eters that depends on the luminosity and might extend to disk galaxy bulges (see e.g., Kormendy et al. 2009). This dichotomy seems to be related with the merger history of the galaxies – i.e., bright core galaxies are a result of dry merger events, while fainter spheroids might form via wet merging – and could imply different M_{BH} - L_{bulge} relations for both kind of systems (Graham 2012a).

Core galaxies follow a bulge luminosity − stellar dispersion relation of the form $L_{\mathrm{bulge}} \propto \sigma_*^5$ and their $M_{\mathrm{BH}} \propto L_{\mathrm{bulge}}^1$, probably as a result of a dry merging formation process (Graham 2012b; see also Kormendy et al. 2009). In contrast, fainter galaxies ($M_B > -20.5\,\mathrm{mag}$) follow $L_{\mathrm{bulge}} \propto \sigma_*^2$ and $M_{\mathrm{BH}} \propto \sigma_*^5$. Therefore a relation of the form $M_{\mathrm{BH}} \propto L^{2.5}$ is expected. Given the lack of studies that investigate the $M_{\mathrm{BH}} - L_{\mathrm{bulge},\,K}$ in such systems, I made the simple exercise of bending the known $M_{\mathrm{BH}} - L_{\mathrm{bulge},\,K}$ relation (Graham 2007, his Eq. (14)) at $\sim 7 \times 10^7\,\mathrm{M_\odot}$ assuming the predicted proportionality. The relation I obtained was

$$\log\left(\frac{M_{\mathrm{BH}}}{\mathrm{M_\odot}}\right) = 2.5 \log\left(\frac{L_{\mathrm{bulge},\,K}}{\mathrm{L_{\odot},K}}\right) - 18.23. \qquad (5.11)$$

When applying it to the IRAS 01072+4954 K-band luminosity, the estimated black hole mass $3.5 \times 10^5\,\mathrm{M_\odot}$ gets in a better agreement with the other M_{BH} estimates.

M_{BH} vs. M_{bulge} relation

Graham (2012a, his Fig. 1) showed that the M_{BH} vs. bulge/spheroid mass relation might also be a broken power law (see also Graham 2012b). As mention before, massive elliptical galaxies might have been formed by mayor dry merging events. At the high mass-end of the black hole population this process involves most probably only two galaxies with similar $M_{\mathrm{BH}}/M_{\mathrm{bulge}}$. Provided that during these merging events there were no significant gravitational ejections, the combined black hole mass and that of the galaxy must increase in parallel, this means $M_{\mathrm{BH}}/M_{\mathrm{bulge}} \sim \mathrm{const}$.

On the other hand, in Sersic galaxies $L_{\mathrm{bulge}} \propto \sigma_*^2$, which implies that $M_{\mathrm{bulge}} \propto \sigma_*^2(M_{\mathrm{bulge}}/L_{\mathrm{bulge}})$. For these systems $(M_{\mathrm{bulge}}/L_{\mathrm{bulge}}) \propto L_{\mathrm{bulge}}^{1/4}$, therefore a relation of the form $M_{\mathrm{BH}} \propto M_{\mathrm{bulge}}^2$ is expected. Figure 5.8, modified from Graham (2012a), shows the broken nature of the $M_{\mathrm{BH}} - M_{\mathrm{bulge}}$ relation, while the $M_{\mathrm{BH}} - \sigma_*$ remains the same for core and Sersic galaxies. These relations were not defined particularly for barred or pseudobulge galaxies, however in the case of IRAS 01072+4954 they seem to provide consistent estimates. Notice that in these plots, IRAS 01072+4954 has not been intentionally located on the correlations, but its measured M_{bulge} − calculated using the luminosity estimates, because the main stellar motion in the bulge is rotational, invalidating the usage of Eq. (5.7) − , its σ_* and the averaged black hole mass estimates $\log(M_{\mathrm{BH}}/\mathrm{M_\odot}) \sim 5.0 \pm 0.25$, have been used instead.

M_{BH} vs. σ_* relation for barred galaxies

Recently Gültekin et al. (2009) and Graham et al. (2011) have recalibrated the $M_{\mathrm{BH}} - \sigma_*$ relation. The former group used 49 objects and 18 upper limits, and
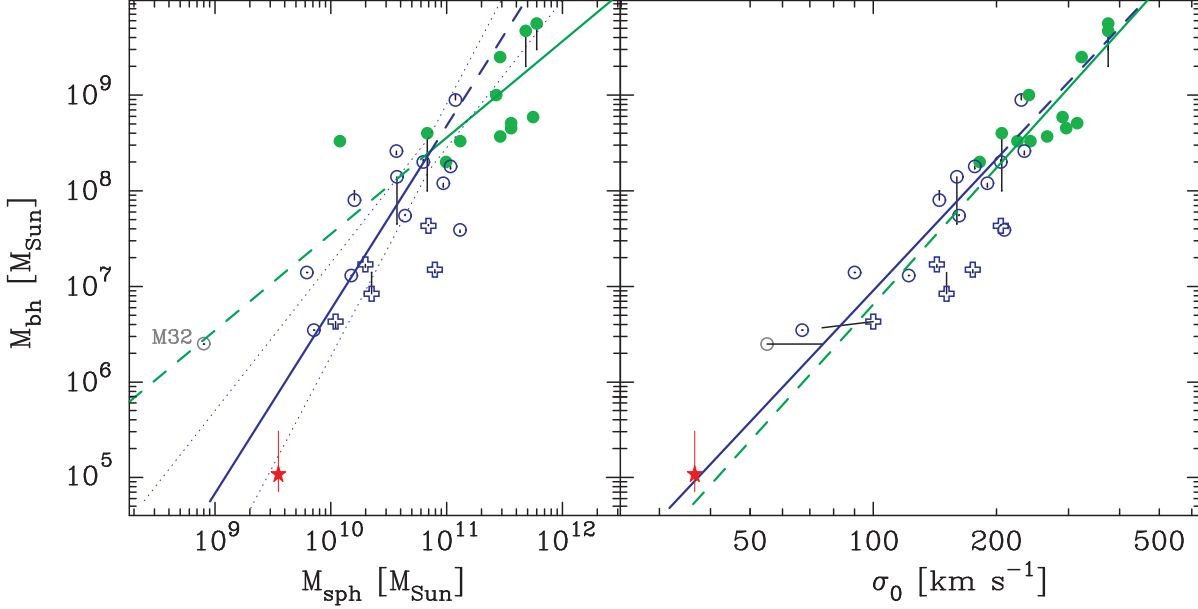
Figure 5.8: *Left:* Black hole mass vs. bulge/spheroid mass relation. *Right:* Black hole mass vs. stellar velocity dispersion relation. 'Core' galaxies are shown as green filled circles, 'Sersic' galaxies as empty blue circles, and barred systems as blue crosses. The relations for core and Sersic galaxies are shown in solid lines of the corresponding color, and the extrapolations of them beyond $M_{sph} = 7 \times 10^{10}\,M_{\odot}$ are plotted in dashed lines. Dotted lines in the left panel correspond to 1σ uncertainty of the relation for Sersic galaxies. The positions of IRAS 01072+4954, marked with red stars, are defined by its bulge mass calculated via the (M/L) ratio, its measured velocity dispersion, and the averaged black hole mass estimation from scaling relations, to which an uncertainty of $\sim 2.5\,\mathrm{dex}$ was arbitrarily assigned. Modified from: Graham (2012a).

the latter 64 objects, with reliable parameter estimations. Also Xiao et al. (2011) studied this relation, focusing on low-M_{BH} sources. I evaluate the black hole mass using the relation they obtained for their whole samples and for barred galaxies only. The results, reported in Table 5.3, are in agreement with $\log(M_{BH}/\,M_{\odot}) < 6$, with the exception of that calculated from the relation found by Gültekin et al. (2009) for barred galaxies.

When looking at the location of the barred galaxies in the M_{BH} vs. σ_* diagram presented by Gültekin et al. (their Fig. 1), the 8 galaxies with dynamically detected black holes lie well within the scatter of the correlation depicted by the full sample (49 sources). Nevertheless, the barred-galaxies relation has a slope of 1.08 ± 0.75, while that of the whole sample is 4.24 ± 0.41. This yields in the case of IRAS 01072+4954 a difference of two orders of magnitude. It is intriguing that although the authors assign a probability of 0.1809 to the case of the barred-sources not having a black hole, compared to the full sample whose probability is 0.0004, the barred-galaxies relation has the smallest scatter and the error in the parameters is also small. I think that it is possible to conclude that the difference between the two M_{BH} estimations is introduced by the inclusion of the upper limits to the

fit which, in the case of the barred galaxies, dominate the subsample. Therefore, I do not consider that black hole mass estimation obtained from this relation as reliable.

On the other hand, pseudobulges and barred galaxies seem not to follow the scaling relations defined by ellipticals and classical ($n \sim 4$) bulges. Pseudobulges appear to lie below both correlations (e.g., Jiang et al. 2011; Kormendy & Bender 2011, but also Graham 2011), while barred galaxies have a larger scatter around them (Hu 2008; Graham 2008; Gültekin et al. 2009; Graham et al. 2011) or follow a steeper relation (Xiao et al. 2011). It is not clear whether IRAS 01072+4954 has a pseudobulge. The low Sersic index of the profile is an indication of it, but it is not enough evidence and the stellar kinematics do not offer conclusive results.

The presence of a bar-like structure is revealed by the photometry and by an increment up to $\sim 50 \, \mathrm{km \, s^{-1}}$ of the stellar velocity dispersion at P.A. $\sim 100°$, while everywhere else in the central $r < 500 \, \mathrm{pc}$, σ_* remains constant at $\sim 35 \, \mathrm{km \, s^{-1}}$ (see Figs. 6.5 and 6.6). This value is consistent with the velocity dispersion found here for the bulge. For that reason, and given the faintness of this structure, it seems that not accounting for it does not change significantly the results – as can be seen by the good agreement between the M_{BH} values estimated from different relations in Table. 5.3.

5.4 The accretion disk

Accretion is the most efficient way to extract energy from matter. Matter infalling onto a black hole sets up in a disk where it inspirals in toward the center while it loses part of its rest-mass energy and angular momentum. In the case of radiatively efficient cooling, the fraction of mass inflow converted to radiation can be expressed as $L_{\mathrm{disk}} = \eta \dot{M} c^2$, where $\eta \sim 0.05 - 0.42$ is the radiation efficiency, which depends on the black hole spin. Observationally there is evidence of the presence of another radiation source in the vicinity of the black hole: the corona. Although it nature is still mysterious, its emission, partly up-scatter photons and partly synchrotron radiation, can be detected in the X-ray spectrum of stellar black holes and AGNs, and in some cases, it can be clearly distinguished from that of the accretion disk. The luminosity arising from the disk-corona system, called bolometric luminosity, is partially absorbed by the surrounding obscuring material and re-processed as infrared radiation. In the following, I use standard methods to estimate the bolometric luminosity of IRAS 01072+4954 accretion disk and the rate at which it accretes matter.

Bolometric luminosity

Fitting the broad-band spectrum of the source can provide a quite accurate determination of its bolometric luminosity L_{bol}. However, that requires high angular resolution observations of the nucleus, in order to isolate, as much as possible, the emission from the AGN. Given the lack of these measurements in other wavelengths

for IRAS 01072+4954, it is not possible to obtain a nuclear spectral energy distribution (SED). Another possibility is to applied a bolometric correction to the hard X-ray luminosity $L_{2-10\text{keV}}$. In other words, to utilize a theoretically calculated or an observationally fitted calibration factor to estimate its L_{bol} from the measured X-ray flux. Marconi et al. (2004) and Hopkins et al. (2007) have found relations for the bolometric correction as a function of luminosity, based on calculated and observed QSO SEDs, respectively. Using the Marconi et al. relation,

$$\log\left(\frac{L_{\text{bol}}}{L_{2-10\,\text{keV}}}\right) = 1.54 + 0.24\mathcal{L} + 0.012\mathcal{L}^2 - 0.0015\mathcal{L}^3, \qquad (5.12)$$

with $\mathcal{L} = \log(L_{\text{bol}} - 12)$, and luminosities measured in $L_{\odot}$, for IRAS 01072+4954 one obtaines $\log(L_{\text{bol}}/\,\text{erg s}^{-1}) = 42.45$. The bolometric luminosity found using the Hopkins et al. relation is consistent with this value within the ~ 0.1 scatter of both expressions.

However, Vasudevan & Fabian (2007) have shown that for Narrow-Line Seyfert 1 galaxies (NLSy1s) bolometric luminosities derived through bolometric corrections can differ significantly from the ones obtained via SED-fitting. Given the similarities of IRAS 01072+4954 with the NLSy1s, it is important to look at the possible deviations introduced by the application of that correction derived for a typical AGN population. In the sample of NLSy1s studied by Vasudevan & Fabian (2007), 6 out of 9 sources have fitted-SED bolometric luminosities higher – 2 sources the same within the errors, and 1 lower – than those estimated via the bolometric correction. Hence, in NLSy1s the L_{bol} obtained via bolometric correction might be underestimated, and in our source it can be considered as a possible lower limit.

Accretion rate

The dimensionless accretion rate is defined as $\dot{m} \equiv \dot{M}/\dot{M}_{\text{Edd}}$, with $\dot{M}_{\text{Edd}} = 2.4(0.1/\eta)(M_{\text{BH}}/10^8\,\text{M}_{\odot})\,\text{yr}^{-1}$. In cases when $\dot{m} \gtrsim 0.01$, it is possible to equate the accretion rate to the Eddington ratio $\lambda_{\text{Edd}} \equiv L_{\text{bol}}/L_{\text{Edd}}$. When $\dot{m} < 0.01$ the accreting fluid becomes radiatively inefficient and λ_{Edd} decreases more rapidly than $\dot{m}$. For example, in low-luminosity AGN (LLAGN) $\langle\lambda_{\text{Edd}}\rangle \lesssim 10^{-3}$ for Sy1s and $\sim 10^{-6}$ for Sy2s, LINERs and transition objects (for a review see e.g., Ho 2008).

This means that $L_{\text{bol}} \gtrsim 2.5 \times 10^{42}\,\text{erg s}^{-1}$ and that the central massive black hole in IRAS 01072+4954 is accreting at a high rate $\lambda_{\text{Edd}} \sim 0.2$ (assuming $M_{\text{BH}} \sim 10^5\,\text{M}_{\odot}$). Such a surprising result for a LLAGN is due to the fact that although its luminosity is low (typical for a LLAGN), its black hole mass is very low compared with classical AGN. The Eddington ratio obtained in this way agrees with the expected value of $\lambda_{\text{Edd}} = 0.30 \pm 0.05$ from the λ_{Edd} - Γ relation found by Shemmer et al. (2008) in unabsorbed, luminous radio-quiet AGN (Fig. reffig:lbol). Here, I used $\Gamma = 2.1$, which is the photon index of the power-law fitted to the X-ray spectrum (Panessa et al. 2005). The agreement between the values of the Eddington ratio found by these completely independent methods gives support to the finding that the black hole mass is of the order of $10^5\,\text{M}_{\odot}$.
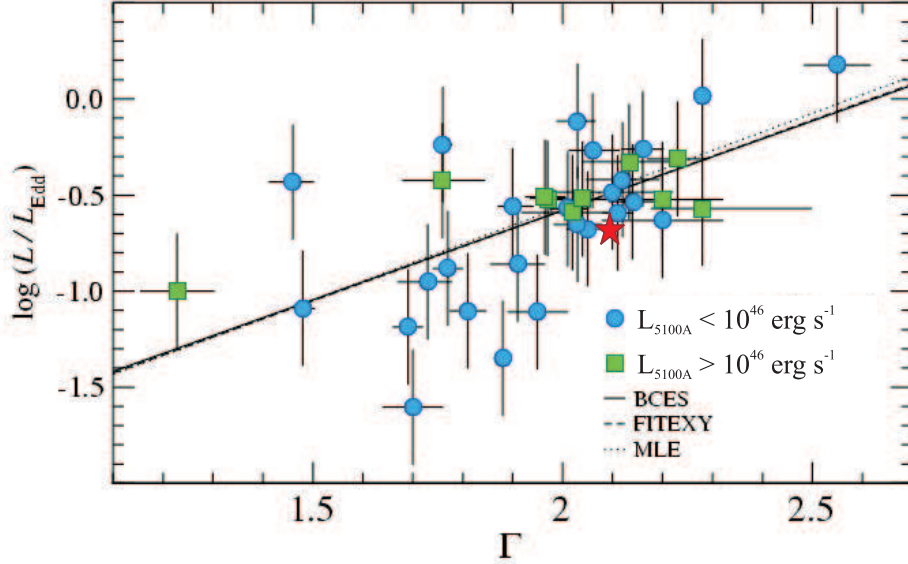
Figure 5.9: Eddington ratio vs. photon index relation. Circles mark sources at $z < 0.5$ with $L_{5100\,\text{Å}} < 10^{46}\,\text{erg}\,\text{s}^{-1}$ and squares luminous sources at $z = 1.3 - 3.2$ with $L_{5100\,\text{Å}} > 10^{46}\,\text{erg}\,\text{s}^{-1}$. Error bars are at the 1σ level. The solid, dotted and dashed lines correspond to the best-fit to the data found by different methods. In all cases the average scatter is $\sim 0.35\,\text{dex}$. The star shows the position of IRAS 01072+4954. Its photon index was calculated by Panessa et al. (2005) from Chandra data, and the Eddington ratio was estimated here using bolometric corrections applied to the hard X-ray flux. Modified from: Shemmer et al. (2008).

5.5   The broad line region

Does IRAS 01072+4954 have a broad line region (BLR)? The origin of the broad-line region is still not known. Theoretical works relate it with some sort of wind/outflow from the accretion disk (e.g., Murray et al. 1995; Elitzur & Shlosman 2006; Nicastro 2000; Elitzur & Ho 2009; Czerny & Hryniewicz 2011). Models associate the production of such wind with the bolometric luminosity of the accretion disk L_{bol}, the mass of the black hole M_{BH} and the accretion rate $\dot{m}$. In this section I use the derived black hole mass and bolometric luminosity to deduce the properties of the expected broad line region (BLR). I show some indications for the predicted broad line emission in our data, I also present other possibilities for the origin of the emission feature observed at the position of Brγ.

Observational limit

Despite the fact that near infrared (NIR) observations are less affected by dust obscuration and even though NIFS mapped the galaxy nucleus at high angular resolution, a classical broad component with a full width half maximum $\text{FWHM}_{\text{broad}} \gtrsim 2\,000\,\text{km}\,\text{s}^{-1}$ was not detected in the spectrum. The median width

of the strong emission lines is FWHM $\sim 80\,\mathrm{km\,s^{-1}}$ (see Table 4.2). The criteria for the detection, at 3 times the level of the noise σ, of the broad component of a line at wavelength λ can be written as

$$\frac{F_{\mathrm{broad},\lambda}}{3\sigma\sqrt{\mathrm{FWHM}_{\mathrm{broad},\lambda}^2 - \Delta\lambda^2}} > 1\,, \qquad (5.13)$$

where $\Delta\lambda$ is the spectral resolution of the instrument and $F_{\mathrm{broad},\lambda}$ is the flux of the broad line, which is assumed to be a Gaussian with a width of $\mathrm{FWHM}_{\mathrm{broad},\lambda}$. So, in our data the minimum flux that the broad-Brγ component should have to be detected is

$$\frac{F_{\mathrm{broad,Br\gamma}}}{\mathrm{erg\,s^{-1}\,cm^{-2}}} = 1.8 \times 10^{-19}\,\sqrt{\mathrm{FWHM}_{\mathrm{broad,Br\gamma}}^2 - (56.7)^2}, \qquad (5.14)$$

with $\mathrm{FWHM}_{\mathrm{broad,Br\gamma}}$ measured in $\mathrm{km\,s^{-1}}$. Assuming a $\mathrm{FWHM}_{\mathrm{broad},\lambda} = 2200\,\mathrm{km\,s^{-1}}$ – which is the median value for the sample of Ho et al. (1997b) – for the broad emission lines, Eq. (5.13) implies that a Brγ broad component would be detectable if it were about two times brighter than the observed narrow one; as a reference, the flux of the reddening-corrected Brγ line is $\simeq 2.1 \times 10^{-16}\,\mathrm{erg\,s^{-1}\,cm^{-2}}$.

Properties of the predicted broad-line region

If IRAS 01072+4954 behaves as other AGN, it must have a BLR. In the following, I will assume that the properties of the BLR scale with the luminosity as has been shown for black holes with higher masses (e.g. Netzer & Laor 1993; Kaspi et al. 2000; Bentz et al. 2009) to derive the observationally expected fluxes and widths of the broad lines.

From the Kaspi et al. (2000) relation, with the updated values of Bentz et al. (2009), I estimated the size of the BLR to be $R_{\mathrm{BLR}} \sim 1$ light-day, equivalently $\sim 10^{-3}\,\mathrm{pc}$ or $\sim 10^5\,\mathrm{R_S}$ (where $\mathrm{R_S} \equiv 2GM_{\mathrm{BH}}/c^2$ is the Schwarzschild radius of the black hole). The uncertainty is around 1 order of magnitude, mainly due to the error of the zero-point of the correlation. Such R_{BLR} is expected from the specific luminosity at 5100Å, $L_{5100} \approx 1.3 \times 10^{41}\,\mathrm{erg\,s^{-1}}$, which was estimated from the bolometric luminosity.

In Seyferts and QSO, the strength of the hydrogen recombination lines scales with the X-ray luminosity (e.g., Kriss et al. 1980; Ward et al. 1988). The total Hα flux (narrow+broad components, when present) of LINERS and LLAGN compared with their X-ray fluxes (soft and hard X-rays) seem to follow the same trend (e.g., Koratkar et al. 1995; Terashima et al. 2000; Ho et al. 2001), suggesting that they could be scaled-down versions of more massive and powerful AGN. Recently, Stern & Laor (2012) studied the relation between the broad Hα emission and the luminosity in a sample of about 3600 type 1 AGN selected from the Sloan Digital Sky Survey, with Hα luminosities in the range $7 \times 10^{39}\,\mathrm{erg\,s^{-1}}$ to $10^{44}\,\mathrm{erg\,s^{-1}}$. They

found that the luminosity of the broad Hα component is related to the specific luminosity at $2\,\mathrm{keV}$ as

$$\log\left(\nu L_{2\,\mathrm{keV}}\right)) = 0.45 + 0.79\,\log\left(L_{\mathrm{broad,H\alpha}}\right), \tag{5.15}$$

where both luminosities are in units of $10^{42}\,\mathrm{erg\,s^{-1}}$. Moreover, assuming that the BLR emitting clouds are virialized ($\mathrm{FWHM}^2 \propto M_{\mathrm{BH}}/R_{\mathrm{BLR}}$; e.g., Laor 1998; Netzer 2009), the authors found that the characteristic parameters of the emitted broad Hα line, i.e. $\mathrm{FWHM}_{\mathrm{broad,H\alpha}}$ and luminosity, are related to the black hole mass through

$$\begin{aligned}
\log\left(\frac{M_{\mathrm{BH}}}{\mathrm{M_\odot}}\right) =\,&7.40 + 2.06\,\log\left(\frac{\mathrm{FWHM}_{\mathrm{broad,H\alpha}}}{1000\,\mathrm{km\,s^{-1}}}\right) \\
&+ 0.545\,\log\left(\frac{L_{\mathrm{broad,H\alpha}}}{10^{44}\,\mathrm{erg\,s^{-1}}}\right),
\end{aligned} \tag{5.16}$$

with a dispersion of $\sim 0.25\,\mathrm{dex}$. Using these expressions, the expected flux of the broad Hα line is $F_{\mathrm{broad,H\alpha}} \simeq 4.8 \times 10^{-14}\,\mathrm{erg\,s^{-1}\,cm^{-2}}$ with a width of $\mathrm{FWHM}_{\mathrm{broad,H\alpha}} \simeq 435\,\mathrm{km\,s^{-1}}$. If on the other hand, the relation $L_{\mathrm{broad,H\alpha}} \approx L_{\mathrm{bol}}/130$, which was also proposed by Stern & Laor (2012), is used then the expected values are $F_{\mathrm{broad,H\alpha}} \simeq 1.7 \times 10^{-14}\,\mathrm{erg\,s^{-1}\,cm^{-2}}$ and $\mathrm{FWHM}_{\mathrm{broad,H\alpha}} = 600\,\mathrm{km\,s^{-1}}$.

Whether or not such a component is present in the optical spectrum (see Moran et al. 1996, their Fig. 5) is not clear. Although their spectral resolution ($\sim 200\,\mathrm{km\,s^{-1}}$) is sufficient to measure such a width, the data covers an area of $\sim (2 \times 1)\,\mathrm{kpc}^2$ on source and the Hα line is blended at the base with the neighboring [N II] lines. Can we see in our observations broad lines with those properties? In the NIFS data, the strongest recombination line is Brγ. I assumed $\mathrm{FWHM}_{\mathrm{broad,Br\gamma}} \simeq \mathrm{FWHM}_{\mathrm{broad,H\alpha}}$ and $F_{\mathrm{broad,Br\gamma}} \approx F_{\mathrm{broad,H\alpha}}/100$ to scale the BL properties in the two bands. Note that, formally, the theoretical case-B is not a pplicable (however see Rhee & Larkin 2000; Zhou et al. 2006; Kim et al. 2010); nevertheless I used it as a first approximation. According to Eq. (5.13) the detection of such a broad Brγ emission is around the limit of our instrumental capabilities. Looking in the NIFS K-band central spectrum for indications of a broad line of that characteristics, it is possible to discover a 'broader' feature around the position of the BRγ line. Fig. 5.10 shows a zoom around $2.166\,\mu\mathrm{m}$ where in the left and right panels, one (only narrow) and two (narrow and broad) simple Gaussian components, respectively, were fitted to the data. In the second case, the broad component has a $\mathrm{FWHM}_{\mathrm{broad,Br\gamma}} \simeq 420\,\mathrm{km\,s^{-1}}$ and $F_{\mathrm{broad,Br\gamma}} \simeq 1.0 \times 10^{-16}\,\mathrm{erg\,s^{-1}\,cm^{-2}}$, with a peak shifted by $0.7 \times 10^{-3}\,\mu\mathrm{m}$.

To check the possibility of this component being a BL, or the tip of a BL, I performed several tests. I fitted the Brγ line with a two Gaussian components, to account for the narrow and the broad emissions, in every spatial pixel of the NIFS field of view. As a result, the broad component peaks and is wider at the center, while the narrow component peaks few pixels towards the north, at a position
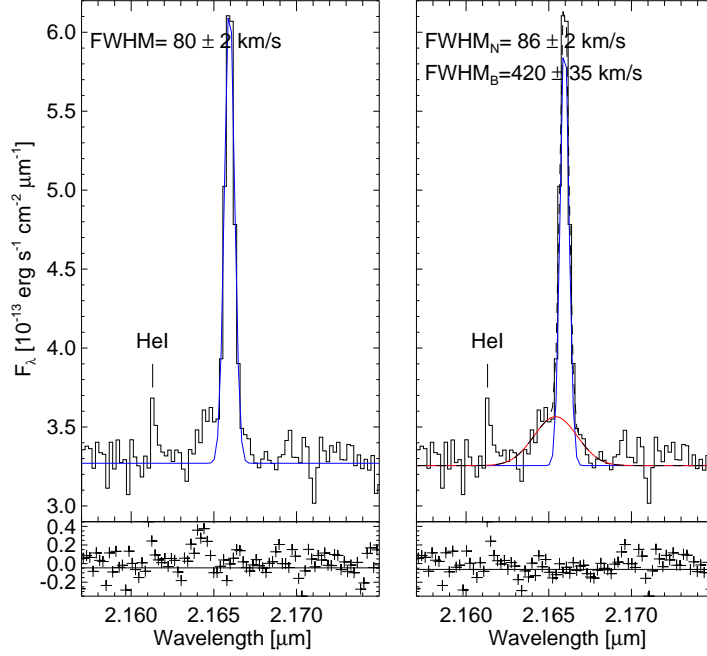
Figure 5.10: Fit of the Brγ line emission. A single Gaussian fitted to the data is shown in the left panel. The right panel shows the data fitted with two Gaussians, where the thin solid lines correspond to the individual components and the dashed line to the overall fit. The FWHM of the fitted lines are marked in each case. At the bottom of both panels the residuals of the individual fits are marked with crosses.

$\sim 100\,$pc away from the center at the redshift of the galaxy. However, that could be a result of the S/N, which increases towards the nucleus, so I took increasingly larger apertures and found that the FWHM of the 'broad' component decreases systematically with the aperture radius. On the other hand, if the feature observed around $2.166\,\mu$m originates in the BLR, it should not be present in the profile of forbidden lines like [Fe II]. Given that the densities in the BLR are higher than the critical densities under which forbidden lines form, both kinds of lines originate from spatially separated regions and are, therefore, kinematically de-coupled. When comparing the LOSVD of Brγ and [Fe II] emissions, using e.g. channel maps, I did not find similarities (see Sect. 6.3). A direct comparison between the Brγ and the [Fe II] line shapes at the nucleus is unfortunately not possible. The reason is that the continuum around the spectral position of the [Fe II] line $\lambda 1.644\,\mu$m cannot be determined accurately enough to recognize the presence of any faint 'broader' emission. The main drawbacks are the lack of spectral templates with high-spectral resolution in the H-band and the presence of strong features in the continuum around $\lambda 1.644\,\mu$m, such us the CO(7-4) absorption band starting at $\lambda 1.640\,\mu$m and a residual-sky line at $1.645\,\mu$m. In general, although the fitted flux

and width of the 'broad' Brγ component agree with the predicted ones, this result is not a firm detection ($S/N = 2.8$), but it is an interesting coincidence that allows us to speculate about the nature of the observed Brγ -'hump'. A confirmation of the existence of such faint BLs will require high-angular and high-spectral resolution observations of stronger lines like Paα or Paβ.

Other explanations for the emission at 2.16 μm

The presence of outflows in the NIR spectrum of Seyfert galaxies is traced by the [Fe II] emission (Blietz et al. 1994; Riffel & Storchi-Bergmann 2011b). In sources like NGC 4151 (Storchi-Bergmann et al. 2009), Mrk 1066 (Riffel & Storchi-Bergmann 2011a) and Mrk 1157 (Riffel & Storchi-Bergmann 2011b) the kinematics of the ionized gas is found to be consistent with previously observed radio emission of jet structures. In Sect 6.3.1 I show that in the inner ~ 250 pc of IRAS 01072+4954 the LOSVD of the [Fe II] emitting gas can be interpreted as an outflow with a line of sight velocity $V_{\rm LOS,[FeII]} \lesssim -60\,{\rm km\,s^{-1}}$. The kinematics of ionized-hydrogen (Brγ) is consistent with motion in a disk, but extra components cannot be discarded. To consider the possibility for the Brγ-'hump' to correspond to a blue-shifted emission from wind, I modeled the Brγ line with two narrow-Gaussian components, one for the observed line and the other for the blue-shifted wing. Although the quality of the fit is good, the resulting shift of the wing-component is $\sim -180\,{\rm km\,s^{-1}}$ which would represent a clear deviation from the disk-profile that is not observed. When mapping the two thin components across the field of view, the velocity field of the blue-shifted component – that represents the Brγ-'wind' – does not follow the LOSVD of the [Fe II], which argues against an outflow as the origin of the Brγ-'hump'.

Another possibility is the presence of a blended emission from other species close to Brγ. Given that He I$\,(2{\rm s}^1{\rm S} - 2{\rm p}^1{\rm P}^0)$ is also detected at 2.0587 μm, I looked for other helium emission lines within 0.002 μm around 2.1661 μm (the resolution of the instrument at that wavelength is $\sim 4 \times 10^{-4}$ μm). Theoretically, two helium lines could be there: He II (14-8) at 2.1653 μm and He I (4-7) at 2.1660 μm. The latter one is impossible to resolve out of Brγ in case it is present. Of the former one, I calculated the maximum flux contribution based on the upper limit of the flux of the undetected He II (14-7) at 1.4882 μm. Using the recombination coefficients of Hummer & Storey (1987) assuming case-B, $T = 10^4$ K and $N_{\rm e} = 10^4\,{\rm cm^{-3}}$, one obtaines $F_{\rm HeII(14-8)} < 0.1 \times 10^{-16}\,{\rm erg\,s^{-1}\,cm^{-2}}$. This implies that a potential helium line could at maximum account for $\sim 10\%$ of the observed emission in the blue-shifted wing.

5.6 Hypotheses on the Seyfert 2 appearence

The X-ray emission of IRAS 01072+4954 is typical of Type 1 AGN. Moreover, the temperature of the hot dust at the center confirms that the AGN is exposed and therefore broad lines should be visible in the spectrum. Although broad

H I lines have not yet been detected in the optical, I showed in Sect. 5.5 that if IRAS 01072+4954 follows the same relations of Type 1 sources, it might have a very faint broad line region (BLR). However, given that the spectral resolution of the optical spectrum was good, and that Hα emission is expected to be ~ 100 times brighter than Brγ, it is still not clear whether the observed broad Brγ component is infact coming from the BLR, nor whether the AGN has a BLR at all. Given the enhanced star formation close to the nucleus, the $\sim 500\,\mathrm{km\,s^{-1}}$ 'broad' component might also be atributed to stellar winds originated by a nuclear central cluster. In the following, the main hypotheses of its Type 2 appearence are discussed.

5.6.1   Cold dust absorption

The obscuration of the BLR can be caused by galactic structures present at all scales from kiloparsecs down to parsecs (see e.g., Bianchi et al. 2012, and references therein). It has been shown, for example, that the orientation of a galaxy has an impact on the classification of its nuclear activity (Shen et al. 2010; Lagos et al. 2011). However, there is not a clear limit on the amount of obscuration necessary to hide a BLR. Here, I compare the extinction at the center of IRAS 01072+4954 with that from other Sy1 and Sy2 galaxies in order to find possible trends that allow to estimate the influence of cold dust on the observability of broad lines.

IRAS 01072+4954 is approximately face-on and no signatures of dust lanes crossing the line of sight to the nucleus are visible. To calculate the extinction toward the nucleus, Brγ and Br10 hydrogen recombination lines were used assuming a homogeneous scatter-free dust screen placed in front of the galaxy (for more details see Sect. 4.3). From the Eq.(4.5), I calculated a visual exitction $A_V = 2.5\,\mathrm{mag}$ in the central $r = 0.16''$ spectrum.

The measured A_V is consistent with the median value $\langle A_{V,\,\mathrm{Sy2}} \rangle = 1.64\,\mathrm{mag}$ of 27 Sy2 galaxies from the database of Ho et al. (1997a). In contrast, the median extinction of the 9 Sy1 sources of the same sample was $\langle A_{V,\,\mathrm{Sy1}} \rangle < 0.03\,\mathrm{mag}$ (Rhee & Larkin 2005). In any case, it is still not clear whether this difference between Sy1s and Sy2s is directly related to the obscuration of the BLR by cold dust, because in their study the extinction was determined from the optical Balmer decrement in apertures of $2'' \times 4.1''$, which map areas from a few pc^2 (in NGC 3031) to nearly $1\,\mathrm{kpc}^2$ (in NGC 1275). From a detailed comparison of the two types of Seyferts of the same dataset, Ho (2003) found differences in the electron densities of the emitting regions and in the environment of the host galaxies, which could somehow influence the previous result.

To get a better spatial correspondence to the region we are considering here ($r \approx 75\,\mathrm{pc}$), I selected from the literature sources observed with high angular resolution and with extinction measured in the NIR. They are listed in the Table 5.4, including the aperture within which the fluxes were extracted, translated into a physical scale at the galaxy redshift. Table 5.4 shows that: (i) The A_V calculated from NIR lines is higher than the median extinction calculated from the optical data. This is expected because NIR observations probe regions with higher optical depths. (ii)

The difference in extinction between the two types of objects is less evident or not present at all when measured in the NIR. For example, for the sources listed in the Table the median extinction in Type 1 sources is $\langle A_{V,\mathrm{Sy1.5-1}} \rangle = (4.1 \pm 3.0)\,\mathrm{mag}$, which is the same as for Type 2s $\langle A_{V,\mathrm{Sy1.8-2}} \rangle = (4.0 \pm 3.1)\,\mathrm{mag}$. This could imply that the optical AGN classifications does not have any relation to the extiction measured in the infrared. It is known that several – optically classified – Sy2 sources show broad components only in the NIR (e.g., NGC 5506 see Nagar et al. 2002; NGC 2992 see Reunanen et al. 2003; Mrk 573 see Ramos Almeida et al. 2008; Veilleux et al. 1997). On the other hand, a physical explanation of this result is not evident, though probably related to the whole obscuring structure around the BLR, which includes the broad-line emitting clouds shadowing themselves; the inclination, distribution, and composition of the torus; and the larger-scale components of the galaxies, such us dust lines in the spiral arms of disk galaxies. The central A_V of IRAS 01072+4954 is comparatively low, but in the view of the previous results, it is not possible to judge the impact of that extinction on the observability of broad components, based only on the extinction value.

Table 5.4: NIR extinction measurements from high spatial resolution observations of randomly selected Seyfert galaxies

Object	Type	Aperture	A_V (mag)	Ref.
NGC 5506	Sy1[a]	$93{\times}155\,\mathrm{pc}^2$	5.0	1
NGC 7582	Sy1[a]	$200{\times}200\,\mathrm{pc}^2$	1.86	2
NGC 4151	Sy1.5	$20{\times}20\,\mathrm{pc}^2$	1.55	3
NGC 3783	Sy1.5	$r = 170\,\mathrm{pc}$	~ 8.0	4
Mrk 609	Sy1.8	$r = 160\,\mathrm{pc}$	1.26	5
Mrk 1066	Sy2	$72{\times}72\,\mathrm{pc}^2$	1.84[b]	6
ESO 428-G14	Sy2	$r = 85\,\mathrm{pc}$	<3.0[c]	4
Mrk 1157	Sy2[d]	$145{\times}145\,\mathrm{pc}^2$	5.03	7
NGC 1068	Sy2	$r = 120\,\mathrm{pc}$	3.50	8
NGC 5135	Sy2	$r = 180\,\mathrm{pc}$	9.71	9

Note. The A_V was calculated from NIR lines.

[a] With observed broad Paβ in the NIR spectrum.

[b] Calculated from the Paβ/Brγ ratio.

[c] From Fig 1. of Storchi-Bergmann et al. (2009).

[d] With observed polarized broad lines.

References. (1) Nagar et al. (2002); (2) Riffel et al. (2009a); (3) Storchi-Bergmann et al. (2009); (4) Reunanen et al. (2003); (5) Zuther et al. (2007); (6) Riffel et al. (2010); (7) Riffel & Storchi-Bergmann (2011b); (8) Martins et al. (2010); (9) Bedregal et al. (2009).

An anomalous gas-to-dust ratio?

Panessa & Bassani (2002) studied in X-rays a sample of 17 'unabsorbed Sy2' galaxies. This objects share some properties with IRAS 01072+4954, like the small column density in X-rays and the lack of broad lines in the optical. One of the hypotheses suggested by the authors is the 'non-standart absorbing medium', i.e. a gas-to-dust ratio different from the Galactic one. Maiolino et al. (2001b) had already shown that Seyferts with X-ray luminosities $L_{2-10\,\mathrm{keV}} \gtrsim 10^{42}\,\mathrm{erg\,s^{-1}}$ seem to have $3-100$ times lower A_V/N_H than the Galactic value[4], $\sim 4.5\times10^{-22}\,\mathrm{mag\,cm^2}$. In contrast, Panessa & Bassani (2002) found that their unabsorbed Sy2s had X-ray obscuration consistent with that measured in the NLR from the Balmer decrement, i.e. $A_V/N_\mathrm{H} \sim (A_V/N_\mathrm{H})_\mathrm{Galactic}$. They interpreted this result as an evidence for the invisibility or inexistance of the torus in this sources, and/or an obscuring material located at larger scales like a dust lane, a bar, or an H II region.

In the case of IRAS 01072+4954, with the extinction measured from the NIR hydrogen lines, which is coincidentally the same as that calculated with the Balmer decrement, $A_V/N_\mathrm{H} \approx 6.25 \times 10^{-21}\,\mathrm{mag\,cm^2}$, i.e. ~ 14 times de Galactic one. If instead of the readening probe by the extinction, the central H-K color is used to calculate $E(B-V)$ throught the Eq.(5.1), it is possible to reach values up to $A_V/N_\mathrm{H} \sim 70 \times (A_V/N_\mathrm{H})_\mathrm{Galactic}$. In contrast to the Seyferts of Maiolino et al., IRAS 01072+4954 does not suffer a depletion of dust at the nucleus, but a dust-excess in comparison to the Galactic interstellar medium. The torus is clearly present, at least in the NIR, and therefore it can not be argued that a dust-to-gas ratio close to the Galactic value is an indication of the opposite, or that only large obscuring structures absorb the central emitted photons.

On the other hand, although there is photometrical and kinematical evidence for a bar in IRAS 01072+4954, its role on the obscuration of the central region seem to be negligible because its presence is not evident in the A_V nor in the H-K maps. Also in the Panessa & Bassani sample, the relation with larger morphological structures is not clear because less than half of their sources show possible signs of a bar or a dust lane. This fact could be parcially related with the availability of cold dust at the center. However, it is interesting to notice that three sources in the Maiolino et al. sample, and 15 out of the 17 objects of Panessa & Bassani, are low luminosity AGN (LLAGN) as IRAS 01072+4954, and that all of them have about the same or higher central dust-to-gas ratios than that in the Wilky Way. An interpretation opposed to that of Maiolino et al. for their high luminosity Seyfert sources might be plausible. While large dust grains and possibly dust-depleted gas in the inner region of the torus can explain low dust-to-gas ratios, it might be

---

[4]In fact, Maiolino et al. (2001b) compared $E(B-V)$ to N_H, and pointed out that the reddening $E(B-V)$ might be due to extinction and be converted using the standart factor $A_V/E(B-V) \equiv R_V = 3.1$ (Rieke & Lebofsky 1985). However, the same authors indicate that this does not need to be the case. In fact, $R_V \sim 2-6$ depends on the dust grains composition and distribution. Low R_V corresponds to diffuse interstellar medium, and large R_V to dense clouds and larger grain sizes (Cardelli et al. 1989; Maiolino et al. 2001a; Calzetti 2001).

that a low luminosity AGN is not able to sublimate as many small grains as high luminosity ones, implying that the extinction curve holds or $R_V \lesssim 3.1$ as in diffuse medium. In this scenario, a mechanism responsible for preventing the coagulation of small grains into bigger ones is still missing. Is the anomalous A_V/N_H responsible for the low Hydrogen column density observed in the X-rays? Is this an indication for different tori in these systems?

5.6.2 Recent strong star formation

Young OB stars emit UV photons that either ionize Hydrogen or are absorbed by dust and converted into far-infrared flux. Given that the intensity of the hydrogen recombination lines is proportional to the Lyman continuum flux, they are reliable tracers of the star formation in cases where the AGN contribution is negligible. We used the star-formation rate (SFR) as an indicator of starburst power. Following the calibration of Panuzzo et al. (2003, see also Sect. 1.3.2.1), it can be calculated as

$$\frac{\text{SFR}}{\text{M}_\odot \, \text{yr}^{-1}} = \frac{L_{\text{Br}\gamma}}{1.585 \times 10^{39} \, \text{erg s}^{-1}}, \tag{5.17}$$

where $L_{\text{Br}\gamma}$ refers to the luminosity of the Brγ line. At the center of IRAS 01072+4954, the SFR $< 0.35 \, \text{M}_\odot \, \text{yr}^{-1}$, implying a star-formation rate density of $\Sigma_{\text{SFR}} \equiv \text{SFR/Proyected area} < 11.6 \, \text{M}_\odot \, \text{yr}^{-1} \, \text{kpc}^{-2}$. Here, I have not removed any contribution from the AGN, therefore this value is an upper limit.

In order to compare with other objects, I calculated the Σ_{SFR} in the same way for the sample of AGN studied by Müller-Sánchez et al. (2011) from the Brγ fluxes and the aperture sizes reported in their Table 2. In general, on scales of tens of parsecs, the star formation ranges from $(50 - 500) \, \text{M}_\odot \, \text{yr}^{-1} \, \text{kpc}^{-2}$, reaching to some $1000 \, \text{M}_\odot \, \text{yr}^{-1} \, \text{kpc}^{-2}$ on parsec scales; over hundreds of parsecs the star-formation rate density reduces to $(1 - 50) \, \text{M}_\odot \, \text{yr}^{-1} \, \text{kpc}^{-2}$. A similar result was also found by Davies et al. (2007) using a different method for the estimation of the SFR. Although our reference sample is not statistically significant (11 sources, 5 Sy1s, 4 Sy2s and 2 intermediate types), it is possible to notice that the region of some tenths of parsecs radius at the nucleus of IRAS 01072+4954 is not among the stronger star-forming regions in other Seyfert galaxies, but closer to the lower end of the Σ_{SFR} range.

Indeed, adding up the emission around the center (regions : Median, EWBrγ, NE,SE, and SW of Sect. 4.5, see also Fig. 4.15 in page 82) the star formation amounts to SFR $\approx 1 \, \text{M}_\odot \, \text{yr}^{-1}$ and when accounting for the proyected area $\Sigma_{\text{SFR}} \approx 1.7 \, \text{M}_\odot \, \text{yr}^{-1} \, \text{kpc}^{-2}$. There is no indication of a stronger star forming process at the center. In the bulge, the region with the youngest population and enhanced star formation is EWBrγ, with $\Sigma_{\text{SFR, EWBr}\gamma} \approx 25 \, \text{M}_\odot \, \text{yr}^{-1} \, \text{kpc}^{-2}$, which is also much lower than the expected value of hundreds of solar masses per year.

In the sample of composite sources studied by Moran et al. (1996), the authors compared the equivalent width of the Hα and [N II] lines of the composite objects with the spiral and starburst galaxies studied by Kennicutt (1992), arriving to a

similar conclusion for the sample: the starburst components in composites are not exceptional among H II-galaxies. Therefore, if this source harbors a classical BLR, the star formation seems not to be an obstacle to observe broad lines.

5.6.3   Is IRAS 01072+4954 a True-Seyfert 2?

Several theoretical studies have predicted the disappearance of the BLR in AGN. Laor (2003) has suggested, based on the correlation between the radius of the BLR and the bolometric luminosity $L_{\rm bol}$ (Kaspi et al. 2000), that in low-luminosity objects the BLR shrinks up to a point at which broad lines cannot be formed. Assuming that the emitting clouds are virialized, the ratio $M_{\rm BH}^{1/2}/L_{\rm bol}^{1/4}$ controls the width of the broad lines. Therefore at a fixed $M_{\rm BH}$, the lower the luminosity, the broader the line widths (up to several thousands $\rm km\,s^{-1}$). In such objects, the visibility of the broad components becomes a problem of detectibility.

Elitzur & Shlosman (2006) suggested that the BLR and torus are two parts of the same disk-driven wind, which turns from hot and ionized to clumpy and dusty while receding from the central source. In low accretion rate sources ($L_{\rm bol} < 10^{42}\,\rm erg\,s^{-1}$) the outflow is no longer supported, which causes the disappearance of the torus and, at somewhat lower accretion rates, the vanishing of the BLR. In a similar approach, Nicastro (2000) proposed the BLR-wind to be maintained by the inner part of the accretion disk, which is radiation-pressure dominated. At some critical accretion rate, $\dot{m} \lesssim 0.3\eta(\alpha_{\rm V}M_{\rm BH})^{-1/8}$ (where η is the mass-to-energy conversion coefficient and $\alpha_{\rm V}$ the viscosity) the transition radius between the radiation-pressure to the gas-pressure dominated disk approaches the innermost marginally stable orbit, and then the BLR cannot form. In addition, it has been suggested that the accretion flow in low-luminosity AGN (LLAGN) cmight be radiatively inefficient (e.g. Narayan 2002; Macchetto & Chiaberge 2007; Ho 2009; Trump et al. 2011). Models predict that when the Eddington ratio drops below $\sim 10^{-2}$, the accretion disk truncates and a geometrically-thick, optically-thin disk emerges in the inner region, leaving the thin Shakura-Sunyaev disk intact at larger radii. Such sources would have weak emission lines and lack the big blue bump in the optical/UV.

Our NIR observations revealed low obscuration in the inner 75 pc and the presence of dust with $T > 1000\,\rm K$ arguing for a clear view towards the nucleus, which is consistent with the X-ray data. If the idea that the toroidal obscuration and the BLR are connected products of the same disk-driven wind (e.g. Elitzur 2008), then this source must have a BLR given the clear signature of hot dust in the central HK-spectrum. Another argument against the True-Sy 2 hypothesis is the high-Eddington ratio ($\lambda_{\rm Edd} \sim 0.2$). This corresponds to a high/soft-accretion state with a geometrically-thin optically-thick disk.

Figure 5.11 shows the $L_{\rm bol}$ vs. $M_{\rm BH}$ diagram where other sources are plotted for comparison. The estimated black hole mass and bolometric luminosity of IRAS 01072+4954 place it far from the region where True-Sy2 are theoretically expected, but closer to the area occupied by IMBHs and well-studied NLSy1s. The

diagram also shows the limits that different authors have predicted for the disappearance of the BLR. For example, in the model proposed by Laor (2003), this could happen at $\mathrm{FWHM_{BLs}} > 25\,000\,\mathrm{km\,s^{-1}}$. In Fig. 5.11 the dashed line labeled as L03 represents $\mathrm{FWHM_{BLs}} = 25\,000\,\mathrm{km\,s^{-1}}$.

Here, it is important to point out that the optical, NIR and X-ray observations were not taken simultaneously. Therefore, intermittent obscuration due to, e.g., a clumpy torus cannot be discarded as a reason for the absence of broad components (see e.g., Risaliti et al. 2005; Longinotti et al. 2009; Marchese et al. 2012). IRAS 01072+4954 presents long-term variability in the X-rays. For example, from 1990 to 2002 the soft X-ray flux decreased by about 1.1 orders of magnitude, but in 2005 it increased again. These variations could be related to a change in the accretion mode, and that would imply a variation in the bolometric luminosity.
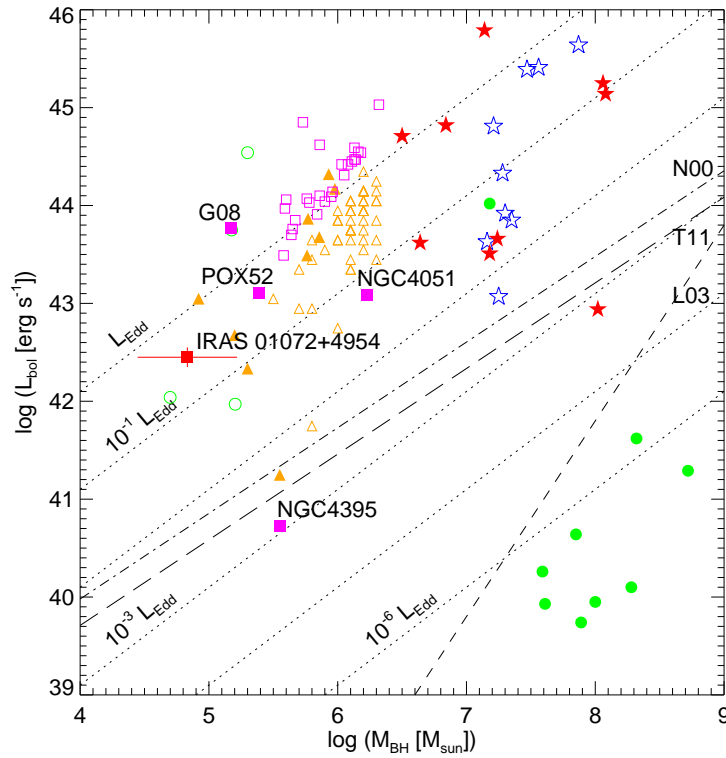
Figure 5.11: Black hole mass vs. bolometric luminosity diagram. The dotted lines correspond to different Eddington ratios. Theoretical upper limits of True-Sy2s predicted by different authors are also marked: Nicastro (2000) 'N00' (dot-dashed line), Laor (2003) 'L03' (short-dashed line) and Trump et al. (2011) 'T11' (long-dashed line). The location of IRAS 01072+4954 is compared with other sources from the literature. Sy1 and Sy2 from Singh et al. (2011) are symbolized as red and blue stars, respectively; IMBH compiled by Dewangan et al. (2008) and low-mass Sy2s from Thornton et al. (2009) are solid and empty triangles. True-Sy2 candidates of Laor (2003) are filled circles. Other well-known NLSy1s: NGC 4395, NGC 4051 and SDSS J114008.71+030711.4 indicated as 'G08' and the dwarf-elliptical Sy1 POX 52 are shown.

However, it is unlikely that a variable X-ray absorber could also cover/uncover significant parts of the BLR and be responsible for the True-Sy2 appearance. Here I always referred to the measurements performed by Panessa et al. (2005), assuming that by the time of our observations (2008) the X-ray emission did not change dramatically. In consequence, I expect the main conclusions still to be valid.

5.7 On the nature of the active nucleus

IRAS 01072+4954 might have a pseudobulge given its low Sersic index, a common characteristic of objects with IMBHs (a counterexample is Pox 52, a dwarf elliptical galaxy with $M_{\mathrm{BH}} \simeq 3 \times 10^5 \, \mathrm{M_\odot}$; Thornton et al. 2008), but photometrical and kinematical evidences are not conclusive. It contains a bar-like structure, which is taken as indicative of secular evolution (e.g., Kormendy & Kennicutt 2004; Mathur et al. 2011; Orban de Xivry et al. 2011). High-angular resolution observations of the whole galaxy are required to perform a better photometric decomposition and to establish the presence of nuclear structures related with the black hole feeding and feedback mechanisms. Here, it has been shown that broad lines might be present, but because of their faintness, they can only be detected with very high spatial and spectral resolution in around strong H I lines. Which kind of AGN is IRAS 01072+4954?

Assuming the validity of the $M_{\mathrm{BH}} - L_{\mathrm{bulge}}$ and $M_{\mathrm{BH}} - \sigma_*$ relations, IRAS 01072+4954 hosts a black hole of $\lesssim 10^6 \, \mathrm{M_\odot}$ and it shares the same X-ray properties of other IMBHs: short-term variability and $\Gamma \sim 1.7 - 2.6$ (e.g., Greene & Ho 2007; Dewangan et al. 2008; Desroches et al. 2009)[5]. If the properties of the BLR scale with the luminosity like in more massive ($M_{\mathrm{BH}} \sim 10^{6-8} \, \mathrm{M_\odot}$) AGN, the width and the flux of the expected broad emission lines in this source are below the lower end of the values observed in classical AGN and in the low range of those in NLSy1s. For example, in the homogeneous sample of $\sim$2000 NLSy1s from the SDSS DR3 by Zhou et al. (2006), there are $\sim$500 objects with $\mathrm{FWHM_{broad,H\alpha}} \leq 1200 \, \mathrm{km \, s^{-1}}$, of which $\sim$25 ($\sim 1\%$) are below $700 \, \mathrm{km \, s^{-1}}$. Those 25 sources have $\langle L_{\mathrm{broad,H\alpha}} \rangle = 4.3 \times 10^{41} \, \mathrm{erg \, s^{-1}}$; in comparison, we estimated $L_{\mathrm{broad,H\alpha}} \sim (2.0 - 6.0) \times 10^{40} \, \mathrm{erg \, s^{-1}}$ for our source.

IRAS 01072+4954 as a Narrow-Line Seyfert 1

Narrow-Line Seyfert 1 (NLSy1) galaxies have been classically defined by three simple criteria: (i) $\mathrm{FWHM_{borad,H\beta}} < 2000 \, \mathrm{km \, s^{-1}}$, (ii) [O III]/H$\beta$ < 3, and (iii) strong Fe II. Other characteristics have been also added to this list: (iv) steep and

---

[5]Here we refer to the photon index obtained when a single power-law is fitted to the 0.3-10 keV data, as used by Dewangan et al. (2008). Other authors describe the X-ray spectra using two power-law functions, hence derive a soft- and a hard-photon index, Γ_{S} and Γ_{H}. Then using Γ_{S} to characterize NLSy1 is justified because the emission of a Shakura-Sunyaev disk peaks close to the soft X-ray domain.

variable soft X-ray spectra, (v) infrequent radio loudness, and (vi) blue asymmetric
C IV profile at $\lambda 1549$ Å .
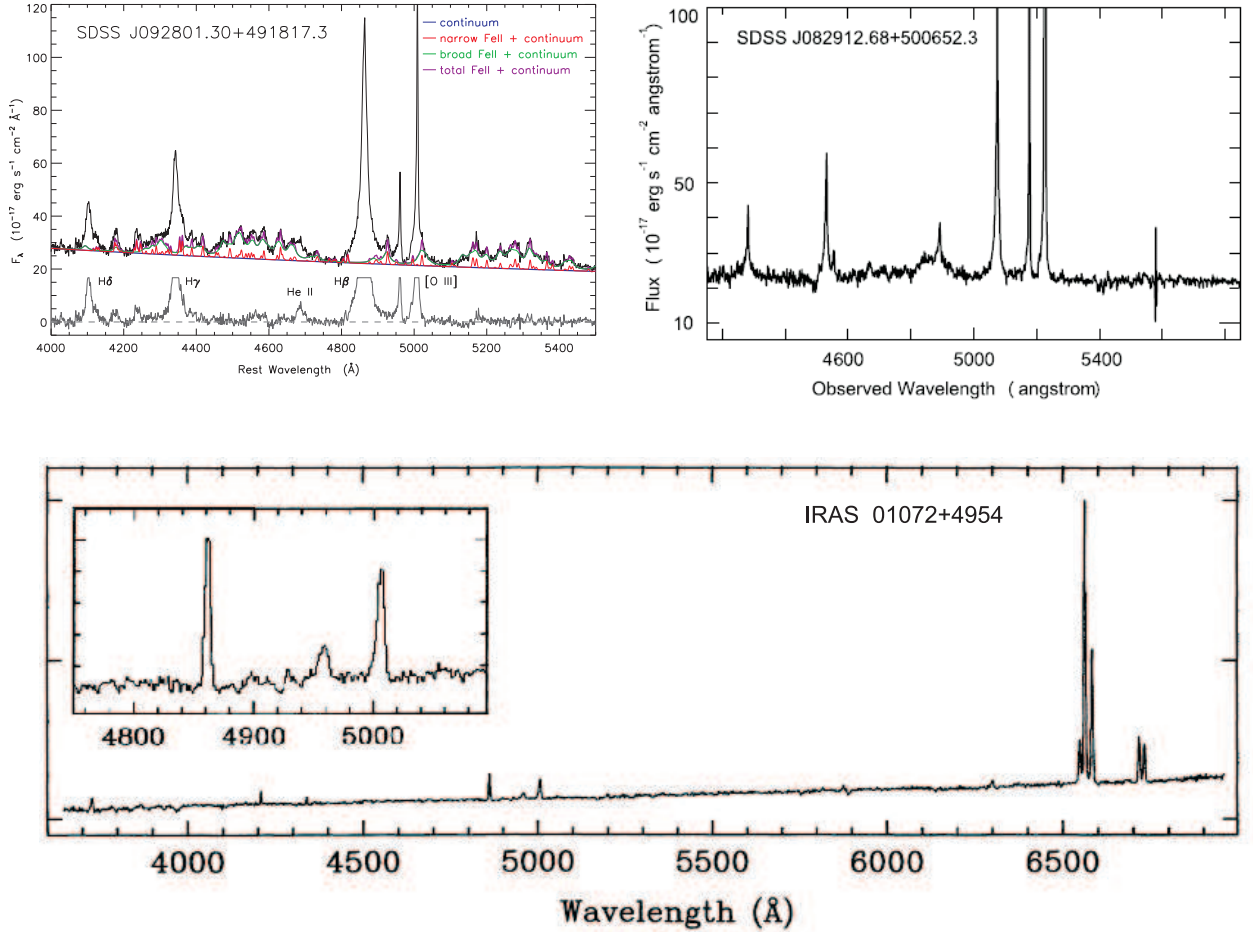
Figure 5.12: Fe II emission in NLSy1s. *Top-left:* Typical spectra of a Narrow-Line Seyfert 1 galaxy. Strong Fe II emission is notorious at around 4500 Å, 5200 Å, and between the Hβ and [O III] lines. Taken from: Dong et al. (2011). *Top-right:* "Fe II-deficient" NLSy1. The broad emission around 4900 Å (observed wavelength) corresponds to He II. Modified from: Zhou et al. (2006). *Bottom:* Optical spectrum of IRAS 01072+4954. The panel at the left corner shows a zoom into the region around Hβ and [O III] emission lines. No Fe II is visible in the spectrum. Modified from: Moran et al. (1996).

Apart from from properties (v) and (vi) that are unknown given the lack of (deeper) radio and UV observations, IRAS 01072+4954 could be an extreme NLSy1. However it does not show the characteristic Fe II emission in the optical spectrum. Ai et al. (2011) suggested the existence of two kinds of IMBH sources, distinguishing the NLSy1s for their well known features, i.e., strong Fe II emission, significant soft X-ray excess and high Eddington ratios. The other IMBHs would have flatter spectral slopes (more typical of Sy1s), non-ubiquity of the soft X-ray

excess, and low accretion rate. The closest and by now the most studied case is NGC 4395 (e.g., Filippenko & Sargent 1989; Peterson et al. 2005; Laor 2007). The authors proposed the Eddington ratio to be the driving mechanism for the observed properties. However, the properties of those two classes get mixed in the case of IRAS 01072+4954.

Zhou et al. (2006) have already commented on the existence of "Fe II-deficient" NLSy1 in sources with high accretion rate and very narrow broad-Balmer lines (Fig. 5.12). Moreover, if the physical conditions for iron production in IMBHs are the same as in more massive AGN then, according to the correlations found by Dong et al. (2011), in sources with Eddington ratios of $\gtrsim 0.2$ (as this one), the expected flux of the broad Fe II line is about the same as the expected flux of the broad Hβ component, and the flux of the narrow Fe II is a tenth of it ($10 \times F_{\mathrm{narrow,Fe\,II}\lambda 4570} \sim F_{\mathrm{broad,Fe\,II}\lambda 4570} \sim F_{\mathrm{broad,H}\beta}$). This means that in cases of very faint broad components, even for objects with high accretion rate, strong Fe II is not expected to be observed.

5.8   Conclusions

The nature of the active nucleus in IRAS 01072+4954 has been studied. The analysis performed in this chapter is based on H- and K-band data from the central $\approx 75\,\mathrm{pc}$. IRAS 01072+4954 has an X-ray emission typical of Sy1s ($N_H < 0.04 \times 10^{22}\,\mathrm{cm}^{-2}$, $\Gamma \sim 2.1$ and strong short-term variability), but the optical spectrum (taken from a $\sim (1 \times 2)\,\mathrm{kpc}^2$ region) lacks the expected broad lines. The results on the individual hypotheses for the apparent absence of the broad components are:

- Extinction from cold dust along the line of sight: The extinction measured from the hydrogen recombination lines in the NIR is $A_V = 2.5\,\mathrm{mag}$ towards the nucleus, which is consistent with the one measured in other Seyfert galaxies from high-angular resolution NIR observations ($\langle A_V \rangle \simeq (4 \pm 3)\,\mathrm{mag}$, in both types of AGN). A relation between the extinction measured in the NIR and the observability of broad lines is not found.

- Nuclear star formation that outshines the AGN emission: The star formation is a dominant process in this galaxy. However, in the central region, the star-formation rate density is $\Sigma_{\mathrm{SFR}} < 11.6\,\mathrm{M}_\odot\,\mathrm{yr}^{-1}\,\mathrm{kpc}^{-2}$, which is below the lower limit of the range $(50 - 500)\,\mathrm{M}_\odot\,\mathrm{yr}^{-1}\,\mathrm{kpc}^{-2}$ observed in Seyferts. Older stellar population with ages $\gtrsim 10^7\,\mathrm{yr}$ accounts for about 75% of the continuum flux.

- Hot dust obscuration, possibly related to the putative torus of the unified model. Without taking into account the presence of a featureless continuum power-law component – which could not be constrained with our data – about 25% of the HK-band continuum is emitted by hot dust at a temperature of $\sim 1100\,\mathrm{K}$. Considering that in Type 1 sources $T \gtrsim 1000\,\mathrm{K}$, whereas in Type 2s $T \lesssim 800\,\mathrm{K}$, this result can be interpreted as an indication of a clear view

towards the center. This is also consistent with the low absorption column density estimated by Panessa et al. (2005) from X-ray observations.

- Non-existence of the BLR, hosting a True-Sy2 nucleus. The unresolved hot-dust emission that signifies the presence of a torus is predicted to form and persist while the broad line region clouds are launched. Therefore, given the clear signature of hot dust at the center of IRAS 01072+4954, and the high Eddington ratio, the presence of a BLR is expected.

Individually, non of the previous possibilities seems to be a satisfactory explanation. The unusual combination of a low black hole mass ($M_{\rm BH} \sim 10^5 \, \rm M_\odot$) with a low bolometric luminosity ($L_{\rm bol} \approx 2.8 \times 10^{42} \, \rm erg \, s^{-1}$) implies that the expected broad components are very faint ($F_{\rm broad, H\alpha} \sim (1.7 - 4.8) \times 10^{-14} \, \rm erg \, s^{-1} \, cm^{-2}$) and their widths are of only few hundreds of $\rm km \, s^{-1}$ ($\rm FWHM_{broad, H\alpha} \sim (400 - 600) \, km \, s^{-1}$). Thus, the main reason for the non-detection of the broad lines is the faintness of the BLR. In the K-band spectrum of the central $r \approx 75 \, \rm pc$, a 'hump' around the position of the Brγ line is observed. This feature coincides in flux and width with the theoretically predicted for a broad Brγ component. A proper detection would require higher S/N data.

With a stellar-velocity dispersion of $33.5 \, \rm km \, s^{-1}$, IRAS 01072+4954 hosts a low mass black hole that accretes at a rate $\dot{m} \cong \lambda_{\rm Edd} \sim 0.2$. This implies a high/soft accretion state with a geometrically-thin accretion disk. These properties are similar to those found in NLSy1s, but IRAS 01072+4954 lacks the Fe II emission typical for these sources. High resolution optical spectroscopy of the nucleus is necessary to measure the strength of the Fe II and confirm the AGN classification.

Chapter 6

Star Formation Vs. AGN

In the previous chapters, detailed studies of the star formation and the central black hole accretion in IRAS 01072+4954 have been presented. Here, some efforts on discriminating between them as the main ionizing source at the nucleus are presented. In particular the [Fe II] and molecular hydrogen emissions are used as tracers of photoionization and shock excitation. Do they show any sign of a connection between the central AGN and the circumnuclear star formation? How is the kinematics of the stars and the gas? Is there any evidence for an inflow or an outflow? Here, I make use of the previous findings to discuss the microphysics in some regions of the bulge, with the aim to discover links between the stellar and the nuclear activity. The availability of cold gas to fuel both processes is also examined. I show signs of an outflow observed in the [Fe II] kinematics, and determine whether it might originate from the star formation or from the AGN. The stellar and AGN feedback are also discussed in the context of the Kennicutt-Schmidt law. Conclusion and implications are presented at the end of the chapter.

6.1 Disentangling the star formation and the AGN contributions

Discriminating the effects of the AGN on its host galaxy and the role of the nuclear and circumnuclear star formation as a possible driving agent of the black hole activity in nearby galaxies is a key step in order to understand galaxy formation and evolution at higher redshifts. In order to do that, high angular resolution observations that allow one to identify the regions where the emission originates from, and to study the ionizing mechanisms present in those regions, are desired. Here, the NIFS IFU and high resolution capabilities are exploited to try to disentangle the AGN and the star-formation imprints on the bulge of IRAS 01072+4954.

Is it possible to determine the influence of the AGN in the central region? In Seyfert galaxies, the emission from the accretion disk ionizes not only the gas that is very close to it in the BLR, but also that located up to several hundreds of parsecs away from the nucleus in the opening angle of the torus. Extended narrow

line regions (NLR) have been observed in H I and [O III]. However, such structure is not visible in IRAS 01072+4954. Other emission lines like [Fe II] and H_2 can be used instead to probe the gas excitation mechanisms that take place at the nucleus. They can further be used as tracers of shocks or star formation.

6.1.1   NIR diagnostic diagram

In analogy to the optical diagnostic diagrams (like the BPT, see Fig. 2.2), Moorwood & Oliva (1988) and Larkin et al.(1998; see also Rodríguez-Ardila et al. 2004, 2005b) suggested that the line ratios of prominent NIR species, such us [Fe II] $\lambda 1.257\,\mu$m, Paβ, $H_2\lambda 2.122\,\mu$m and Brγ, could be used to determine the type of nuclear activity. In this case, I used the spectrum taken from the central $r \approx 75$ pc. Given that [Fe II]$\lambda 1.257\,\mu$m and Paβ were not covered by our observations, those fluxes were calculated from [Fe II]$\lambda 1.644\,\mu$m and Brγ using the theoretical value calculated by Nussbaumer & Storey (1988) for the ratio of the iron lines ($F_{[\text{Fe II}]\lambda 1.644\,\mu\text{m}}/F_{[\text{Fe II}]\lambda 1.257\,\mu\text{m}} = 0.74$) and the case-B for the hydrogen recombination (assuming $T = 10^4$ K and an electron density of 10^4 cm^{-3}. Previously the spectrum was corrected for extinction using $f_{\lambda,\,\text{corr}}(\lambda) = f_{\lambda,\,\text{observ}}(\lambda) \times 10^{0.4\,A_V\,A_{\lambda,\text{V}}(\lambda)}$ with $A_V = 2.5$ mag and the parametrization of the interstellar reddening $A_{\lambda,\text{V}}(\lambda)$ of Cardelli et al. (1989). The originally proposed line ratios are essentially insensitive to obscuration, but here it is important to account for it because the considered lines are located in different bands. In the case of IRAS 01072+4954, $\log(H_2/\text{Br}\gamma) = -0.24 \pm 0.07$ and $\log([\text{Fe II}\,1.257]/\text{Pa}\beta) = -0.65 \pm 0.10$. Fig. 6.1 shows the NIR-diagram where the line ratios of this source are compared with those of the starbursts, Seyferts and LINERs compiled by Rodríguez-Ardila et al. (2005b).

In the diagram, a moderate correlation between both line ratios along different activity types can be recognized. Such a trend is believed to correspond to an increasing progression from pure photoionization to pure shock excitation of [Fe II] and H_2. IRAS 01072+4954 falls in between the areas occupied by starbursts and Seyfert galaxies; this implies a mixture of ionization mechanisms of the gas in the central region.

6.1.2   [Fe II] and H_2 excitation mechanisms

The emission of low ionization species such us [Fe II] and molecular hydrogen can be excited by several processes including photoionization by UV radiation, and/or X-rays; and shocks from supernova explosions, or from the action of a jet in the interstellar medium. These mechanisms take place near to starburst regions and to an AGN. Theoretically, different ionization mechanisms produce different spectra, and therefore it is possible to use emission line ratios from [Fe II] and H_2 in combination with H I to recognize the main source of excitation in selected regions in the bulge of IRAS 01072+4954.
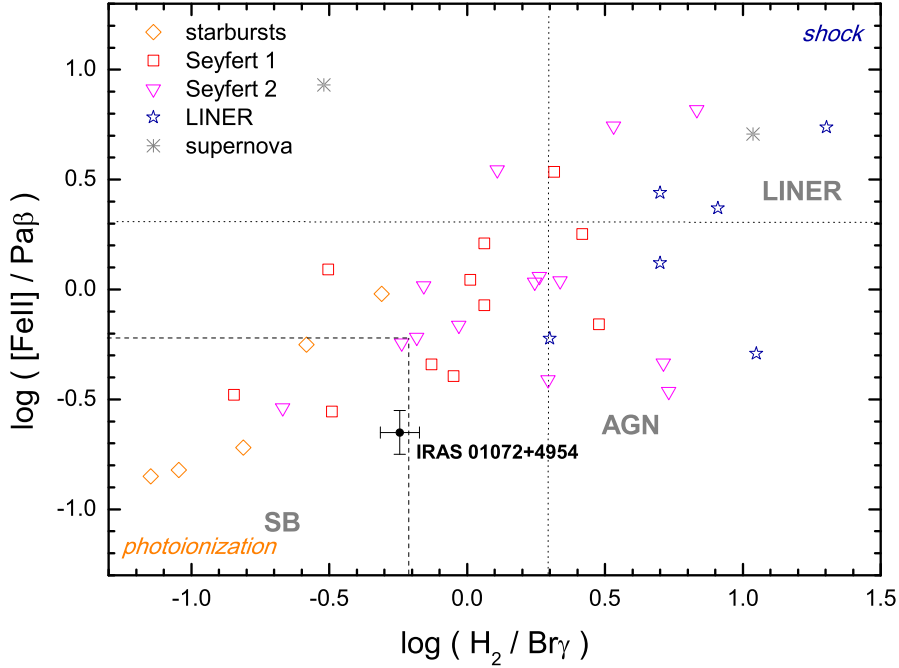
Figure 6.1: Near-infrared diagnostic diagram. The line ratios obtained from the central region of IRAS 01072+4954 are shown in comparison with those calculated from spatially unresolved observations of other sources taken from the literature. The different type of activity in these objects is represented as shown in the label. The observational divisions between starbursts, Seyferts and LINERS are shown by dashed lines. The ratio [Fe II]$\lambda 1.644\,\mu$m/Brγ was converted to [Fe II]$\lambda 1.257\,\mu$m/Paβ using theoretical values as explained in the text.

[Fe II] excitation

The [Fe II] emission is produced in partially ionized hydrogen regions rich in Fe^+ and free electrons. This kind of environment can be generated by supernova driven-shocks or X-ray emission from an AGN. In both cases, also radio emission is produced. The observed tight correlation between [Fe II] and the radio flux at 6 cm supports this scenario (see e.g., Forbes & Ward 1993). Mouri et al. (2000) found that the electron temperature can be used to discriminate between this two thermal processes: $T \sim 6000$ K indicates that the [Fe II] is heated by shocks, while $T \sim 8000$ K is associated with X-ray heating.

Also UV radiation from massive OB stars is capable to ionize their surroundings, creating transition regions where [Fe II] can be excited. The ratio between [Fe II] and any strong NIR recombination line (Paβ or Brγ) can be used to identify the [Fe II] ionization mechanism (Goodrich et al. 1994; Alonso-Herrero et al. 1997). That is because in H II regions the fully ionized hydrogen interacts with the iron atoms creating higher excited Fe species and preventing the efficient [Fe II] production. As mentioned previously, increasing progression of the [Fe II]/Paβ ratio from pure photoionization to pure shock excitation has been found (Rodríguez-Ardila et al.

2005b). An empirical boundary between the sources with [Fe II] ionization dominated by star formation and by the AGN was placed at [Fe II] $1.257\,\mu$m/Pa$\beta \approx 0.4$ (or correspondingly [Fe II] $1.644\,\mu$m/Br$\gamma \approx 1.5$), while [Fe II] $1.257\,\mu$m/Pa$\beta \gtrsim 2$ ([Fe II] $1.644\,\mu$m/Br$\gamma \gtrsim 8.5$) correspond to the area occupied by LINERs and supernova remnants (Rodríguez-Ardila et al. 2005b).

High spatial resolution observations of starbursts and Seyferts have been used to map the [Fe II] and H I emissions inside the galaxies (e.g. NGC253, Forbes et al. 1993; Alonso-Herrero et al. 2003; M82 Greenhouse et al. 1997; Alonso-Herrero et al. 2003; N5135, Bedregal et al. 2009). In spatially resolved starburst regions, [Fe II]/Br$\gamma \lesssim 1$ has been found (Mouri et al. 1990) which is in agreement with the starburst models of Colina (1993) that predict ratios between 0.1 and 1.4. Higher values [Fe II]/Br$\gamma > 10$ seem to be related with supernova remnants (Oliva et al. 1989; Lumsden & Puxley 1995). In NGC5135, at the position of the AGN, Bedregal et al. (2009) calculated [Fe II] $1.644\,\mu$m/Br$\gamma \approx 5.7$; in a region with very recent star formation (age ≤ 6 Myr) the same ratio was ~ 1.5, and in a third region where star formation is going through the peak of the supernova phase [age $\sim (8-12)$ Myr] they obtained ~ 14.1 for this ratio, in agreement with the previous spatially unresolved observations.

Figure 6.2 shows the [Fe II] $1.644\,\mu$m/Brγ map of the IRAS 01072+4954 bulge. The variations in the map, ranging from 0.5 to ~ 2.5, are dominated by the asymmetric Brγ emission. Slightly lower values at the north are consistent with the presence of a young stellar population. This is also suggested by the equivalent width of the Brγ line, which can be used as an age indicator. The regions marked in the map are not exactly the same than those studied in Chapter 4, but roughly coincide spatially with each other. The only exception is the south-west (SW) aperture, which in this case has been displaced to the north to cover the region with higher [Fe II] excitation. The overall [Fe II]/Brγ ratio is consistent with photoionization by massive stars as the dominant ionizing mechanism. This picture is consistent with the significant soft component found in the X-ray spectrum. Panessa et al. (2005) reported a faint extended emission that was more pronounced in the 0.3-2 keV band and fitted it as a thermal component with a temperature $\sim 10^4$ K typical of starburst galaxies.

Surprisingly there is not any indication of the AGN presence in the [Fe II] 1.644/Brγ map. In order to estimate the amount of [Fe II] that would be excited by the hard X-ray emission from the AGN, I used the models of Maloney et al. (1996) and the X-ray information from Panessa et al. (2005). The models predict the expected [Fe II] emission of a cloud with electron density n_e that is heated by a source with intrinsic luminosity L_X located at a distance d. The parameter that characterizes the state of the gas cloud is the effective (attenuated) ionization parameter ξ_eff,

$$\xi_\mathrm{eff} \simeq 100 \, \frac{L_X}{10^{44}\,\mathrm{erg\,s^{-1}}} \left(\frac{d}{\mathrm{pc}}\right)^{-2} \left(\frac{n_\mathrm{e}}{10^5\,\mathrm{cm^{-3}}}\right)^{-1} \left(\frac{N_H}{10^{22}\mathrm{cm^{-2}}}\right)^{-1.03} \tag{6.1}$$

with the attenuation calculated for an incident power law photon spectral index
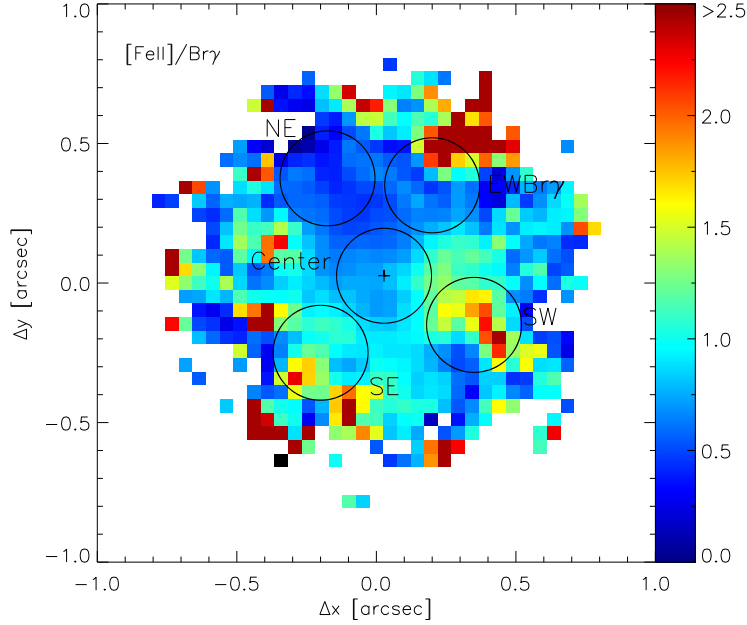
Figure 6.2: [Fe II] $\lambda 1.644\,\mu$m / Brγ map of the IRAS 01072+4954 bulge. The circular apertures are used below to study the [Fe II] and H$_2$ ionization mechanisms. The white pixels replace unreliable data points. North is up, east is left.

$\Gamma = 2.1$ according to the value reported by Panessa et al. (2005). I calculated the outcoming emission from a region within aperture of radius $r \approx 0.2''$ – or correspondingly, $\theta \approx 2.7 \times 10^{-12}$ sr. Then, from Fig. 6b of Maloney et al. (1996) it is possible to read the emergent integrated [Fe II] intensities $I_{N_{22}}$ from a cloud with electron density of $n_{\rm e} = 10^3\,{\rm cm}^{-3}$. The intensities have been attenuated for a column density of $N_H = 10^{22}\,{\rm cm}^{-2}$, so we use $I_{N_{20}} = I_{N_{22}} \times \exp(\sigma_0\,\Delta N_H)$ with $\sigma_0 = 2.6 \times 10^{-22}{\rm cm}^2$ to recover the intensity for our lower N_H. The result is an expected $F_{\rm [Fe\,II]} = 8.8 \times 10^{-17}\,{\rm erg\,s}^{-1}\,{\rm cm}^{-2}$, which corresponds only to $\sim 30\%$ of the emitted [Fe II] in that region. Maloney et al. also computed the theoretical Brγ emission. For our fiducial parameters in such a low density environment, the ratio [Fe II]/Br$\gamma = 0.4$ is well in agreement with what it is observed. On the other hand, for higher density clouds $n_{\rm e} = 10^5\,{\rm cm}^{-3}$, the model predicts a [Fe II] flux less than $3.5 \times 10^{-21}\,{\rm erg\,s}^{-1}\,{\rm cm}^{-2}$. It is possible to conclude that, assuming these models apply to our case, at the nucleus the electron density is critically in the range $(10^3 - 10^5)\,{\rm cm}^{-3}$, and that the observed [Fe II]/Brγ ratio is in agreement with the expectations of X-ray photoionization, although the observed value is well below that in other sources.

H_2 excitation

The H_2 molecule can be formed in the same transition region as [Fe II]. However, it is not clear if they also share the same ionizing sources (Rodríguez-Ardila et al. 2004). Molecular hydrogen is created in two forms, para-H_2 and ortho-H_2, which are named according to the alignment of the nuclear spins of the H atoms – parallel in the former case and opposite in the latter. It can be excited trough three mechanisms: (i) The absorption of far-ultraviolet (FUV) photons belonging to Lyman and Werner bands ($> 11.2\,$eV, $12.3\,$eV, i.e. 912A-1108A) pumps the molecule to electronic excited states. While it decays back to the ground state, it emits optical and IR fluorescence radiation (e.g., Black & van Dishoeck 1987; Sternberg 1989). (ii) Shocks produce strong changes in the physical properties and chemical composition of the environment generating the collisional excitation of the H_2 molecule (e.g., Brand et al. 1989; Hollenbach & McKee 1989). (iii) Hard X-rays are able to penetrate deeply into dense molecular clouds heating zones that are opaque to UV radiation and exciting H_2 emission (e.g., Maloney et al. 1996; Tine et al. 1997). Each of these processes excites in different amounts the roto-vibrational levels of the H_2 molecule, and therefore the ratios of the line intensities can be use to distinguish among them.

Molecular hydrogen emission was detected in the central $r \sim 250\,$pc of IRAS 01072+4954. Here, I selected five regions of $r \approx 0.16''$ aperture radius to study the H_2 excitation (see Fig. 6.2). In the K-band the first rotational levels ($J = 0, 1, 2$) of the vibrational transition $v = 1 \rightarrow 0$, S(0), S(1) and S(2) were observed and in some regions also the $J = 1, 2, 3$ of $v = 2 \rightarrow 1$ were detected. In the H-band H_2 lines corresponding to high rotational quantum numbers J of these transitions are emitted, but unfortunately they are placed in spectral zones with strong stellar or atmospheric absorption and hence their identification is unsecure. Odd numbers of rotational levels correspond to excited states of the ortho-H_2 and even J of the para-H_2. Under normal conditions, ortho-H_2 constitutes 75% of the H_2 molecular gas, and para-H_2 the remaining 25%. Ortho-para conversions might occur due to proton exchange reactions with H or H I atoms.

H_2-fluorescence preferably populates the high energy levels ($v \geq 2$), while thermal processes excite the lower levels and quenches the excitation of the higher ones. Hence, the ratio between 2-1 S(1) and 1-0 S(1) indicates the percentage in which each mechanism contributes to the H_2 excitation. Note that both lines are emitted by ortho-H_2 so that the ratio is insensitive to the difference between the ortho and para populations. Mouri (1994) showed that a ratio of $0.1 - 0.2$ corresponds to gas heated by shocks and/or heating photons, and a value of ~ 0.5 is produced by fluorescence. Moreover, Mouri proposed a graphical method to discriminate between thermal and non-thermal H_2-excitation and to estimate the excitation temperature. Such a H_2 diagnostic diagram for the selected regions is depicted in Fig. 6.3. The values of the line ratios from different models of thermal and non-thermal excitation are also shown, as well as the mixture model of Rodríguez-Ardila et al. (2004).
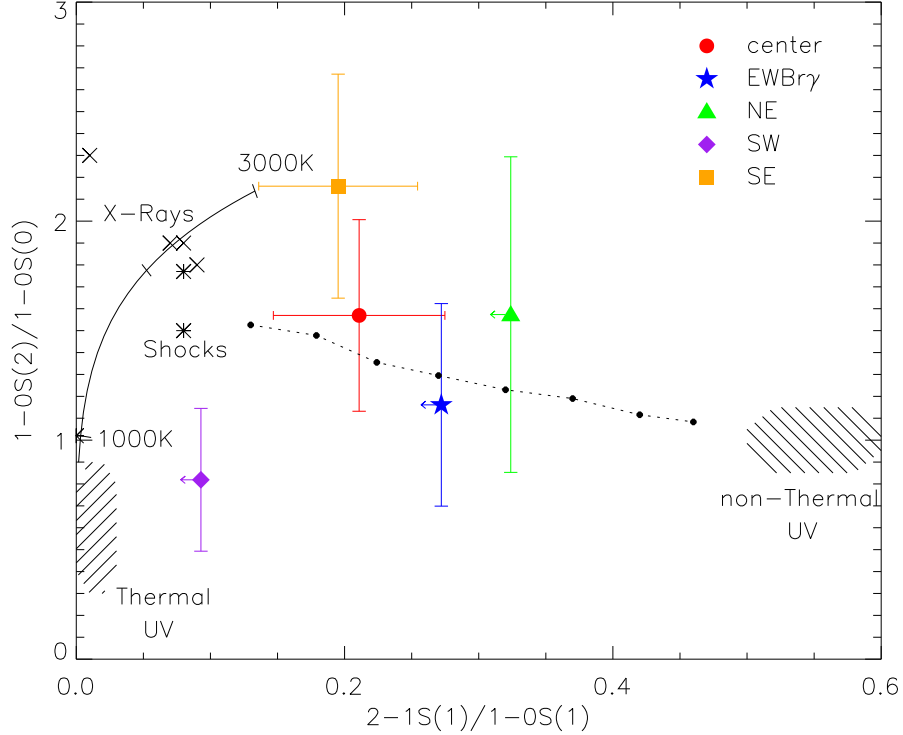
Figure 6.3: H_2 diagnostic diagram with $1\text{-}0\,S(2)/1\text{-}0\,S(0)$ vs. $2\text{-}1\,S(1)/1\text{-}0\,S(1)$. The studied regions are represented as indicated in the label. Several ionizing mechanisms are also shown. The curve represents thermal emission from $1000\,K$ to $3000\,K$, calculated from Eq. (6.5). Shaded areas are occupied by the thermal-UV models of Sternberg (1989) and non-thermal-UV models of Black & van Dishoeck (1987), as indicated. Crosses mark X-ray heating models of Draine & Woods (1990). Asterisks correspond to shock models of Brand et al. (1989) and Black & van Dishoeck (1987). The dotted line represents the mixed model constructed by Rodríguez-Ardila et al. (2004), where the first black point is composed by 90% thermal and 10% fluorescence excitation and then the non-thermal excitation increases to the right in steps of 10% .

In the H_2 diagnostic diagram all points are closer to the zone of thermal excitation. The south-west region (SW) is located in the area of $1\text{-}0\,S(2)/1\text{-}0\,S(0) \lesssim 1.0$ which is also occupied by starburst galaxies like NGC 253 and galactic photodissociation regions (PDRs). The central, south-east (SE), and EWBrγ regions show a combination of both kinds of excitation with $\sim 25\%$ of fluorescence. The position of the central line ratios is in agreement with the results found by Rodríguez-Ardila et al. (2004, 2005b) in a sample of 42 Seyfert galaxies. Rodríguez-Ardila et al. studied the H_2 emission in apertures of $\sim 200 - 300\,\mathrm{pc}$ around the AGN and concluded that the thermal excitation is the main ionizing mechanism of the observed H_2 emission with $\lesssim 30\%$ of fluorescence. On the other hand, small X-ray contributions to the excitation of the central-aperture can be insinuated from the plot. No correlation has been found between the hard X-ray luminosity of AGNs and

their nuclear 2-1 (1)/1-0 S(1) ratio (Rodríguez-Ardila et al. 2005b), nor with the 1-0 S(2)/1-0 S(0), but it seems that X-ray heated regions are preferentially located above 1-0 S(2)/1-0 S(0) $\gtrsim$ 1.0.

In order to further investigate the excitation from different vibrational levels, I constructed the population diagram for the observed H_2 lines. In this diagram the column density of each rotational level $N(v, J)$ is plotted against its excitation energy. Assuming local thermodynamic equilibrium (LTE) of the gas, the relation between $N(v, J)$ and the emitted flux in the transition is linear. For a particular H_2 line of measured flux $F(v, J)$ (in $W\,m^{-2}$) detected in a region that subtends a solid angle Ω, the column density in the optically thin case is given by

$$N(v, J) = \frac{F(v, J)}{A_{\mathrm{ul}}} \frac{\lambda}{hc} \frac{4\pi}{\Omega}, \tag{6.2}$$

where A_{ul} is the Einstein A-coefficient of the transition taken from Wolniewicz et al. (1998), and λ the rest wavelength of the emitted line. Figure 6.4 shows the population level diagram for the different regions in the IRAS 01072+4954 bulge. The column densities are divided by their statistical weights $g(v, J)$ and scaled to the population of the $(v, J) = (1, 3)$ level. The slopes of straight lines that join two ortho (or equivalently, two para) transitions give a direct measurement of the excitation temperature. The rotational temperature is calculated from two ortho(para) lines that belong to the same vibrational level, and the vibrational temperature from transitions that having the same J are from consecutive v levels. Therefore, for the present observations, the vibrational temperature T_{v} and the rotational temperatures T_{r} of the para-H_2 in the $v{=}1$ level and of the ortho-H_2 in the $v{=}2$ level can be calculated as

$$T_{\mathrm{r}(v=1)} = \frac{1113\,\mathrm{K}}{1.130 + \ln\left(\frac{F_{1\text{-}0\ \mathrm{S}(0)}}{F_{1\text{-}0\ \mathrm{S}(2)}}\right)}, \tag{6.3a}$$

$$T_{\mathrm{r}(v=2)} = \frac{1340\,\mathrm{K}}{0.680 + \ln\left(\frac{F_{2\text{-}0\ \mathrm{S}(1)}}{F_{2\text{-}1\ \mathrm{S}(3)}}\right)}. \tag{6.3b}$$

$$T_{\mathrm{v}} = \frac{5594}{0.304 + \ln\left(\frac{F_{1\text{-}0\ \mathrm{S}(1)}}{F_{2\text{-}1\ \mathrm{S}(1)}}\right)}. \tag{6.4}$$

Given the proximity of the H_2 lines along the K-band spectrum, the line ratios are not much affected by extinction. However, that is not necessarily the case for the excitation temperatures (Smith et al. 1997). An additional term $0.92\,(A_{\lambda_1, V} - A_{\lambda_2, V})$ in the denominator must be added to account for the extinction when the fluxes are not de-reddened. Here, I have used the reddening-corrected fluxes. The A_V coefficients were derived from every aperture using nebular lines as explained in Sect. 4.3. The calculated rotational and vibrational temperatures for each aperture are reported in Table. 6.1.
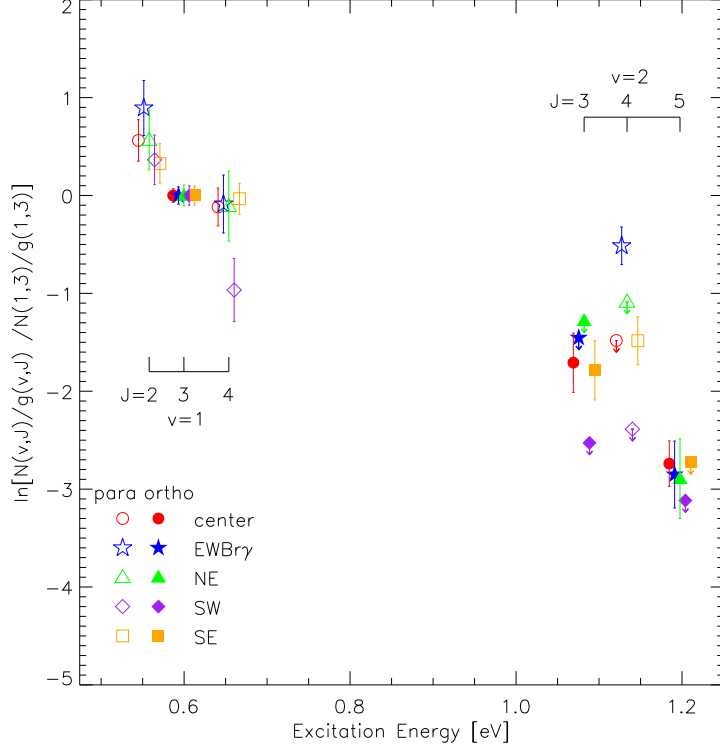
Figure 6.4: H_2 population level diagram. The level population is normalized to the one at the $(v, J) = (1, 3)$ level. The para (ortho) lines emitted in each region are represented with empty (filled) symbols as indicated in the label. If the thermal excitation was dominant in a certain region, the observed H_2 population levels would lie above a straight line.

If the collisional de-excitation was dominant, there would not be a major difference between the vibrational and rotational temperatures $T_v \simeq T_r \simeq T_{exc}$ and the population of the energy levels would follow a Boltzmann distribution, i.e.

$$\frac{N(v, J)}{g(v, J)} \propto \exp \left[\frac{-E(v, J)}{k_b \, T_{exc}} \right], \qquad (6.5)$$

where $E(v, J)$ is the energy required to excite the (v, J) level of the H_2 molecule. This seems to be case in the SW region, although the excitation temperature is so low that the emission lines in the $v = 2$ level lie below the detection limits. Their upper limits, derived from the fluxes and shown in Fig. 6.4, correspond to $3\times$ the noise measured at both sides of the expected line. In the NE region a similar situation is suggested by the population diagram and by the excitation temperatures. There the gas can be in a LTE at $T_{exc} \approx 2200 \, \mathrm{K}$.

From the calculated T_r and T_v in the EWBRγ and SE regions the action of non-thermal-UV photons is not clear. However, in these two regions, the populations of the $v{=}2$, $J{=}4$ level are significantly higher that in the adjacent $(2,3)$ and $(2,5)$

levels. This seems to be a characteristic signature of non-thermal excitation as has been pointed out by several authors (e.g., Sternberg et al. 1987). I have tried to reproduce this strong feature with the fluorescence models of Davies et al. (2005) and those of Draine & Bertoldi (1996). The models basically assume plane-parallel geometry of a semi-infinite H_2-cloud, which is isotropically irradiated with UV-photons in the Lyman and Warmer bands from one side. The parameters are the gas density n_H, the temperature at which the first layer of the cloud is heated T_0, and the intensity of the radiation field χ (relative to the local interstellar medium). In all cases the best fit led to $N(2,3)/g(2,3) \approx N(2,4)/g(2,4)$, and an extra thermal component was required to reproduce the populations of the $v = 2$ level to the observed values. The best fit was reached by models with $n_H = 10^4 \, cm^{-3}$, $T_0 \approx 500 - 1000 \, K$ and radiation field with $\chi = 10^2$.

In the central region the presence of a non-thermal agent is evident from the difference between T_r and T_v. Other galaxies like Mrk 1210, Mrk 504, and NGC 5728 show the similar mixed excitation around the central $\sim 100 \, pc$ (Rodríguez-Ardila et al. 2004). However, this is far from being common. In bigger samples of AGN with detected molecular hydrogen emission at the center, the thermal excitation is the dominant mechanism, with temperatures $\sim 2000 \, K$ (Rodríguez-Ardila et al. 2005b; Reunanen et al. 2002).

Table 6.1: Rotational and vibrational temperatures and the ortho-para ratio in different regions on the IRAS 01072+4954 bulge

Region	$T_{r(v=1)}$ (K)	$T_{r(v=2)}$ (K)	T_v (K)	ϕ_1	$1/\phi_2$
Center	1650 ± 650	1550 ± 650	3000 ± 500	2.3 ± 0.3	> 2.0
EWBrγ	1150 ± 450	> 1200	< 3250	1.9 ± 0.3	< 0.6
NE	1650 ± 1100	> 1000	< 3700	2.3 ± 0.4	$-$
SW	850 ± 250	$-$	< 1650	3.7 ± 0.6	$-$
SE	3100 ± 2050	< 1600	2900 ± 550	2.5 ± 0.3	< 1.5

An indicator of H_2-fluorescence is the ortho-para ratio ϕ, which represents the relative populations of molecular hydrogen in ortho and para states. The ortho-para ratio can be calculated following Smith et al.(1997; see also, Davis et al. 2003) from the column densities of three rotationally-consecutive lines in the same vibrational transition as

$$\phi = \left[\frac{N_1/(2J_1+1)}{N_2/(2J_2+1)} \right]^{\frac{T_1-T_0}{T_2-T_0}} \left[\frac{N_1/(2J_1+1)}{N_0/(2J_0+1)} \right]^{\frac{T_2-T_1}{T_2-T_0}}, \tag{6.6}$$

where T_0, T_1, and T_2 are the excitation temperatures, i.e. the energy required to excite the lines to the upper level of the transition in Kelvin. N_1 and N_3 are

para-H_2, and N_2 correspond to ortho-H_2, otherwise – i.e, for sequences containing two ortho transitions – the ortho-para ratio would be the inverse of this quantity (Smith et al. 1997). Using Eq. (6.2), the ortho-para ratio in the first ϕ_1, and in the second $1/\phi_2$ vibrational levels can be found from the fluxes of the lines as

$$\phi_1 = 0.809 \left[\frac{F_{1-0\,S(1)}}{F_{1-0\,S(2)}}\right]^{0.431} \left[\frac{F_{1-0\,S(1)}}{F_{1-0\,S(0)}}\right]^{0.569}, \qquad (6.7a)$$

$$1/\phi_2 = 0.898 \left[\frac{F_{2-1\,S(2)}}{F_{2-1\,S(3)}}\right]^{0.448} \left[\frac{F_{2-1\,S(2)}}{F_{2-1\,S(1)}}\right]^{0.552}, \qquad (6.7b)$$

where the negligible (of the order of 10^{-3}) reddening correction to the ratios has been omitted in these expressions (for more details see Smith et al. 1997). The ortho-para ratios derived from the selected apertures are shown in Table 6.1. In some regions, the faintness of the observed $v = 2$ lines did not allow such calculation. In regions where the gas is collisionally excited via shocks, heated by ionizing radiation or where the density $n_H \geq 10^4\,cm^{-3}$, the ratio of H_2-ortho to H_2-para is $3 : 1$ (e.g., Sternberg et al. 1987). Any of these mechanisms or a combination of them can be in place in the SW region, where $\phi \sim 3.0$ confirms the results of the excitation diagram (Fig. 6.3). In contrast, observed ratios $\phi \sim 1.7$ indicate FUV irradiated H_2, like in the EWBrγ region. Ratios in the range $1.5 - 2.2$ have been reported in PDRs (e.g., Chrysostomou et al. 1993; Levenson et al. 2000; Stacey et al. 2010). In such clouds the 'true' ortho-para ratio can still be 3. Sternberg & Neufeld (1999) showed that the observed ϕ depends on the FUV-pumping rate, and given that fluorescence occurs via optically thick absorption lines, this rate depends on the optical depth of the H_2-species. The ortho-H_2 is optically thicker than the para-H_2 and therefore, the higher vibrational level ortho-H_2 transitions look less populated. This scenario offers an explanation for the ortho-para ratio in the first vibrational level of most of the regions. However, considering the very low $1/\phi_2$ in the EWBrγ and in the SE apertures, it is probable that the populations of the $v = 2$ level there are not in thermodynamic equilibrium and therefore, the 'intrinsic' ortho-para ratio is less than 3.0.

6.2 Stellar kinematics

Though the bar-like structure is barely detected photometrically, the kinematics of the stars very close to the center are clearly affected by its presence. To elaborate a map of the stellar line-of-sight velocity distribution (LOSVD), the data was binned in apertures of three different sizes such that each bin had $S/N > 15$. Then, the LOSVD of the spectra integrated in every aperture was fitted using the pPXF routine (Cappellari & Emsellem 2004; a detailed explanation of the fitting procedure and the error estimation is presented in Sect. 5.3.4), and finally the results were combined by averaging the maps of different aperture-bin sizes. In this way it is possible to obtain a first estimate of the stellar velocity field: LOS velocity and velocity dispersion σ_* (Fig. 6.5). Special care has to be taken when interpreting the

maps, because the combining procedure smooths the velocity gradients, and the error of the values increases with the distance to the center. Given the low values of LOS velocity and velocity dispersion, and the low S/N of single pixel spectra, even after binning the data only information of the central square arcsecond ($\sim 460\,\mathrm{pc}$) can be recovered.
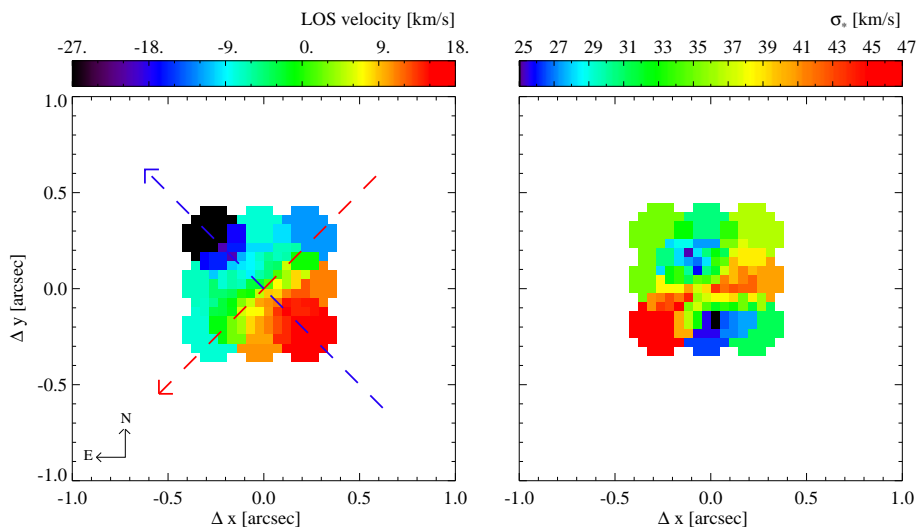
Figure 6.5: Stellar kinematics in the central arcsecond of IRAS 01072+4954. Line of sight velocity (*left*) and velocity dispersion (*right*) obtained from the combination of apertures of different sizes. In each aperture, the LOSVD parameters were determined by fitting stellar templates. The maps are consistent with a low-inclined disk + bar (or inner-disk). The two axes shown in the left-hand panel correspond to the highest LOS velocity gradient (blue dashed line) and axis perpendicular to it (red dashed line).

Figure 6.5 shows the stellar LOS velocity and the velocity dispersion maps constructed from the NIFS *K*-band data cube. The first one displays a characteristic rotation pattern with a low gradient, consistent with the expectations for a disk galaxy viewed nearly face-on. In the dispersion map, there is a clear evidence for an internal structure with P.A. $\approx 120°$.

To get a better estimation of the rotation curve and the uncertainties, I simulate a long slit of $\sim 1\,\mathrm{arcsec}$ width that cross the center with different orientations. The data of every slit were binned in rectangular sections perpendicular to the orientation axes. The width of the rectangular sections was defined to have the maximum number of pixels and an overall S/N in the range 10-20. Then, the pPXF routine was applied tuning the bias in every single bin to obtain the best fit and the uncertainties in each case. Figure 6.6 shows the derived rotation and dispersion curves for the slit oriented along the highest LOS velocity gradient (P.A. $\approx 45°$) and for the slit perpendicular to it.

The LOS velocity curve obtained along the axis with P.A. $\approx 30°$ displays a typical disk rotation pattern, while that derived from the slit rotated 90° with respect to the previous one is consistent with zero rotation. The stellar dispersion
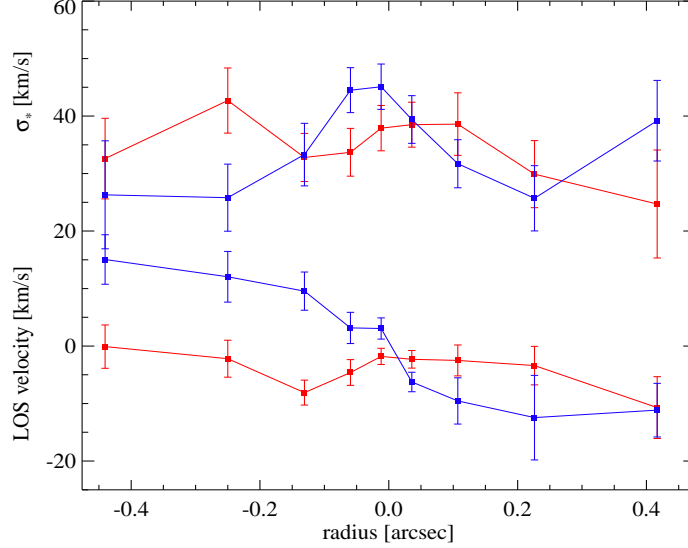
Figure 6.6: Rotation (*bottom*) and dispersion (*top*) curves in the central arcsecond of IRAS 01072+4954. The curves were obtained from the simulated long-slit spectroscopy along the two axes shown in Fig. 6.5. Blue curves+points correspond to the slit along the axis with highest LOS velocity gradient, red curves+points to a slit perpendicular to the previous one. The radius to the center increases from west to east.

along the first axis increases toward the center, as expected from stars in non-circular orbital motions located preferentially perpendicular to the axis and crossing the center of the galaxy. The dispersion curve along the second axis is more difficult to interpret. The data does not allow to clearly identify the ending positions of the stellar central structure. In the first and last data points, the uncertainties are still very high, and probably under-represented in the plots, given the faintness of this bar-like structure in the NIFS observations.

6.3   Gas kinematics

Three species in the NIR IRAS 01072+4954 emission are well resolved and have good S/N to map their velocity fields: [Fe II], H_2 1-0 S(1) and Brγ. In every spatial pixel of the field of view, the lines were modeled as Gaussians over a flat continuum, which was calculated as the median over neighboring regions. Although at some positions the lines show very skewed profiles, I did not attempt to fit them with higher-order polynomials because of the low LOS velocity and velocity dispersion, which are close to the velocity scale ($km\,s^{-1}$ per spectral pixel) of our observations. Figures 6.7 - 6.9 show the motion along the line of sight and the velocity dispersion of the Brγ, H_2, and [Fe II]. In general, the velocity fields are dominated by rotation, with the north(-east?) side approaching and the south(-west?) receding from us. This is a similar pattern to that observed in the stellar LOS velocity, but the velocity dispersion maps reveal more disturbed kinematics. Toward the north-east

('blue part'), Brγ and [Fe II] show a gas component with a higher receding velocity compared to the surroundings. Interestingly, H$_2$ shows a similar feature, but at the very center of the LOS velocity map (gas inflow?), which corresponds to a 'hollow' in the velocity dispersion map. The $\sigma_{\text{Br}\gamma}$ and σ_{H_2} maps show elongated structures along the axis with the highest velocity gradient. The $\sigma_{\text{[Fe II]}}$ map reveals a mirrored 'C'-like feature at the south-west, which has been observed in the velocity dispersion map of other forbidden species in other galaxies. This seems to be an indication for gas outflow.
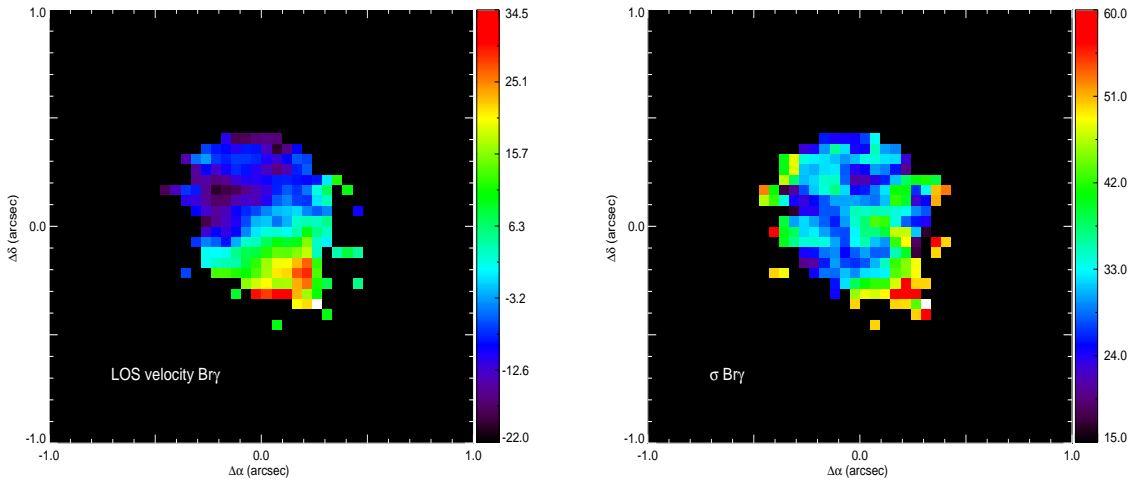
Figure 6.7: Kinematics of the ionized Hydrogen (Brγ) in the central arcsecond of IRAS 01072+4954. *Left:* Line of sight velocity in km s^{-1} with respect to the systemic velocity of the galaxy. *Right:* Velocity dispersion in km s^{-1} and corrected for instrumental broadening. The minimum was set arbitrarily to 15 km s^{-1} for displaying purposes. Black pixels replace unreliable data points.
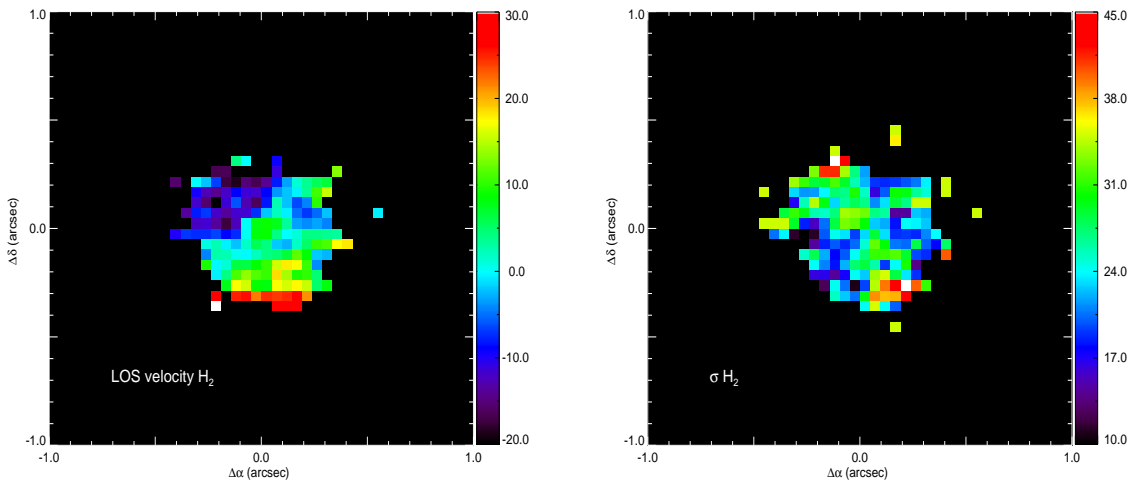
Figure 6.8: Same as in Fig. 6.7, but for the warm molecular hydrogen (H$_2$ 1-0 S(1)).
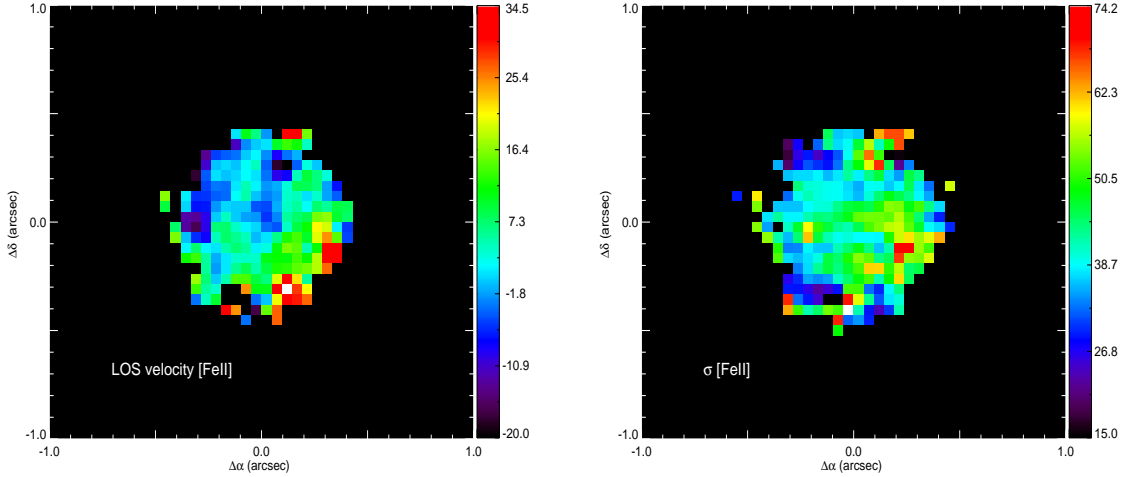
Figure 6.9: Same as in Fig. 6.7, but for the [Fe II].

6.3.1 Indications for a central outflow: AGN Feedback?

Using channel maps it is possible to see the position of the gas mass that is moving with certain velocity along the line of sight. To create them, an image of the intensity of the continuum was subtracted from every spectral slide of the data cube. Then all the slides that compose the profile of the lines are plotted. Their spectral position relative to the systemic position of the line is registered in $\mathrm{km\,s^{-1}}$, and reflects our spectral sampling $\sim 25\,\mathrm{km\,s^{-1}}$. Figures 6.10 - 6.11 show the channel velocity maps of $Br\gamma$, H_2 and [Fe II]. The color gradient corresponds to the specific flux of the line, i.e. $f_\lambda - f_{\lambda,\,\mathrm{continuum}}$ in $\mathrm{erg\,s^{-1}\,cm^{-2}\,\mu m^{-1}}$. It has been normalized to the maximum value of each image. Points with specific flux less than 10% of the peak value were masked.

The interpretation of the channel maps is not straightforward due to the low spatial and spectral sampling, however some trends can be seen. For example, the ionized hydrogen seems to move preferentially from north-east to south-west, which could be interpreted as a typical rotation pattern. The gas extension to the south that turns toward the west in the bottom three panels, however, might be a different component. The semi-circular feature in the last channel is usually associated to a conical outflow. In contrast, the molecular hydrogen shows a stream of gas from the north-east (probably bending also at the tip from the north) that feed gas into the diagonal structure revealed by the σ_{H_2}-map. At the systemic velocity the gas spreads perpendicularly (along the stellar bar?), and continues to the south at $29\,\mathrm{km\,s^{-1}}$ and south-west at $58\,\mathrm{km\,s^{-1}}$. This kind of H_2 motion has also been observed in the nearby Seyfert galaxy Mrk 1066 (Riffel & Storchi-Bergmann 2011a). With better sampling and resolution, the authors interpreted the velocity
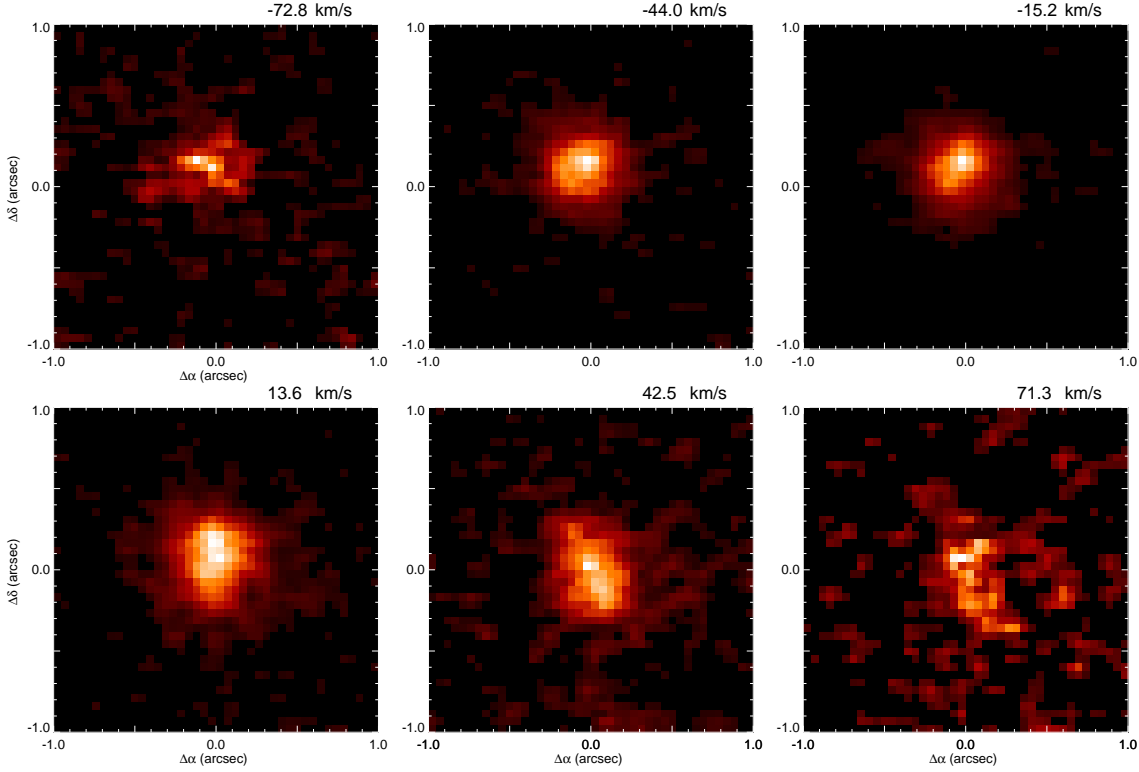
Figure 6.10: Channel velocity maps along the Brγ emission-line profile. The color coding corresponds to a linear gradient of the specific flux, normalized to the maximum in each map.

field as an inclined disk that is fed by gas from two streamers that connect to the spirals arms of the disk as seen from an optical HST image. The presence of circumnuclear molecular disks has also been revealed by IFU NIR observations of other Seyfert galaxies (Hicks et al. 2009).

On the other hand, there are also indications for an outflow. First, the high LOS velocity components visible at the north-east in the Brγ and [Fe II] maps. A direct comparison with the stellar velocity suggests gas outflow LOS velocities of $\sim 30\,\mathrm{km\,s^{-1}}$. Second, the [Fe II] channel maps resemble a bicone with the symmetry axis close to that of the highest stellar velocity gradient. Although that would speak in favor of the motion driven by the stellar rotation, the gas does not move uniformly from north-east to south-west as it would be expected in that case. In contrast, the [Fe II] gas displays blue- and red-shifted 'X'-shape patterns, which would correspond geometrically to a pair of longitudinal cuts of a bicone by planes parallel to each other (and to the plane of the sky) placed close to the symmetry axis (in Fig. 6.11, channel with velocities $-55\,\mathrm{km\,s^{-1}}$ and $59\,\mathrm{km\,s^{-1}}$). As we get closer to the systemic velocity the emission is elongated and at $\sim 30\,\mathrm{km\,s^{-1}}$ the gas shows two peaks. Moving toward higher receding velocities the '8'-shape and
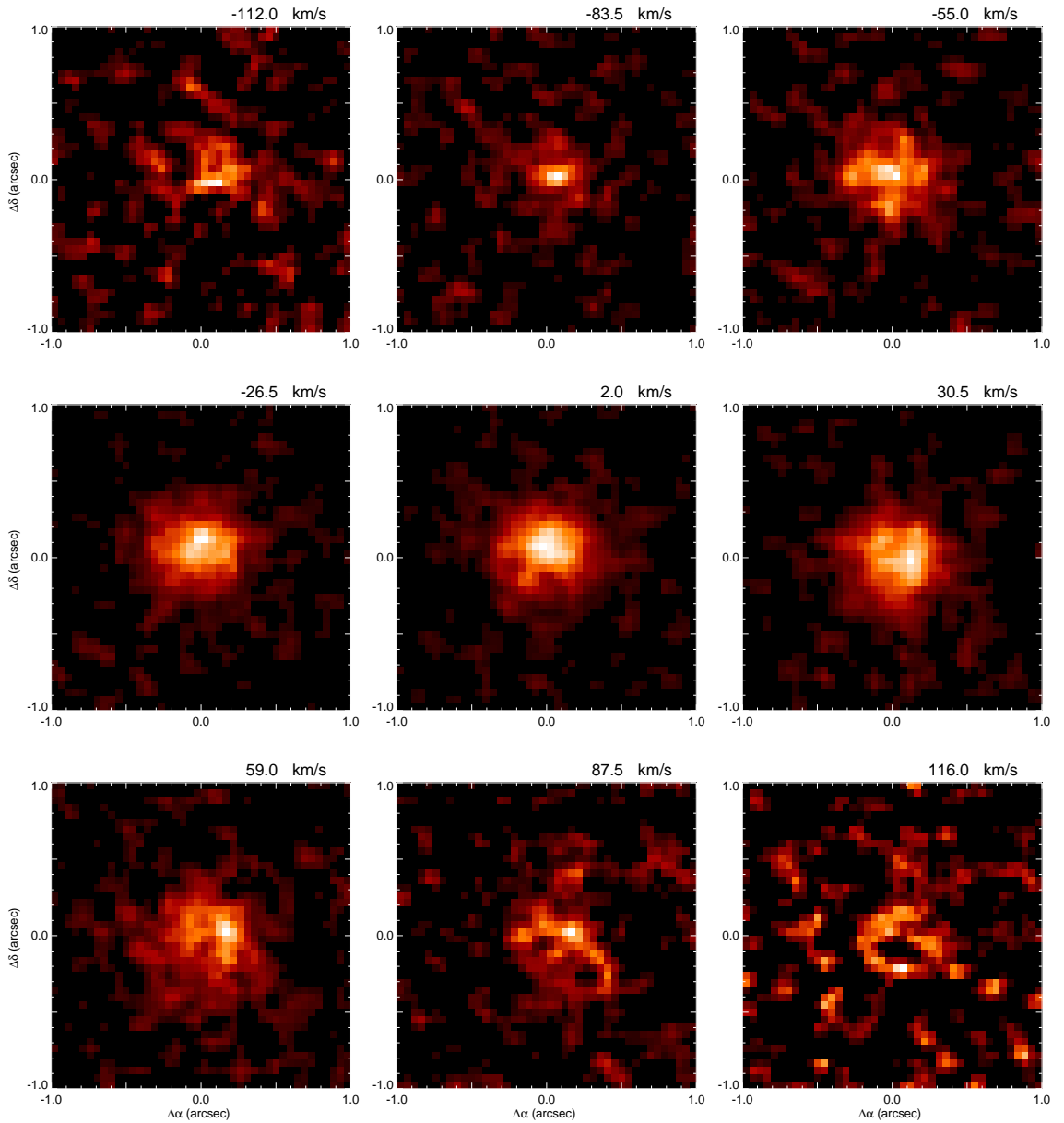
Figure 6.11: Same as in Fig. 6.10, but for the [Fe II]. Some typical outflow features are seen in the panels, e.g., the 'X'-shape at $-55\,\mathrm{km\,s^{-1}}$ and $59\,\mathrm{km\,s^{-1}}$, the double peaks at $30\,\mathrm{km\,s^{-1}}$, and the inclined '8'-shape at $88\,\mathrm{km\,s^{-1}}$.

elongated circular pattern represent what it is expected for further longitudinal cuts of the bicone at somewhat larger distances from the center. A proper modeling of the [Fe II] line of sight velocity distribution is necessary to have an estimate of

the characteristics of this outflow, e.g., inclination, opening angle, and velocity. However, because of the limited S/N is not possible to get a proper fit of the parameters. The procedure is described and applied to nearby galaxies in Das et al. (2005, 2006); Müller-Sánchez et al. (2011), see also Riffel & Storchi-Bergmann (2011a); Friedrich et al. (2010).
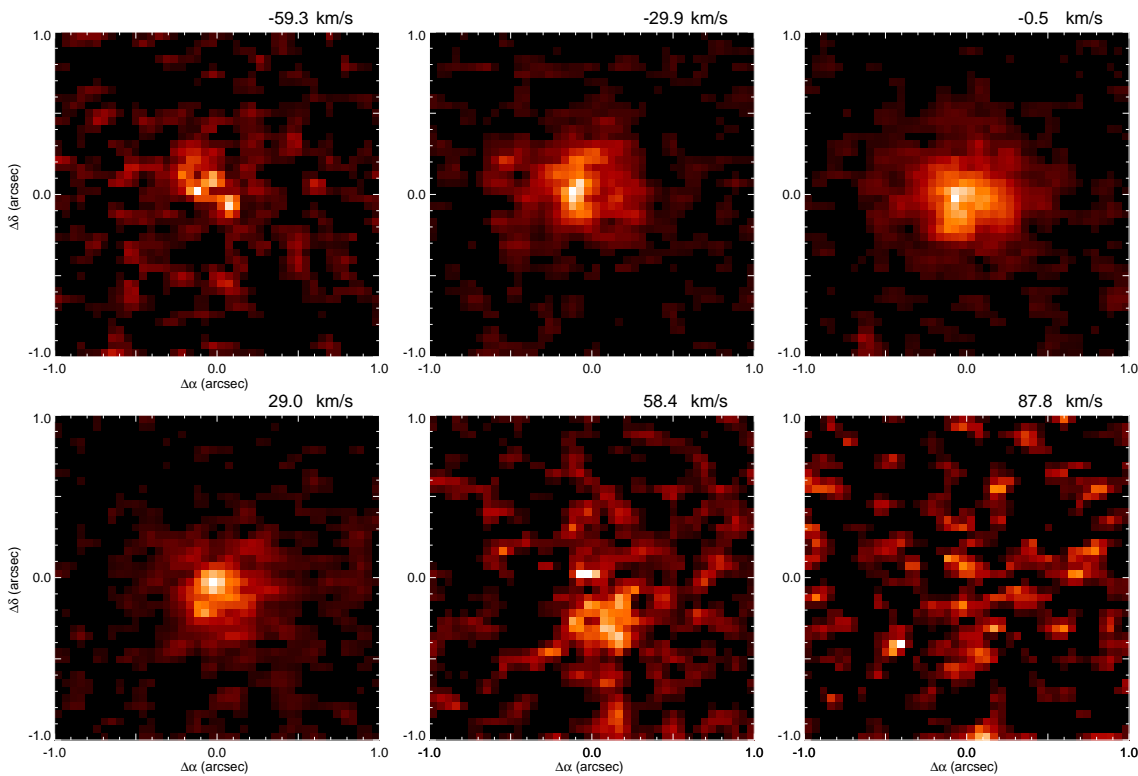
Figure 6.12: Same as in Fig. 6.10, but for the warm molecular hydrogen (H_2 1-0 S(1)). The last channel map is shown to get a direct comparison with the H II channel maps, but no significant H_2 emission is detected with that velocity.

6.4 Symbiotic relation between the AGN and the star formation

Dedicated observations have shown that disentangling the star formation and AGN activity in sources with no-clear dominant ionization mechanism might not be only difficult, but probably physically impossible. For example, hard X-ray emission seems to undoubtedly signify the presence of an AGN, but this is only in the case of low obscured objects. Polycyclic aromatic hydrocarbons (PAHs), which are considered as some of the clearest star formation tracers, can be easily destroyed by

a hard radiation field as well as by energetic shocks. The far-infrared flux-density ratio $f_{25\,\mu m}/f_{60\,\mu m}$ has been used to distinguish between 'cool' (star formation dominated) and 'warm' (AGN dominated) dust heaters, but also as an indicator of tori inclination. The optical diagnostic diagrams, on the other hand, are very successful in classifying luminous sources, but fail at low metallicity and low luminosity AGN independent on their Eddington rate. The star formation and the AGN partially mimic, but also destroy, the signatures of each other. The reason is that they take place in environments that might be interconnected in different ways.

During a merger process, both stellar and nuclear activities are simultaneously enhanced. Other fueling mechanisms, like bars and minor galaxy interactions, might also indicate a coincidental, more than causal, connection between the two activities (e.g., González Delgado 2002; Orban de Xivry et al. 2011). However, it has been proposed that star formation might disturb the interstellar medium favoring the gas infall into the central engine (see e.g., Hill et al. 1999; Ivanov et al. 2000; Watabe et al. 2008). On the other hand, AGN-outflows can have an important impact on the galaxy host, blowing material away, forming cavities and quenching the star formation (Fabian 2012, and references therein). But also star formation can power strong galactic wind, such that a considerable percentage of the gas mass is expelled out of the galaxy (Veilleux et al. 2005, and references therein).

6.4.1 Positive Feedback?

The gas kinematics in the central arcsecond of IRAS 01072+4954 show two distinct components: one in rotational motion that roughly follows that of the stars, but with the line-of-nodes on a probably different position angle; and a second one, which is traced mainly by the [Fe II], that shows signs of a biconical outflow. Although the star formation seems not to be much enhanced in the central $\sim 0.15''$ in comparison to the surrounding regions[1], in Chapter 4, the boxy-like hump at $\sim 1.55\,\mu$m in the central spectrum reveals the presence of young supergiants with spectral type later than K3 and luminosity class brighter than III. Can the observed outflow be powered by a central young nuclear cluster or is it a sign of AGN feedback? Müller-Sánchez et al. (2011) pointed out that for a typical SFR $\sim 1\,M_\odot\,\mathrm{yr}^{-1}$ in the central 200 pc, the energy injected by post-starbursts in the interstellar medium, $\dot{E} = 7.0 \times 10^{41}(\mathrm{SFR}/\,M_\odot\,\mathrm{yr}^{-1})\,\mathrm{erg\,s}^{-1}$ (Veilleux et al. 2005), is in the range of that calculated by modeling the NIR biconical coronal outflows in a sample of six nearby Seyfert galaxies. This means that looking at the energy budget, a young-to-intermediate stellar population could power the observed outflow.

The main consideration against the starburst-driven outflow is the dynamical time-scale. Until now, using the line emission and the K-band tracers, only upper limits on the star formation activity at the center could be obtained. This is due

---

[1]$\mathrm{SFR}_{0.15''} < 0.35\,M_\odot\,\mathrm{yr}^{-1}$, while $\mathrm{SFR}_{0.8''} \approx 1\,M_\odot\,\mathrm{yr}^{-1}$

to the impossibility to disentangle the AGN and the star formation contributions. However, looking only at the stellar absorption features in the H-band spectrum, where the hot dust emission is negligible, it is possible to estimate the approximate age of the stellar population in that region. Table 4.3 reports the equivalent widths of Si I and CO(6-3), which can be compared with stellar evolution synthesis models to estimate the age of the burst. Using the code Starburst99, assuming the Salpeter IMF in the mass range $(0.1-120)\,M_\odot$ and the Padova AGB tracks with solar metallicity, the resulting age was 10 Myr and 20 Myr, for instantaneous and continuous star formation, respectively. On the other hand, the dynamical time-scale of the outflow is determined by its radial size, which in our case is $r_{\rm out} \approx 150\,{\rm pc}$, and the maximum outflow velocity, that it is assumed to be $v_{\rm max} \gtrsim 100\,{\rm km\,s^{-1}}$, although this corresponds only to the motion along the line of sight, and that is why it was set as a lower limit. In these circumstances, the outflow might have originated in an event at most 1.5 Myr ago, which means that the burst of the stellar population at the center could not have caused the observed outflow. Another argument against the post-starburst as the main trigger of this event is the collimated shape of the outflow, which can be recognized in the [Fe II] channel maps as well as in the $\sigma_{\rm [Fe\,II]}$ map.

Can the low-luminosity AGN in IRAS 01072+4954 power the outflow? In a first approximation, following Heckman et al. (1990), the energy of a bubble inflated into a medium with uniform density n_0 can be found as

$$\frac{\dot{E}}{\rm erg\,s^{-1}} = 3n_0 \times 10^{41} \left(\frac{r_{\rm out}}{\rm kpc}\right)^2 \left(\frac{v}{100\,{\rm km\,s^{-1}}}\right)^3. \tag{6.8}$$

Using the previously estimated values and $n_0 \sim 3\,{\rm cm^{-3}}$ (Heckman et al. 1990), one finds $\dot{E} \lesssim 2 \times 10^{40}\,{\rm erg\,s^{-1}}$. Note that in this case, the velocity in the model corresponds to a constant expansion rate, which in our case might be $v \lesssim 100\,{\rm km\,s^{-1}}$ and the calculated power would be an upper limit. Comparing this result with the bolometric luminosity of the AGN found in Sect 5.4, $L_{\rm bol} \sim 10^{42.5}\,{\rm erg\,s^{-1}}$, it seems totally plausible that it is responsible for the observed gas outflow. Note that although the energy injection was estimated under the assumption of a spherically symmetric outflow, the result is in agreement with the kinetic luminosities derived from warm X-ray absorbers $\dot{E} \sim (10^{-3} - 10^{-6})L_{\rm bol}$ (cf. Wang et al. 2007).

The outflow opening angle points to the north-east (NE) and to the south-west (SE), although the former looks 'more collimated' than the latter. This might be the visual appearance derived from the fact that most of the northern-part of the cone lies under an optically thick screen, which could be the galactic disk. In the southern-part, the situation is the opposite. The increased $\sigma_{\rm [Fe\,II]}$ toward the SE might be indicative for this. Does the outflow affect the star formation in the bulge? At the NE, a region with enhanced star formation was already identified in Chapter 4. Its SFR is not comparable with that in the EWBrγ region, but it also exhibits a predominantly young stellar population. The H_2 diagnostic diagram also showed that these two regions are ionized by a non-negligible fraction of Lyman/Werner

photons, which produce H_2-cooling via fluorescence and suggests the presence of young OB stars.

Is this a case of positive feedback? Did the AGN outflow cause the star formation burst? In order to estimate the age of the burst, in a similar way as was done before, the equivalent width of the $Br\gamma$ emission line measured in the aperture can be compared with synthesis models. In this case, given that there is an underlying older stellar population, and it is desired to isolate the emission from the young stars, I compared the K-band magnitude in the NE region with that of the Median aperture, finding that $\sim 85\%$ of the continuum flux in the region can be attributed to the older component. When correcting for it, $W_{Br\gamma}$ increases from what is reported in Table 4.3 to ~ 55Å. Using Starburst99, with the same assumptions as before, the age of the burst is $\sim 5\,\mathrm{Myr}$, implying that the outflow did not cause the star formation burst in this region. However, it might contribute to stimulate the process. Moreover, it must be pointed out that the so-called 'negative' feedback is usually associated with collimated jets that hit the interstellar medium destroying the dense clouds where the star formation should take place. In this case, given the different physical conditions, such an extreme situation is not expected.

At the other side of the outflow, strong emission of ionized helium compared to hydrogen is registered, $He\,\textsc{i}/Br\gamma > 0.3$. Similar values have been observed in other starburst galaxies like M 82, NGC 3256A, and NGC 3690A, which show signs of recent ($\sim 10\,\mathrm{Myr}$) bursts. Although it was thought that the $He\,\textsc{i}/Br\gamma$ ratio might trace or put constraints on the conditions of the young stellar population bursts (Doyon et al. 1992), Lumsden et al. (2003) have shown that the $He\,\textsc{i}\,2^1P - 2^1S$ at $\lambda\,2.058\,\mu$m is also sensitive to collisional excitation, which indicates it might be expected in shock environments. In that sense, the location of the SW aperture in an H_2 diagnostic diagram is also misleading. Mapping the H_2 line ratio 1-0 S(2)/1-0 S(0) across the field of view shows a hollow at the position of the high $[Fe\,\textsc{ii}]/Br\gamma$ ratio, but it is enhanced around it, i.e. also surrounding the mirrored 'C'-like shape of the $\sigma_{[Fe\,\textsc{ii}]}$ map in that area. This might be indicative for shock excitation.

6.4.2   Gas content

Cold gas provides a reservoir for feeding the clouds where star formation can take place, and also for fueling the central black hole. Observationally, the surface gas density Σ_{gas} correlates with the projected star formation rate density Σ_{SFR}. Meanwhile, models of supernova explosions-driven turbulence predict a dependence of the black hole mass accretion rate on the surface mass density of the gas in the central $\sim 100\,\mathrm{pc}$. Here, I calculate the gas inventory in the bulge of IRAS 01072+4954 and study its association with the star formation and the accretion onto the black hole.

The gas in the bulge can be considered as composed by ionized and neutral hydrogen, and hot and cold H_2. Helium can amount up to $\sim 25\%$, while other elements are present in much smaller quantities. The ionized hydrogen mass can be calculated as $M_{H\,\textsc{ii}} = m_H n_e V_{H\,\textsc{ii}}$, where n_e is the electron density and $V_{H\,\textsc{ii}}$

the volume of the region. Moreover, the factor $n_{\mathrm{e}}^2 V_{\mathrm{H\,II}}$ can be obtained from the luminosity of the Brγ emission line as

$$L_{\mathrm{Br}\gamma} = 3.3446 \times 10^{-27} n_{\mathrm{e}}^2 V_{\mathrm{H\,II}}, \tag{6.9}$$

with the luminosity in $\mathrm{erg\,s^{-1}}$. Therefore,

$$\frac{M_{\mathrm{H\,II}}}{\mathrm{M_\odot}} = 2.5157 \times 10^{-31} \left(\frac{L_{\mathrm{Br}\gamma}}{\mathrm{erg\,s^{-1}}} \right) \left(\frac{n_{\mathrm{e}}}{\mathrm{cm^{-3}}} \right)^{-1}, \tag{6.10}$$

where $T = 10^4\,\mathrm{K}$ was assumed. With the Brγ flux obtained for the bulge and reported in Table 4.2, and taking $n_{\mathrm{e}} = 100\,\mathrm{cm^{-3}}$, I obtain $M_{\mathrm{H\,II}} \approx 2.8 \times 10^6\,\mathrm{M_\odot}$. The neutral hydrogen H I is believed to densely populate regions out of the inner galactic disk and toward its outskirts. Here for the bulge, its mass is assumed to be only few times that of H II.

The mass of the hot molecular hydrogen can be derived from the observed $\mathrm{H_2}$ 1-0 S(1) emission, which is one of the strongest lines in the K-band spectrum. From Eq. (6.2), the flux of this line can be written as

$$F(1,3) \equiv F_{1-0\,\mathrm{S}(1)} = \frac{n_{\mathrm{H_2}} V_{\mathrm{H_2}} f_{(1,3)} A_{\mathrm{ul}\,(1,3)}}{4\pi D^2} \frac{hc}{\lambda}, \tag{6.11}$$

where the column density is expressed as the fraction $f_{(1,3)}$ of the hot $\mathrm{H_2}$ in the $(v, J) = (1.3)$ level, multiplied by the molecular hydrogen number density $n_{\mathrm{H_2}}$, in the volume $V_{\mathrm{H_2}}$ and the projected area. Following Scoville et al.(1982; see also Dale et al. 2005), the mass of the ionized molecular hydrogen is

$$
\begin{aligned}
M_{\mathrm{H_2\,(hot)}} &= 2\,m_{\mathrm{H}}\,n_{\mathrm{H_2}} V_{\mathrm{H_2}} \\
&= 2\,m_{\mathrm{H}}\,4\pi D^2 \frac{F_{1-0\,\mathrm{S}(1)}}{f_{(1,3)}\,A_{\mathrm{ul}\,(1,3)}} \frac{\lambda}{hc} \\
&\approx 5.0776 \times 10^{13}\,\mathrm{M_\odot} \left(\frac{F_{1-0\,\mathrm{S}(1)}}{\mathrm{erg\,s^{-1}\,cm^{-2}}} \right) \left(\frac{D}{\mathrm{Mpc}} \right)^2. \tag{6.12}
\end{aligned}
$$

Using $A_{\mathrm{ul}\,(1,3)} = 3.47 \times 10^{-7}\,\mathrm{s^{-1}}$ (Wolniewicz et al. 1998) and $f_{(1,3)} = 1.22 \times 10^{-2}$ for a temperature $T \approx 2000\,\mathrm{K}$ (Scoville et al. 1982), the hot molecular-gas mass in the IRAS 01072+4954 bulge is $M_{\mathrm{H_2\,(hot)}} \approx 290\,\mathrm{M_\odot}$.

However, the hot $\mathrm{H_2}$ is only a small fraction of the molecular gas available in the bulge. In order to estimate the mass of the cold $\mathrm{H_2}$, which is usually derived from submillimeter observations of the CO (1-0), it is possible to use the scaling relation derived by Mazzalay et al. (2012) from ~ 50 sources. The selected objects covered a wide range of luminosities, morphological types and nuclear activity. According to the authors, the ratio $M_{\mathrm{H_2\,(cold)}}/M_{\mathrm{H_2\,(hot)}} \simeq (0.3 - 1.6) \times 10^6$ in the whole sample. In our case, this means $M_{\mathrm{H_2\,(cold)}} \approx (87 - 464) \times 10^6\,\mathrm{M_\odot}$. This value is consistent with that found using other estimators like the f_{60}/f_{100} ratio (Dale et al. 2005).

6.4.3   Kennicutt-Schmidt law, feeding and feedback

Figure 6.13, modified from Bigiel et al.(2008; see also Kennicutt & Evans 2012), shows the relation between the star formation rate density $\Sigma_{\rm SFR} \equiv {\rm SFR}/\pi r^2$, and the total (atomic and molecular) gas surface density $\Sigma_{\rm gas} \equiv (M_{\rm H\,I} + M_{\rm H_2})/\pi r^2$, for spatially and non-spatially resolved objects. This diagram is known as the Kennicutt-Schmidt law. Two or three regimes, marked with vertical dotted lines, can be seen through the correlation. In low surface density sources ($\Sigma_{\rm gas} \lesssim 9\,{\rm M_\odot\,pc^{-1}}$), the SFR does not correlate with the H\,I density, partially because at that surface density, the H\,I column density $N_{\rm H\,I} \sim 10^{21}\,{\rm cm^{-2}}$ indicates an efficient conversion from atomic to molecular hydrogen. This transition phase might be in part responsible for the slope variation in the diagram (Kennicutt & Evans 2012). On the other hand, starbursts reach surface gas densities $\Sigma_{\rm gas} \sim (200 - 10\,000)\,{\rm M_\odot\,pc^{-2}}$. It might be possible that the physical conditions under which the star formation processes in such dense environments take place are different from those in the Milky Way giant molecular clouds where $\Sigma_{\rm gas} \sim 150\,{\rm M_\odot\,pc^{-2}}$ (Bigiel et al. 2008). However, as discussed in Chapter 1 (Sect. 1.3.2.2), the position of LIRGs and ULIRGs in this diagram depends strongly on the assumptions made to estimate the mass content.

The diagonal lines in Fig. 6.13 depict the star formation efficiency – or its inverse, the gas depletion time – defined as $\epsilon_{\rm SF} \equiv \Sigma_{\rm SFR}/\Sigma_{\rm gas}$. The IRAS 01072+4954 bulge position in the diagram is obtained from the measured SFR using the Brγ as tracer[2], which gives $\Sigma_{\rm SFR} \approx 1.7\,{\rm M_\odot\,yr^{-1}\,kpc^{-2}}$, and the combined atomic and molecular gas estimations found above This indicates a star formation efficiency of $\sim 54\%$ per 10^8 years.

The strong correlation (Fig. 6.13 excluding the Seyfert galaxies) of the Kennicutt-Schmidt (K-S) law seems to indicate that the star formation process is mainly driven by the availability of cold gas. What is the effect of the AGN on this relation? The black hole accretes mass at a rate proportional to its bolometric luminosity[3],

$$\frac{\dot{M}}{\rm M_\odot\,yr^{-1}} \approx 1.75 \times 10^{-46} \left(\frac{\eta}{0.1}\right)^{-1} \left(\frac{L_{\rm bol}}{\rm erg\,s^{-1}}\right). \qquad (6.13)$$

This means, that a $L_{\rm bol} = 10^{43}\,{\rm erg\,s^{-1}}$ black hole accretes $\sim 2 \times 10^4\,{\rm M_\odot}$ during its duty cycle ($\sim 10^7$ yr), assuming $\eta = 0.1$. If the consumed mass was taken from the interstellar medium, Seyfert galaxies would lie at the left-side of the $\rm K-S$ law.

However, according to the SFR and gas-content estimations in Seyfert galaxies

---

[2]The Brγ flux was integrated over all regions around the nucleus, excluding the central $r \approx 75pc$ where the AGN as significant ionization agent can not be neglected. The area used was that of the integrated apertures.

[3]Strictly, the bolometric luminosity is related to the accretion luminosity $L_{\rm bol} = \eta \dot{M}_{\rm acc} c^2$, where $\eta \sim 0.05 - 0.42$ is the radiation efficiency, that is usually set to 0.1. For $\eta \dot{M}_{\rm acc}$ unit masses radiated in certain period of time, $\dot{M} = (1 - \eta)\dot{M}_{\rm acc}$ unit masses are accreted. This means, $L_{\rm bol} = [\eta/(1 - \eta)]\dot{M}c^2$, but for $\eta = 0.1$, $[\eta/(1 - \eta)] \approx 0.11$, which makes both expressions equivalent.
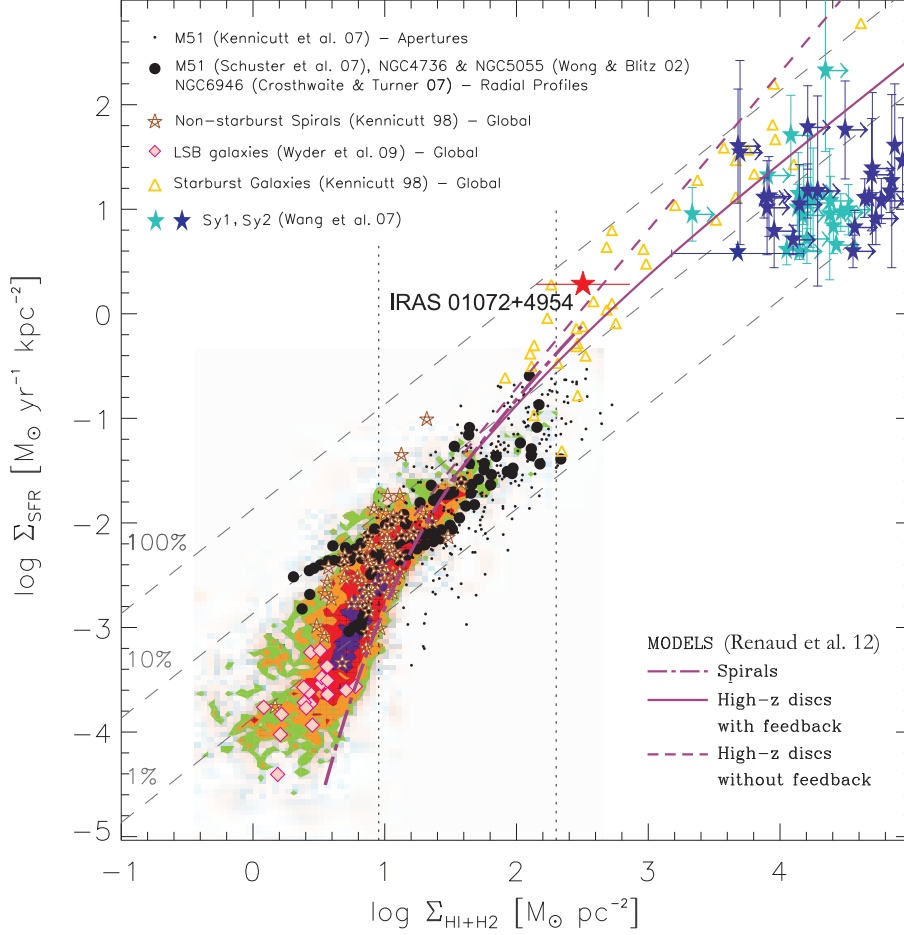
Figure 6.13: Star formation rate density vs. surface gas (atomic and molecular) density. The colored areas represent measurements on subregions of SINGS galaxies by Bigiel et al. (2008). Other resolved measurements include those from small apertures on M 51 (black dots), and from radial profiles (filled black circles) in M51, NGC 4736, NGC 5055, and NGC 6946 obtained by different groups as registered in the labels at the top-left. Measurements from unresolved data of spirals (empty brown stars), starbursts (gold triangles) and low surface brightness galaxies (LSB; filled pink diamonds) are also shown. In those sources, the authors adjusted the gas mass using the same conversion factor from CO(1-0) emission to H_2 for all objects. Diagonal dashed lines correspond to different star formation efficiencies (see text). Modified from: Bigiel et al. (2008). Circumnuclear regions of Seyfert galaxies (green and blue stars) from Wang et al. (2007) where also included. The vertical bar indicate the maximum and minimum $\Sigma_{\rm SFR}$ derived from the far-infrared and the $3.3\,\mu$m (which corresponds to the wavelength at which polycyclic aromatic hydrocarbons produce line emission) luminosities, respectively. The models of Renaud et al. (2012) for low-redshift sources without accounting for star formation feedback, and high-redshift objects with and without stellar feedback were overplotted with purple lines as indicated in the label at the bottom. IRAS 01072+4954 bulge is plotted as a red star. The horizontal bar reflect 1σ scatter of the conversion from warm to cold H_2.

made by Wang et al. (2007), the opposite seems to happen. There are two main reasons: (i) Most probably, the mass accreted by the black hole is that contained in the accretion disk and the torus, as two connected entities of the same accretion flow. In chapter 5, the hot dust mass was estimated in $\sim 10^{-3}\,\mathrm{M}_\odot$, but this corresponds only to the part of the dust that is very close to the central engine and that is in the process of sublimation. The total dust mass, derived from modeling the mid- and far-infrared AGN SEDs (e.g., Nenkova et al. 2008a,b), could amount to $\sim 10^3 - 10^4\,\mathrm{M}_\odot$. In the case of IRAS 01072+4954, the molecular hydrogen at the center ($r \approx 75\,\mathrm{pc}$) has a mass of $\sim 10^7 - 10^8\,\mathrm{M}_\odot$. The unresolved H_2 cloud shows an infall LOS velocity of $v_{\mathrm{H}_2} - v_{\mathrm{star}} \approx 10\,\mathrm{km\,s}^{-1}$, implying an inflow rate of $M_{\mathrm{inflow}} \sim 6.8\,\mathrm{M}_\odot\,\mathrm{yr}^{-1}$. However, to feed the black hole at the current rate, less than 10^{-4} times that amount of mass would be required. In fact at the current L_{bol}, IRAS 01072+4954 could consume its torus during its active lifetime leaving the rest ideally untouched. This would keep sources like IRAS 01072+4954 on the K-S law. (ii) On the other hand, inflow of gas into the circumnuclear region (CNR) implies an increasing gas density. Wang et al. (2007) showed that when the CNR medium becomes optically thick, the AGN activity heats the gas and blows it away to lower the star formation rates. The condition for the AGN feedback to take place is

$$\frac{\Sigma_{\mathrm{gas}}}{\mathrm{M}_\odot\,\mathrm{pc}^{-2}} \geq 9.0 \times 10^2 \left(\frac{\kappa}{5}\right)^{-1}, \tag{6.14}$$

where κ is the opacity, which in CNR medium has a median value of 5 (cf. Wang et al. 2007). The authors estimated the timescale of the AGN feedback as

$$\tau_{\mathrm{FB}} \sim \frac{E_{\mathrm{gas}}}{f_{\mathrm{FB}}\mathcal{C}L_{\mathrm{bol}}}, \tag{6.15}$$

where $E_{\mathrm{gas}} \approx kTM_{\mathrm{gas}}/m_p$ is the thermal energy of the gas, $\mathcal{C} = \Delta\Omega/4\pi$ is the covering factor, and f_{FB} is the feedback efficiency. In terms of the surface gas density (Wang et al. 2007),

$$\frac{\tau_{\mathrm{FB}}}{\mathrm{yr}} \sim 1.3 \times 10^5 \left(\frac{\mathcal{C}}{0.5}\frac{f_{\mathrm{FB}}}{100}\frac{L_{\mathrm{bol}}}{10^{43}\,\mathrm{erg\,s}^{-1}}\right)^{-1} \left(\frac{r}{200\,\mathrm{pc}}\right)^2 \left(\frac{T}{10^3\,\mathrm{K}}\right) \left(\frac{\Sigma_{\mathrm{gas}}}{10^4\,\mathrm{M}_\odot\,\mathrm{pc}^{-2}}\right).$$

The short timescales indicate an efficient AGN feedback. In this case, the galaxies would lie below the K-S law once the AGN switch of.

Stellar feedback is also responsible for quenching star formation. Saintonge et al. (2012) found that in a sample of about 100 sources from the COLD GASS survey the bulge-dominated systems lie systematically below the K-S law (but within the scatter of the relation), meaning that at a given surface gas density, these sources produce stars less efficiently. With a simple analytical approach Renaud et al. (2012) predicted that behavior. They showed that, assuming a local star formation law, in a turbulent interstellar medium, the Mach number (varying between 1 and 10), the thickness of the clouds (100 pc), and the density at which the turbulence becomes supersonic ($\rho_0 \sim 10 - 100\,\mathrm{cm}^{-3}$) are the only parameters

required to reproduce the K-S law. That even at low Σ_{gas} were the star formation is driven by the atomic, in contrast to the molecular, gas mass. Fig 6.13 show three of Renaud et al. models with and without star formation feedback. It can be notice that although the supersonic turbulence and stellar feedback regulation reduce the star formation efficiency, they can not account alone for the low Σ_{SFR} observed in Seyfert galaxies.

6.5   Conclusions

In this chapter, the relation between the star formation and the AGN in IRAS 01072+4954 was studied. In the first part, different techniques for disentangling both contributions were used, finding the following results:

- The NIR-diagnostic diagram that combines the line ratios from the strongest emission features is a powerful tool to distinguish between photo-ionization and shock excitation as the main excitation mechanism. Like in the optical diagnostic diagram, the line ratios measured in the central $r \approx 75\,\mathrm{pc}$ of IRAS 01072+4954, place it in the limits between H II galaxies and Seyferts, indicating an important contribution of these two processes.

- In agreement with the previous findings, the [Fe II]/Brγ map does not show any strong sign of shocks at the center. Using the models of Maloney et al. (1996) for hard X-ray excitation, it is found that the [Fe II] emission is $\sim 30\%$ lower than expected. However, the [Fe II]/Brγ ratio is in agreement with the model predictions, although below the average in other sources.

- The H_2 diagnostic diagram indicates that in the central, NE and EWBrγ regions, part of the H_2 excitation is produced by fluorescence, i.e., by very energetic UV photons that excite more strongly the upper energy levels of the molecule. This is consistent with the finding of the previous chapter which indicated that in the two northern regions recent star formation has taken place, and young stars ionize the molecular hydrogen. In the central region, this role is accomplished by the AGN.

- The difference in the rotational and vibrational temperatures of the H_2 molecule are consistent with the presence of a non-thermal component across the bulge. The enhanced emission of the $v = 2, J = 4$ transition, that has also been observed in the nuclei of other Seyfert galaxies, was not found to correlate with star-formation activity, nor with shocks, nor the AGN. It is still not well understood how it can be produced.

- In general, the ortho-para ratio across the bulge is in agreement with local-thermodynamic equilibrium with the exception of two regions EWBrγ and SE. It has been suggested that ortho-para ratios significantly less than 3.0 might be found in regions with gas inflow – where the infalling gas has not

had enough time to reach LTE. I speculate that this might be related with the fact that the stellar bar tips are located approximately in those regions. However, the faint $v = 2$ emission does not allow to get better constraints in that respect.

In the second part, some indications for inflow and outflow were found. Based on the kinematics of the gas and the stars, and on the position of the source relative to the Kennicutt-Schmidt law, the fueling and feedback in the bulge was discussed. The main results are:

- The stellar kinematics shows a typical rotation and an increase in the velocity dispersion at P.A $\approx 135°$, in agreement with the photometric low-pass filtering. This signifies the presence of a nuclear structure like disk or bar, that might be responsible for the gas transport to the center.

- The Brγ and molecular hydrogen LOS velocity maps are consistent with rotation in a disk, but it is not clear whether the gas follows the stellar component or moves with a slightly different orientation. The H II gas also shows somewhat lower velocities at the NE compared with the stars, indicating probably the presence of an outflow in that region.

- The [Fe II] gas tomography shows indications of a biconical outflow with P.A $\approx 45°$. This would be moving towards us in the NE, and receding from us in the SW. This is consistent with enhanced He I emission in the NE region. Evidences for this kind of outflow traced by the [Fe II] emission have been found in other nearby Seyfert galaxies.

- The dynamical timescale of the outflow indicates that it originated $\sim 1.5\,\mathrm{Myr}$ ago. On the other hand, the star formation timescale in the central $r \approx 75\,\mathrm{pc}$, estimated from the stellar absorption features in the H-band spectrum, indicates that the last burst was $\sim 10 - 20\,\mathrm{Myr}$ ago and therefore it can not be responsible for the observed outflow. In contrast, the kinetic energy of the outgoing gas is $\dot{E} \lesssim 10^{40}\,\mathrm{erg\,s^{-1}}$, which represents $\sim 6 \times 10^{-3}$ times that of the AGN. This does mean that the active nucleus might have powered the observed [Fe II] wind.

- Based on the timescales as before, there was no relation found between the outflow and the star formation burst in the NE region. The hypothesis of positive feedback in this case is rejected.

- The estimated mass of the cold gas in the bulge is $M_{\mathrm{gas}} \sim (90 - 470) \times 10^6\,\mathrm{M_\odot}$. Comparing the surface gas density in the bulge with the star formation rate density in the same region, $\Sigma_{\mathrm{SFR}} \approx 1.7\,\mathrm{M_\odot\,yr-1\,kpc^{-2}}$, the efficiency of the starburst is $> 50\%$ per 10^8 years.

- Also the AGN is very active, with a doubling mass timescale of only $\sim 200\,\mathrm{Myr}$. There is an indication of H_2 inflow at the nucleus, with a rate

$\dot{M}_{\text{inflow}} \sim 6.8\,\text{M}_\odot\,\text{yr}^{-1}$. However, only 10^{-4} times that amount is required to feed the black hole at the current accretion rate.

- The estimated black hole mass implies that strong fueling events can last for $\sim 10^5/N\,\text{yr}$, with N the number of accreting events (Heckman et al. 2004). This means that the overlapping windows of black hole and star formation activity, whose timescale is of the order of $\sim 10^{8-9}\,\text{yr}$, is very narrow. The fact that both are so active in the current epoch seems seems to indicate a causality relation and is consisting with the cosmological downsizing scenario.

List of Figures

List of Tables

Bibliography

Ai, Y. L., Yuan, W., Zhou, H. Y., Wang, T. G., & Zhang, S. H. 2011, ApJ, 727, 31

Ali, B., Carr, J. S., Depoy, D. L., Frogel, J. A., & Sellgren, K. 1995, AJ, 110, 2415

Allington-Smith, J. & Content, R. 1998, PASP, 110, 1216

Alonso-Herrero, A., Rieke, G. H., Rieke, M. J., & Kelly, D. M. 2003, AJ, 125, 1210

Alonso-Herrero, A., Rieke, M. J., Rieke, G. H., & Ruiz, M. 1997, ApJ, 482, 747

Alonso-Herrero, A., Simpson, C., Ward, M. J., & Wilson, A. S. 1998, ApJ, 495, 196

Amorín, R., Pérez-Montero, E., Vílchez, J. M., & Papaderos, P. 2012, ApJ, 749, 185

Andredakis, Y. C., Peletier, R. F., & Balcells, M. 1995, MNRAS, 275, 874

Andredakis, Y. C. & Sanders, R. H. 1994, MNRAS, 267, 283

Antonucci, R. 1993, ARA&A, 31, 473

Antonucci, R. 2012, ArXiv:astro-ph/1210.2716

Baldwin, J. A., Phillips, M. M., & Terlevich, R. 1981, PASP, 93, 5

Baldwin, J. R., Frogel, J. A., & Persson, S. E. 1973, ApJ, 184, 427

Barthel, P. D. 1989, ApJ, 336, 606

Barvainis, R. 1987, ApJ, 320, 537

Bauer, A. E., Drory, N., Hill, G. J., & Feulner, G. 2005, ApJ, 621, L89

Bedregal, A. G., Colina, L., Alonso-Herrero, A., & Arribas, S. 2009, ApJ, 698, 1852

Bell, E. F., McIntosh, D. H., Katz, N., & Weinberg, M. D. 2003, ApJS, 149, 289

Bentz, M. C., Peterson, B. M., Netzer, H., Pogge, R. W., & Vestergaard, M. 2009, ApJ, 697, 160

Bertelli, G., Nasi, E., Girardi, L., & Marigo, P. 2009, A&A, 508, 355

Bianchi, S., Corral, A., Panessa, F., et al. 2008, MNRAS, 385, 195

Bianchi, S., Maiolino, R., & Risaliti, G. 2012, AdAst, 2012

Bigiel, F., Leroy, A., Walter, F., et al. 2008, AJ, 136, 2846

Black, J. H. & van Dishoeck, E. F. 1987, ApJ, 322, 412

Blietz, M., Cameron, M., Drapatz, S., et al. 1994, ApJ, 421, 92

Boisson, C. & Durret, F. 1986, A&A, 168, 32

Brand, P. W. J. L., Toner, M. P., Geballe, T. R., et al. 1989, MNRAS, 236, 929

Brinchmann, J., Charlot, S., White, S. D. M., et al. 2004, MNRAS, 351, 1151

Bruzual, G. 2010, Phil. Trans. R. Soc. A, 368, 783

Bruzual, G. & Charlot, S. 2003, MNRAS, 344, 1000

Bruzual A., G. & Charlot, S. 1993, ApJ, 405, 538

Burstein, D., Faber, S. M., Gaskell, C. M., & Krumm, N. 1984, ApJ, 287, 586

Calzetti, D. 2001, PASP, 113, 1449

Calzetti, D. 2011, in EAS Publications Series, Vol. 46, EAS Publications Series, ed. C. Joblin & A. G. G. M. Tielens, 133–141

Calzetti, D. 2012, ArXiv e-prints

Calzetti, D., Armus, L., Bohlin, R. C., et al. 2000, ApJ, 533, 682

Calzetti, D., Kinney, A. L., & Storchi-Bergmann, T. 1994, ApJ, 429, 582

Calzetti, D., Wu, S.-Y., Hong, S., et al. 2010, ApJ, 714, 1256

Cappellari, M., Bacon, R., Bureau, M., et al. 2006, MNRAS, 366, 1126

Cappellari, M. & Emsellem, E. 2004, PASP, 116, 138

Cardamone, C., Schawinski, K., Sarzi, M., et al. 2009, MNRAS, 399, 1191

Cardelli, J. A., Clayton, G. C., & Mathis, J. S. 1989, ApJ, 345, 245

Chen, Y., Trager, S., Peletier, R., & Lançon, A. 2011, Journal of Physics Conference Series, 328, 012023

Chiaberge, M. & Marconi, A. 2011, MNRAS, 416, 917

Chrysostomou, A., Brand, P. W. J. L., Burton, M. G., & Moorhouse, A. 1993, MNRAS, 265, 329

Close, L. M., Wildi, F., Lloyd-Hart, M., et al. 2003, ApJ, 599, 537

Colbert, E. J. M., Heckman, T. M., Ptak, A. F., Strickland, D. K., & Weaver, K. A. 2004, The Astrophysical Journal, 602, 231

Colina, L. 1993, ApJ, 411, 565

Condon, J. J. 1992, ARA&A, 30, 575

Condon, J. J., Cotton, W. D., Greisen, E. W., et al. 1998, AJ, 115, 1693

Contini, M. 2011, MNRAS, 418, 1935

Corbin, M. R., Vacca, W. D., Cid Fernandes, R., et al. 2006, ApJ, 651, 861

Cushing, M. C., Rayner, J. T., & Vacca, W. D. 2005, ApJ, 623, 1115

Czerny, B. & Hryniewicz, K. 2011, A&A, 525, L8

Daddi, E., Elbaz, D., Walter, F., et al. 2010, The Astrophysical Journal Letters, 714, L118

Dale, D. A., Bendo, G. J., Engelbracht, C. W., et al. 2005, ApJ, 633, 857

Dale, D. A., Helou, G., Contursi, A., Silbermann, N. A., & Kolhatkar, S. 2001, The Astrophysical Journal, 549, 215

Das, V., Crenshaw, D. M., Hutchings, J. B., et al. 2005, AJ, 130, 945

Das, V., Crenshaw, D. M., Kraemer, S. B., & Deo, R. P. 2006, AJ, 132, 620

Davies, B., Oudmaijer, R. D., & Sahu, K. C. 2007, ApJ, 671, 2059

Davies, R. & Kasper, M. 2012, Annual Review of Astronomy and Astrophysics, 50, null

Davies, R. I. 2007, MNRAS, 375, 1099

Davies, R. I., Sternberg, A., Lehnert, M. D., & Tacconi-Garman, L. E. 2005, ApJ, 633, 105

Davis, C. J., Smith, M. D., Stern, L., Kerr, T. H., & Chiar, J. E. 2003, MNRAS, 344, 262

Denney, K. D., Watson, L. C., Peterson, B. M., et al. 2009, ApJ, 702, 1353

Desroches, L.-B., Greene, J. E., & Ho, L. C. 2009, ApJ, 698, 1515

Dewangan, G. C., Mathur, S., Griffiths, R. E., & Rao, A. R. 2008, ApJ, 689, 762

DiPompeo, M. A., Brotherton, M. S., De Breuck, C., Laurent-Muehleisen, S., & Myers, A. D. 2012, in American Astronomical Society Meeting Abstracts, Vol. 219, American Astronomical Society Meeting Abstracts #219, 435.02

Dong, X.-B., Wang, J.-G., Ho, L. C., et al. 2011, ApJ, 736, 86

D'Onofrio, M., Marziani, P., & Sulentic, J. W., eds. 2012, Fifty Years of Quasars. From early observations and ideas to future research (Springer)

Dopita, M. 1997, PASA, 14, 230

Dopita, M. A. 2005, in American Institute of Physics Conference Series, Vol. 761, The Spectral Energy Distributions of Gas-Rich Galaxies: Confronting Models with Data, ed. C. C. Popescu & R. J. Tuffs, 203–222

Dopita, M. A., Heisler, C., Lumsden, S., & Bailey, J. 1998, ApJ, 498, 570

Doyon, R., Puxley, P. J., & Joseph, R. D. 1992, ApJ, 397, 117

Draine, B. T. & Bertoldi, F. 1996, ApJ, 468, 269

Draine, B. T. & Lee, H. M. 1984, ApJ, 285, 89

Draine, B. T. & Woods, D. T. 1990, ApJ, 363, 464

Elbaz, D., Dickinson, M., Hwang, H. S., et al. 2011, A&A, 533, A119

Elitzur, M. 2008, New A Rev., 52, 274

Elitzur, M. & Ho, L. C. 2009, ApJ, 701, L91

Elitzur, M. & Shlosman, I. 2006, ApJ, 648, L101

Esposito, S., Riccardi, A., Fini, L., et al. 2010, in Society of Photo-Optical Instrumentation Engineers (SPIE) Conference Series, Vol. 7736, Society of Photo-Optical Instrumentation Engineers (SPIE) Conference Series

Exposito, J., Gratadour, D., Clénet, Y., & Rouan, D. 2011, A&A, 533, A63

Faber, S. M., Friel, E. D., Burstein, D., & Gaskell, C. M. 1985, ApJS, 57, 711

Fabian, A. C. 2012, ARA&A, 50, 455

Fernandez, B. R., Holloway, A. J., Meaburn, J., Pedlar, A., & Mundell, C. G. 1999, MNRAS, 305, 319

Ferrarese, L. & Merritt, D. 2000, ApJ, 539, L9

Filippenko, A. V. & Sargent, W. L. W. 1989, ApJ, 342, L11

Floc'h, E. L., Papovich, C., Dole, H., et al. 2005, The Astrophysical Journal, 632, 169

Forbes, D. A. & Ward, M. J. 1993, ApJ, 416, 150

Forbes, D. A., Ward, M. J., Rotaciuc, V., et al. 1993, ApJ, 406, L11

Förster Schreiber, N. M. 2000, AJ, 120, 2089

Franceschini, A., Braito, V., Persic, M., et al. 2003, MNRAS, 343, 1181

Frank, J., King, A. R., & Raine, D. J. 2002, Accretion Power in Astrophysics. 3rd. ed. (Cambridge University Press)

Fried, D. L. 1965, Journal of the Optical Society of America (1917-1983), 55, 1427

Fried, D. L. 1966, Journal of the Optical Society of America (1917-1983), 56, 1372

Friedrich, S., Davies, R. I., Hicks, E. K. S., et al. 2010, A&A, 519, A79

Frogel, J. A., Stephens, A., Ramírez, S., & DePoy, D. L. 2001, AJ, 122, 1896

Ganda, K., Peletier, R. F., Balcells, M., & Falcón-Barroso, J. 2009, MNRAS, 395, 1669

García-Burillo, S., Usero, A., Alonso-Herrero, A., et al. 2012, A&A, 539, A8

Gaskell, C. M. 1988, ApJ, 325, 114

Gaskell, C. M. 2009, New A Rev., 53, 140

Gaskell, C. M., Klimek, E. S., & Nazarova, L. S. 2007, ArXiv:astro-ph/0711.1025

Gebhardt, K., Bender, R., Bower, G., et al. 2000, ApJ, 539, L13

Genzel, R., Tacconi, L. J., Gracia-Carpio, J., et al. 2010, MNRAS, 407, 2091

Georgantopoulos, I. 2000, MNRAS, 315, 77

Gilfanov, M., Grimm, H.-J., & Sunyaev, R. 2004, MNRAS, 347, L57

Girardi, L. & Bertelli, G. 1998, MNRAS, 300, 533

Gliozzi, M., Panessa, F., La Franca, F., et al. 2010, ApJ, 725, 2071

González Delgado, R. M. 2002, in Astronomical Society of the Pacific Conference Series, Vol. 258, Issues in Unification of Active Galactic Nuclei, ed. R. Maiolino, A. Marconi, & N. Nagar, 101

Goodrich, R. W. & Miller, J. S. 1994, ApJ, 434, 82

Goodrich, R. W., Veilleux, S., & Hill, G. J. 1994, ApJ, 422, 521

Graham, A. W. 2007, MNRAS, 379, 711

Graham, A. W. 2008, ApJ, 680, 143

Graham, A. W. 2011, arXiv:astro-ph/1103.0525

Graham, A. W. 2012a, ApJ, 746, 113

Graham, A. W. 2012b, MNRAS, 422, 1586

Graham, A. W. & Driver, S. P. 2007, ApJ, 655, 77

Graham, A. W., Onken, C. A., Athanassoula, E., & Combes, F. 2011, MNRAS, 412, 2211

Granato, G. L. & Danese, L. 1994, MNRAS, 268, 235

Greene, J. E. & Ho, L. C. 2005, ApJ, 627, 721

Greene, J. E. & Ho, L. C. 2007, ApJ, 656, 84

Greenhouse, M. A., Satyapal, S., Woodward, C. E., et al. 1997, ApJ, 476, 105

Gültekin, K., Richstone, D. O., Gebhardt, K., et al. 2009, ApJ, 698, 198

Guseva, N. G., Papaderos, P., Izotov, Y. I., et al. 2003, A&A, 407, 105

Guzman, R., Gallego, J., Koo, D. C., et al. 1997, ApJ, 489, 559

Häring, N. & Rix, H.-W. 2004, ApJ, 604, L89

Hawkins, M. R. S. 2004, A&A, 424, 519

Heckman, T. M., Armus, L., & Miley, G. K. 1990, ApJS, 74, 833

Helou, G., Khan, I. R., Malek, L., & Boehmer, L. 1988, ApJS, 68, 151

Hicks, E. K. S., Davies, R. I., Malkan, M. A., et al. 2009, ApJ, 696, 448

Hill, T. L., Heisler, C. A., Sutherland, R., & Hunstead, R. W. 1999, AJ, 117, 111

Ho, L. C. 2003, in PASP, Vol. 290, Active Galactic Nuclei: From Central Engine to Host Galaxy, ed. S. Collin, F. Combes, & I. Shlosman, 379

Ho, L. C. 2008, ARA&A, 46, 475

Ho, L. C. 2009, ApJ, 699, 626

Ho, L. C., Feigelson, E. D., Townsley, L. K., et al. 2001, ApJ, 549, L51

Ho, L. C., Filippenko, A. V., & Sargent, W. L. W. 1997a, ApJS, 112, 315

Ho, L. C., Filippenko, A. V., Sargent, W. L. W., & Peng, C. Y. 1997b, ApJS, 112, 391

Hollenbach, D. & McKee, C. F. 1989, ApJ, 342, 306

Hopkins, P. F., Richards, G. T., & Hernquist, L. 2007, ApJ, 654, 731

Hu, J. 2008, MNRAS, 386, 2242

Hubin, N. & Noethe, L. 1993, Science, 262, 1390

Hummer, D. G. & Storey, P. J. 1987, MNRAS, 224, 801

Hyland, A. R. & Allen, D. A. 1982, MNRAS, 199, 943

Ivanov, V. D., Rieke, G. H., Groppi, C. E., et al. 2000, ApJ, 545, 190

Ivanov, V. D., Rieke, M. J., Engelbracht, C. W., et al. 2004, ApJS, 151, 387

Iwasawa, K., Sanders, D. B., Evans, A. S., et al. 2009, The Astrophysical Journal Letters, 695, L103

Iwasawa, K., Sanders, D. B., Teng, S. H., et al. 2011, A&A, 529, A106

Jiang, Y.-F., Greene, J. E., & Ho, L. C. 2011, ApJ, 737, L45

Kartaltepe, J. S., Dickinson, M., Alexander, D. M., et al. 2012, ApJ, 757, 23

Kaspi, S., Smith, P. S., Netzer, H., et al. 2000, ApJ, 533, 631

Kauffmann, G., Heckman, T. M., White, S. D. M., et al. 2003, MNRAS, 341, 33

Kennicutt, R. C. & Evans, N. J. 2012, Annual Review of Astronomy and Astrophysics, 50, 531

Kennicutt, Jr., R. C. 1992, ApJ, 388, 310

Kennicutt, Jr., R. C. 1998a, ARA&A, 36, 189

Kennicutt, Jr., R. C. 1998b, ApJ, 498, 541

Kewley, L. J., Heisler, C. A., Dopita, M. A., et al. 2000, ApJ, 530, 704

Kim, D., Im, M., & Kim, M. 2010, ApJ, 724, 386

King, A. 2008, New A Rev., 52, 253

Kishimoto, M., Hönig, S. F., Beckert, T., & Weigelt, G. 2007, A&A, 476, 713

Kleinmann, S. G. & Hall, D. N. B. 1986, ApJS, 62, 501

Kolmogorov, A. N. 1941, Comptes rendus (Doklady) de l'Académie des Sciences de l'U.R.S.S., 32, 16

Koratkar, A., Deustua, S. E., Heckman, T., et al. 1995, ApJ, 440, 132

Kormendy, J. & Bender, R. 2011, Nature, 469, 377

Kormendy, J., Fisher, D. B., Cornell, M. E., & Bender, R. 2009, ApJS, 182, 216

Kormendy, J. & Ho, L. 2001, Supermassive Black Holes in Inactive Galaxies (Murdin, P.)

Kormendy, J. & Kennicutt, Jr., R. C. 2004, ARA&A, 42, 603

Kriss, G. A., Canizares, C. R., & Ricker, G. R. 1980, ApJ, 242, 492

Krolik, J. H. 1999, Active galactic nuclei : from the central black hole to the galactic environment (Princeton U Press)

Lagos, C. D. P., Padilla, N. D., Strauss, M. A., Cora, S. A., & Hao, L. 2011, MNRAS, 414, 2148

Lancon, A. & Rocca-Volmerange, B. 1992, A&AS, 96, 593

Landt, H., Elvis, M., Ward, M. J., et al. 2011, MNRAS, 414, 218

Laor, A. 1998, ApJ, 505, L83

Laor, A. 2003, ApJ, 590, 86

Laor, A. 2007, in PASP, Vol. 373, The Central Engine of Active Galactic Nuclei, ed. L. C. Ho & J.-W. Wang, 384

Larkin, J. E., Armus, L., Knop, R. A., Soifer, B. T., & Matthews, K. 1998, ApJS, 114, 59

Larson, R. B. & Tinsley, B. M. 1978, ApJ, 219, 46

Lawrence, A. 1987, PASP, 99, 309

Lebzelter, T., Seifahrt, A., Uttenthaler, S., et al. 2012, A&A, 539, A109

Leggett, S. K., Currie, M. J., Varricatt, W. P., et al. 2006, MNRAS, 373, 781

Lehmer, B. D., Alexander, D. M., Bauer, F. E., et al. 2010, ApJ, 724, 559

Leitherer, C. 2005, in American Institute of Physics Conference Series, Vol. 783, The Evolution of Starbursts, ed. S. Hüttmeister, E. Manthey, D. Bomans, & K. Weis, 280–295

Leitherer, C., Otálvaro, P. A. O., Bresolin, F., et al. 2010, The Astrophysical Journal Supplement Series, 189, 309

Leitherer, C., Schaerer, D., Goldader, J. D., et al. 1999, ApJS, 123, 3

Levenson, N. A., Cid Fernandes, Jr., R., Weaver, K. A., Heckman, T. M., & Storchi-Bergmann, T. 2001, ApJ, 557, 54

Levenson, N. A., Graham, J. R., McLean, I. S., et al. 2000, ApJ, 533, L53

Longinotti, A. L., Bianchi, S., Ballo, L., de La Calle, I., & Guainazzi, M. 2009, MNRAS, 394, L1

Lonsdale, C. J., Farrah, D., & Smith, H. E. 2006, Ultraluminous Infrared Galaxies (Mason, J. W.), 285

Lumsden, S. L. & Puxley, P. J. 1995, MNRAS, 276, 723

Lumsden, S. L., Puxley, P. J., Hoare, M. G., Moore, T. J. T., & Ridge, N. A. 2003, MNRAS, 340, 799

Macchetto, F. D. & Chiaberge, M. 2007, in IAU Symposium, Vol. 238, IAU Symposium, ed. V. Karas & G. Matt, 273

Magorrian, J., Tremaine, S., Richstone, D., et al. 1998, AJ, 115, 2285

Maiolino, R., Marconi, A., & Oliva, E. 2001a, A&A, 365, 37

Maiolino, R., Marconi, A., Salvati, M., et al. 2001b, A&A, 365, 28

Maiolino, R., Ruiz, M., Rieke, G. H., & Keller, L. D. 1995, ApJ, 446, 561

Maloney, P. R., Hollenbach, D. J., & Tielens, A. G. G. M. 1996, ApJ, 466, 561

Mannucci, F., Basile, F., Poggianti, B. M., et al. 2001, MNRAS, 326, 745

Maoz, D. 2007, MNRAS, 377, 1696

Maraston, C. 2003, in Extragalactic Globular Cluster Systems, ed. M. Kissler-Patig, 237

Maraston, C. 2005, MNRAS, 362, 799

Marchese, E., Braito, V., Della Ceca, R., Caccianiga, A., & Severgnini, P. 2012, MNRAS, 421, 1803

Marco, O. & Alloin, D. 1998, A&A, 336, 823

Marconi, A. & Hunt, L. K. 2003, ApJ, 589, L21

Marconi, A., Risaliti, G., Gilli, R., et al. 2004, MNRAS, 351, 169

Markwardt, C. B. 2009, in PASP, Vol. 411, Astronomical Data Analysis Software and Systems XVIII, ed. D. A. Bohlender, D. Durand, & P. Dowler, 251

Mármol-Queraltó, E., Cardiel, N., Cenarro, A. J., et al. 2008, A&A, 489, 885

Martin, D. C., Small, T., Schiminovich, D., et al. 2007, ApJS, 173, 415

Martins, L. P., Rodríguez-Ardila, A., de Souza, R., & Gruenwald, R. 2010, MNRAS, 406, 2168

Masciadri, E., Stoesz, J., Hagelin, S., & Lascaux, F. 2010, MNRAS, 404, 144

Mathur, S., Fields, D., Peterson, B. M., & Grupe, D. 2011, arXiv:astro-ph/1102.0537

Mazzalay, X. & Rodríguez-Ardila, A. 2007, A&A, 463, 445

Mazzalay, X., Saglia, R. P., Erwin, P., et al. 2012, ArXiv e-prints

McGregor, P. J., Hart, J., Conroy, P. G., et al. 2003, in Society of Photo-Optical Instrumentation Engineers (SPIE) Conference Series, Vol. 4841, Society of Photo-Optical Instrumentation Engineers (SPIE) Conference Series, ed. M. Iye & A. F. M. Moorwood, 1581

McLure, R. J. & Dunlop, J. S. 2002, MNRAS, 331, 795

Middelberg, E. & Bach, U. 2008, Reports on Progress in Physics, 71, 066901

Miller, J. S. & Goodrich, R. W. 1990, ApJ, 355, 456

Moorwood, A. F. M. & Oliva, E. 1988, A&A, 203, 278

Mor, R. & Trakhtenbrot, B. 2011, ApJ, 737, L36

Moran, E. C., Halpern, J. P., & Helfand, D. J. 1996, ApJS, 106, 341

Mouri, H. 1994, ApJ, 427, 777

Mouri, H., Kawara, K., & Taniguchi, Y. 2000, ApJ, 528, 186

Mouri, H., Nishida, M., Taniguchi, Y., & Kawara, K. 1990, ApJ, 360, 55

Müller-Sánchez, F., Prieto, M. A., Hicks, E. K. S., et al. 2011, ApJ, 739, 69

Murphy, E. J., Condon, J. J., Schinnerer, E., et al. 2011, The Astrophysical Journal, 737, 67

Murray, N., Chiang, J., Grossman, S. A., & Voit, G. M. 1995, ApJ, 451, 498

Nagar, N. M., Oliva, E., Marconi, A., & Maiolino, R. 2002, A&A, 391, L21

Narayan, R. 2002, in Lighthouses of the Universe: The Most Luminous Celestial Objects and Their Use for Cosmology, ed. M. Gilfanov, R. Sunyeav, & E. Churazov, 405

Narayan, R. & McClintock, J. E. 2012, MNRAS, 419, L69

Nardini, E., Risaliti, G., Watabe, Y., Salvati, M., & Sani, E. 2010, MNRAS, 405, 2505

Natta, A. & Panagia, N. 1984, ApJ, 287, 228

Nenkova, M., Sirocky, M. M., Ivezić, Ž., & Elitzur, M. 2008a, ApJ, 685, 147

Nenkova, M., Sirocky, M. M., Nikutta, R., Ivezić, Ž., & Elitzur, M. 2008b, ApJ, 685, 160

Netzer, H. 2008, New A Rev., 52, 257

Netzer, H. 2009, ApJ, 695, 793

Netzer, H. & Laor, A. 1993, ApJ, 404, L51

Nicastro, F. 2000, ApJ, 530, L65

Nicastro, F., Martocchia, A., & Matt, G. 2003, ApJ, 589, L13

Nussbaumer, H. & Storey, P. J. 1988, A&A, 193, 327

Oliva, E., Moorwood, A. F. M., & Danziger, I. J. 1989, A&A, 214, 307

Oliva, E., Origlia, L., Kotilainen, J. K., & Moorwood, A. F. M. 1995, A&A, 301, 55

Orban de Xivry, G., Davies, R., Schartmann, M., et al. 2011, MNRAS, 417, 2721

Origlia, L., Moorwood, A. F. M., & Oliva, E. 1993, A&A, 280, 536

Osterbrock, D. E. & Fernand, G. J. 2006, Astrophysics of gaseous nebulae and active galactic nuclei, 2nd. ed. (University Science Books)

Panessa, F. & Bassani, L. 2002, A&A, 394, 435

Panessa, F., Carrera, F. J., Bianchi, S., et al. 2009, MNRAS, 398, 1951

Panessa, F., Wolter, A., Pellegrini, S., et al. 2005, ApJ, 631, 707

Panuzzo, P., Bressan, A., Granato, G. L., Silva, L., & Danese, L. 2003, A&A, 409, 99

Papaderos, P., Guseva, N. G., Izotov, Y. I., & Fricke, K. J. 2008, A&A, 491, 113

Papadopoulos, P. P., van der Werf, P. P., Xilouris, E. M., et al. 2012, MNRAS, 426, 2601

Peeters, E., Spoon, H. W. W., & Tielens, A. G. G. M. 2004, The Astrophysical Journal, 613, 986

Peng, Y.-j., Lilly, S. J., Kovač, K., et al. 2010, ApJ, 721, 193

Persic, M. & Rephaeli, Y. 2007, A&A, 463, 481

Persic, M., Rephaeli, Y., Braito, V., et al. 2004, A&A, 419, 849

Peterson, B. M. 2006, An Introduction to active galactic nuclei (Cambridge University Press)

Peterson, B. M., Bentz, M. C., Desroches, L.-B., et al. 2005, The Astrophysical Journal, 632, 799

Peterson, B. M., Ferrarese, L., Gilbert, K. M., et al. 2004, ApJ, 613, 682

Pickles, A. J. 1998, PASP, 110, 863

Pier, E. A. & Krolik, J. H. 1992, ApJ, 399, L23

Prieto, M. A., Reunanen, J., Tristram, K. R. W., et al. 2010, Monthly Notices of the Royal Astronomical Society, 402, 724

Pych, W. 2004, PASP, 116, 148

Ramirez, S. V., Depoy, D. L., Frogel, J. A., Sellgren, K., & Blum, R. D. 1997, AJ, 113, 1411

Ramírez, S. V., Stephens, A. W., Frogel, J. A., & DePoy, D. L. 2000, AJ, 120, 833

Ramos Almeida, C., Pérez García, A. M., Acosta-Pulido, J. A., & González-Martín, O. 2008, ApJ, 680, L17

Ranalli, P., Comastri, A., & Setti, G. 2003, A&A, 399, 39

Rayner, J. T., Cushing, M. C., & Vacca, W. D. 2009, ApJS, 185, 289

Renaud, F., Kraljic, K., & Bournaud, F. 2012, ApJ, 760, L16

Renzini, A. 2006, ARA&A, 44, 141

Reunanen, J., Kotilainen, J. K., & Prieto, M. A. 2002, MNRAS, 331, 154

Reunanen, J., Kotilainen, J. K., & Prieto, M. A. 2003, MNRAS, 343, 192

Rhee, J. H. & Larkin, J. E. 2000, ApJ, 538, 98

Rhee, J. H. & Larkin, J. E. 2005, ApJ, 620, 151

Rich, R. M. & Origlia, L. 2005, The Astrophysical Journal, 634, 1293

Rieke, G. H. & Lebofsky, M. J. 1985, ApJ, 288, 618

Rieke, G. H. & Low, F. J. 1972, ApJ, 176, L95

Riffel, R., Pastoriza, M. G., RodrÃŋguez-Ardila, A., & Maraston, C. 2007, The Astrophysical Journal Letters, 659, L103

Riffel, R. A. & Storchi-Bergmann, T. 2011a, MNRAS, 411, 469

Riffel, R. A. & Storchi-Bergmann, T. 2011b, arXiv:astro-ph/1107.2564

Riffel, R. A., Storchi-Bergmann, T., Dors, O. L., & Winge, C. 2009a, MNRAS, 393, 783

Riffel, R. A., Storchi-Bergmann, T., & McGregor, P. J. 2009b, ApJ, 698, 1767

Riffel, R. A., Storchi-Bergmann, T., & Nagar, N. M. 2010, MNRAS, 404, 166

Risaliti, G. & Elvis, M. 2004, in Astrophysics and Space Science Library, Vol. 308, Supermassive Black Holes in the Distant Universe, ed. A. J. Barger, 187

Risaliti, G., Elvis, M., Fabbiano, G., Baldi, A., & Zezas, A. 2005, ApJ, 623, L93

Robertson, J. G. 2001, The Observatory, 121, 368

Roddier, F. 1981, Progress in optics. Volume 19. Amsterdam, North-Holland Publishing Co., 1981, p. 281-376., 19, 281

Rodríguez-Ardila, A., Contini, M., & Viegas, S. M. 2005a, MNRAS, 357, 220

Rodríguez-Ardila, A., Pastoriza, M. G., Viegas, S., Sigut, T. A. A., & Pradhan, A. K. 2004, A&A, 425, 457

Rodríguez-Ardila, A., Riffel, R., & Pastoriza, M. G. 2005b, MNRAS, 364, 1041

Rousselot, P., Lidman, C., Cuby, J.-G., Moreels, G., & Monnet, G. 2000, A&A, 354, 1134

Rush, B., Malkan, M. A., & Spinoglio, L. 1993, ApJS, 89, 1

Saintonge, A., Tacconi, L. J., Fabello, S., et al. 2012, ApJ, 758, 73

Sajina, A., Yan, L., Fadda, D., Dasyra, K., & Huynh, M. 2012, The Astrophysical Journal, 757, 13

Salim, S., Rich, R. M., Charlot, S., et al. 2007, ApJS, 173, 267

Salpeter, E. E. 1955, ApJ, 121, 161

Salpeter, E. E. 1977, ARA&A, 15, 267

Sanders, D. B. & Mirabel, I. F. 1996, ARA&A, 34, 749

Sanders, D. B., Scoville, N. Z., & Soifer, B. T. 1991, ApJ, 370, 158

Sanders, D. B., Soifer, B. T., Elias, J. H., et al. 1988, ApJ, 325, 74

Sani, E., Marconi, A., Hunt, L. K., & Risaliti, G. 2011, MNRAS, 413, 1479

Sargent, W. L. W. & Searle, L. 1970, ApJ, 162, L155

Schiminovich, D., Wyder, T. K., Martin, D. C., et al. 2007, ApJS, 173, 315

Schimoia, J. S., Storchi-Bergmann, T., Nemmen, R. S., Winge, C., & Eracleous, M. 2012, ApJ, 748, 145

Schmidt, M. 1959, ApJ, 129, 243

Schmidt, M. 1963, ApJ, 137, 758

Schneider, P. 2006, Extragalactic Astronomy and Cosmology. An Introduction. (Springer)

Scoville, N. Z., Hall, D. N. B., Ridgway, S. T., & Kleinmann, S. G. 1982, ApJ, 253, 136

Shemmer, O., Brandt, W. N., Netzer, H., Maiolino, R., & Kaspi, S. 2008, ApJ, 682, 81

Shen, S., Shao, Z., & Gu, M. 2010, ApJ, 725, L210

Shi, Y., Rieke, G. H., Smith, P., et al. 2010, ApJ, 714, 115

Silk, J. & Rees, M. J. 1998, A&A, 331, L1

Singh, V., Shastri, P., & Risaliti, G. 2011, A&A, 533, A128

Skrutskie, M. F., Cutri, R. M., Stiening, R., et al. 2006, AJ, 131, 1163

Smajić, S., Fischer, S., Zuther, J., & Eckart, A. 2012, A&A, 544, A105

Smith, J. E., Robinson, A., Young, S., Axon, D. J., & Corbett, E. A. 2005, MNRAS, 359, 846

Smith, M. D., Davis, C. J., & Lioure, A. 1997, A&A, 327, 1206

Solomon, P. & Vanden Bout, P. 2005, Annual Review of Astronomy and Astrophysics, 43, 677

Stacey, G. J., Charmandaris, V., Boulanger, F., et al. 2010, ApJ, 721, 59

Stern, J. & Laor, A. 2012, MNRAS, 2870

Sternberg, A. 1989, ApJ, 347, 863

Sternberg, A. 1998, ApJ, 506, 721

Sternberg, A., Dalgarno, A., & Lepp, S. 1987, ApJ, 320, 676

Sternberg, A. & Neufeld, D. A. 1999, ApJ, 516, 371

Storchi-Bergmann, T., McGregor, P. J., Riffel, R. A., et al. 2009, MNRAS, 394, 1148

Strickland, D. K. & Stevens, I. R. 2000, MNRAS, 314, 511

Tadhunter, C. 2008, New A Rev., 52, 227

Tatarski, V. I. 1961, Wave propagation in a turbulent medium (New York, United States of America: Dover Publications)

Tchekhovskoy, A. & McKinney, J. C. 2012, MNRAS, 423, L55

Telesco, C. M. 1988, ARA&A, 26, 343

Terashima, Y., Ho, L. C., & Ptak, A. F. 2000, ApJ, 539, 161

Thornley, M. D., Schreiber, N. M. F., Lutz, D., et al. 2000, ApJ, 539, 641

Thornton, C. E., Barth, A. J., Ho, L. C., & Greene, J. E. 2009, ApJ, 705, 1196

Thornton, C. E., Barth, A. J., Ho, L. C., Rutledge, R. E., & Greene, J. E. 2008, ApJ, 686, 892

Tine, S., Lepp, S., Gredel, R., & Dalgarno, A. 1997, ApJ, 481, 282

Tokunaga, A. T., Simons, D. A., & Vacca, W. D. 2002, PASP, 114, 180

Tokunaga, A. T. & Vacca, W. D. 2005, PASP, 117, 421

Toomre, A. & Toomre, J. 1972, ApJ, 178, 623

Tran, H. D. 2001, ApJ, 554, L19

Tran, H. D., Lyke, J. E., & Mader, J. A. 2011, ApJ, 726, L21

Tremaine, S., Gebhardt, K., Bender, R., et al. 2002, ApJ, 574, 740

Trump, J. R., Impey, C. D., Kelly, B. C., et al. 2011, ApJ, 733, 60

Urry, C. M. & Padovani, P. 1995, PASP, 107, 803

Valencia-S, M., Eckart, A., Zuther, J., et al. 2012, Journal of Physics Conference Series, 372, 012048

Vasudevan, R. V. & Fabian, A. C. 2007, MNRAS, 381, 1235

Vázquez, G. A. & Leitherer, C. 2005, ApJ, 621, 695

Veilleux, S., Cecil, G., & Bland-Hawthorn, J. 2005, ARA&A, 43, 769

Veilleux, S., Goodrich, R. W., & Hill, G. J. 1997, ApJ, 477, 631

Veilleux, S., Kim, D.-C., & Sanders, D. B. 2002, The Astrophysical Journal Supplement Series, 143, 315

Veilleux, S. & Osterbrock, D. E. 1987, ApJS, 63, 295

Veilleux, S., Rupke, D. S. N., Kim, D.-C., et al. 2009, ApJS, 182, 628

Wallace, L. & Hinkle, K. 1996, ApJS, 107, 312

Wang, J.-M., Chen, Y.-M., Yan, C.-S., Hu, C., & Bian, W.-H. 2007, ApJ, 661, L143

Ward, M. J., Done, C., Fabian, A. C., Tennant, A. F., & Shafer, R. A. 1988, ApJ, 324, 767

Watabe, Y., Kawakatu, N., & Imanishi, M. 2008, ApJ, 677, 895

Willner, S. P., Fabbiano, G., Elvis, M., et al. 1984, PASP, 96, 143

Winge, C., Riffel, R. A., & Storchi-Bergmann, T. 2009, ApJS, 185, 186

Wolniewicz, L., Simbotin, I., & Dalgarno, A. 1998, ApJS, 115, 293

Woo, J.-H., Treu, T., Barth, A. J., et al. 2010, ApJ, 716, 269

Worthey, G., Faber, S. M., Gonzalez, J. J., & Burstein, D. 1994, ApJS, 94, 687

Xiao, T., Barth, A. J., Greene, J. E., et al. 2011, ApJ, 739, 28

Yan, L., Sajina, A., Fadda, D., et al. 2007, ApJ, 658, 778

Younes, G., Porquet, D., Sabra, B., Reeves, J. N., & Grosso, N. 2012, A&A, 539, A104

Yun, M. S., Reddy, N. A., & Condon, J. J. 2001, ApJ, 554, 803

Zhang, E.-P. & Wang, J.-M. 2006, ApJ, 653, 137

Zhou, H., Wang, T., Yuan, W., et al. 2006, ApJS, 166, 128

Zibetti, S., Gallazzi, A., Charlot, S., Pasquali, A., & Pierini, D. 2012, in IAU Symposium, Vol. 284, IAU Symposium, 63–65

Zuther, J., Iserlohe, C., Pott, J.-U., et al. 2007, A&A, 466, 451

Zwicky, F. & Kowal, C. T. 1968, "Catalogue of Galaxies and of Clusters of Galaxies", Volume VI (California Institute of Technology)

Acknowledgements

his encourage. Gunther and Sabine, for very interestic scientific and non-scientific conversations. Christoph, Lilia, Constanza and Rainer: It was a pleasure. Devy, thank you for being there. For going around Prague many times, for serving as interpreter in the Hospital, and for very nice moments here and there.

I want to thank my former professors in Colombia, who support my interest to do a PhD. in Astronomy: Antonio Uribe, Benjamin Calvo, Gregorio Portilla, Robel Arenas, Armando Higuera, Guillermo Franco, Juan Manuel Tejeiro, and Leonardo Castañeda. Also to those from whom I derived my love for Physics: Plamen Neichev, Julian Urrea, and Mauricio Mendivelso. To the people of the group 'The relation Physics and Mathematics' in the Universidad Pedagogica Nacional. To Elizabeth Suesca and Miguel Valdivieso. To those who I had the pleasure to supervise: Natalia, Daniel, Edwin. And those who have shared with me the experience of studying abroad: Camilo, Eduardo Emilio, and Harvey. Many many Thanks.

Finally, this work would not have been possible without the constant support and love of my family. To all of them (~ 100 people), thank you very much. Erika, danke dass Du meine Mutter bist hier in Deutschland. Al Rdo. P. Edisom Guarnizo y al Rdo. P. Segundo A. Anacona muchas gracias por su apoyo y sus oraciones. Mamita, muchas gracias por todo lo que me has enseñado, ya estamos llegando a la cumbre. A mi papá, quien fué la persona que me guió a estudiar física y me apoyó en todo momento, que el Señor lo tenga en su Gloria. A mis hermanas Janice y Diana. Y a Natalia por llegar a nuestras vidas y llenarlas de alegría. To my loved husband Peter, I have deep gratitude for your support during all the time of the PhD. For standing the mono-thematic discussions over the past three months. For driving the ship alone so many times. For all your help until the very last hours. Amor, I would not have make it without you, thank you very very much.

–

Erklärung

Ich versichere, daß ich die von mir vorgelegte Dissertation selbständig angefertigt, die benutzten Quellen und Hilfsmittel vollständig angegeben und die Stellen der Arbeit – einschließlich Tabellen, Karten und Abbildungen –, die anderen Werken im Wortlaut oder dem Sinn nach entnommen sind, in jedem Einzelfall als Entlehnung kenntlich gemacht habe; daß diese Dissertation noch keiner anderen Fakultät oder Universität zur Prüfung vorgelegen hat; daß sie – abgesehen von unten angegebenen Teilpublikationen – noch nicht veröffentlicht worden ist sowie, daß ich eine solche Veröffentlichung vor Abschluß des Promotionsverfahrens nicht vornehmen werde. Die Bestimmungen dieser Promotionsordnung sind mir bekannt. Die von mir vorgelegte Dissertation ist von Prof. Dr. Andreas Eckart betreut worden.
Köln, 18.11.2011

Teilpublikationen

- **Valencia-S., M.**; Zuther, J.; Eckart, A.; Garcia-Marin, M.; Iserlohe, C.; Wright, G. (2012) *"Is IRAS 01072+4954 a True-Seyfert 2?. Hints from near-infrared integral field spectroscopy"* A&A, 544, 129

- **Valencia-S, M.**; Eckart, A.; Zuther, J.; Fischer, S.; Smajic, S.; Iserlohe, C.; Garcia-Marin, M.; Moser, L.; Bremer, M.; Vitale, M. (2012) *"Discovery of an Intermediate Mass Black Hole at the center of the starburst/Seyfert composite galaxy IRAS 01072+4954"* in J. Phys.: Conf. Ser., 372, 2048

- **Valencia-S, M.**; Bursa, M.; Karssen, G.; Dovciak, M.; Eckart, A.; Horak, J.; Karas, V. (2012) *"Modeling polarization signatures of NIR radiation from the Sgr A* black hole environs"* in J. Phys.: Conf. Ser., 372, 2073

- **Valencia-S., M.**; Zuther, J.; Eckart, A.; Iserlohe, C. (2012) *"Star formation and Feedback in IRAS 01072+4954 reveald by Gemini/NIFS"* (to be submitted)

- **Valencia-S., M.**; Zuther, J.; Eckart, A. (2012) *"IRAS 01072+4954: a low-mas black hole with high accretion rate = NLSy1? or Are NLSy1 a speciall class of AGN?"* (to be submitted)

Weitere Publikationen

- Eckart, A.; Muzic, K.; Yazici, S.; Sabha, N.; Shahzamanian, B.; Witzel, G.; Moser, L.; Garcia-Marin, M.; **Valencia-S., M.**; Jalali, B.; Bremer, M.; Straubmeier, C.; Rauch, C.; Buchholz, R.; Kunneriath, D.; Moultaka, J. (2012) *"Near-infrared proper motions and spectroscopy of infrared excess sources at the Galactic Center"* A&A (submitted)

- Witzel, G.; Eckart, A.; Bremer, M.; Zamaninasab, M.; Shahzamanian, B.; **Valencia-S., M.**; Schodel, R.; Karas, V.; Lenzen, R.; Marchili, N.; Sabha, N.; Garcia-Marin, M.; Buchholz, R. M.; Kunneriath, D.; Straubmeier, C. (2012) *"Source-intrinsic near-infrared properties of Sgr A*: Total intensity measurements"* ApJS, 203, 18

- Eckart, A.; Garcia-Marin, M.; Vogel, S. N.; Teuben, P.; Morris, M. R.; Baganoff, F.; Dexter, J.; Schodel, R.; Witzel, G.; **Valencia-S., M.**; Karas, V.; Kunneriath, D.; Straubmeier, C.; Moser, L.; Sabha, N.; Buchholz, R.; Zamaninasab, M.; MuÅ¿iÄ, K.; Moultaka, J.; Zensus, J. A. (2012) *"Millimeter to X-ray flares from Sagittarius A*"* A&A, 537, 52

- Kunneriath, D.; Eckart, A.; Vogel, S. N.; Teuben, P.; Muzic, K.; Schodel, R.; Garcia-Marin, M.; Moultaka, J.; Staguhn, J.; Straubmeier, C.; Zensus, J. A.; **Valencia-S., M.**; Karas, V. (2012) *"The Galactic centre mini-spiral in the mm-regime"* A&A, 538, 127

- Vitale, M.; Zuther, J.; Garcia-Marin, M.; Eckart, A.; Bremer, M.; **Valencia-S., M.**; Zensus, A. (2012) *"Classifying radio emitters from the Sloan Digital Sky Survey. Spectroscopy and diagnostics"* A&A, 546, 17

- Sabha, N.; Eckart, A.; Merritt, D.; Zamaninasab, M.; Witzel, G.; Garcia-Marin, M.; Jalali, B.; **Valencia-S., M.**; Yazici, S.; Buchholz, R.; Shahzamanian, B.; Rauch, C.; Horrobin, M.; Straubmeier, C. (2012) *"The S-star cluster at the center of the Milky Way. On the nature of diffuse NIR emission in the inner tenth of a parsec"* A&A, 545, 70

- Eckart, A.; Sabha, N.; Witzel, G.; Straubmeier, C.; Shahzamanian, B.; **Valencia-S., M.**; Garcia-Marin, M.; Horrobin, M.; Moser, L.; Zuther, J.; Fischer, S.; Rauch, C.; Rost, S.; Iserlohe, C.; Yazici, S.; Smajic, S.; Wiest, M.; Araujo-Hauck, C.; Wank, I. (2012) *"Beating the confusion limit: The necessity of high angular resolution for probing the physics of Sagittarius A* and its environment: Opportunities for LINC-NIRVANA (LBT), GRAVITY (VLTI) and and METIS (E-ELT)"* in Conf. Proc. SPIE, No. 8445-4

- Bremer, M.; Scharwaechter, J.; Eckart, A.; Zuther, J.; Fischer, S.; **Valencia-S, M.** (2012) *"Optical Integral Field Spectroscopy of NGC 5850"* in J. Phys.: Conf. Ser., 372, 2054

- Fischer, S.; Smajic, S.; **Valencia-S, M.**; Vitale, A.; Zuther, J.; Eckart, A. (2012) *"A close look at Seyfert 2 nuclei"* in J. Phys.: Conf. Ser., 372, 2057

- Kunneriath, D.; Eckart, A.; Vogel, S. N.; Teuben, P.; Muzic, K.; Schoedel, R.; Garcia-Marin, M.; Moultaka, J.; Staguhn, J.; Straubmeier, C.; Zensus, J. A.; **Valencia-S, M.**; Karas, V. (2012) *"The Galactic centre mini-spiral with CARMA* in J. Phys.: Conf. Ser., 372, 2063

- Eckart, A.; Garcia-Marin, M.; Vogel, S. N.; Teuben, P.; Morris, M. R.; Baganoff, F.; Dexter, J.; Schoedel, R.; Witzel, G.; **Valencia-S, M.**; Karas, V.; Kunneriath, D.; Bremer, M.; Straubmeier, C.; Moser, L.; Sabha, N.; Buchholz, R.; Zamaninasab, M.; Muzic, K.; Moultaka, J.; Zensus, J. A. (2012) *"Flare emission from Sagittarius A** in J. Phys.: Conf. Ser., 372, 2022

- de Ugarte Postigo, A.; De Breuck, C.; Stanke, T.; Agurto, C.; **Valencia-S., M.**; Remy, A.; Montenegro, F.; Gorosabel, J.; Sanchez-Ramirez, R.; Fynbo, J. P. U. (2012) *"GRB 120514A: APEX observations of the submm counterpart"* GRB Coordinates Network, Circular Service, 13293, 1

- Zamaninasab, M.; Eckart, A.; Dovciak, M.; Karas, V.; Schoedel, R.; Witzel, G.; Sabha, N.; Garcia-Marin, M.; Kunneriath, D.; Muzic, K.; Straubmeier, C.; **Valencia-S, M.**; Zensus, J. A. (2011). *"Near-infrared polarimetry as a tool for testing properties of accreting supermassive black holes"* MNRAS, 413, 322

- Kunneriath, D.; Eckart, A.; Zamaninasab, M.; Witzel, G.; **Valencia-S, M.**; Sabha, N.; Garcia-Marin, M. (2011) *"Flare emission from Sagittarius A*"* in Mem. S.A.It, 82, 91

- Zamaninasab, M.; Witzel, G.; Eckart, A.; Sabha, N.; Dovciak, M.; Karas, V.; Schoedel, R.; Garcia-Marin, M.; Kunneriath, D.; Nishiyama, S.; Straubmeier, C.; **Valencia-Schneider, M.**; Zensus, A. (2011). *"Near Infrared Polarimetry as a Tool for Testing the Properties of Radiation from Sagittarius A*"* ASPC, 439, 323

- Eckart, A.; Zamaninasab, M.; Sabha, N.; Garcia-Marin, M.; Kunneriath, D.; Straubmeier, C.; Muzic, K.; Witzel, G.; Bremer, M.; **Valencia-Schneider, M.**; Karas, V.; Dovciak, M.; Morris, M. R.; Baganoff, F.; Schoedel, R.; Moultaka, J.; Buchholz, R. M.; Duschl, W.; Zensus, A. (2011) *"Coordinated Multi-Wavelength Observations of Variable Emission from the Galactic Center"* ASPC, 439, 294